Naturalness confronts nature: searches for supersymmetry with the CMS detector in pp collisions at $\sqrt{s} = 8$ and 13 TeV

Thesis by
Javier M. G. Duarte

In Partial Fulfillment of the Requirements for the
degree of
Doctor of Philosophy

CALIFORNIA INSTITUTE OF TECHNOLOGY
Pasadena, California

2017
(Defended August 11, 2016)

Javier M. G. Duarte
ORCID: 0000-0002-5076-7096

To my mother and sister.

ACKNOWLEDGMENTS

First, I thank my advisor, Maria Spiropulu. Her wisdom, experience, and warmth have shaped me as I've developed as a scientist. For her endless contributions to my life and career, I am in her debt.

I thank Maurizio Pierini for his intense mentorship beginning at CERN in 2011 and continuing to this day. Maurizio taught me how to be a modern particle physicist, by sharing his expertise in computing, statistics, and phenomenology. He was also invaluable in helping me prepare this manuscript.

I also thank Chris Rogan for guiding me during my first days of graduate school and for being a good friend. Cristián Peña and Dustin Anderson have been constant friends and fellow soldiers in graduate school. I thank my other colleagues in the Caltech CMS group for their help and advice during graduate school: Si Xie, Artur Apresyan, Jean-Roch Vlimant, and Adi Bornheim.

I thank my roommates and close friends: Ingmar Saberi, Tristan McKinney, Eric Quintero, and Evelyn Gomez. They continually inspire me and remind me to have fun every once in a while. I also thank the other two legs of our marathon running team, Alex Tuna and Phil Hebda, for their friendship, which has spanned many years and two continents, and for constantly challenging me to improve my marathon PR.

I dedicate this thesis to my mother, Bruny, and my sister, Rossy, for loving and supporting me throughout my life.

Finally, I thank my girlfriend, Kristen Jezior. Without her love, kindness, and humor, I would be lost.

This thesis is based upon work supported by the National Science Foundation Graduate Research Fellowship under Grant No. DGE-1144469 and the U.S. Department of Energy, Office of Science, Office of High Energy Physics under Award No. DE-SC0011925. Fermilab, where test beam studies were conducted, is operated by Fermi Research Alliance, LLC under Contract No. DE-AC02-07CH11359 with the United States Department of Energy.

ABSTRACT

In this thesis, we present two inclusive searches for supersymmetric particles at $\sqrt{s} = 8$ and 13 TeV using the razor variables and guided by the principle of naturalness. We build a framework to explore the natural supersymmetry parameter space of gluino and top squark masses and branching ratios, which is a unique attempt to cover this parameter space in a more complete way than ever before using LHC data. With this approach, the production of top squarks and gluinos are excluded below $\sim$ 700 GeV and $\sim$ 1.6 TeV, respectively, independent of the branching ratios, constituting one of the tightest constraints on natural supersymmetry from the LHC. Motivated by the need to mitigate the effects of multiple interactions per bunch crossing (pileup), an essential feature of present and future hadron colliders, in this thesis we also study the precision timing capabilities of a LYSO-based sampling calorimeter, and achieve a time resolution of $\sim$ 30 ps in electron test beam measurements. The achieved resolution corresponds to the precision needed to significantly reduce the inclusion of pileup particles in the reconstruction of the event of interest. This study is foundational in building an R&D program on precision timing for the high-luminosity LHC and other future hadron colliders. We also propose alternative simplified models to study Higgs-plus-jets events at the LHC, and reinterpret an excess observed at 8 TeV in the context of these models. Finally, we discuss a search for narrow resonances in the dijet mass spectrum at 13 TeV using the data-scouting technique at CMS, which records a smaller event format to increase the maximum recordable rate. For the benchmark models with a vector or axial-vector mediator that couples to quarks and dark matter particles, the dijet search excludes mediator masses from 0.5 TeV up to $\sim$ 2.7 TeV largely independent of the dark matter particle mass, which constitutes a larger exclusion than traditional mono-X searches at the LHC. In the plane of the dark matter-nucleon interaction cross section versus dark matter mass, the dijet search is also more sensitive than direct detection experiments for spin-dependent cross sections.

PUBLISHED CONTENT AND CONTRIBUTIONS

[1] Vardan Khachatryan et al. "Search for Supersymmetry Using Razor Variables in Events with b-Tagged Jets in pp Collisions at $\sqrt{s} = 8$ TeV". In: *Phys. Rev.* D91 (2015), p. 052018. DOI: 10.1103/PhysRevD.91.052018. arXiv: 1502.00300 [hep-ex].
J. M. G. D. was the lead data analyst for this search using CMS data and contributed to writing the manuscript for publication.

[2] Vardan Khachatryan et al. "Inclusive search for supersymmetry using razor variables in pp collisions at $\sqrt{s} = 13$ TeV". In: *Phys. Rev. D* (2016). [Phys. Rev.D95,012003(2017)]. DOI: 10.1103/PhysRevD.95.012003. arXiv: 1609.07658 [hep-ex].
J. M. G. D. performed the maximium-likelihood-fit-based background estimation and statistical interpretation using CMS data for this analysis and contributed to writing the manuscript for publication.

[3] D. Anderson et al. "On timing properties of LYSO-based calorimeters". In: *Nuclear Instruments and Methods in Physics Research Section A: Accelerators, Spectrometers, Detectors and Associated Equipment* 794 (2015), pp. 7–14. ISSN: 0168-9002. DOI: http://dx.doi.org/10.1016/j.nima.2015.04.013. URL: http://www.sciencedirect.com/science/article/pii/S0168900215004829.
J. M. G. D. participated in the test beam measurements at Fermilab, including recording and analyzing the data, and assisted in preparing the manuscript for publication.

[4] Vardan Khachatryan et al. "Search for dark matter particles in proton-proton collisions at $\sqrt{s} = 8$ TeV using the razor variables". In: *JHEP* 12 (2016), p. 088. DOI: 10.1007/JHEP12(2016)088. arXiv: 1603.08914 [hep-ex].
J. M. G. D. was one of the lead analysts for this analysis using CMS data, especially for the low-dijet-mass portion of the search, and edited the manuscript for publication.

TABLE OF CONTENTS

LIST OF ILLUSTRATIONS

LIST OF TABLES

Part I

Introduction, fundamentals, and naturalness

Chapter 1

INTRODUCTION

The standard model (SM) of particle physics is a fundamental description of nature composed of two main ingredients:

(a) a list of elementary particles and their quantum properties, and

(b) an inventory of the interactions of these particles through the fundamental forces (except for gravity): the strong force, the weak force, and the electromagnetic force.

The discovery of the Higgs boson, announced by the CMS and ATLAS collaborations on July 4, 2012 [1, 2], was thought to be one of the final missing pieces[1] that completes and confirms the SM as a description of nature. However, several theoretically- and experimentally-motivated questions remain unanswered. Three of the most important questions are:

(a) What is the origin of *dark matter* whose existence is inferred from measurements of galactic rotation curves [3, 4] and weak gravitational lensing observations of, for example, the "Bullet cluster" [5]?

(b) Do the strong, weak, and electromagnetic forces unify at a high energy scale?

(c) How does a fundamental scalar like the Higgs boson remain "light" when its mass is sensitive to new particles at high energy scales through radiative corrections?

In the 1970s, *supersymmetry* was proposed as a possible extension of spacetime symmetry that relates fermions and bosons [6, 7, 8, 9, 10]. Little more than a mathematical curiosity at first, supersymmetry emerged as the leading candidate for a theory of physics beyond the standard model in the

[1] Two other missing pieces are due to the strong CP problem, which demands the existence of something like an axion in Peccei–Quinn theory, and nonzero neutrino masses, which require the addition of a right-handed neutrinos.

1980s and 1990s, as it was understood that this principle may provide an economical and beautiful solution to three pressing issues in the SM by (a) providing a weakly interacting particle candidate for dark matter [11, 12], (b) exhibiting gauge coupling unification [13, 14, 15, 16, 17, 18], and (c) alleviating the fine-tuning of the Higgs mass [19, 20, 21, 22, 23, 24].

This thesis focuses on efforts to search for supersymmetric particles in proton-proton collisions and is divided into five parts. It is the story of how we examined the principal motivation for supersymmetry, identified the most relevant event topologies based on this guiding principle, and exhaustively searched the supersymmetric phase space using a signal-sensitive basis of observables, known as the *razor variables*.

In Part I, the SM, supersymmetry, and naturalness are introduced, motivating the search for natural SUSY. The razor approach to supersymmetric kinematics is detailed in Sec. 3.10. Part II describes the LHC and the CMS experiment, especially those aspects critical to the searches, such as the high-level trigger. In Part III, chapters 7 and 8 present two searches for natural SUSY performed at $\sqrt{s} = 8\,\text{TeV}$ and 13 TeV, which together represent a unique attempt to cover the phase space of natural SUSY in a more complete way than ever before.

Part IV motivates probing the TeV and multi- TeV scale with high-luminosity colliders as "the final hiding place" of natural SUSY. Chapter 9 discusses the requirements for detectors at future high-luminosity colliders, specifically the need for calorimeters with precision timing capabilities due to the high rate of simultaneous interactions per bunch crossing (pileup) anticipated. Finally, we present a proof-of-concept LYSO-based sampling calorimeter, and estimate its ultimate timing performance capability based on test-beam measurements.

Part VI is composed of two appendices related to other searches for new physics at the LHC. In Chapter A, we reinterpret an excess observed in $\text{H} + \text{jets}$ events at $\sqrt{s} = 8\,\text{TeV}$ and propose alternative simplified SUSY models to study this final state at $\sqrt{s} = 13\,\text{TeV}$. Chapter B describes an important search for exotic new physics in the dijet mass spectrum at $\sqrt{s} = 13\,\text{TeV}$ with far-reaching consequences for many different models. Partially motivated by the excess at 750 GeV in both the CMS [25] and ATLAS [26]

diphoton mass spectra[2], the search extends the previous dijet searches by searching in the low-mass end of the spectrum ($> 450\,\text{GeV}$) using the CMS data scouting technique. The dijet resonance search is also interpreted in the context of dark matter (DM) production at the LHC. In this scenario, the search is sensitive to the production of a vector or axial-vector mediator that couples to quarks and DM particles.

[2]More recent results using additional 13 TeV data collected in 2016 by CMS [27] and ATLAS [28] suggest the diphoton excess at 750 GeV is most likely a statistical fluctuation.

Chapter 2

FUNDAMENTALS

2.1 The standard model of particle physics

The standard model (SM) of particle physics is a renormalizable quantum field theory based on a gauge symmetry [29, 30]. A fundamental consequence of relativity and quantum mechanics is that there are only two types of particles: those with integer spins, whose wave functions are symmetric under particle exchange, called *bosons*, and those with half-integer spin, whose wave functions are anti-symmetric under particle exchange, called *fermions* [31]. The forces in the SM arise due to the exchange of spin-1 bosons among the spin-$\frac{1}{2}$ fermions that make up matter.

Each factor in the gauge symmetry group $\mathrm{SU}(3)_\mathrm{C} \times \mathrm{SU}(2)_\mathrm{L} \times \mathrm{U}(1)_Y$ corresponds to a fundamental force, represented by a gauge field, whose excitations are the gauge bosons that act as force carriers:

$$\begin{array}{ccccc} \mathrm{SU}(3)_\mathrm{C} & \times & \mathrm{SU}(2)_\mathrm{L} & \times & \mathrm{U}(1)_Y\,. \\ \downarrow & & \downarrow & & \downarrow \\ G^\alpha_\mu & & W^a_\mu & & B_\mu \\ \alpha = 1,...,8 & & a = 1,2,3 & & \end{array}$$

There are eight bosons, called gluons, represented by the fields G^α_μ and associated with the factor $\mathrm{SU}(3)_\mathrm{C}$. The three bosons, represented by the fields W^a_μ and associated with the factor $\mathrm{SU}(2)_\mathrm{L}$, and the boson, represented by the field B_μ and associated with the factor $\mathrm{U}(1)_Y$, mix to form the $\mathrm{W}^\pm$ and Z bosons, and the photon γ.

The matter fields are fermions, which fall into two categories: the quarks u, d, c, s, t, and b, which participate in the strong interactions, and the leptons, e, μ, τ, ν_e, ν_μ, and ν_τ, which do not. The fermions, represented by left- and right-handed Weyl spinors, also naturally fit into three generations of matter, as displayed in Fig. 2.1.

The second ingredient of the SM, an inventory of the interactions between

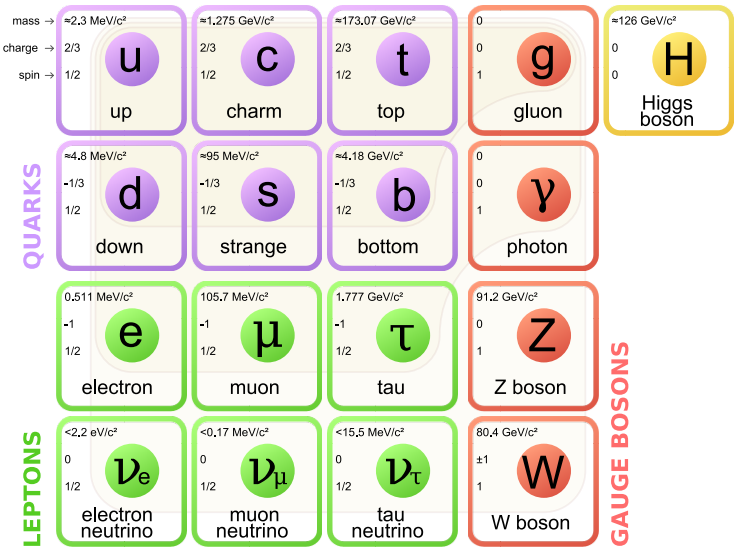

Figure 2.1: The particles in the standard model.

the particles, is given by the Lagrangian density,

$$\begin{aligned}
\mathcal{L}_{\text{SM}} = & -\frac{1}{4}B_{\mu\nu}B^{\mu\nu} - \frac{1}{4}W^{a}_{\mu\nu}W^{a\mu\nu} - \frac{1}{4}G^{\alpha}_{\mu\nu}G^{\alpha\mu\nu} && \text{(gauge terms)} \\
& + \bar{\ell}_{\text{L}}\tilde{\sigma}^{\mu}iD_{\mu}\ell_{\text{L}} + \bar{e}_{\text{R}}\sigma^{\mu}iD_{\mu}e_{\text{R}} + (\text{h.c.}) \\
& + \bar{\nu}_{\text{R}}\sigma^{\mu}iD_{\mu}\nu_{\text{R}} + (\text{h.c.}) && \text{(lepton kinetic and gauge terms)} \\
& + \bar{q}_{\text{L}}\tilde{\sigma}^{\mu}iD_{\mu}q_{\text{L}} + \bar{u}_{\text{R}}\sigma^{\mu}iD_{\mu}u_{\text{R}} + (\text{h.c.}) \\
& + \bar{d}_{\text{R}}\sigma^{\mu}iD_{\mu}d_{\text{R}} + (\text{h.c.}) && \text{(quark kinetic and gauge terms)} \\
& + \mathcal{L}_{\text{Higgs}} + \mathcal{L}_{\text{Yukawa}}\,, && \text{(Higgs and Yukawa terms)}
\end{aligned} \tag{2.1}$$

where D_μ is the gauge-covariant derivative, $q_{\text{L}} = \binom{u_{\text{L}}}{d_{\text{L}}}$ and $\ell_{\text{L}} = \binom{e_{\text{L}}}{\nu_{\text{L}}}$ are $\text{SU}(2)_{\text{L}}$ doublets, and the three-component generation indices are suppressed. Tab. 2.1 summarizes another way to visualize the interactions of the particles, which are the representations in which the matter fields transform under the SM gauge group. The Higgs terms $\mathcal{L}_{\text{Higgs}}$ are discussed in Sec. 2.2, while the Yukawa terms $\mathcal{L}_{\text{Yukawa}}$ are discussed in Sec. 2.3.

2.2 Electroweak symmetry breaking

A central feature of nonabelian gauge theories, or *Yang-Mills theories* [32], is that the gauge bosons are massless due to the fact that the gauge symmetry forbids explicit mass terms in the Lagrangian. Thus Yang-Mills theory

field	$SU(3)_C$	$SU(2)_L$	$U(1)_Y$
q	**3**	**2**	$1/6$
$\overline{u}_R$	$\overline{\mathbf{3}}$	**1**	$-2/3$
$\overline{d}_R$	$\overline{\mathbf{3}}$	**1**	$1/3$
ℓ	**1**	**2**	$-1/2$
$\overline{e}_R$	**1**	**1**	1
h	**1**	**2**	$1/2$

Table 2.1: Table summarizing the representations in which the matter fields transform under the standard model gauge group. **n** ($\overline{\mathbf{n}}$) is the fundamental (antifundamental) representation of SU(n). For the $U(1)_Y$ factor, the representations are labeled by the weak hypercharge Y. The electric charge is given by $Q = T_{3L} + Y$.

gives rise to massless spin-1 particles. Concurrently, whenever a continuous symmetry is *spontaneously broken*[1], *Nambu-Goldstone bosons* [33, 34] – one for each generator of the broken symmetry – appear in the spectrum of possible excitations. These additional bosons are massless spin-0 particles.

In the early 1960s, these massless bosons, both from nonabelian gauge symmetry and spontaneous symmetry breaking, were seen as inconsistent with nature since they were not observed. In 1962, Anderson realized a mechanism for incorporating spontaneous symmetry breaking into nonrelativistic gauge theories "without any difficulties involving either zero-mass Yang-Mills gauge bosons or zero-mass Goldstone bosons. These two types of bosons seem capable of 'canceling each other out' and leaving finite mass bosons only" [35]. In 1964, this approach was extended to relativisitic gauge theories through the introduction of a scalar field [36, 37, 38, 39, 40, 41]. In the SM, the mechanism of electroweak symmetry breaking is a framework to keep the structure of gauge symmetry and interactions at high energy, and still generate the observed masses of the $W^{\pm}$ and Z gauge bosons [29, 42, 43].

The part of the SM Lagrangian that accomplishes this is:

$$\mathcal{L}_{\text{Higgs}} = (D_\mu \Phi)^\dagger (D^\mu \Phi) - V(\Phi) \,, \quad V(\Phi) = -\mu^2 \Phi^\dagger \Phi + \lambda (\Phi^\dagger \Phi)^2 \,, \quad (2.2)$$

where the field Φ is a complex, spin-0, self-interacting $SU(2)_L$ doublet with

[1] Spontaneous symmetry breaking means the equations of the dynamics are exactly symmetric, but they admit solutions that are not.

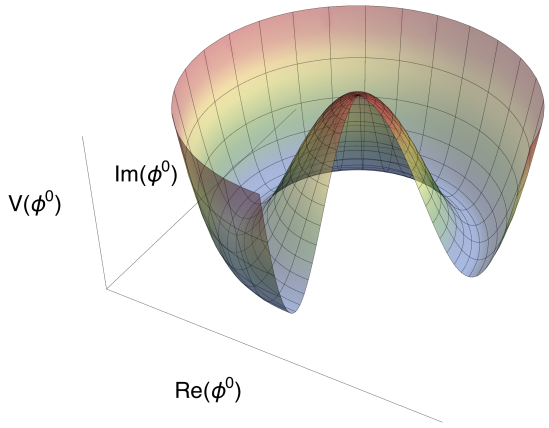

Figure 2.2: The shape of the "Mexican hat" potential. The minimum of the potential occurs at a field value that is not 0 [44].

weak hypercharge $Y = 1/2$:

$$\Phi = \begin{pmatrix} \phi^+ \\ \phi^0 \end{pmatrix} . \tag{2.3}$$

If $\mu^2 > 0$, then the potential will have a "Mexican hat" shape, illustrated in 2.2, and the minimum of the potential will occur at a value of the field that is not $\mathrm{SU}(2)_\mathrm{L} \times \mathrm{U}(1)_Y$ invariant. Due to this, Φ acquires a nonzero vacuum expectation value (*vev*), corresponding to the minimum of the potential,

$$\langle \Phi \rangle_0 \equiv \langle 0|\Phi|0\rangle = \frac{1}{\sqrt{2}} U(x) \begin{pmatrix} 0 \\ v \end{pmatrix} , \qquad v = \sqrt{\frac{\mu^2}{\lambda}} , \tag{2.4}$$

where $U(x)$ is a unitary transformation that rotates the field to the other degenerate solutions. Since the vev is still symmetric under a $\mathrm{U}(1)$ subgroup of the full electroweak symmetry, we say the electroweak symmetry $\mathrm{SU}(2)_\mathrm{L} \times \mathrm{U}(1)_Y$ is *spontaneously broken* to $\mathrm{U}(1)_\mathrm{EM}$.

This mechanism is responsible for generating the masses of the gauge bosons in the SM, as can be seen by evaluating the covariant derivative in Eqn. 2.2,

$$D_\mu \Phi = (\partial_\mu - i g_2 \frac{\sigma_a}{2} W^a_\mu - i g_1 \frac{1}{2} B_\mu)\Phi , \tag{2.5}$$

on the vacuum Higgs field. In this case, the kinetic term is:

$$
\begin{aligned}
|D_\mu \Phi|^2 &= \frac{1}{2}\left|\begin{pmatrix} \partial_\mu - \frac{i}{2}(g_2 W_\mu^3 + g_1 B_\mu) & -\frac{ig_2}{2}(W_\mu^1 - iW_\mu^2) \\ -\frac{ig_2}{2}(W_\mu^1 + iW_\mu^2) & \partial_\mu + \frac{i}{2}(g_2 W_\mu^3 - g_1 B_\mu) \end{pmatrix} \begin{pmatrix} 0 \\ v \end{pmatrix}\right|^2 \\
&= \frac{1}{8}\left(g_2^2 v^2 |W_\mu^1 + iW_\mu^2|^2 + v^2 |g_2 W_\mu^3 - g_1 B_\mu|^2\right) \\
&= m_W^2 W_\mu^+ W^{-\mu} + \frac{1}{2} m_Z^2 Z_\mu Z^\mu + \frac{1}{2} m_\gamma^2 A_\mu A^\mu,
\end{aligned} \tag{2.6}
$$

where we can identify three field combinations, $W_\mu^\pm$ and Z_μ, which have bilinear mass terms, and a fourth A_μ, which does not:

$$
W_\mu^\pm = \frac{1}{\sqrt{2}}(W_\mu^1 \mp iW_\mu^2)\,, \qquad m_W = \frac{1}{2} v g_2\,, \tag{2.7}
$$

$$
Z_\mu = \frac{g_2 W_\mu^3 - g_1 B_\mu}{\sqrt{g_1^2 + g_2^2}}\,, \qquad m_Z = \frac{1}{2} v \sqrt{g_1^2 + g_1^2}\,, \tag{2.8}
$$

$$
A_\mu = \frac{g_2 W_\mu^3 + g_1 B_\mu}{\sqrt{g_1^2 + g_2^2}}\,, \qquad m_\gamma = 0. \tag{2.9}
$$

The $W^\pm$ and Z bosons have acquired mass, while the photon γ remains massless.

An important consequence of this symmetry breaking mechanism is the emergence of a physical spin-0 boson [37, 38]. If we expand the field around its potential minimum

$$
\Phi(x) = \frac{1}{\sqrt{2}} U(x) \begin{pmatrix} 0 \\ v + H(x) \end{pmatrix} \tag{2.10}
$$

and write out the terms associated to this field, we find

$$
\mathcal{L}_{\text{Higgs}} \supset \frac{1}{2}(\partial^\mu H)^2 - \lambda v^2 H^2 - \lambda v H^3 - \frac{\lambda}{4} H^4\,, \tag{2.11}
$$

which means this scalar boson, called the *Higgs boson*, is self-interacting and has a mass squared of $m_H^2 = 2\lambda v^2$ at tree-level.

2.3 Fermion masses

As proposed by Weinberg [29], fermions acquire mass through interaction with the Φ field, which has a nonzero vev. This is accomplished by adding Yukawa terms to the Lagrangian for each generation,

$$
\mathcal{L}_{\text{Yukawa}} = -y_e \bar{\ell}_L \Phi e_R - y_u \bar{q}_L \Phi u_R - y_d \bar{q}_L \tilde{\Phi} d_R + (\text{h.c.})\,, \tag{2.12}
$$

where the doublet $\tilde{\Phi} = i\sigma_2\Phi^*$ with hypercharge $Y = -1/2$ is needed to generate masses for the down-type quarks. Then we can identify the fermion masses as

$$m_{\mathrm{e}} = \frac{y_e v}{2} , \qquad m_{\mathrm{u}} = \frac{y_{\mathrm{u}} v}{2} , \qquad m_{\mathrm{d}} = \frac{y_{\mathrm{d}} v}{2} . \tag{2.13}$$

Besides giving masses to the fermions, the Yukawa terms have another important consequence: they allow the fermions to affect the observed mass of the Higgs boson through quantum corrections.

Chapter 3

THE HIERARCHY PROBLEM, NATURALNESS, AND SUPERSYMMETRY

3.1 The hierarchy problem and naturalness in the standard model

The leading quantum correction to the Higgs mass is due to the large Yukawa coupling of the top quark, which gives the top quark its large mass. In an effective field theory approach, where momenta of virtual particles are cut off at the scale Λ_{UV}, we can compute the top quark's contribution in the SM to leading order [45],

$$m_{\text{H}}^2 = m_{\text{H(bare)}}^2 + \Delta(m_{\text{H}}^2) \tag{3.1}$$

$$\Delta(m_{\text{H}}^2) = \quad + \quad \cdots \tag{3.2}$$

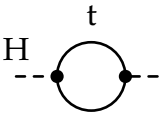

$$= -\frac{3|y_{\text{t}}|^2}{8\pi^2}\Lambda_{\text{UV}}^2 + \cdots\,, \tag{3.3}$$

The quadratic dependence in Eqn. 3.3 on Λ_{UV}, usually taken to be the Planck scale 10^{19} GeV, means the Higgs mass is sensitive to new physics in the ultraviolet. Taken literally, this sensitivity implies an enormous fine tuning of $m_{\text{H(bare)}}^2$ to achieve almost perfect cancellation[1] with $\Delta(m_{\text{H}}^2)$ in order to explain how m_{H} is measured to be so small at 125.09 ± 0.24 GeV [46]. The conundrum of how a light fundamental scalar particle can exist in the presence of (presumably) new physics in the ultraviolet is called the *hierarchy problem* or the *naturalness problem* and is one of the key motivations for new physics at the TeV scale, especially *supersymmetry*.

3.2 Renormalization group running in the standard model

In the renormalization group (RG) approach to quantum field theory, the Lagrangian parameters may be thought of as "running" parameters that depend on the energy scale μ of a given physical process. The beta function

[1] to 1 part in 10^{34}

$\beta(g)$ encodes the dependence of a coupling g on μ,

$$\beta(g) = \frac{\mathrm{d}g}{\mathrm{d}\log\mu} \,. \tag{3.4}$$

By integrating the beta function, we obtain a relationship between the couplings evaluated at different energy scales. The beta functions for the gauge couplings in the SM may be computed by considering loop diagrams up to a certain order. The one-loop beta functions for $g_1 = \sqrt{5/3}g'$, $g_2 = g$, and $g_3 = g_\mathrm{s}$ are

$$\frac{\mathrm{d}g_1}{\mathrm{d}\log\mu} = \frac{g_1^3}{20\pi^2}\left(\sum_{\text{Weyl ferm.}} \frac{1}{2}Y^2 + \sum_{\mathbb{C}\text{ scalars}} \frac{1}{4}Y^2\right) \tag{3.5}$$

$$= \frac{g_1^3}{20\pi^2}\left(\frac{41}{8}\right) \,, \tag{3.6}$$

$$\frac{\mathrm{d}g_2}{\mathrm{d}\log\mu} = \frac{g_2^3}{16\pi^2}\left(-\frac{11}{3}\times 2 + \frac{2}{3}\sum_{\text{Weyl ferm.}\in\mathbf{2}} \frac{1}{2} + \frac{2}{3}\sum_{\mathbb{C}\text{ scalars}\in\mathbf{2}} \frac{1}{4}\right) \tag{3.7}$$

$$= \frac{g_2^3}{16\pi^2}\left(-\frac{19}{6}\right) \,, \tag{3.8}$$

$$\frac{\mathrm{d}g_3}{\mathrm{d}\log\mu} = \frac{g_3^3}{16\pi^2}\left(-\frac{11}{3}\times 3 + \frac{2}{3}\sum_{\text{Weyl ferm.}\in\mathbf{3}} \frac{1}{2}\right) \tag{3.9}$$

$$= \frac{g_3^3}{16\pi^2}\left(-7\right) \,, \tag{3.10}$$

where g_s, g, and g' are the gauge couplings for the gauge groups $\mathrm{SU}(3)_\mathrm{C}$, $\times\mathrm{SU}(2)_\mathrm{L}$, and $\times\mathrm{U}(1)_Y$, respectively. The running of these couplings, extrapolated all the way up to the Planck scale (assuming there is no new physics) is shown in Fig. 3.2 using with the three-loop RG equations and including the two-loop threshold corrections at the weak scale [47]. Given the particle content of the SM and assuming no additional particles, the gauge couplings do not appear to intersect near the mass scale of 10^{16} GeV, an essential feature of grand unification theories (GUTs) [48, 45]. Instead, if there are new particles that interact via the SM forces, they will modify the running of the coupling constants leaving open the possibility of grand unification.

Vacuum instability

The one-loop beta functions for the top-quark Yukawa coupling y_t and the Higgs quartic coupling λ in the SM may be computed from one-loop dia-

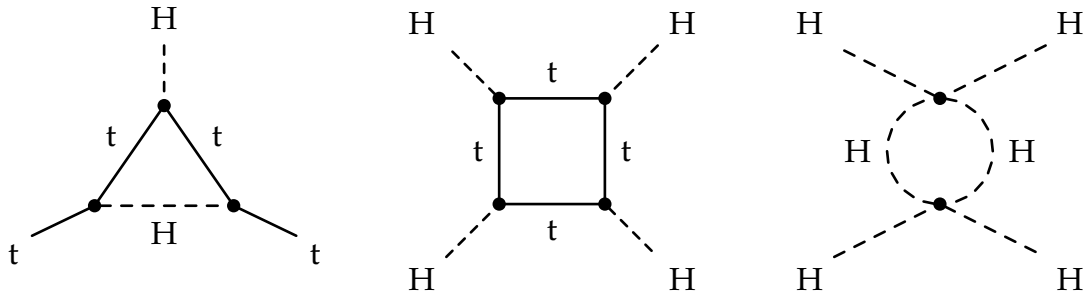

Figure 3.1: Example one-loop diagrams contributing to the running of y_t and λ [44].

grams such as those shown in Fig 3.1:

$$16\pi^2 \frac{dy_t}{d\log\mu} = -\frac{17}{20}g_1^2 y_t - \frac{9}{4}g_2^2 y_t - 8g_3^2 y_t + \frac{9}{2}y_t^3 \,, \tag{3.11}$$

$$16\pi^2 \frac{d\lambda}{d\log\mu} = -\frac{9}{5}g_1^2\lambda - 9g_2^2\lambda + \frac{27}{100}g_1^4 + \frac{9}{10}g_2^2 g_1^2 + \frac{9}{4}g_2^4 + 12\lambda^2 + 12\lambda y_t^2 - 12y_t^4 \,. \tag{3.12}$$

The running of λ is of particular interest because if it runs to $\lambda < 0$, the present electroweak vacuum of the SM may correspond to a local minimum, or metastable "false vacuum," which will eventually decay [49, 50]. Based on the running of these two Lagrangian parameters, we can visualize the SM phase diagram in (m_H, m_t), divided into regions of absolute stability ($\lambda > 0$ for all μ), metastability ($\lambda < 0$ for some μ but with a long lifetime), and instability ($\lambda < 0$ for some μ and a short lifetime). Ref. [47] computes with three-loop RG equations and two-loop threshold corrections at the weak scale as seen in Fig. 3.2. Curiously, if the SM is valid up to the Planck scale without any new physics, the SM vacuum appears to be teetering on the edge between metastability and absolute stability [47].

3.3 Supersymmetry

Supersymmetry (SUSY) is a proposed symmetry of spacetime that introduces a bosonic (fermionic) partner for every fermion (boson) [9, 7, 8, 51, 52, 10, 53, 54, 6]. For many years, such a symmetry was thought to be impossible since in 1967, Coleman and Mandula [55] published their no-go theorem that says internal symmetries, those that act on internal degrees of freedom (like spin) cannot be combined with spacetime symmetries in a nontrivial way. SUSY evades this theorem because it is based on a *super Lie*

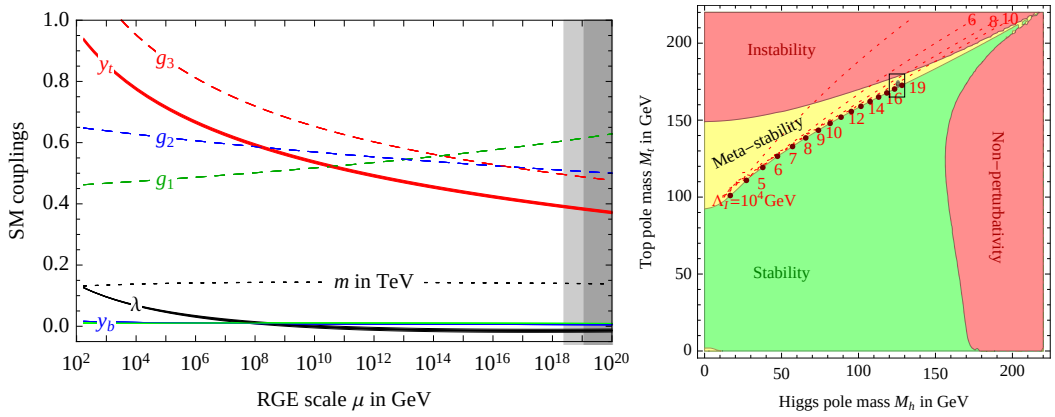

Figure 3.2: Renormalization of the SM gauge couplings $g_1 = \sqrt{5/3}g'$, g_2, g_3, of the top, bottom and τ couplings (y_t, y_b, y_τ), of the Higgs quartic coupling λ, and of the Higgs mass parameter m_H (left) and SM phase diagram in terms of Higgs and top pole masses (right). The plane is divided into regions of absolute stability, metastability, instability of the SM vacuum, and nonperturbativity of the Higgs quartic coupling. The top Yukawa coupling becomes non-perturbative for $m_t > 230\,\text{GeV}$. The dotted contour-lines show the instability scale Λ_I assuming $\alpha_3(m_Z) = 0.1184$ [47].

algebra, which may include fermionic symmetries and anticommutation relations as well as the usual bosonic symmetries and commutation relations.

Supersymmetric extensions of the SM are compelling mainly because they

(a) yield a solution to the hierarchy problem, alleviating the fine-tuning of fundamental parameters [19, 20, 21, 22, 23, 24], explained further in Sec. 3.5.

(b) exhibit gauge coupling unification [13, 14, 15, 16, 17, 18], and

(c) provide a weakly interacting particle candidate for dark matter [11, 12].

SUSY can be thought of as an extension of the usual group of spacetime symmetries, known as the Poincaré group. This group has generators related to translation symmetry, P_m, and Lorentz symmetry, $M_{mn} = -M_{nm}$, which form a Lie algebra:

$$\begin{aligned}
[P_m, P_n] &= 0 \\
[P_m, M_{np}] &= i(\eta_{mn}P_p - \eta_{mp}P_n) \\
[M_{mm}, M_{pq}] &= i(\eta_{mp}M_{np} - \eta_{np}M_{mq} + \eta_{nq}M_{mp} - \eta_{mq}M_{np})\,. \qquad (3.13)
\end{aligned}$$

As shown by Coleman and Mandula [55], the only way to extend this symmetry with a new internal symmetry group G with bosonic generators B_r and Lie algebra,

$$[B_r, B_s] = f_{rs}{}^t B_t \,, \tag{3.14}$$

with structure functions $f_{rs}{}^t$, is if the extended symmetry group is simply the direct product (Poincaré) $\times$ G with a trivial Lie algebra,

$$[B_r, P_m] = [B_r, M_{mn}] = 0 \,. \tag{3.15}$$

However, SUSY exploits a loophole in the Coleman-Mandula theorem, which only considers bosonic symmetry generators, by incorporating fermionic symmetry generators Q that generate SUSY transformations,

$$Q|\text{boson}\rangle = |\text{fermion}\rangle, \quad Q|\text{fermion}\rangle = |\text{boson}\rangle \,. \tag{3.16}$$

Supersymmetries can be combined with the spacetime symmetries in a way that mixes the two symmetries, as exemplified by the super Lie algebra for $\mathcal{N} = 1$ SUSY,

$$\begin{aligned} \{Q_\alpha, \overline{Q}_{\dot\beta}\} &= 2\sigma^m_{\alpha\dot\beta} P_m \\ \{Q_\alpha, Q_\beta\} &= \{\overline{Q}_{\dot\alpha}, \overline{Q}_{\dot\beta}\} = 0 \\ [P_m, Q_\alpha] &= [P_m, \overline{Q}_{\dot\alpha}] = 0 \,. \end{aligned} \tag{3.17}$$

In other words, two SUSY generators can combine to generate a spacetime translation.

The most economical supersymmetric extension of the standard model is the Minimal Supersymmetric Standard Model (MSSM). For supersymmetric theories, the Lagrangian can be written in terms of vector superfields $V(x, \theta, \overline{\theta})$ and chiral superfields $\Phi_l(x, \theta, \overline{\theta})$ that are functions of *superspace*, an extension of spacetime that includes anticommuting Grassmanian variables θ and $\overline{\theta}$. Tab 3.1 shows the particles of the MSSM, described by chiral superfields $Q_i, U_i^c, L_i, E_i^c, H_u, H_d$, and the representations in which they transform under the MSSM gauge group.

The MSSM Lagrangian can be split into three terms, the Kähler potential $K(\Phi_l, \Phi_l^\dagger, V)$, which describes the kinetic and gauge-covariant terms, a superpotential $W(\Phi_l)$, which describes the mass and interaction terms, and a

	$SU(3)_C$	$SU(2)_L$	$U(1)_Y$
Q	$\mathbf{3}$	$\mathbf{2}$	$1/6$
U^c	$\overline{\mathbf{3}}$	$\mathbf{1}$	$-2/3$
D^c	$\overline{\mathbf{3}}$	$\mathbf{1}$	$1/3$
L	$\mathbf{1}$	$\mathbf{2}$	$-1/2$
E^c	$\mathbf{1}$	$\mathbf{1}$	1
H_u	$\mathbf{1}$	$\mathbf{2}$	$1/2$
H_d	$\mathbf{1}$	$\mathbf{2}$	$-1/2$

Table 3.1: Table summarizing the representations in which the chiral superfields transform under the MSSM gauge group. See Tab. 2.1 for a description of the columns.

gauge kinetic term $G(V)$,

$$\begin{aligned}\mathcal{L}_{\text{MSSM}} &= \int \mathrm{d}^4\theta K(\Phi_l, \Phi_l^\dagger, V) + \left(\int \mathrm{d}^2\theta W(\Phi_l) + \text{h.c.}\right) + \left(\int \mathrm{d}^2\theta G(V) + \text{h.c.}\right) \\ &= \int \mathrm{d}^4\theta \sum_V \Phi_l^\dagger e^{gV}\Phi_l + \left(\int \mathrm{d}^2\theta W(\Phi_l) + \text{h.c.}\right) + \left(\int \mathrm{d}^2\theta \frac{1}{4}\mathcal{W}^\alpha\mathcal{W}_\alpha + \text{h.c.}\right) ,\end{aligned} \tag{3.18}$$

where $\mathcal{W}_\alpha$ is the vector superfield strength[2] and the index l runs over all the matter superfields $\Phi_l = Q_i, U_i^c, L_i, E_i^c, H_u, H_d$. The superpotential can be split into two components based on R-parity [56], a discrete $\mathbb{Z}_2$ symmetry often assumed in SUSY model building, defined for each particle as

$$P_R = (-1)^{3(B-L)+2s} , \tag{3.19}$$

where B is the baryon number, L is the lepton number, and s is the spin of the particle. With this assignment, all SM particles have even R-parity ($P_R = +1$), while the superpartners have odd R-parity ($P_R = -1$). The R-parity conserving terms in the superpotential are

$$W_{\text{RPC}} = -U^c\mathbf{y}_u Q H_u + D^c\mathbf{y}_d Q H_d + E^c\mathbf{y_e} L H_d + \mu H_u H_d , \tag{3.20}$$

and the R-parity violating terms are

$$W_{\text{RPV}} = \frac{1}{2}\lambda^{ijk} L_i L_j E_k^c + \lambda'^{ijk} L_i Q_j D_k^c + \mu'^i H_u L_i + \frac{1}{2}\lambda''^{ijk} U_i^c D_j^c D_k^c . \tag{3.21}$$

If R-parity is conserved, there are three important phenomenological consequences:

[2]The vector superfield strength is $\mathcal{W}_\alpha = -\frac{1}{4}\overline{\mathcal{D}}^2(e^{-V}\mathcal{D}_\alpha e^V)$.

- The lightest superparter, called the "lightest supersymmetric particle" or LSP, must be stable.
- Each superpartner other than the LSP must eventually decay into a state that contains an odd number of LSPs (usually just one).
- In collider experiments, superpartners can only be produced in even numbers (usually two).

In particular, at a proton-proton collider like the LHC (described in Ch. 4), the SUSY processes with the largest cross sections are the pair production of gluinos and squarks through gluon-gluon and gluon-quark fusion, which are among the reactions of QCD-level strength [45]:

$$gg \to \widetilde{g}\widetilde{g}, \widetilde{q}_i\overline{\widetilde{q}}_j \,, \tag{3.22}$$

$$gq \to \widetilde{g}\widetilde{q}_i \,, \tag{3.23}$$

$$q\overline{q} \to \widetilde{g}\widetilde{g}, \widetilde{q}_i\overline{\widetilde{q}}_j \,, \tag{3.24}$$

$$qq \to \widetilde{q}_i\widetilde{q}_j \,. \tag{3.25}$$

Some of the diagrams corresponding to the gluon-gluon fusion reactions in Eqn. 3.22 are depicted in Fig. 3.3 [45]. Assuming all SUSY particles other than those being pair-produced are decoupled from the theory (as is done in the simplified model approach, see Sec. 3.8 [57, 58, 59, 60, 61, 62]), the SUSY pair-production cross sections for each SUSY particle may be computed at next-to-leading-order (NLO) plus next-to-leading-logarithm (NLL) accuracy [63, 64, 65, 66, 67, 68, 69]. For the $\sqrt{s} = 8\,\text{TeV}$ and $13\,\text{TeV}$ LHC, these SUSY production cross sections are plotted as a function of the superpartner mass in Fig. 3.4. Due to the hierarchy of SUSY cross sections, there is a corresponding hierarchy in terms of discovery potential at the LHC, with the largest mass reach for gluinos then squarks then top and bottom squarks then electroweak SUSY partners (see Sec.3.4) then, finally, sleptons.

3.4 Electroweak supersymmetric sector

In the MSSM, the description of electroweak symmetry breaking involves two complex Higgs doublets, $H_u = (H_u^+, H_u^0)$ and $H_d = (H_d^0, H_d^-)$. The neutral components of the Higgs doublets, H_u^0 and H_d^0, both get vacuum expectation values,

$$v_u = \langle H_u^0 \rangle \,, \qquad\qquad v_d = \langle H_d^0 \rangle \,, \tag{3.26}$$

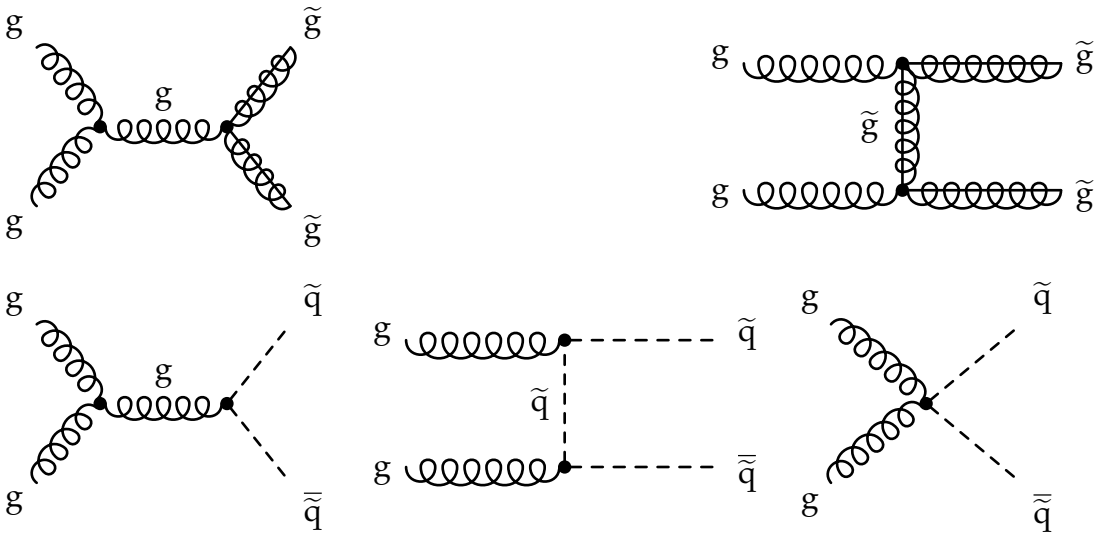

Figure 3.3: Example diagrams for the production of gluinos and squarks from gluon-gluon fusion [45, 44].

with their ratio being written as $\tan\beta = v_u/v_d$.

The superpartners of the neutral gauge bosons (neutral gauginos), and the fermionic partners of the neutral Higgs bosons (neutral higgsinos), $\psi^0 = (\widetilde{B}, \widetilde{W}^0, \widetilde{H}_d^0, \widetilde{H}_u^0)$, mix to form the *neutralinos* $(\widetilde{\chi}_1^0, \widetilde{\chi}_2^0, \widetilde{\chi}_3^0, \widetilde{\chi}_4^0)$. Similarly, the superpartners of the charged gauge bosons (charged gauginos) and the fermionic partners of the charged Higgs bosons (charged higgsinos), $\psi^\pm = (\widetilde{W}^+, \widetilde{H}_u^+, \widetilde{W}^-, \widetilde{H}_d^-)$ mix to form the charginos $(\widetilde{\chi}_1^+, \widetilde{\chi}_2^+, \widetilde{\chi}_1^-, \widetilde{\chi}_2^-)$. In this gauge-eigenstate basis, the neutralino and chargino mass terms in the Lagrangian are

$$\mathcal{L}_{\text{MSSM}} \supset -\frac{1}{2}\psi^{0T}\mathbf{M}_N\psi^0 - \frac{1}{2}\psi^{\pm T}\mathbf{M}_C\psi^\pm + \text{h.c.}\,, \tag{3.27}$$

with the neutralino mass matrix,

$$\mathbf{M}_N = \begin{pmatrix} M_1 & 0 & -m_Z s_W c_\beta & m_Z s_W s_\beta \\ 0 & M_2 & -m_Z c_W c_\beta & -m_Z c_W s_\beta \\ -m_Z s_W c_\beta & m_Z c_W c_\beta & 0 & -\mu \\ m_Z s_W s_\beta & -m_Z c_W s_\beta & \mu & 0 \end{pmatrix}, \tag{3.28}$$

where $s_W = \sin\theta_W$, $c_W = \cos\theta_W$, θ_W is the weak mixing angle, $s_\beta = \sin\beta$, $c_\beta = \cos\beta$, and M_2 and M_1 are the wino and bino masses, respectively. Likewise, the chargino mass matrix is

$$\mathbf{M}_C = \begin{pmatrix} 0 & \mathbf{X}^T \\ \mathbf{X} & 0 \end{pmatrix}, \text{ where } \mathbf{X} = \begin{pmatrix} M_2 & \sqrt{2}m_W s_\beta \\ \sqrt{2}m_W c_\beta & \mu \end{pmatrix} \tag{3.29}$$

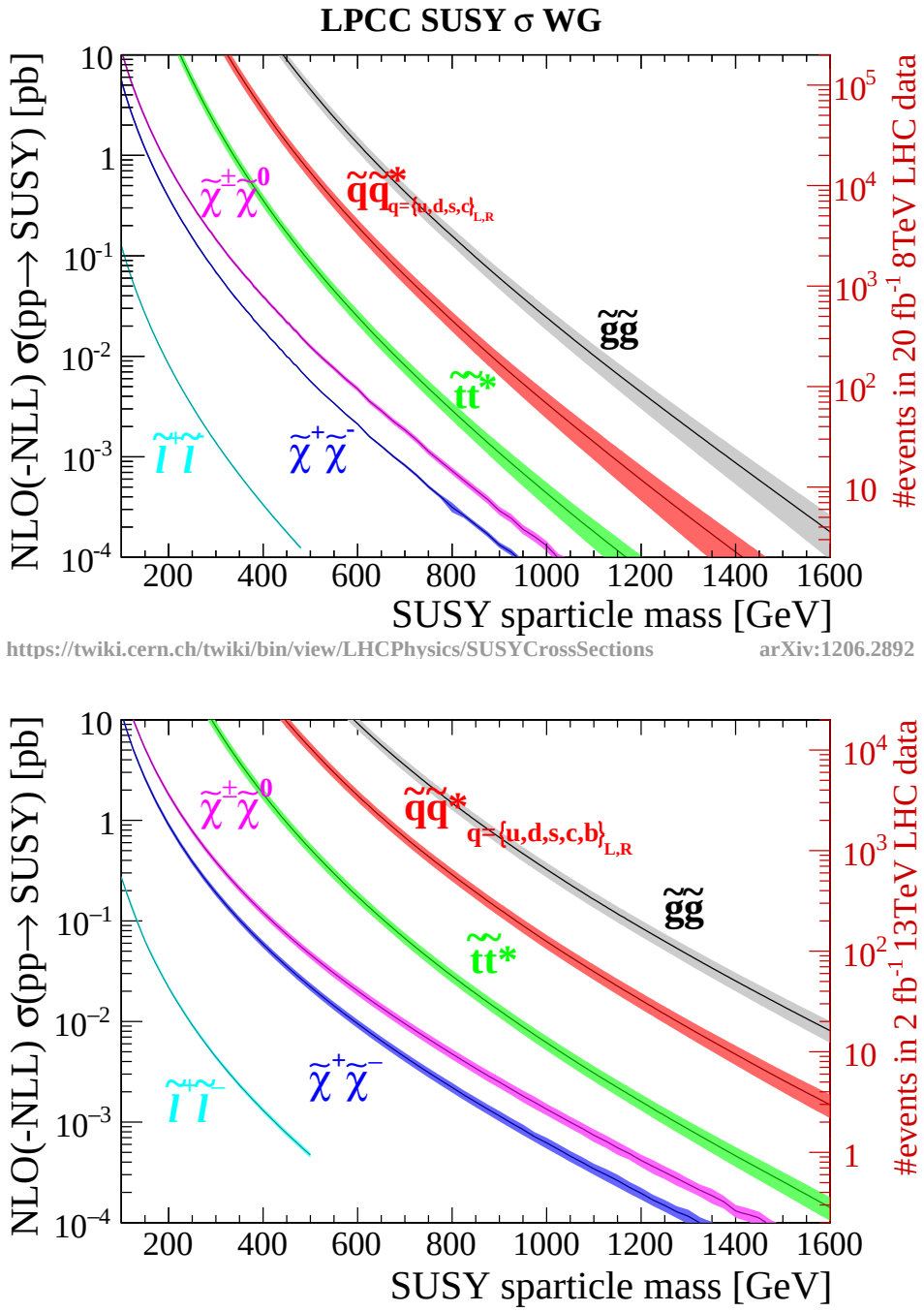

Figure 3.4: The production cross sections of SUSY particles as a function of their masses computed at next-to-leading-order (NLO) with next-to-leading-logarithm (NLL) resummation at the LHC for 8 TeV (top) and 13 TeV (bottom) [63, 64, 65, 66, 67, 68, 69, 70, 71, 72, 44].

The eigenvalues of these matrices are the masses of the neutralinos and charginos.

3.5 Naturalness in supersymmetry

For SUSY to provide a "natural" solution to the gauge hierarchy problem, the top squark, bottom squark, and gluino must have masses below a few TeV, making them accessible at the CERN LHC. To make this statement quantitative, we first need to define a measure of fine-tuning, such as [73, 74]:

$$\Delta = \left| \frac{\Delta(m_{\mathrm{H}}^2)}{m_{\mathrm{H}}^2} \right| . \tag{3.30}$$

Other measures of fine-tuning are possible, such as the one given by Barbieri and Giudice [75, 76]:

$$\Delta_x = \left| \frac{\partial \log m_{\mathrm{Z}}^2}{\partial \log x} \right| , \tag{3.31}$$

which quantifies the sensitivity of the Z-boson mass to an underlying, high-energy scale parameter x. Although no single measure of fine-tuning is perfect, each has its merits and can act as a proxy for our intuitive sense of fine-tuning [77]. For a model to be natural, it is traditionally desired that $\Delta \lesssim 10$, which corresponds to 10% fine-tuning.

In the decoupling limit of the MSSM at tree-level, the mass of the physical Higgs boson satisfies

$$m_{\mathrm{H}}^2 = -2(m_{\mathrm{H_u}}^2 + |\mu|^2) = m_{\mathrm{Z}}^2 \cos^2(2\beta) . \tag{3.32}$$

Due to this tree-level relation between μ, which controls the masses of the higgsinos, and m_{H}^2, we expect both μ to be small and the higgsinos to be light in order to keep m_{H}^2 small. When μ is small ($\mu \ll M_1, M_2$), the two lightest neutralinos and the lightest chargino are higgsino-like and their masses are close together [78],

$$m_{\widetilde{\chi}_1^0} = |\mu| + \frac{m_{\mathrm{Z}}^2(1 + s_\beta)(\mu - M_1 c_{\mathrm{W}}^2 - M_2 s_{\mathrm{W}}^2)}{2(\mu - M_1)(\mu - M_2)} + \cdots \tag{3.33}$$

$$m_{\widetilde{\chi}_2^0} = |\mu| + \frac{m_{\mathrm{Z}}^2(1 - s_\beta)(\mu + M_1 c_{\mathrm{W}}^2 + M_2 s_{\mathrm{W}}^2)}{2(\mu + M_1)(\mu + M_2)} + \cdots \tag{3.34}$$

$$m_{\widetilde{\chi}_1^\pm} = |\mu| - \frac{m_{\mathrm{W}}^2(\mu + M_2 \sin 2\beta)}{M_2^2 - \mu^2} + \cdots . \tag{3.35}$$

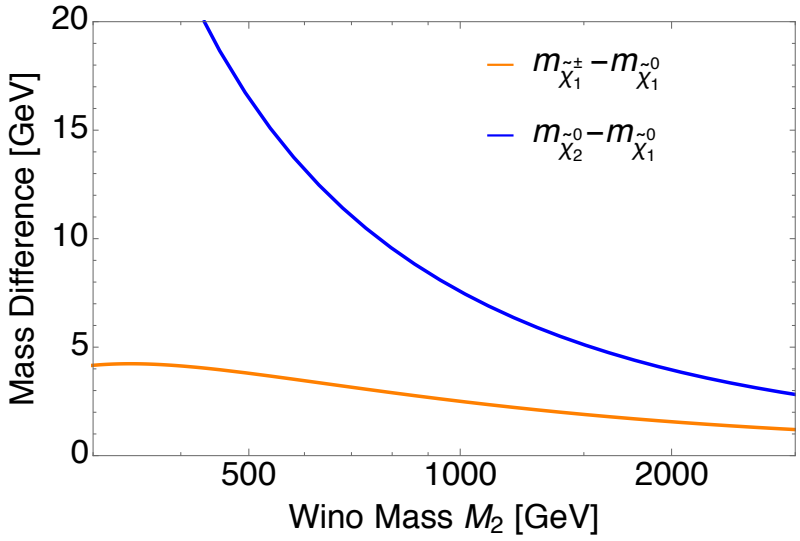

Figure 3.5: The mass difference between the lightest chargino and the lightest neutralino as a function of the wino mass M_2 assuming $\tan\beta = 10$, $\mu = 200\,\text{GeV}$, and $M_1 = 3\,\text{TeV}$ [44].

Fig. 3.5 shows the mass differences $m_{\tilde{\chi}_1^\pm} - m_{\tilde{\chi}_1^0}$ and $m_{\tilde{\chi}_2^0} - m_{\tilde{\chi}_1^0}$ as a function of the wino mass M_2.

There are additional considerations at loop level. In particular the top squark has a large radiative correction which partially cancels with the contribution from the top quark in Eqn. 3.3:

$\Delta(m_H^2) =$ 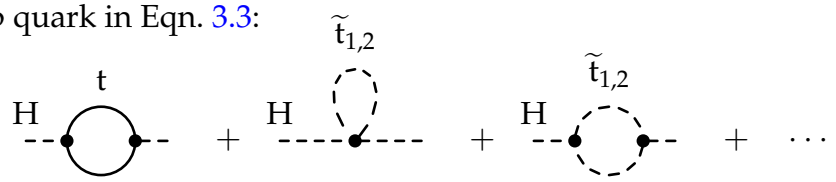

$$= -\frac{3|y_t|^2}{8\pi^2}\Lambda_{UV}^2 + \sum_{i=1}^{2}\left(\frac{3|y_t|^2}{16\pi^2}\Lambda_{UV}^2 - \frac{3|y_t|^2 m_{\tilde{t}_i}^2}{8\pi^2}\log\left(\frac{\Lambda_{UV}}{m_{\tilde{t}_i}}\right)\right) + \cdots \tag{3.37}$$

$$= -\sum_{i=1}^{2}\left(\frac{3|y_t|^2 m_{\tilde{t}_i}^2}{8\pi^2}\log\left(\frac{\Lambda_{UV}}{m_{\tilde{t}_i}}\right)\right) + \cdots . \tag{3.38}$$

The cancellation of the term proportional to Λ_{UV}^2 in Eqn. 3.38 is one of the major successes of SUSY as a candidate for physics beyond the SM. The sensitivity of the Higgs mass to ultraviolet new physics is now logarithmic instead of quadratic. If SUSY were an exact symmetry (and $m_t = m_{\tilde{t}_{1,2}}$) then

the cancellation would be exact and there would be no further hierarchy problem. As it stands, however, we know SUSY is broken, and the remaining term may also be large depending on the difference in masses between the top quark and top squarks. Therefore, naturalness places constraints on the allowed masses of the top squarks given an "acceptable" level of fine tuning.

Very roughly, naturalness requires $m_{\tilde{t}_i} \lesssim 400\,\text{GeV}$ if $\Lambda_{\text{UV}} \approx 10\,\text{TeV}$, implying a fine tuning of the order of 10% [73, 79].

There is also a two-loop contribution to the Higgs mass parameter from the gluino, which is closely related to the one-loop contribution to the top squark mass from the gluino [79]:

$$\Delta(m_{\tilde{t}_i}^2) = \quad + \quad \cdots \tag{3.39}$$

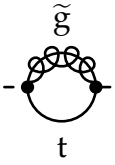

$$= \frac{2g_s^2 m_{\tilde{g}}^2}{3\pi^2} \log\left(\frac{\Lambda_{\text{UV}}}{m_{\tilde{g}}}\right) + \cdots\,, \tag{3.40}$$

With this, we have roughly that $m_{\tilde{g}} \lesssim 2m_{\tilde{t}_i}$.

Prior to the work described in this thesis, constraints from collider searches, especially those from the LHC at $\sqrt{s} = 7\,\text{TeV}$ [80, 81, 82, 83, 84, 85, 86, 87, 88, 89, 90, 91, 92, 93], pushed the allowed mass range for neutralinos and charginos up to $\gtrsim 200\,\text{GeV}$, for top and bottom squarks up to $\gtrsim 500\,\text{GeV}$, and for gluinos up to $\gtrsim 1\,\text{TeV}$. Taking into consideration the experimental and theoretical constraints at tree, one-loop, and two-loop levels, there are three requirements for a minimal natural SUSY spectrum [74]:

(a) quasi-degenerate higgsino-like chargino $\tilde{\chi}_1^\pm$ and two neutralinos $\tilde{\chi}_1^0, \tilde{\chi}_2^0$, below $200 - 350\,\text{GeV}$,

(b) two top squarks $\tilde{t}_{1,2}$ and one (left-handed) $\tilde{b}_1$ below $500 - 700\,\text{GeV}$, and

(c) a gluino below $1 - 1.5\,\text{TeV}$.

3.6 Soft supersymmetry breaking

Since superpartners have not already been discovered with exactly the same masses as the SM particles, we know SUSY is a broken symmetry. However, the form of nature of SUSY breaking is constrained by the fact that we

should preserve the relationships between the dimensionless couplings that create the cancellation of the quadratic divergence of the Higgs mass. This means that the effective Lagrangian of the MSSM can be written as the sum of two terms,

$$\mathcal{L}_{\text{MSSM}} + \mathcal{L}^{\text{soft}}_{\text{MSSM}} \,, \tag{3.41}$$

where $\mathcal{L}_{\text{MSSM}}$ contains all of the gauge and Yukawa interactions that preserve SUSY, and $\mathcal{L}^{\text{soft}}_{\text{MSSM}}$ violates SUSY but contains only mass terms and couplings with *positive* mass dimension. Explicitly, the soft SUSY breaking part of the MSSM Lagrangian can be written [45],

$$\mathcal{L}^{\text{soft}}_{\text{MSSM}} = -\frac{1}{2}\left(M_3\widetilde{g}\widetilde{g} + M_2\widetilde{W}\widetilde{W} + M_1\widetilde{B}\widetilde{B} + \text{h.c.}\right) \tag{3.42}$$

$$-\left(\widetilde{U}^{\text{c}}\boldsymbol{a_{\text{u}}}\widetilde{Q}H_{\text{u}} - \widetilde{D}^{\text{c}}\boldsymbol{a_{\text{d}}}\widetilde{Q}H_{\text{d}} - \widetilde{E}^{\text{c}}\boldsymbol{a_{\text{e}}}\widetilde{L}H_{\text{d}} + \text{h.c.}\right) \tag{3.43}$$

$$-\widetilde{Q}^{\dagger}\boldsymbol{m^2_{\widetilde{Q}}}\widetilde{Q} - \widetilde{L}^{\dagger}\boldsymbol{m^2_{\widetilde{L}}}\widetilde{L} - \widetilde{U}^{\text{c}}\boldsymbol{m^2_{\widetilde{U}^{\text{c}}}}\widetilde{U}^{\text{c}\dagger} - \widetilde{D}^{\text{c}}\boldsymbol{m^2_{\widetilde{D}^{\text{c}}}}\widetilde{D}^{\text{c}\dagger} - \widetilde{E}^{\text{c}}\boldsymbol{m^2_{\widetilde{E}^{\text{c}}}}\widetilde{E}^{\text{c}\dagger} \tag{3.44}$$

$$-m^2_{H_{\text{u}}}H^*_{\text{u}}H_{\text{u}} - m^2_{H_{\text{d}}}H^*_{\text{d}}H_{\text{d}} - (bH_{\text{u}}H_{\text{d}} + \text{h.c.}) \,, \tag{3.45}$$

where M_3, M_2, and M_1 are the gluino, wino, and bino mass parameters, respectively. The trilinear coupling parameters $\boldsymbol{a_{\text{u}}}$, $\boldsymbol{a_{\text{d}}}$, and $\boldsymbol{a_{\text{e}}}$ are a complex 3×3 matrices in generation space with dimensions of mass. They are in one-to-one correspondence with the Yukawa couplings of the superpotential. Each of $\boldsymbol{m^2_{\widetilde{Q}}}$, $\boldsymbol{m^2_{\widetilde{L}}}$, $\boldsymbol{m^2_{\widetilde{U}^{\text{c}}}}$, $\boldsymbol{m^2_{\widetilde{D}^{\text{c}}}}$, and $\boldsymbol{m^2_{\widetilde{E}^{\text{c}}}}$ is a 3×3 hermitian matrix in generation space and corresponds to the different sfermion mass terms. Finally, $m^2_{H_{\text{u}}}$ and $m^2_{H_{\text{d}}}$ are squared-mass parameters for the Higgs bosons and b is a cross term in the Higgs potential.

If the largest mass scale associated with the soft SUSY breaking terms is m_{soft}, then the additional non-supersymmetric corrections to the Higgs mass squared must vanish in the $m_{\text{soft}} \to 0$ limit, so by dimensional analysis they cannot be proportional to Λ^2_{UV}. They also cannot be proportional to $m_{\text{soft}}\Lambda_{\text{UV}}$ because momentum loop integrals do not depend linearly on the cut-off scale. Thus they must be proportional to m^2_{soft}. Following a similar line of argument, we expect that the coefficients of the soft SUSY breaking terms are also proportional to appropriate powers of m_{soft}:

$$M_1, M_2, M_3, \boldsymbol{a_{\text{u}}}, \boldsymbol{a_{\text{d}}}, \boldsymbol{a_{\text{e}}} \sim m_{\text{soft}} \,, \tag{3.46}$$

$$\boldsymbol{m^2_{\widetilde{Q}}}, \boldsymbol{m^2_{\widetilde{L}}}, \boldsymbol{m^2_{\widetilde{U}^{\text{c}}}}, \boldsymbol{m^2_{\widetilde{D}^{\text{c}}}}, \boldsymbol{m^2_{\widetilde{E}^{\text{c}}}}, m^2_{H_{\text{u}}}, m^2_{H_{\text{d}}}, b \sim m^2_{\text{soft}} \,. \tag{3.47}$$

3.7 Renormalization group in supersymmetry

The one-loop beta functions in the MSSM are modified with respect to the ones in the SM due to the additional particle content. Numerically, they become

$$\frac{\mathrm{d}g_1}{\mathrm{d}\log\mu} = \frac{g_1^3}{20\pi^2}\left(\frac{33}{4}\right) , \tag{3.48}$$

$$\frac{\mathrm{d}g_2}{\mathrm{d}\log\mu} = \frac{g_2^3}{16\pi^2}\left(1\right) , \tag{3.49}$$

$$\frac{\mathrm{d}g_3}{\mathrm{d}\log\mu} = \frac{g_3^3}{16\pi^2}\left(-3\right) . \tag{3.50}$$

Fig. 3.6, shows how the gauge couplings, expressed as $\alpha_i^{-1} = 4\pi/g_i^2$, run in both the SM and the MSSM [45]. Unlike the SM, the MSSM includes the right particle content to ensure that the gauge couplings can unify at a mass scale of $\sim 2 \times 10^{16}$ GeV near the GUT scale [45].

3.8 Simplified natural supersymmetry models

Motivated by the discussion of Sec. 3.5, we may outline an explicit minimal natural SUSY scenario. In this scenario, the LSP is the lightest neutralino $\widetilde{\chi}_1^0$ while the NLSP is the lightest chargino $\widetilde{\chi}_1^\pm$. They are both higgsinos and quasi-degenerate. To reduce the dimensionality of this parameter space, and the NLSP-LSP mass splitting is taken to be 5 GeV. This specific choice of mass splitting is supported by Fig. 3.5, but does not have a large impact on the results of the interpretation. The NLSP decays to the LSP and a virtual W boson ($\widetilde{\chi}_1^\pm \rightarrow \mathrm{W}^*\widetilde{\chi}_1^0$), whose decay products mostly have too low momentum to identified. The other SUSY particles accessible at the LHC are the gluino and the lightest top and bottom squarks. All other SUSY particles are assumed to be too heavy to participate in the interactions. We only allow the gluino decay modes involving third-generation quarks because their corresponding decay rates are enhanced if the masses of the third-generation squarks are lighter than those of the first two generations. The SUSY particles and their possible decay modes within this natural SUSY spectrum are summarized in Fig. 3.7.

In the context of this natural spectrum, several simplified models [57, 58, 59, 60, 61, 62] are considered in Ch. 7 and Ch. 8 for gluino pair production based on three-body gluino decays, in which each gluino decays to one of the following final states [95]:

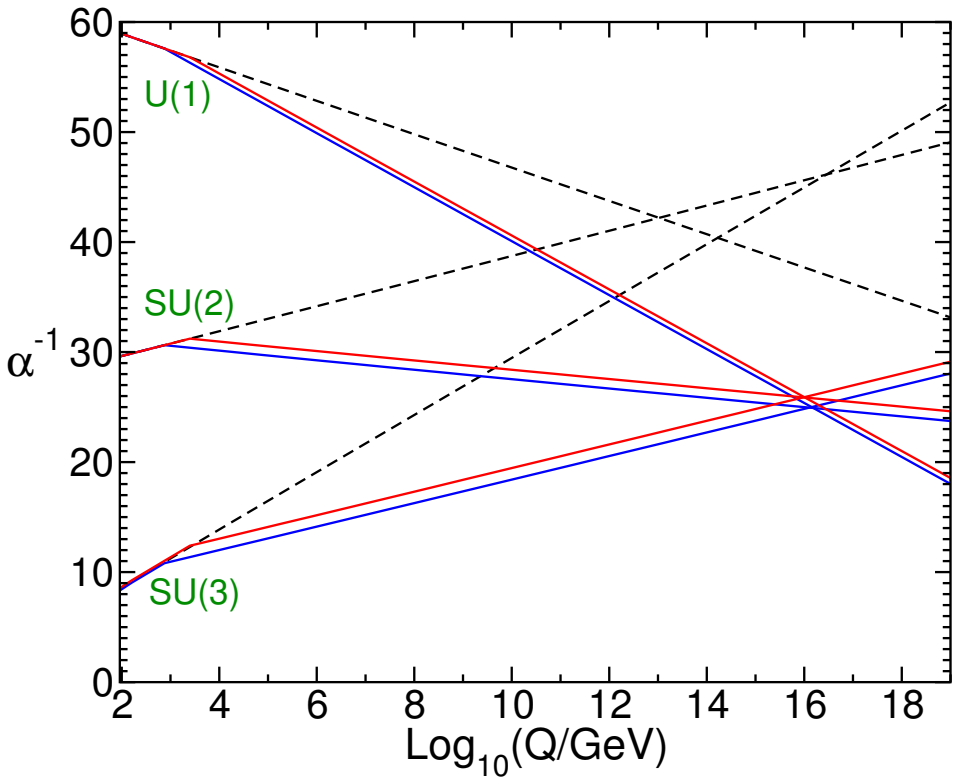

Figure 3.6: Two-loop renormalization group evolution of the inverse gauge couplings $\alpha_i^{-1}(\mu)$ in the SM (dashed lines) and the MSSM (solid lines). In the MSSM case, the sparticle masses are treated as a common threshold varied between 500 GeV and 1.5 TeV, and $\alpha_3(m_Z)$ is varied between 0.117 and 0.121 [45].

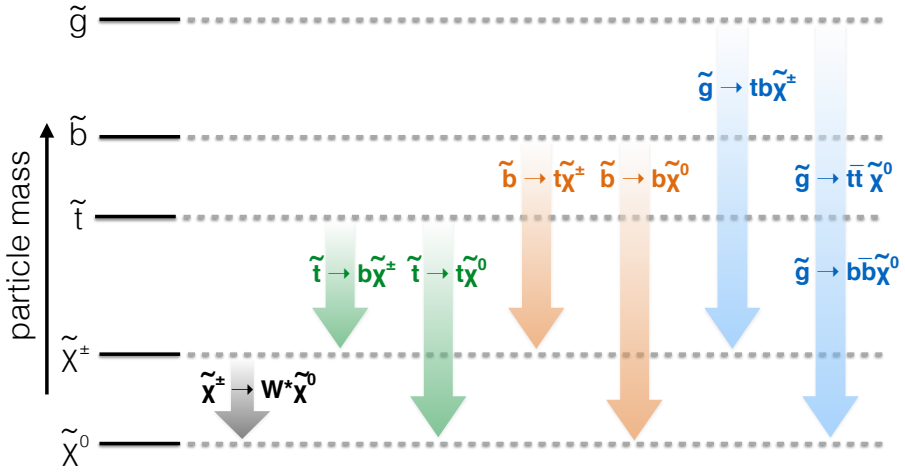

Figure 3.7: The simplified natural SUSY spectrum considered in this thesis, along with the assumed decay modes [94, 44].

- a top quark (antiquark) and a bottom antiquark (quark), and the NLSP;
- a top quark-antiquark ($t\bar{t}$) pair and the LSP;
- a bottom quark-antiquark ($b\bar{b}$) pair and the LSP.

The full range of branching fractions to the three possible decay modes ($b\bar{b}\widetilde{\chi}_1^0$, $b\bar{t}\widetilde{\chi}_1^+$ or $\bar{b}t\widetilde{\chi}_1^-$, and $t\bar{t}\widetilde{\chi}_1^0$) is considered, assuming that these sum to 100%. The three-body gluino decays considered here capture all of the possible final states within this natural SUSY context including those of two-body gluino decays with intermediate top or bottom squarks. Other studies have shown that LHC searches exhibit a similar sensitivity to three-body and two-body gluino decays with a only a weak dependence on the intermediate squark mass [96]. We also consider a model in which the gluino decays to

- a first or second generation quark-antiquark ($q\bar{q}$) pair and the LSP.

In addition, several simplified models are considered for the production of top-squark pairs, in which each top squark decays to one of the following final state:

- a bottom quark and the NLSP;
- a top quark and the LSP.

Similarly, the full range of branching fractions to both decay modes ($b\widetilde{\chi}_1^+$ or $\bar{b}\widetilde{\chi}_1^-$, and $t\widetilde{\chi}_1^0$) is considered, assuming that these sum to 100%.

The corresponding Feynman diagrams showing the event topologies are displayed in Fig. 3.8.

Technical implementation of chargino decays in PYTHIA

To simplify the treatment of the sparticle decays in PYTHIA v6.4.26, we directly implement three-body decays of the form $\widetilde{\chi}_1^\pm \to \widetilde{\chi}_1^0 ff'$, with branching ratios as shown in Tab. 3.2.

decay mode	branching ratio
$\widetilde{\chi}_1^+ \to \widetilde{\chi}_1^0 u\bar{d}$	35%
$\widetilde{\chi}_1^+ \to \widetilde{\chi}_1^0 c\bar{s}$	35%
$\widetilde{\chi}_1^+ \to \widetilde{\chi}_1^0 e^+ \nu_e$	12%
$\widetilde{\chi}_1^+ \to \widetilde{\chi}_1^0 \mu^+ \nu_\mu$	12%
$\widetilde{\chi}_1^+ \to \widetilde{\chi}_1^0 \tau^+ \nu_\tau$	6%

Table 3.2: Table of branching ratios implemented in PYTHIA v6.4.26 for the NLSP $\widetilde{\chi}_1^\pm$ in the simplified natural SUSY model considered in this chapter.

3.9 Constraints from previous searches

At the LHC, previous searches from ATLAS [97, 98, 99, 100, 101] and CMS [102, 103, 104, 105, 106] at $\sqrt{s} = 8$ TeV excluded top squarks up to 700 GeV, and gluinos up to 1.4 TeV. In each case, search results were interpreted within simplified models with only one SUSY particle decay mode considered at a time. Fig. 3.9 summarizes the state of SUSY mass exclusions for the top squark and the gluino prior to the work described in this thesis[3].

[3]The SUSY exclusion summaries from CMS show a preliminary version of the results presented in this thesis labeled "SUS-13-004 (Razor)"

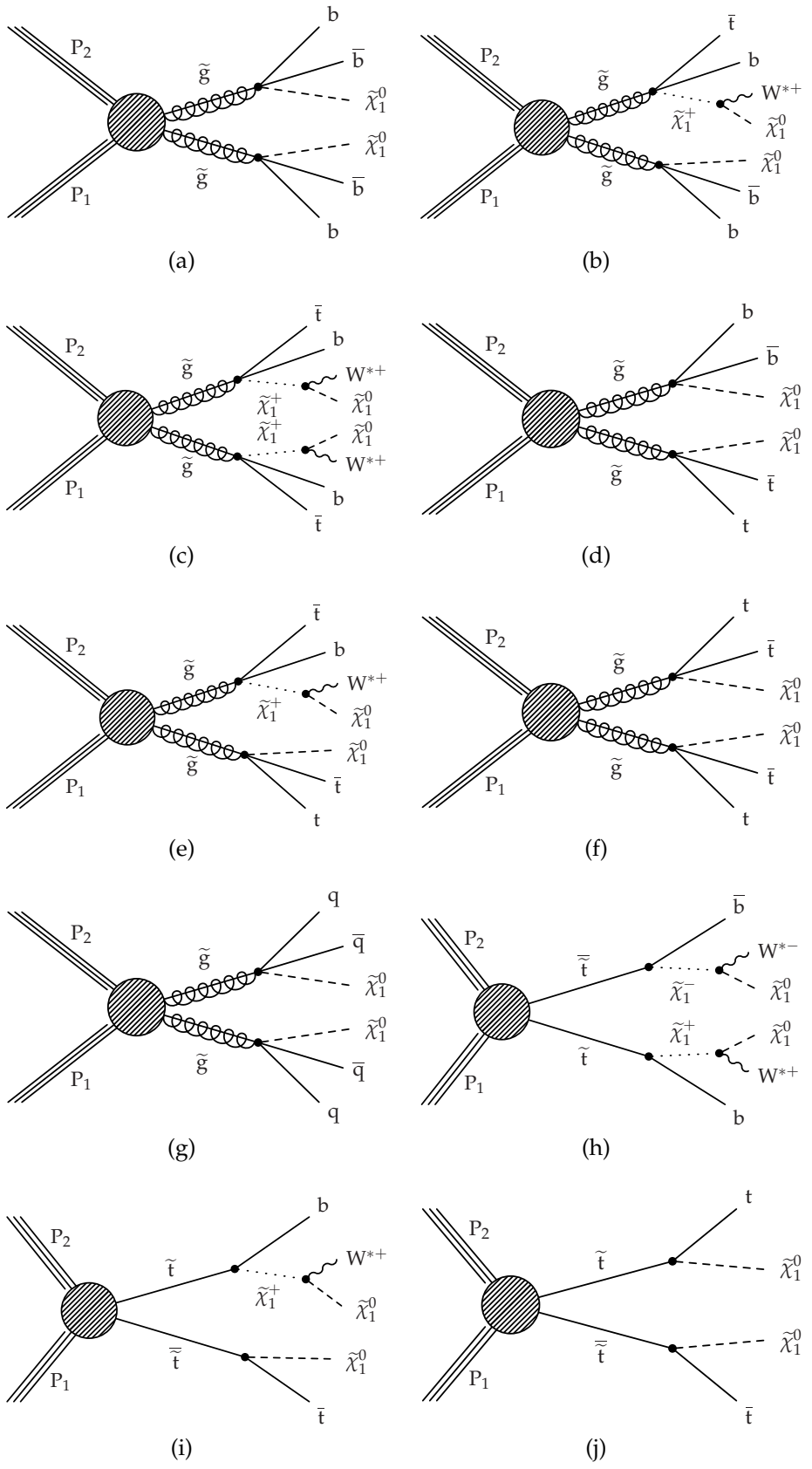

Figure 3.8: Diagrams displaying the event topologies of gluino (a-g) and top-squark (h-j) pair production considered in this thesis [94, 44]. Diagrams corresponding to charge conjugate decay modes are implied. The symbol W^* is used to denote a virtual W boson.

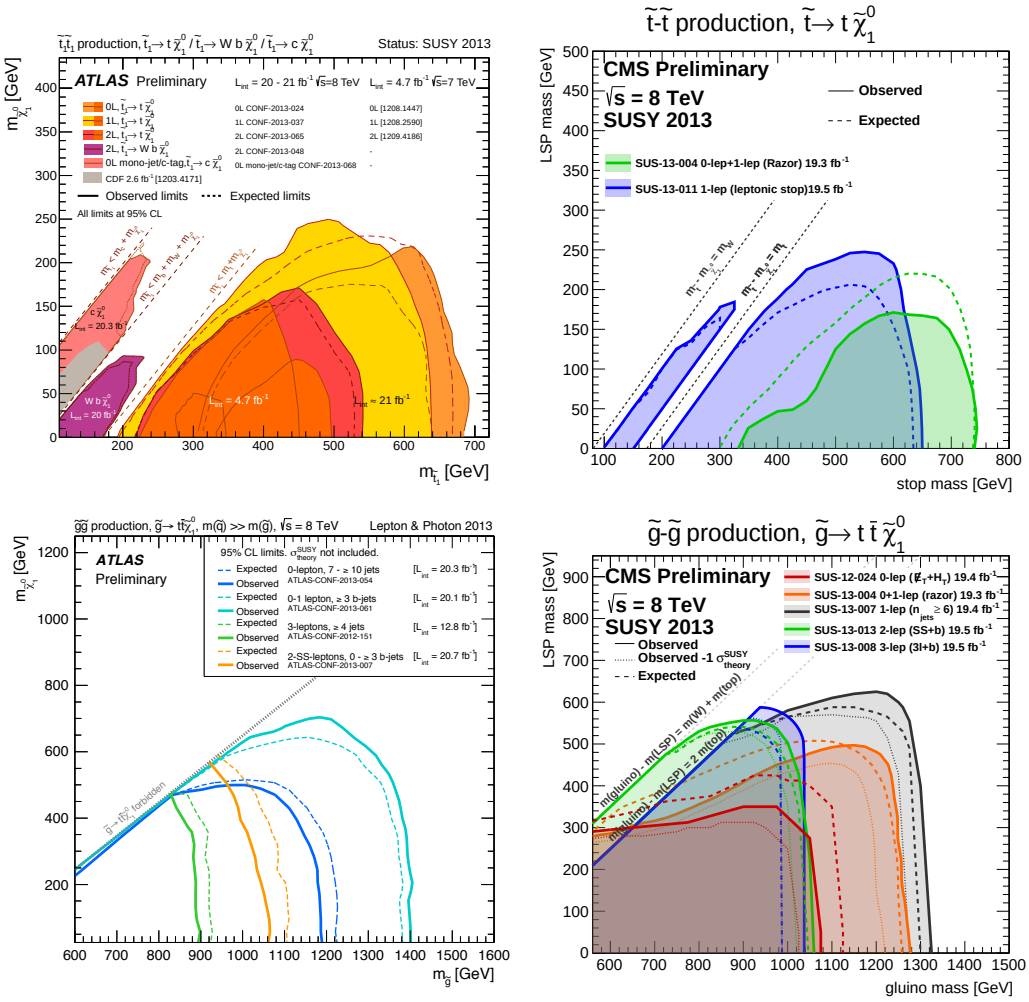

Figure 3.9: ATLAS (left) and CMS (right) 8 TeV limits presented during summer 2013 for top squark (top) and gluino (bottom) pair production.

3.10 The razor approach to supersymmetric kinematics

The production of supersymmetric particles at hadron colliders may be broadly described as:

(i) pair production of heavy particles (such as a $\tilde{g}$ or a $\tilde{q}$), and

(ii) decay of the heavy particle into a set of final state particles consisting of a *visible* subset and an *invisible* subset (usually including the neutralino LSP $\tilde{\chi}^0$).

Although motivated by supersymmetry, the *razor variables* are intended for use in any generic new physics scenario with visible and invisible final state particles [107, 81, 108, 82, 94, 109, 110].

In defining the razor variables, it is useful to consider the explicit example of symmetric squark pair production $\tilde{q}_1\tilde{q}_2$, where each squark decays to a quark and a neutralino LSP $\tilde{q}_i \to q_i\tilde{\chi}_i^0$, as shown in Fig. 3.10. In the following, we treat the quarks as massless. In the the rest frame of the squarks, the

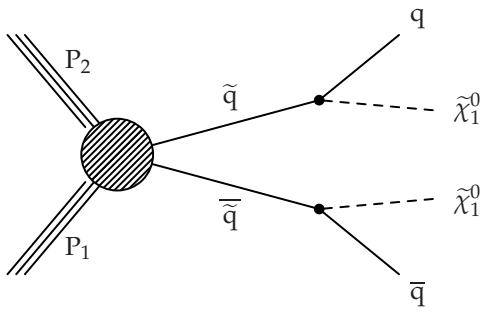

Figure 3.10: Diagram featuring squark pair production [44].

momenta of the quark and the LSP are back-to-back and satisfy

$$2|\vec{p}^{\,q_i}| = 2|\vec{p}^{\,\tilde{\chi}_i^0}| = \sqrt{\frac{\left[m_{\tilde{q}}^2 - (m_q + m_{\tilde{\chi}^0})^2\right]\left[m_{\tilde{q}}^2 - (m_q - m_{\tilde{\chi}^0})^2\right]}{m_{\tilde{q}}^2}} \equiv M_\Delta \,. \tag{3.51}$$

M_Δ is a characteristic mass scale related to the masses of the heavy pair-produced squark and the invisible LSP. In the limit of massless quarks, this simplifies to

$$M_\Delta = \frac{m_{\tilde{q}}^2 - m_{\tilde{\chi}^0}^2}{m_{\tilde{q}}} \,. \tag{3.52}$$

We would like to construct kinematic variables which are sensitive to this mass scale and provide good signal-to-background discrimination.

If we could identify this rest frame, we could boost the quarks' momenta, evaluate them in the new frame, and gain information about the unseen sparticle masses. Unfortunately there are too many missing degrees of freedom to do this.

In principle, we need all eight components of the invisible particles' four-momenta to construct the desired boosts. At a hadron collider, we do not know the momentum along the beam line the initial state interacting partons. As such, we only have access only to the missing transverse momentum $\vec{p}_{\mathrm{T}}^{\,\mathrm{miss}}$, which in the ideal case of no initial/final state radiation (ISR/FSR), no pileup contamination, and perfect detector measurement, is equal to $\vec{p}_{\mathrm{T}}^{\,\tilde{\chi}_1^0} + \vec{p}_{\mathrm{T}}^{\,\tilde{\chi}_2^0}$, giving us two constraints. After making the simplifying assumption of symmetry between the two sides of the decay chain , we are left with four underconstrained degrees of freedom, which can be thought of as the components of $\vec{\beta}^{\mathrm{CM}}$, the longitudinal boost from the lab frame to the center-of-momentum (CM) frame, and $\pm\vec{\beta}^{\mathrm{decay}}$, the boost from the CM frame to the individual squark rest frames. These three types of rest frames and the boosts relating them are illustrated in Fig. 3.11.

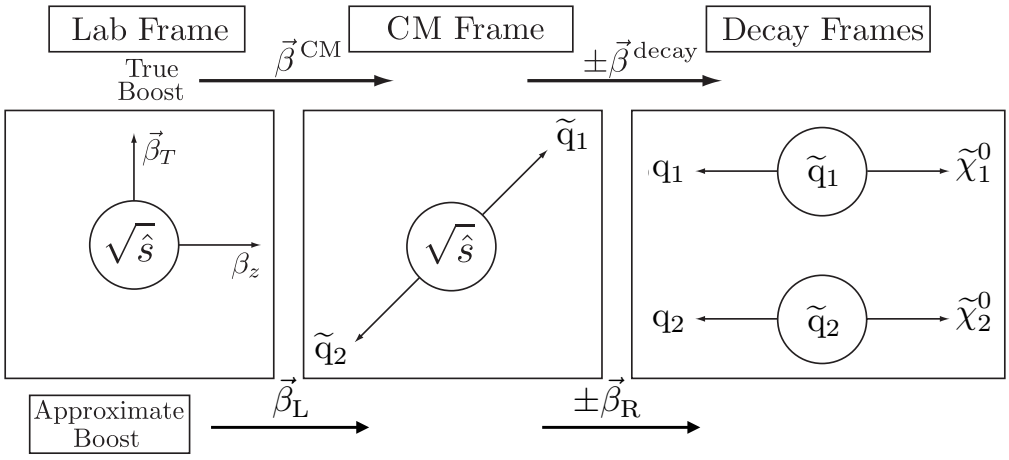

Figure 3.11: Three types of rest frames relevant to LHC pair production and the boosts relating them [110].

The crux of the razor approach is constructing estimators for these boosts using physically-motivated assumptions and minimizing or maximizing certain quantities-of-interest to determine any underconstrained degrees of

freedom.

Following this blueprint, we first construct an estimator of $\vec{\beta}^{\mathrm{CM}}$ called $\vec{\beta}_{\mathrm{L}}$ [107, 110],

$$\vec{\beta}_{\mathrm{L}} = \beta_{\mathrm{L}}\hat{z} = \frac{p_z^{q_1} + p_z^{q_2}}{E^{q_1} + E^{q_2}}\hat{z}\,. \tag{3.53}$$

This boost can be thought of as "zeroing" out the z-component of the total visible momentum $P_z^{\mathrm{visible}} = 0$, which approximates the fact that in the true CM frame, we would have

$$P_z^{\mathrm{visible}} + P_z^{\mathrm{invisible}} = 0\,. \tag{3.54}$$

After performing this boost, we can compute the longitudinally boost-invariant mass,

$$M_{\mathrm{R}} = E'_{q_1} + E'_{q_2}\,, \tag{3.55}$$

where

$$E'_{q_i} = \gamma_{\mathrm{L}} E_{q_i} - \vec{\beta}_{\mathrm{L}} \cdot \vec{p}^{\,q_i}\,. \tag{3.56}$$

Here, primed quantities refer to the approximate CM frame.

To complete the "razor picture" of approximate rest frames, we can construct another boost $\vec{\beta}_{\mathrm{R}}$, an estimator of $\vec{\beta}^{\mathrm{decay}}$, intended to be applied asymmetrically to q_1 and q_2 [107, 110]. We know that after applying this boost, the particles q_1 and q_2 should have the same energy in their respective decay frames. This symmetry condition imposes a constraint on $\vec{\beta}_{\mathrm{R}}$:

$$E''_{q_1} = E''_{q_2} \tag{3.57}$$

$$\Rightarrow \quad \gamma_{\mathrm{R}} E'_{q_1} - \vec{\beta}_{\mathrm{R}} \cdot \vec{p}^{\,q_1\prime} = \gamma_{\mathrm{R}} E'_{q_2} + \vec{\beta}_{\mathrm{R}} \cdot \vec{p}^{\,q_2\prime} \tag{3.58}$$

$$\Rightarrow \quad \vec{\beta}_{\mathrm{R}} \cdot (\vec{p}^{\,q_1\prime} + \vec{p}^{\,q_2\prime}) = E^{q_1\prime} - E^{q_2\prime}\,. \tag{3.59}$$

Here, double primed quantities refer to the approximate decay frames. Using this symmetry and one additional constraint, we can uniquely specify the boost $\vec{\beta}_{\mathrm{R}}$. One possible choice of this additional constraint is the extremal condition,

$$\frac{\partial(E''_{q_1} + E''_{q_2})}{\partial \vec{\beta}_{\mathrm{R}}} = 0\,. \tag{3.60}$$

This choice does not necessarily produce the true boost event-by-event. As such, this contributes to an increase in the M_{R} resolution. On average, however, this choice produces an M_{R} variable that estimates (i.e. peaks at) the

correct mass scale M_Δ. The resulting boost that satisifies the extremal condition of Eqn. 3.60 is

$$\vec{\beta}_R = \frac{\vec{p}^{q_1\prime} - \vec{p}^{q_2\prime}}{E^{q_1\prime} + E^{q_2\prime}} \,. \tag{3.61}$$

In the approximate decay frames, M_R can be expressed as

$$M_R = 2\gamma_R E''_{q_1} = 2\gamma_R E''_{q_2} \,. \tag{3.62}$$

We expect that the distribution of M_R for signal events will have a peak near M_Δ if the assumptions that the pair production is near threshold and $p_z^{q_1} \approx -p_z^{q_2}$ are correct in an average statistical sense. Background events, in general, will not have any special feature near M_Δ. For example, events consisting only of visible particles and $\vec{p}_T^{\,miss}$ from mismeasurement, such as QCD dijet production, would be expected to have a steeply falling M_R distribution related to the distribution of the CM energy $\sqrt{\hat{s}}$.

We can also define a second mass variable that is sensitive to the mass splitting M_Δ using the visible and invisible transverse momentum in the event. Note that this information was not directly used in the definition of M_R. Motivated by the fact that dijet backgrounds with no invisible particles must have q_1 and q_2 back-to-back, we define a transverse mass variable:

$$M_T^R = \sqrt{\frac{E_T^{miss}(p_T^{q_1} + p_T^{q_2}) - \vec{p}_T^{\,miss} \cdot (\vec{p}_T^{\,q_1} + \vec{p}_T^{\,q_2})}{2}} \,. \tag{3.63}$$

While M_R estimates the mass scale of new-physics particle production, M_T^R quantifies the transverse momentum imbalance in the event. Assuming pair production at threshold, $M_T^R \leq M_\Delta$ for signal events. Finally, the razor dimensionless ratio is defined as

$$R^2 \equiv \left(\frac{M_T^R}{M_R}\right)^2 \,. \tag{3.64}$$

We expect $R^2 \sim 1/4$ for signal events , while for background without real missing transverse energy, we expect $R^2 \sim 0$. Note that by construction, $M_T^R \leq M_R$ and thus $R^2 \leq 1$ if the missing transverse momentum perfectly balances the visible transverse momentum (as is necessarily true in the dijet case). The behavior of the razor variables M_R and R^2 in the case of squark pair production for different squark and LSP mases can be seen in Fig 3.12.

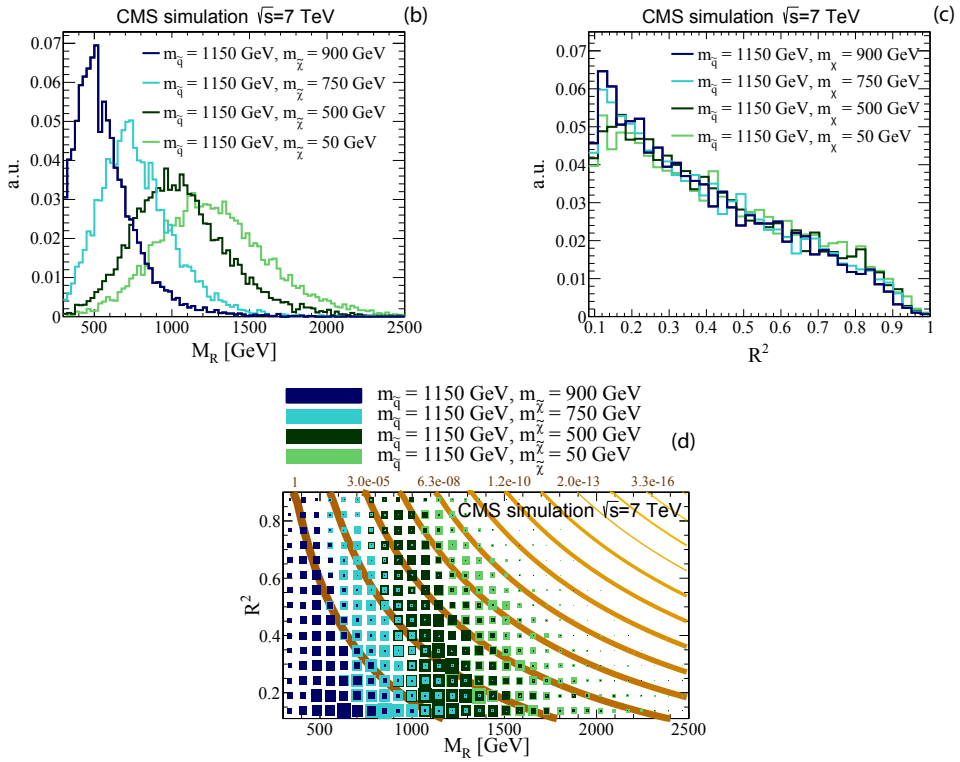

Figure 3.12: Distribution of R^2 and M_R in the case of squark pair production for different squark and LSP masses [108]. The peak of the M_R distribution scales with M_Δ and the R^2 distribution has a larger mean value and falls less steeply than the corresponding distribution for the backgrounds.

To generalize this approach to the case with an arbitrary number of visible final state particles, we treat each event as a dijet-like event by clustering particles into two pseudojets called *megajets*. All possible assignments of objects to the megajets are considered, with the requirement that a megajet consist of at least one object. The sum of the four-momenta of the objects assigned to a megajet defines the megajet four-momentum. When more than two objects are reconstructed, more than one megajet assignment is possible[4]. We select the assignment that minimizes the sum of the invariant masses of the two megajets $m_{j_1}^2 + m_{j_2}^2$, where m_{j_i} is the mass of the ith megajet.

Conceptually, this is similar to minimizing the opening angles between the constituent particles in the megajets. For example, in the simplest nontrivial case of a three-particle event, there are three distinct megajet assignment.

[4]The number of ways of partitioning a set of n particles into two megajets is given by a Stirling number of the second kind, $\{{n \atop 2}\} = \frac{1}{2!}\sum_{j=0}^{2}(-1)^{2-j}\binom{2}{j}j^n = 2^{n-1} - 1$.

We choose the clustering of the three particles labeled i, j, k that minimizes the sum

$$\min_{i \neq j \neq k} m_{ij}^2 + m_k^2 \,, \tag{3.65}$$

which for massless particles reduces to

$$\min_{i \neq j \neq k} \frac{1 - \cos\theta_{ij}}{E_k} \approx \frac{\theta_{ij}^2}{2E_k} \tag{3.66}$$

for small opening angles θ_{ij}.

After forming the megajets, we may compute M_{R}, $M_{\mathrm{T}}^{\mathrm{R}}$, and R^2 in terms of lab-frame quantities for an arbitrary number of final state particles,

$$M_{\mathrm{R}} \equiv \sqrt{(|\vec{p}^{\,j_1}| + |\vec{p}^{\,j_2}|)^2 - (p_z^{j_1} + p_z^{j_2})^2} \,, \tag{3.67}$$

$$M_{\mathrm{T}}^{\mathrm{R}} \equiv \sqrt{\frac{E_{\mathrm{T}}^{\mathrm{miss}}(p_{\mathrm{T}}^{j_1} + p_{\mathrm{T}}^{j_2}) - \vec{p}_{\mathrm{T}}^{\,\mathrm{miss}} \cdot (\vec{p}_{\mathrm{T}}^{\,j_1} + \vec{p}_{\mathrm{T}}^{\,j_2})}{2}} \,, \tag{3.68}$$

$$\mathrm{R}^2 \equiv \left(\frac{M_{\mathrm{T}}^{\mathrm{R}}}{M_{\mathrm{R}}}\right)^2 \,, \tag{3.69}$$

where $\vec{p}_{j_i}$, $\vec{p}_{\mathrm{T}}^{\,j_i}$, and $p_z^{j_i}$ are the momentum of the ith megajet, its transverse component with respect to the beam axis, and its longitudinal component, respectively, with $E_{\mathrm{T}}^{\mathrm{miss}}$ the magnitude of $\vec{p}_{\mathrm{T}}^{\,\mathrm{miss}}$.

Part II

The LHC and CMS

Chapter 4

THE LARGE HADRON COLLIDER

The Large Hadron Collider (LHC) is a 27 km two-ring superconducting proton accelerator and collider located at CERN, spanning the border between France and Switzerland. The LHC was built to discover the Higgs boson, or the corresponding relic of the mechanism responsible for electroweak symmetry breaking, and seach for beyond-the-standard-model (BSM) phenomena at the TeV scale, like supersymmetric partners of SM particles. In 2016, the LHC collided protons at a center-of-mass energy of 13 TeV and instantaneous luminosity exceeding the design value of $10^{34}\,\mathrm{cm}^{-2}\,\mathrm{s}^{-1}$.

The LHC is the pinnacle of the accelerator complex at CERN, pictured in Fig. 4.1. To accelerate protons to a beam energy of 6.5 TeV in the LHC, a chain of smaller accelerators are needed. Starting from a bottle of hydrogen gas, electrons are stripped from the hydrogen atoms by an electric field and the resulting protons enter the Linac 2, which accelerates the protons to 50 MeV. Subsequently, the Proton Synchrotron Booster (PSB), Proton Synchrotron (PS), and the Super Proton Synchrotron (SPS) accelerate the protons to 1.4 GeV, 25 GeV, and 450 GeV, respectively, before they are finally injected into the two LHC rings as counter-rotating beams.

One of the main features influencing the design of the LHC is the re-use of the existing 26.7 km tunnel from the Large Electron Positron collider (LEP), which is composed of eight crossing points (or arcs) and eight straight sections for RF cavities. The tunnel in the arc sections has an internal diameter

Table 4.1: Comparison between LHC design parameters and achieved parameters in 2012, 2015, and 2016.

Parameter	**Design**	**Achieved (2012)**	**Achieved (2015)**	**Achieved (2016)**
Proton energy [GeV]	7000	4000	6500	6500
Relativistic gamma factor γ_r	7461	4263	6928	6928
Number of particles per bunch N_b	1.15×10^{11}	$1.6 - 1.7 \times 10^{11}$	1.15×10^{11}	1.3×10^{11}
Number of bunches n_b	2808	1374	2244	2220
Bunch spacing [ns]	25	50	25	25
Transverse normalized emittance ε_n [μm rad]	3.75	2.5	2.5	1.4
β^* at IP1 and IP5 [m]	0.55	0.6	0.8	0.4
Half crossing angle at IP1 and IP5 $\theta_c/2$ [μrad]	$\pm$142.5	$\pm$145.0	$\pm$185.0	
Peak luminosity in IP1 and IP5 [$\mathrm{cm}^{-1}\mathrm{s}^{-1}$]	1.0×10^{34}	7.7×10^{33}	5.2×10^{33}	1.3×10^{34}
Max. mean number of events per bunch crossing	19	40	17	43

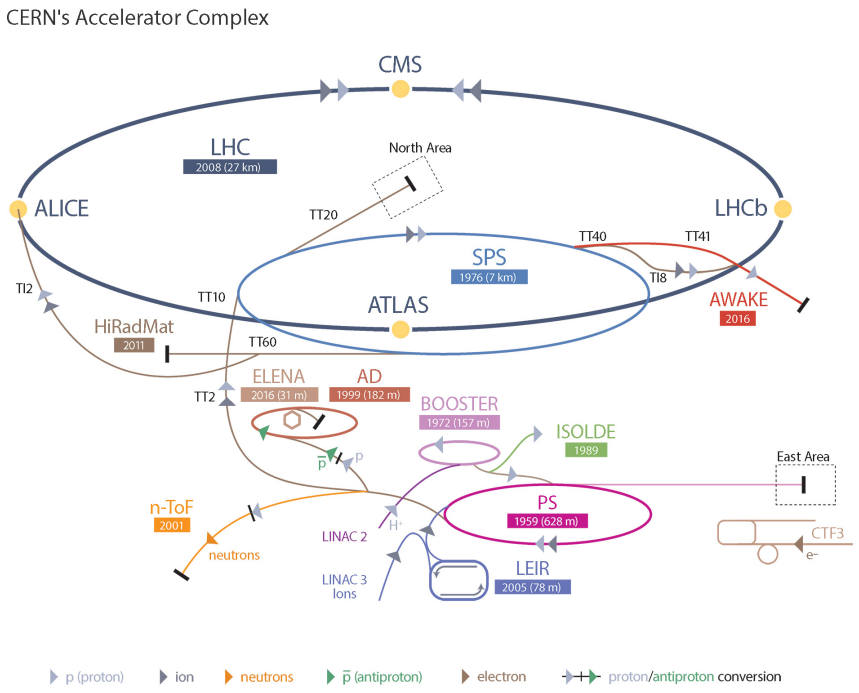

Figure 4.1: CERN's accelerator complex [111].

of 3.7 m. Due to the limited available space, two completely separate proton rings with separate magnet systems would be extremely difficult to install, which makes the twin-bore magnet design proposed by John Blewett in 1971 [112] ideal due to its "two-in-one" use of the limited space. A cross-section of the main superconducting dipole magnet is shown in 4.2.

The observed number of events N_{exp} is the product of the cross section of interest σ_{exp} and the time integral of the instantaneous luminosity,

$$N_{\text{exp}} = \sigma_{\text{exp}} \int \mathscr{L}(t)dt \,. \tag{4.1}$$

The instantaneous luminosity depends on the beam parameters and can be written for a Gaussian beam distribution as [111]:

$$\mathscr{L} = \frac{N_b^2 n_b f_{\text{rev}} \gamma_r}{4\pi\varepsilon_n \beta^*} F \,, \tag{4.2}$$

where N_b is the number of particles per bunch, n_b the number of bunches per beam, f_{rev} the revolution frequency, γ_r the relativistic gamma factor, ε_n the normalized transverse beam emittance, β^* the beta function at the collision point, and F the geometric luminosity reduction factor due to the

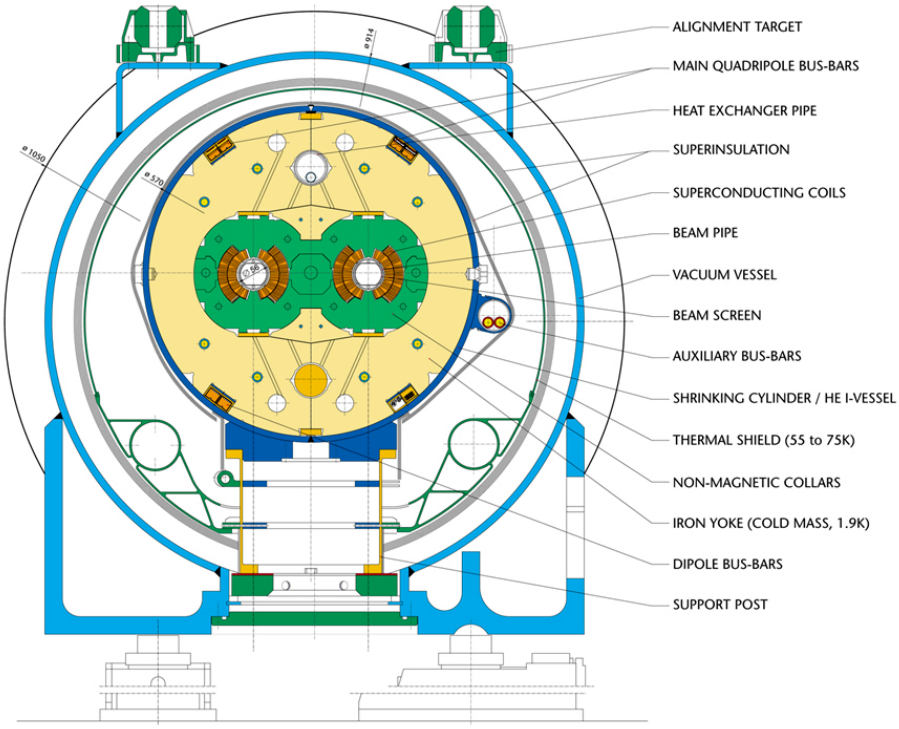

Figure 4.2: Cross-section of the LHC dipole magnet [111].

crossing angle at the interaction point (IP):

$$F = \left(1 + \left(\frac{\theta_c \sigma_z}{2\sigma^*}\right)^2\right)^{-1/2}, \tag{4.3}$$

where θ_c is the full crossing angle, σ_z is the RMS bunch length, and σ^* is the RMS bunch size.

The integrated luminosity of proton-proton collisions delivered by the LHC to the CMS experiment versus time from 2010 through 2016 is shown in Fig. 4.3. The LHC also delivers lead-proton and lead-lead collisions for one month each year to the experiments.

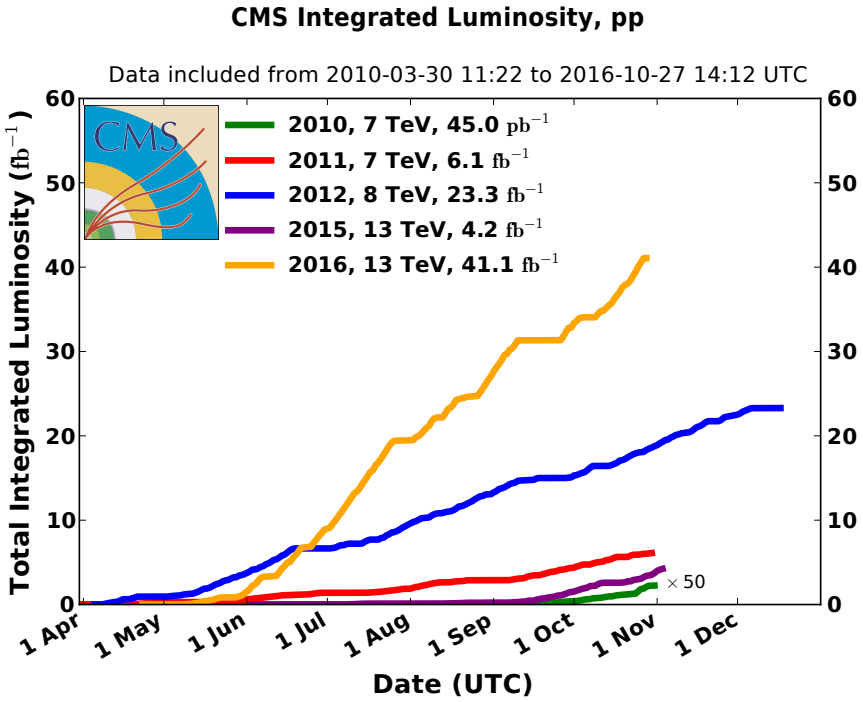

Figure 4.3: Cumulative luminosity versus day delivered to CMS during stable beams for pp collisions. This is shown for 2010 (green), 2011 (red), 2012 (blue), 2015 (purple), and 2016 (orange) data-taking [113].

Chapter 5

THE COMPACT MUON SOLENOID EXPERIMENT

The Compact Muon Solenoid (CMS) detector is a multi-purpose detector conceived to study proton-proton, proton-lead, and lead-lead collisions produced by the Large Hadron Collider (LHC) at CERN [114].

The ultimate goals of the LHC physics programme are to elucidate the nature of electroweak symmetry breaking and search for evidence of new symmetries, new forces, or new constituents of matter that could pave the way toward a unified theory beyond the standard model. There are several detector and readout requirements for CMS to meet these goals:

- Good muon identification and momentum resolution over a wide range of momenta, good dimuon mass resolution ($\approx$ 1% at 100 GeV), and the ability to unambiguously determine the charge of muons with $p < 1$ TeV. See Sec. 5.4;
- Good charged particle momentum resolution and reconstruction efficiency in the inner tracker. Efficient triggering and offline identification of τ leptons and b-jets, requiring pixel detectors close to the interaction region. See Sec. 5.1;
- Good electromagnetic energy resolution, good diphoton and dielecron mass resolution ($\approx$ 1% at 100 GeV), wide geometric coverage, π^0 rejection, and efficient photon and lepton isolation at high luminosities. See Sec. 5.2;
- Good missing-transverse-energy and dijet-mass resolution, requiring hadron calorimeters with hermetic geometric coverage and fine lateral segmentation. See Sec. 5.3;
- Fast online event selection processes (*triggers*) to reduce the rate from 10^9 inelastic collision events per second to $\lesssim$ 1000 events per second for storage and subsequent analysis. See Sec. 5.6;
- Infrastructure for the alignment and calibration of the detector. See Sec. 5.7.

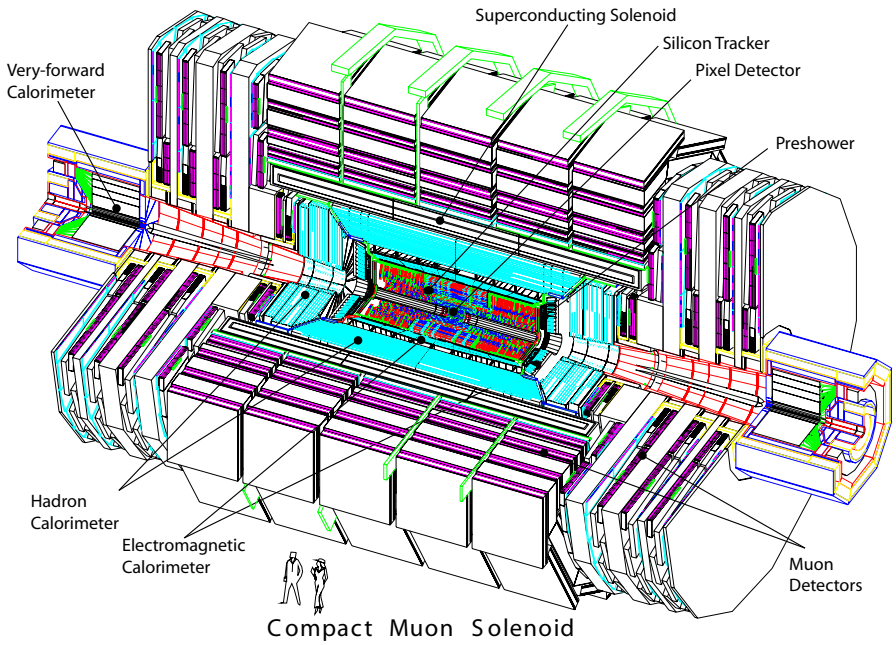

Figure 5.1: Perspective view of the CMS detector [114].

The design of CMS, pictured in Fig. 5.1 and detailed in the following sections, meets these requirements. Each detector subsystem is integral to the performance of CMS as a whole and is specialized to a particular class of particles, as seen in Fig. 5.2: the silicon tracker measures the tracks of charged particles, the electromagnetic calorimeter measures the energy of electrons and photons, the hadron calorimeter measures the energy of charged and neutral hadrons, and the muon detectors identify and measure the momentum of muons.

All of the subdetectors are built around the central feature of the CMS detector, which is a superconducting solenoid providing a uniform axial magnetic field of 3.8 T over a magnetic length of 12.5 m and a free-bore radius of 3.15 m. The large bending power (11.4 T m) of the superconducting magnet permits a precise measurement of the momentum of high-energy charged particles in silicon tracker. The return field is large enough to saturate 1.5 m of iron, allowing four *muon stations* to be integrated and the bore of the magnet coil is large enough to accommodate the inner tracker and the calorimetry inside, thereby reducing the amount of material in front of the calorimeters.

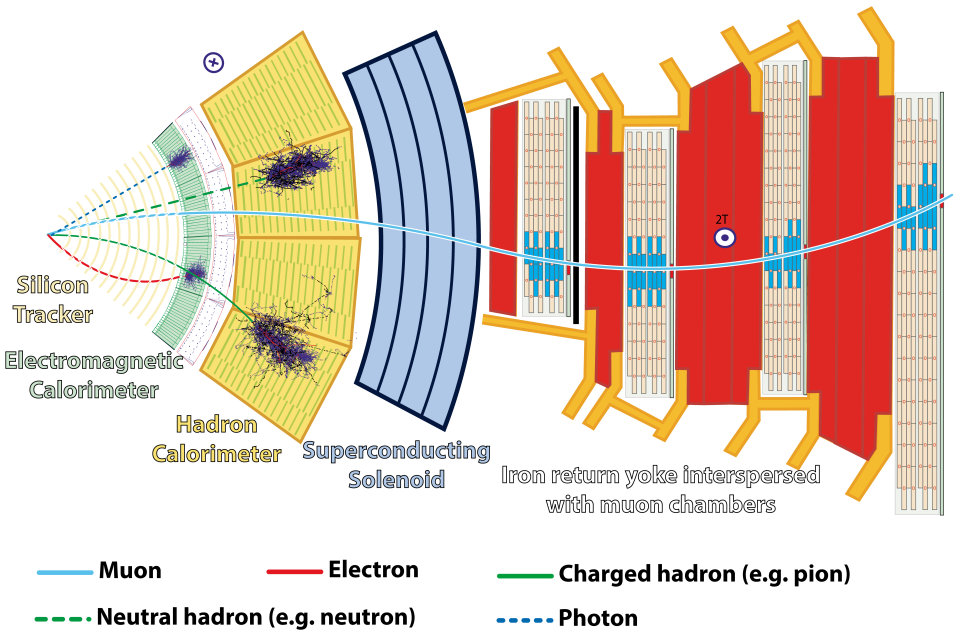

Figure 5.2: A slice of the CMS detector [114].

5.1 Silicon tracker

The first layer of the detector encountered by outgoing particles from the collisions is the tracker, composed of a small silicon pixel surrounded by a large silicon strip tracker [115]. Both tracker subdetectors are cylinder-shaped and occupy a total 5.8 m in length and 2.5 m in diameter. The pixel detector barrel (endcaps) is composed of three (two) layers of pixel detectors, providing three-dimensional position measurements of the hits arising from the interaction of charged particles with its sensors. The hit position resolution is approximately 10 μm in the transverse coordinate and 20–40 μm in the longitudinal coordinate, while the third coordinate is given by the sensor plane position. In total, its 1440 modules cover an area of about 1 m^2 and have 66 million pixels.

Surrounding this is the silicon strip tracker. The silicon detector barrel (endcaps) has ten (twelve) layers of micro-strip detectors. In total, the with 15,148 silicon modules, which cover an active area of about 198 m^2 and have 9.3 million strips.

The fine granularity of the two tracker subdetectors offers separation of closely-spaced particle trajectories in energetic jets. Fig. 5.3 shows a schematic layout of the tracker in the $r - z$ plane and the material budget of the CMS tracker, both in units of radiation lengths and nuclear interaction lengths, as

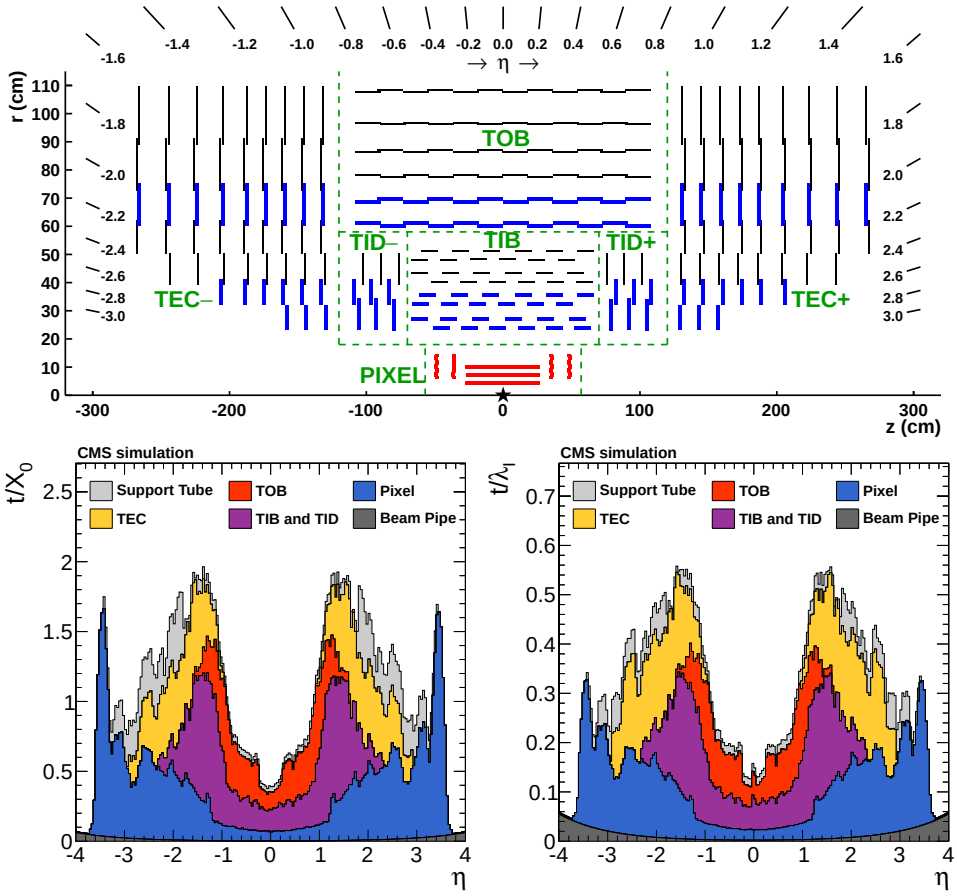

Figure 5.3: (Top) Schematic cross section through the CMS tracker in the $r-z$ plane. (Bottom) Total thickness t of the tracker material traversed by a particle produced at the nominal interaction point, as a function of pseudorapidity η, expressed in units of radiation length X_0 (left) and nuclear interaction length λ_I (right) [115].

estimated from simulation. Due to the tracker's material budget, a consistent fraction of electrons and photon begin showering already in the tracker, which implies the need for a global strategy to event reconstruction (detailed in Sec. 5.5).

5.2 Electromagnetic calorimeter

Within the superconducting solenoid volume and just outside of the tracker, lies the electromagnetic calorimeter (ECAL) schematically pictured in Fig. 5.4. The ECAL is a hermetic homogenous calorimeter composed of 61,200 lead-tungstate ($PbWO_4$) scintillating crystals mounted in the barrel covering $|\eta| < 1.479$, and 7,324 crystals mounted in each of the two endcap disks cover-

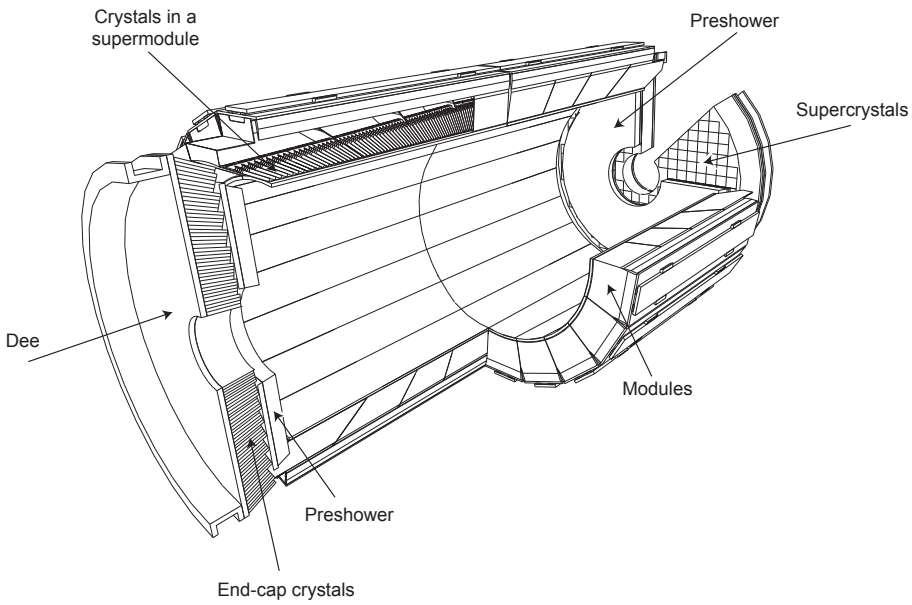

Figure 5.4: Layout of the CMS ECAL, showing the barrel supermodules, the two endcaps, and the preshower detectors. The ECAL barrel coverage is up to $|\eta| = 1.48$; the endcaps extend the coverage to $|\eta| = 3.0$; the preshower detector fiducial area is approximately $1.65 < |\eta| < 2.6$ [116].

ing $1.479 < |\eta| < 3.0$. The crystals in the barrel are arranged in a quasi-projective geometry, meaning that they point back to the center of the detector. The high-density ($8.28\,\mathrm{g/cm^3}$), short radiation length ($X_0 = 0.89$ cm), and small Moliére radius ($R_M = 2.2$ cm) of $PbWO_4$ allow the construction of a compact calorimeter with fine granularity.

The crystal length of 23 (22) cm, corresponding to 25.8 (24.7) radiation lengths in the barrel (endcaps), is sufficient to contain more than 98% of the energy of electrons and photons up to 1 TeV. The crystal material also amounts to about one nuclear interaction length, causing about two thirds of the hadrons to start showering in the ECAL.

The barrel crystal front face has an area of 2.2×2.2 cm^2, equivalent to 0.0174×0.0174 in the (η, ϕ) plane, while in the endcaps, the crystals are arranged instead in a rectangular (x, y) grid, with a front-face area of 2.9×2.9 cm^2. The crystal transverse size in the barrel matches the small Molière radius of $PbWO_4$ (2.2 cm). This fine transverse granularity makes it possible to fully resolve hadron and photon energy deposits as close as 5 cm.

The $PbWO_4$ crystals emit predominantly blue scintillation light with a broad

maximum at wavelengths 420–430 nm. The quantum efficiency and surface coverage of the photodetectors are such that a particle depositing 1 MeV of energy in a crystal produces an average signal of about 4.5 photoelectrons.

The ECAL barrel energy resolution for electrons is measured in an electron test beam to be [117, 116],

$$\frac{\sigma_E}{E} = \frac{S}{\sqrt{E(\text{GeV})}} \oplus \frac{N}{E(\text{GeV})} \oplus C \tag{5.1}$$

$$= \frac{2.8\%}{\sqrt{E(\text{GeV})}} \oplus \frac{12\%}{E(\text{GeV})} \oplus 0.3\% \tag{5.2}$$

where the three contributions are the stochastic, noise, and constant terms.

The actual energy resolution in CMS for electrons and photons are measured using known resonances, such as $Z \to e^+e^-$ and $H \to \gamma\gamma$, in data and simulation. Fig. 5.5 (left) shows an example of the $Z \to e^+e^-$ invariant mass distibutons, in which each electron is well measured and has a single-cluster supercluster in the barrel. The distributions in data and in simulation are fitted with a Breit–Wigner function convolved with a Crystal Ball function [118],

$$P(m_{e^+e^-}|m_Z, \Gamma_Z, \alpha, n, m_{CB}, \sigma_{CB}) = \text{BW}(m_{e^+e^-}|m_Z, \Gamma_Z) \otimes f_{CB}(m_{e^+e^-}|\alpha, n, m_{CB}, \sigma_{CB}), \tag{5.3}$$

where m_Z and Γ_Z are fixed to the nominal values of 91.188 GeV and 2.485 GeV [119]. The effective resolution σ_{eff}, defined as the half-width of the narrowest interval containing 68.3% of the distribution, in data for the $Z \to e^+e^-$ invariant mass in this category is 1.13 ± 0.01 GeV (or about 1%). Considering only the Gaussian core of the distribution, the resolution is $\sigma_{CB} = 1.00 \pm 0.01$ GeV.

Since there is excellent agreement between data and simulation for reconstructed photons [120], the energy resolution of photons in simulated events provides an accurate estimate of their resolution in data. Fig. 5.5 (right) shows the distribution of reconstructed energy divided by the true energy, $E_{\text{meas}}/E_{\text{true}}$, of photons in simulated $H \to \gamma\gamma$ events that pass the selection requirements given in Ref. [121], with $0.2 < |\eta| < 0.3$ and $R_9 \geq 0.94$, where the R_9 is the energy sum of the 3×3 crystals centered on the most energetic crystal in the supercluster divided by the energy of the supercluster[1] The σ_{eff} in simulated $H \to \gamma\gamma$ events for $E_{\text{meas}}/E_{\text{true}}$ in this category is 1%.

[1] The showers of photons that convert before reaching the calorimeter have wider transverse profiles and lower values of R_9 than those of unconverted photons.

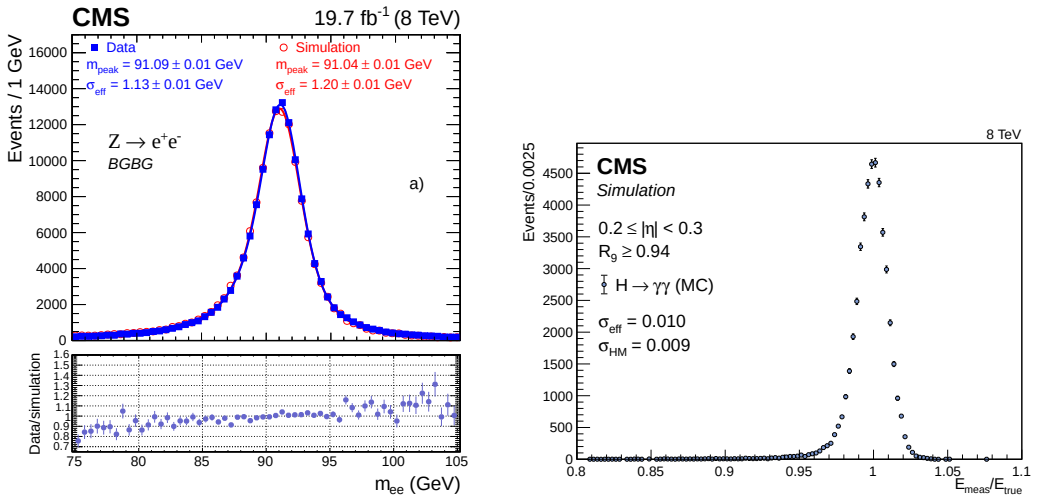

Figure 5.5: (Left) Dielectron invariant mass distribution from $Z \rightarrow e^+e^-$ events in data (solid squares) compared to simulation (open circles) fitted with a convolution of a Breit–Wigner function and a Crystal Ball function [118], for the best-resolved event category with two well-measured single-cluster electrons in the barrel. The masses at which the fitting functions have their maximum values, termed m_{peak}, and the effective standard deviations σ_{eff} are given in the plots. The data-to-simulation scale factors are shown below the main panels [116]. (Right) The distribution of measured over true energy, $E_{\text{meas}}/E_{\text{true}}$, for photons in simulated $H \rightarrow \gamma\gamma$ events, in a narrow η range in the barrel, $0.2 < |\eta| < 0.3$ for photons with $R_9 \geq 0.94$ [120].

A finer-grained detector, known as the preshower, is installed in front of each endcap disks. It consists of two layers, each comprising a lead radiator followed by a plane of silicon strip sensors, with a pitch of 1.9 mm. The goal of the preshower is to enhance photon identification capabilities.

Since the ECAL crystals are approximately one Moliére radius in the lateral dimension, high energy electromagnetic showers spread laterally over several crystals. Clustering algorithms are used to sum together energy deposits in adjacent crystals belonging to the same electromagnetic shower. The clustering algorithm proceeds first with the formation of "basic clusters", corresponding to local maxima of energy deposits. The basic clusters are then merged together to form a "supercluster," which is extended in ϕ (because charged particle tracks bend in ϕ, but not in η), to recover the radiated energy. Because of the differences between the geometric arrangement of the crystals in the barrel and endcap regions, a different clustering algo-

rithm is used in each region. The clustering algorithm used in the barrel, called the "hybrid" algorithm, is described in Ref. [122]. In the endcap and preshower, the algorithm merges together fixed-size 5×5 crystal basic clusters and associates each with corresponding preshower energy deposits.

5.3 Hadron calorimeter

The ECAL is surrounded by a hermetic sampling hadron calorimeter (HCAL) consisting of several interleaved layers of brass absorber and plastic scintillator tiles. A barrel detector ($|\eta| < 1.3$) and two endcap disks ($1.3 < |\eta| < 3.0$) provide pseudorapidity coverage up to 3.0. The scintillation light is converted by wavelength-shifting (WLS) fibers embedded in the scintillator tiles and channeled to photodetectors via clear fibers. This light is detected by photodetectors (hybrid photodiodes, or HPDs) that can provide gain and operate in high axial magnetic fields. This central calorimetry is complemented by a tail-catcher in the barrel region (HO) ensuring that hadronic showers are sampled with nearly 11 hadronic interaction lengths.

The HCAL is read out in individual towers with a cross section of $\Delta\eta \times \Delta\phi = 0.087 \times 0.087$ for $|\eta| < 1.6$ and 0.17×0.17 at larger pseudorapidities. The HCAL energy resolution is measured in a pion test beam to be [123]

$$\frac{\sigma_E}{E} = \frac{110\%}{\sqrt{E(\,\mathrm{GeV})}} \oplus 9\% \,. \tag{5.4}$$

Coverage up to a pseudorapidity of 5.0 is provided by a forward hadron calorimeter (HF) situated at 11 m from the interaction point.The HF consists of a steel absorber composed of grooved plates. Radiation-hard quartz fibers are inserted in the grooves along the beam direction. The signals from the fibers are grouped so as to define calorimeter towers with a cross section of $\Delta\eta \times \Delta\phi = 0.175 \times 0.175$ over most of the pseudorapidity range. The Čerenkov light emitted in the quartz fibers is detected by photomultipliers. The forward calorimeters ensure full geometric coverage, which is especially important for the measurement of the transverse energy in the event.

5.4 Muon system

The most outward part of the CMS detector is the muon spectrometer, made up of four stations of gas-ionization detectors sandwiched between three

layers of iron return yoke. Drift tube (DT) chambers and cathode strip chambers (CSC) detect muons in the regions $|\eta| < 1.2$ and $0.9 < |\eta| < 2.4$, respectively, and are complemented by a system of resistive plate chambers (RPC) covering the range $|\eta| < 1.6$. The reconstruction involves a global trajectory fit across the muon stations and the inner tracker. Due to the large amount of material before the muon chambers, low-p_{T} muons undergo multiple scattering and thus the inner tracker dominates the momentum measurement up to a muon p_{T} of about 300 GeV.

5.5 Particle-flow reconstruction

Each particle yields a specific signature in the CMS detector: compared to charged hadrons, electrons have no HCAL cluster; neutral hadrons have no tracks; photons have neither of those; and muons leave a signal in the muon chambers (see Fig. 5.2). Traditional reconstruction methods typically utilize the information from only one subdetector in reconstructing a particular physics object: for example, jets are traditionally reconstructed using only information from the HCAL.

The *particle-flow (PF) reconstruction algorithm*, developed before the start of the LHC, commissioned with the first 2010 data at $\sqrt{s} = 7$ TeV, and still in use during Run 2, is an attempt to construct a global event description based on an optimal combination of information from all subdetectors. Individual particles (PF candidates) are reconstructed by combining the information from the inner tracker, the calorimeters, and the muon system. Five categories of PF candidates are defined: muons, electrons, photons (including their conversions to $\mathrm{e}^+\mathrm{e}^-$ pairs), charged hadrons, and neutral hadrons. This global event description leads to an improved performance for electron and muon identification, jet and hadronic τ decay reconstruction, and missing transverse energy. The improvements for τ's, jets, and $E_{\mathrm{T}}^{\mathrm{miss}}$ are especially significant because of the advantage gained by consistently integrating the muon and electron reconstruction into the global event description so that there is no ambiguity in the interpretation of each detected signal.

In detail, the PF reconstruction proceeds as follows. To suppress noise in the calorimeters, only cells with energies above a given threshold are considered, this procedure is referred to as "zero suppression". The energy

of photons is obtained directly from the ECAL measurement, corrected for zero-suppression effects. The energy of electrons is determined from a combination of the track momentum at the main interaction vertex, the corresponding ECAL cluster energy, and the energy sum of all bremsstrahlung photons associated with the track. The energy of muons is obtained from the corresponding track momentum. The energy of charged hadrons is determined from a combination of the track momentum and the corresponding ECAL and HCAL energies, corrected for zero-suppression effects, and calibrated for the nonlinear response of the calorimeters. Finally, the energy of neutral hadrons is obtained from the corresponding calibrated ECAL and HCAL energies. In the forward region, energy deposits collected by the HF are considered as electromagnetic or hadronic, depending on the respective energy collected by long and short fibers.

The PF approach enables additional mitigation of effects due to particles produced by additional pp collisions in the same or in neighboring bunch crossings (known as pileup). Charged PF candidates whose tracks are unambiguously associated with pileup vertices are discarded before entering the downstream reconstruction steps (e.g., jet clustering and computing lepton isolation). The contamination from neutral particles is subtracted on average by applying an event-by-event correction based on the jet-area method[2] [124, 125, 126, 127]. The median energy density ρ is calculated using the k_{T} clustering algorithm [128, 129, 130] with distance parameter $D = 0.6$ and $|\eta| < 4.7$. For this calculation, a large number of nonphysical particles (ghosts) with infinitesimal momenta and random direction, effectively mapping all the (η, ϕ) space, is added to the event. When the jet clustering is run on the event, the hard particles in the event are clustered together with such ghosts: a few jets will contain high-momentum particles from the hard-scattering interaction, but most of the jets will be entirely made of ghosts, for which the main real energy contributions come from detector noise and especially pileup. The median energy density ρ is defined, in each event, as the median of jet momenta p_{T}^{i} divided by their area A_i, $\rho = \mathrm{median}(p_{\mathrm{T}}^{i}/A_i)$. Using the median instead of the mean makes ρ insensitive to hard jets in the event, and including zero-energy jets composed of only ghost particles reduces bias for low pileup energy densities. Finally,

[2]The jet-area method may be applied to Calo jets as well as PF jets.

this median energy is subtracted to compute the corrected jet p_{T},

$$p_{\mathrm{T}}^{\mathrm{corr}} = p_{\mathrm{T}}^{\mathrm{uncorr}} - \rho A_j - \rho_1(\eta, \log p_{\mathrm{T}}^{\mathrm{uncorr}}) A_j \,, \tag{5.5}$$

where $p_{\mathrm{T}}^{\mathrm{uncorr}}$ is the uncorrected jet p_{T}, A_j is the jet area and $\rho_1(\eta, \log p_{\mathrm{T}}^{\mathrm{uncorr}})$ is a small residual η- and $\log p_{\mathrm{T}}^{\mathrm{uncorr}}$-dependent correction [127].

Jets and missing transverse energy

To demonstrate the effectiveness of PF reconstruction over traditional calorimeter-based reconstruction, we can examine the response and resolution of jets and missing transverse energy, two of the most important physics objects in the searches for SUSY outlined in Ch. 7 and Ch. 8, with both methods of reconstruction.

Jets are reconstructed with the anti-k_{T} algorithm [131, 132] and a distance parameter of $R = 0.4$ ($R = 0.5$) for 13 TeV data (7 TeV and 8TeV data), clustering either the four-momentum vectors of particles reconstructed by the particle-flow algorithm (PF jets), the energy deposits observed in the calorimeters (Calo jets), or the stable particles (lifetime $c\tau > 1$ cm) except neutrinos produced by the event generator (Ref jets).

In reconstructing the PF candidate four-momentum, photons are assumed massless and charged hadrons are assigned the charged pion mass. The Calo jet four-momentum is built from the four-momenta assigned to each calorimeter tower deposit as follows. A calorimeter tower consists of one or more HCAL cells and the geometrically corresponding ECAL crystals. For example, in the barrel region of the calorimeters, the unweighted sum of one single HCAL cell and 5×5 ECAL crystals form a projective calorimeter tower. The association between HCAL cells and ECAL crystals is more complex in the endcap regions. A four-momentum is associated with each tower deposit above a certain threshold, assuming zero mass, and taking the direction of the tower position as seen from the interaction point.

Each PF (Calo) jet is matched to the closest Ref jet within a cone of angle 0.1 (0.2) in the (η, ϕ) space. The use of a twice smaller cone angle for PF jets is justified by a twice better resolution on the measurement of the jet direction, shown in Fig. 5.6. The improved angular resolution for PF jets is mainly due to the precise determination of the charged-hadron direction and momentum. In Calo jets, the energy deposits of charged hadrons are

spread along the ϕ direction by the magnetic field, leading to a degraded azimuthal resolution. In CMS, the integration of the track reconstruction into the PF jet clustering, which is not traditionally done in other collider experiments, results in a better energy and angular resolution for PF jets.

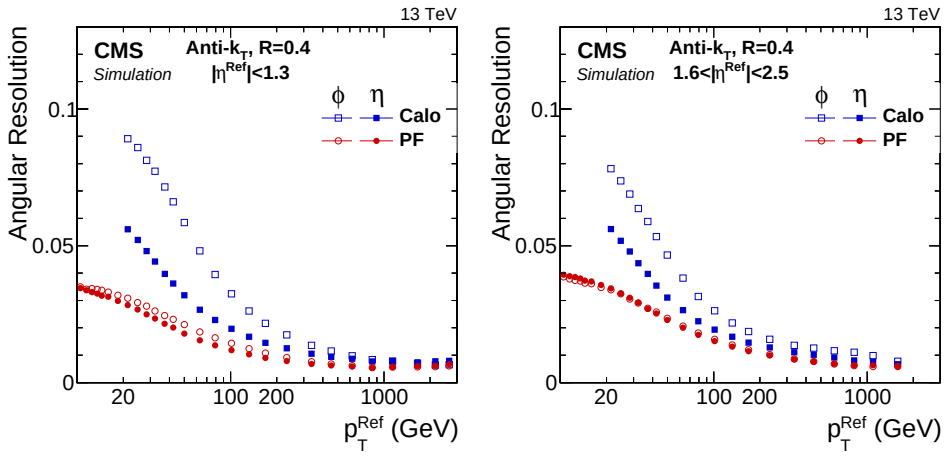

Figure 5.6: Jet angular resolution in the barrel (left) and endcap (right) regions, as a function of the transverse momentum of the reference jet [127].

The raw jet energy response, defined as the mean ratio of the reconstructed jet energy to the reference jet energy, is shown in Fig. 5.7. The PF jet response is, to a good approximation, linear as a function of the jet transverse momentum and is above 90% across the whole detector acceptance. A jet energy correction procedure is used to bring the jet energy response to unity, removing any dependence on p_{T} and η [127]. After this correction, the jet energy resolution, defined as the Gaussian width of the ratio between the corrected and reference jet energies, is also shown in Fig. 5.7.

The presence of particles that do not interact with the detector material, such as hypothetical dark matter particles or neutrinos, is indirectly revealed by the missing transverse momentum in an event [133]. The raw missing transverse momentum vector is defined in such a way as to balance the vectorial sum of the transverse momenta of all particles,

$$\vec{p}_{\mathrm{T}}^{\,\mathrm{miss}}(\mathrm{PF,raw}) = -\sum_{i=1}^{N_{\mathrm{particles}}} \vec{p}_{\mathrm{T}}^{\,i}. \tag{5.6}$$

The jet-energy-corrected missing transverse momentum,

$$\vec{p}_{\mathrm{T}}^{\,\mathrm{miss}}(\mathrm{PF}) = -\sum_{i=1}^{N_{\mathrm{particles}}} \vec{p}_{\mathrm{T}}^{\,i} - \sum_{j=1}^{N_{\mathrm{PF\,jets}}} (\vec{p}_{\mathrm{T}}^{\,\mathrm{corr}\,j} - \vec{p}_{\mathrm{T}}^{\,j}), \tag{5.7}$$

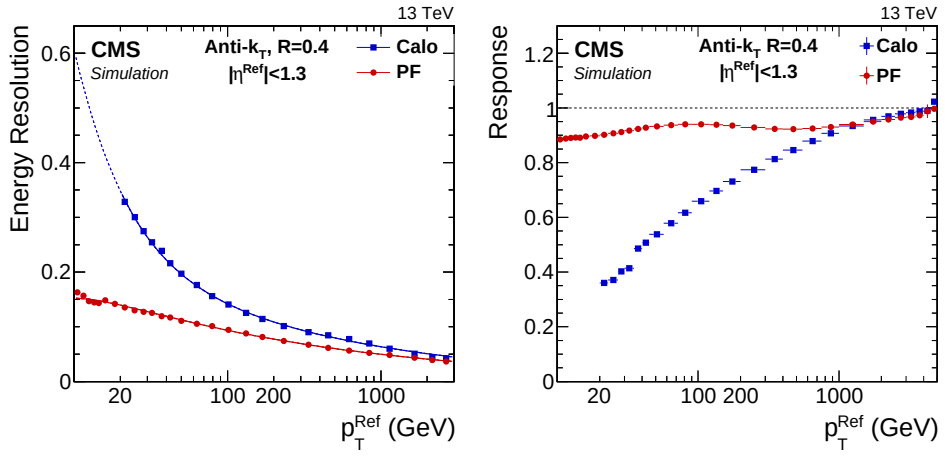

Figure 5.7: Jet p_T resolution (left) and jet p_T response (right) as a function of p_T^{Ref} in the barrel [127].

includes a jet energy correction term that replaces the raw momentum $\vec{p}_T^{\,j}$ of each PF jet with $\vec{p}_T^{\,j} > 10$ GeV by its corrected value $\vec{p}_T^{\,\mathrm{corr}\,j}$. As seen in Fig. 5.7, the PF jet response is close to unity, making this correction term small when the missing transverse energy is evaluated with reconstructed particles.

Before the advent of PF reconstruction, the missing transverse momentum was evaluated using information from the calorimeters and the muon system as,

$$\vec{p}_T^{\,\mathrm{miss}}(\mathrm{Calo}) = -\sum_{i=1}^{N_{\mathrm{cells}}} \vec{p}_T^{\,i} - \sum_{j=1}^{N_{\mathrm{Calo\,jets}}} (\vec{p}_T^{\,\mathrm{corr}\,j} - \vec{p}_T^{\,j}) - \sum_{k=1}^{N_{\mathrm{muons}}} \vec{p}_T^{\,k}\,, \tag{5.8}$$

where in the first term, the transverse momentum $\vec{p}_T^{\,i}$ of a given calorimeter cell is calculated assuming that the energy measured by the cell has been deposited by a massless particle coming from the origin. The jet energy correction term, computed with all Calo jets with $p_T > 20$ GeV, is sizeable given the relatively low energy response of Calo jets. The second correction term accounts for the presence of identified muons, which do not deposit significant energy in the calorimeters.

The performance improvement due to PF reconstruction may be quantified by comparing $\vec{p}_T^{\,\mathrm{miss}}(\mathrm{PF})$ and $\vec{p}_T^{\,\mathrm{miss}}(\mathrm{Calo})$ in terms of E_T^{miss} response and resolution. The E_T^{miss} resolution is measured for a simulated QCD multijet sample of events in Fig 5.8 as a function of ΣE_T, the total transverse energy developed in the event. Since the vast majority of QCD multijet events have

no true $E_{\mathrm{T}}^{\mathrm{miss}}$, the distribution of the transverse components of the $\vec{E}_{\mathrm{T}}^{\mathrm{miss}}$, $\vec{E}_{\mathrm{x,y}}^{\mathrm{miss}}$, can be approximated as a Gaussian[3] centered at zero and its width provides an estimate of the $E_{\mathrm{T}}^{\mathrm{miss}}$ resolution as $\sigma(E_{\mathrm{T}}^{\mathrm{miss}}) = \sqrt{2} \times \sigma(E_{\mathrm{x,y}}^{\mathrm{miss}})$. The ΣE_{T} response, defined as the average fraction of the true ΣE_{T} to be reconstructed, is also shown in Fig 5.8. Finally, the $\vec{E}_{\mathrm{T}}^{\mathrm{miss}}$ angular resolution, measured for a sample of $\mathrm{t\bar{t}}$ events in which at least one neutrino is produced in the decay of a W boson, is shown in Fig. 5.9. As in the case of jets, the superior response and resolution mainly arises from the improved measurement of the momenta of charged hadrons.

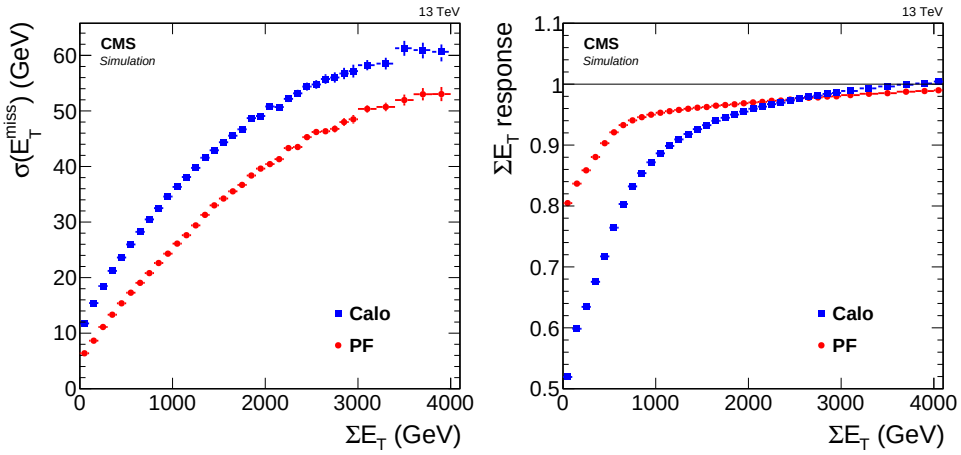

Figure 5.8: Absolute $E_{\mathrm{T}}^{\mathrm{miss}}$ resolution (left) and ΣE_{T} response (right) for a simulated QCD multijet sample [127]. In the case of the particle flow estimate, $E_{\mathrm{T}}^{\mathrm{miss}}$ stands for $E_{\mathrm{T}}^{\mathrm{miss}}(\mathrm{PF})$ and ΣE_{T} for $\Sigma E_{\mathrm{T}}(\mathrm{PF})$. In the case of the calorimeter-based estimate, they stand for $E_{\mathrm{T}}^{\mathrm{miss}}(\mathrm{Calo})$ and $\Sigma E_{\mathrm{T}}(\mathrm{Calo})$, respectively.

Rare failures related to the detector, the reconstruction of the PF inputs, and the algorithm itself generally translate to unexpectedly large values of the $E_{\mathrm{T}}^{\mathrm{miss}}$. Events with such large values are systematically scrutinized and when a shortcoming of the PF algorithm is fixed, the global performance of the PF reconstruction typically improves as a whole population of events were affected at lower values of the $E_{\mathrm{T}}^{\mathrm{miss}}$.

The performance of $\vec{E}_{\mathrm{T}}^{\mathrm{miss}}$ reconstruction with all corrections applied is assessed with a sample of observed events selected in the dimuon final state that is dominated by events with a Z boson decaying to two muons [133].

[3]Typically non-Gaussian tails emerge due to non-Gaussian response functions of the detector.

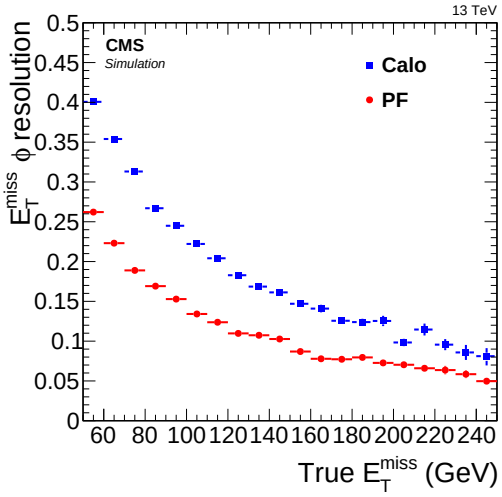

Figure 5.9: Resolution on the measurement of the $\vec{E}_{\mathrm{T}}^{\mathrm{miss}}$ azimuthal angle as a function of the true $E_{\mathrm{T}}^{\mathrm{miss}}$ for a simulated $\mathrm{t\bar{t}}$ sample [127].

The dataset is collected with a trigger requiring the presence of two muons passing p_{T} thresholds of 17 and 8 GeV, respectively. The two reconstructed muons must fulfill $p_{\mathrm{T}} > 20\,\mathrm{GeV}$ and $|\eta| < 2.1$, satisfy isolation requirements, and have opposite charge. Events where the invariant mass of the dimuon system is outside the window $60 < m_{\mu\mu} < 120\,\mathrm{GeV}$ are rejected. Fig. 5.10 shows the spectrum of $E_{\mathrm{T}}^{\mathrm{miss}}(\mathrm{PF})$ in the $\mathrm{Z} \to \mu^+\mu^-$ event sample. The simulation describes the observed distribution over more than five orders of magnitude.

Identification of b-quark jets

Jets that arise from bottom-quark hadronization (b-jets) are present in many physics processes, such as the decay of top quarks, the Higgs boson, and top and bottom squarks predicted by natural supersymmetric models. The ability to accurately identify b-jets is crucial in reducing the otherwise overwhelming background from processes involving jets from gluons (g), light-flavor quarks (u, d, s), and from c-quark fragmentation.

The properties of the bottom and, to a lesser extent, the charm hadrons can be used to identify the hadronic jets into which the b and c quarks fragment. These hadrons have relatively large masses, long lifetimes ($c\tau \sim 450\ \mu\mathrm{m}$) and daughter particles with hard momentum spectra. Their semileptonic decays can be exploited as well.

Within the CMS collaboration, these special features of b-quark hadroniza-

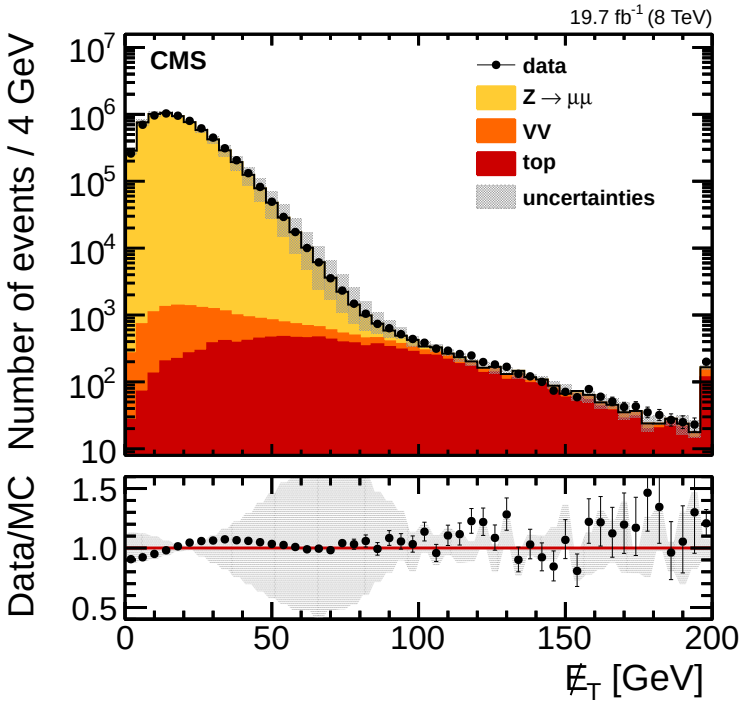

Figure 5.10: Spectrum of E_T^{miss}(PF) in the $Z \to \mu^+\mu^-$ dataset [127]. The observed data are compared to simulated $Z \to \mu^+\mu^-$, diboson (V V), and $t\bar{t}$ plus single-top-quark events (top). The lower frame shows the ratio of data to simulation, with the uncertainty bars of the points including the statistical uncertainties of both observed and simulated events and the grey uncertainty band displaying the systematic uncertainty of the simulation. The last bin contains the overflow.

tion are exploited in a set of b-jet tagging algorithms. A variety of reconstructed objects – tracks, vertices, and identified leptons – can be used to build observables that discriminate between q_b- and light-parton jets. Several simple and robust algorithms use just a single observable, while others combine several of these objects to achieve a higher discrimination power. Each of these algorithms yields a single discriminator value for each jet. The minimum thresholds on these discriminators define loose ("L"), medium ("M"), and tight ("T") operating points with a misidentification probability for light-parton jets of close to 10%, 1%, and 0.1%, respectively, at an average jet p_T of about 80 GeV.

The b-tag algorithm that was shown to have the best performance in terms of b-jet identification efficiency and light-parton-jet fake rate in Run 1 is the *Combined Secondary Vertex* (CSV) algorithm, which makes use of multi-

variate techniques to combine discriminating variables built from displaced track and secondary vertex information as well as jet kinematics [134, 135]. The following set of variables with high discriminating power and low correlations is used:

- the vertex category (real, "pseudo," or "no vertex");
- the flight distance significance (ratio of the flight distance to its estimated uncertainty) in the transverse plane ("2D");
- the vertex mass;
- the number of tracks at the vertex;
- the ratio of the energy carried by tracks at the vertex with respect to all tracks in the jet;
- the pseudorapidities of the tracks at the vertex with respect to the jet axis;
- the 2D impact parameter (IP) significance (ratio of the IP to its estimated uncertainty,) of the first track that raises the invariant mass above the charm threshold of 1.5 GeV (tracks are ordered by decreasing IP significance and the mass of the system is recalculated after adding each track);
- the number of tracks in the jet;
- the 3D IP significances for each track in the jet.

If no secondary vertex is reconstructed, only the last two variables in the preceding list are available. Two likelihood ratios are built from these variables to discriminate between b- and c-jets and between b and light-parton jets. They are combined with prior weights of 0.25 and 0.75, respectively.

The b-jet identification efficiency is about 70% for a misidentification probability for light-parton jets of about 1% for jets with p_{T} between 80 and 120 GeV, as seen in Fig. 5.11. For Run 2, the CSV algorithm was significantly improved (CSVv2) by updating the multivariate algorithm from a simple likelihood ratio to a neural network, improving the track selection and adding new variables, and using a new algorithm for the reconstruction

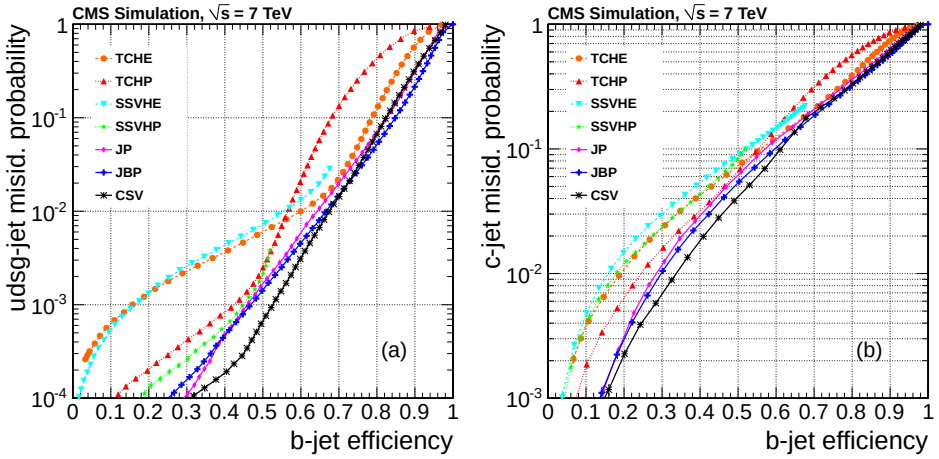

Figure 5.11: Performance curves obtained from simulation for the different b-jet tagging algorithms [134]. Light-parton- (left) and c-jet (right) misidentification probabilities as a function of the b-jet efficiency. Jets with $p_{\mathrm{T}} > 60\,\mathrm{GeV}$ in a sample of simulated multijet events are used to obtain the efficiency and misidentification probability values.

of the secondary vertices, the so-called Inclusive Vertex Finder (IVF). These updates turn into a net improvement in performance of about a 10% increase in the b-jet identification efficiency at a 1% of light-parton-jet misidentification rate, as pictured in Fig. 5.12. The b-jet identification at HLT uses the same algorithm as in the offline reconstruction, optimized to reduce the execution time [136].

5.6 Level-1 and high-level trigger

The role of the trigger is to reduce the rate of recorded collisions to a level which is manageable by the following data acquisition (DAQ) and online reconstruction procedures. At the LHC, the proton beams are organized in bunches separated in time by 50 ns during Run 1 (2010-2013) and 25 ns during Run 2 (2015-present), implying a collision rate on the order of 40 MHz[4]. The maximum acceptable rate for data acquisition and storage is of the order of 1 kHz, and the trigger is designed to reduce the rate to that level, while maintaining the largest possible acceptance of interesting physics signal events from the collisions and efficiently rejecting the non-interesting

[4] A 25{unitns bunch spacing gives a peak crossing rate of 40 MHz, however due to unoccupied gaps in the filling scheme, the actual average crossing rate is equal to the number of colliding bunches times the LHC revolution frequency, which was $2029 \times 11245\,\mathrm{Hz} = 22.8\,\mathrm{MHz}$ in 2015 and $2808 \times 11245\,\mathrm{Hz} = 31.6\,\mathrm{MHz}$ in 2016.

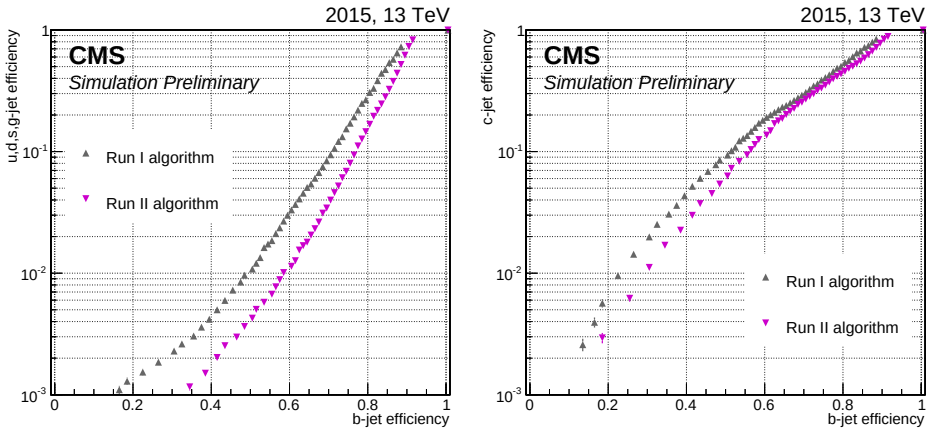

Figure 5.12: Light-parton- (left) and c-jet (right) misidentification probabilities as a function of the b-jet efficiency for the b-jet tagging algorithms used at HLT [136]. The gray and magenta curves show the performance of the Run 1 and Run 2 algorithms, respectively. Jets from simulated $\mathrm{t\bar{t}}$ events at $\sqrt{s} = 13$ TeV with 40 average pileup interactions and a bunch spacing of 25 ns are considered.

ones. Fig. 5.13 shows the typical data collection event rates corresponding to the different data streams, including those for physics analyses, trigger studies, alignment, calibration, and luminosity measurements, and data quality monitoring.

The design chosen for the trigger of the CMS experiment is a two-level system. The Level 1 (L1) trigger is based on FPGA and custom ASIC technology and uses information from the calorimeters and muon spectrometers of the experiment in order to accept or reject an event; it reduces the event rate down to approximately 100 kHz, acceptable by the readout electronics. The high-level trigger (HLT) is implemented in software running on a farm of commercial computers which includes approximately 16,000 CPU cores, and reduces the L1 output rate to the sustainable level for storage and physics analysis of about 1 kHz. The HLT software consists of a streamlined version of the offline reconstruction algorithms; it exploits the same software used for offline reconstruction and analysis, optimized in order to comply with the strict time requirements of the online selection.

The L1 trigger decision is made within a fixed time interval of less than 4 μs. The operational L1 output rate of 100 kHz, together with the number of CPUs in the HLT farm, imposes a fundamental constraint on the amount of

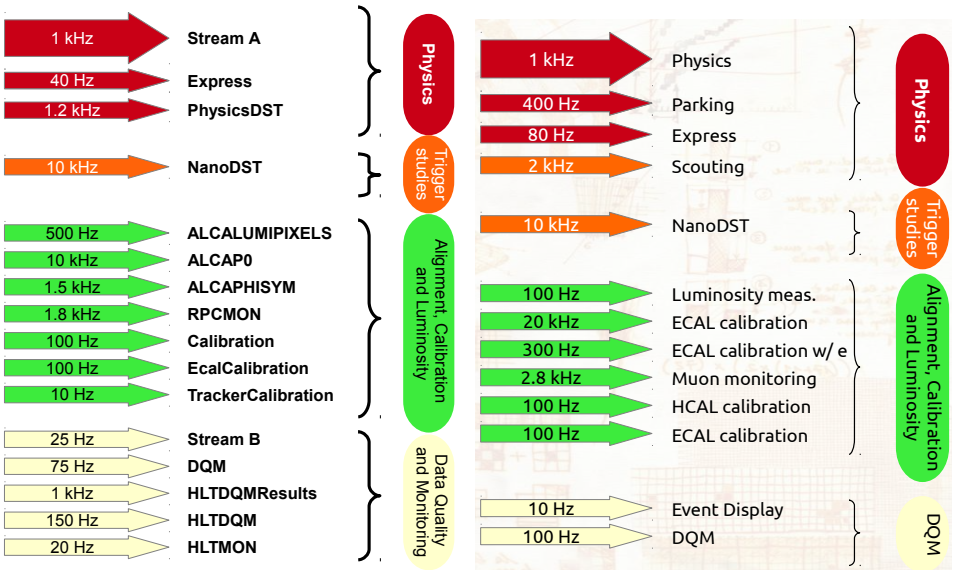

Figure 5.13: Data streams for physics analyses (red), trigger studies (orange), alignment, calibration, and luminosity measurements (green), and data quality monitoring (tan) during 2012 (left) and 2015 (right) [137].

time available for the HLT to process events. Exceeding this limit impacts the ability of CMS to collect data efficiently. Given the CPUs available in 2015, the timing budget of the HLT is measured to be about 300 ms when the machines are fully loaded (or 160 ms when the machines are running a single job) [138].

The HLT menu in CMS has a modular structure, which is graphically depicted in Fig 5.14. The menu is subdivided into logically independent paths, which may be run in parallel; more than 400 different HLT paths are used for Run 2 data taking. Each path is a sequence of reconstruction modules (producers) and filtering modules (filters). Filters typically select events based on the properties of a given physics object (photons, electrons, muons, jets, $\vec{p}_{\mathrm{T}}^{\,\mathrm{miss}}$, b-tagged jets, etc.), or, as in the case of the razor triggers detailed in Ch. 6, the properties of a combination of physics objects along with the values of topological variables M_{R} and R^2. The modules within a path are arranged in blocks of increasing complexity, so that faster algorithms are run first and their products are filtered: if a filter fails, the rest of the path is skipped.

In order to keep the online reconstruction of physics objects at HLT as close as possible to offline reconstruction, PF algorithms are used at the HLT

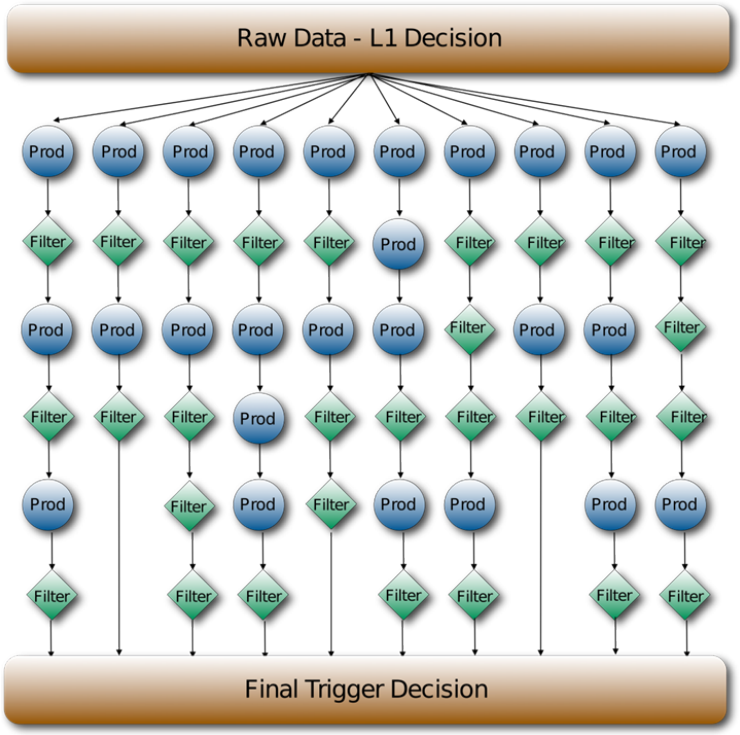

Figure 5.14: Schematic representation of the modular design of an HLT menu in CMS. The final trigger decision is the logical OR of the decisions of the single paths.

whenever possible. However, to stay within the limited timing budget due to the available CPU resources, the online reconstruction of a single event for the HLT must be done more than one hundred times faster than offline on average. Offline, most of the processing time is spent reconstructing the inner tracks for the PF algorithm. For the HLT, the tracking is reduced to three iterations, dropping the time-consuming reconstruction of tracks with a low transverse momentum or arising from nuclear interactions in the tracker material. These modifications preserve the reconstruction efficiency for tracks with $p_{\mathrm{T}} > 0.8$ GeV originating from the primary vertex, even when these tracks are produced in the decay of b hadrons. After track reconstruction, a specific instance of the particle identification and reconstruction algorithm runs online, with only two minor differences with respect to the offline algorithm: the electron identification and reconstruction is not integrated in the PF algorithm, and the reconstruction of nuclear interactions in the tracker is not performed. The main effect of these modifications is a slightly higher jet energy scale for jets featuring an electron or a

nuclear interaction.

One of the main technical limitations of LHC data processing is the available bandwidth at which events can be recorded on disk. Typically, this limitation forces the LHC experiments to increase the thresholds of their triggers, in order to keep an acceptable data volume despite the increasing collision rate. The CMS experiment implemented special solutions to circumvent these limitations, combining the standard trigger approach (event filtering) with datasize reduction. By limiting the amount of recorded information per event, one can accept more events without allocating more bandwidth. This strategy is adopted both for the alignment and calibration of the detector (Sec. 5.7) and for increasing the acceptance to specific physics signals (Sec. 5.8).

5.7 Alignment and calibration

Fast and efficient methods for the calibration and the alignment of the detector are a key ingredient in exploiting the physics potential of CMS [139, 140, 141]. To this end, CMS has a powerful framework for alignment and calibration, which is based on dedicated "skims," or subsets of data samples, providing a highly compact input for the various workflows computing the calibration and alignment constants.

Most of the alignment and calibration workflows are fed with dedicated data samples, called AlCaReco datasets, optimized both in terms of event selection and event content. Depending on the needs of the specific workflow, these samples can be selected offline, while performing the reconstruction, or directly online, at the HLT level.

An example of an online calibration stream is the one selecting events containing π^0 and η candidates detected in the ECAL and used for the intercalibration of the $PbWO_4$ scintillating crystals [116]. The calibration performance depends on the number of selected π^0 candidates per crystal and on the signal-to-background ratio. The candidate diphoton decays are selected at the HLT level from events passing single-e/γ and single-jet L1 triggers. After selection, only information about a limited region of ECAL (energy deposits in 20 to 40 individual crystals) near the π^0 candidates is stored for the actual calibration. This allows one to sustain a high rate of calibration events (1 to 10 kHz) while saving bandwidth and CPU time.

Detector conditions that change on a short time scale require a special calibration workflow designed to allow updates with very short latency. To meet this need, the organization of data streams is as follows [139, 140, 141]:

- express processing: reconstruction of a limited selection of data in order to give quick feedback about the detector status and physics performance and to provide data for calibration workflows. The results of the express reconstruction for a given run are usually available one or two hours after the raw data are collected;
- bulk processing: reconstruction of the main data stream for physics analysis. This step, called prompt reconstruction, is delayed by 48 hours to allow for the computation and usage of new calibration constants relating to fast-changing conditions. The output is divided in several Primary Datasets (PD) on the basis of the HLT paths that select the events;
- calibration streams: streams of events selected at the HLT level and processed at Tier-0 for calibration purposes.

During Run 1 normal operation, about $300 - 400$ Hz of data were processed in the bulk processing, while about $30 - 40$ Hz was allocated for express processing in order to guarantee a fast reconstruction. A selection of data from the express and calibration streams is used to compute the updated conditions for a given run while the bulk of the data is buffered on disk. The calibration workflows run on a dedicated farm at CERN called the CMS Analysis Facility (CAF). In this way the prompt reconstruction can profit from the updated constants, reducing the need for offline reprocessing of the data. This workflow is called the *prompt calibration loop* and is illustrated schematically in Fig. 5.15. The conditions currently updated through this kind of workflow are [139, 140, 141]:

- measurement of the beam-line parameters;
- monitoring and masking of problematic channels of the silicon strip tracker to respond to HV trips or noise;
- transparency corrections based on the laser monitoring system [142, 143] for the $PbWO_4$ crystals of the ECAL calorimeter.

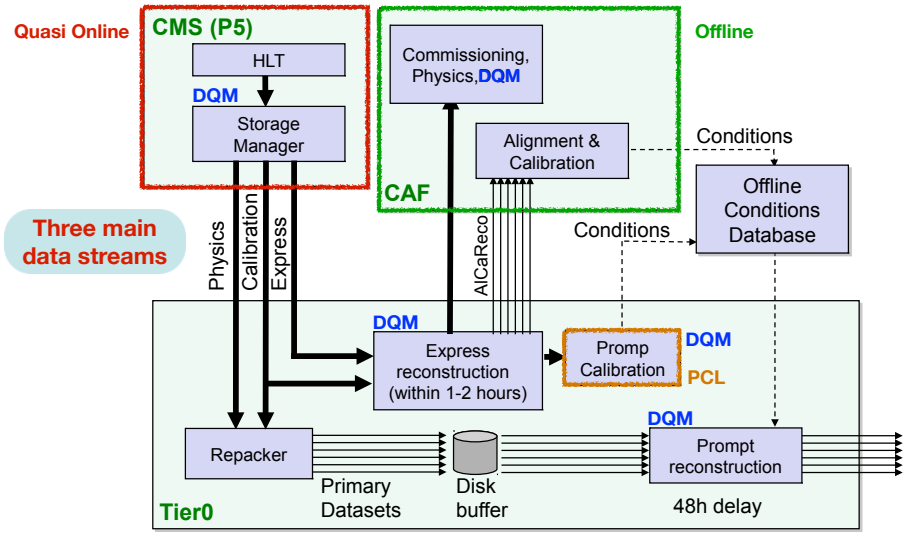

Figure 5.15: Alignment and calibration data-processing flow in CMS [141].

The delayed prompt reconstruction is also exploited to monitor possible movements of large structures of the silicon tracker, mainly due to thermal stress, and problematic channels in the electromagnetic and hadronic calorimeters allowing for quick reaction time in case of "hot" regions identified in the express reconstruction.

In order to reach the ultimate accuracy, more sophisticated alignment and calibration workflows are run offline. No time constraints are present in this case and the full treatment of the detector's alignment and calibration interdependencies can be studied and taken into account. The full data sample is exploited to provide the final set of conditions which are then used in the reprocessing of the data. In normal conditions the full dataset is reprocessed once per year. Some important offline workflows are as follows:

- energy calibration of the ECAL response (single channel and overall energy scale calibration);
- measurement and correction of the tracker orientation with respect to the magnetic field;
- tracker module alignment.

A third class of calibration workflows, the quasi-online calibration, is meant to update conditions at HLT for data taking. For some very stable correc-

tions that do not need to be validated, such as the measurement of beam-line parmaters, an application running in the Data Quality Monitoring (DQM) framework [144] automatically derives and stores conditions in a database which is then accessed at the HLT during the online event reconstruction. This feedback from the DQM to the HLT happens with a time granularity of 2 minutes (5 luminosity sections) [139, 140, 141]. For other corrections that do need to be validated, such as the ECAL transparency corrections, a validation workflow is run, involving ECAL experts who derive, carefully check, and upload the corrections to the database on a weekly basis during data taking.

ECAL laser monitoring

The ECAL crystals receive large doses of radiation throughout the duration of LHC operation. The expected integrated ionizing dose in the ECAL is up to 4 kGy in the barrel and 200 kGy at $|\eta| = 3$ after 10 years of LHC operation, while the expected hadron fluence varies between about 10^{13} cm^{-2} in the barrel and 10^{14} cm^{-2} at $|\eta| = 3$ [145]. The crystal response is subject to time-dependent changes in trasparency under this irradiation due to the formation of color centers, as well as lattice defects caused by hadronic interactions in the crystals [146]. In order to measure and correct for response changes during LHC operation, the ECAL is equipped with a light monitoring (LM) system [142, 143].

The evolution of the ECAL response to the laser light (440 nm in 2011 and 447 nm from 2012 onwards) from 2011 through 2016 is shown in Fig. 5.16, as a function of time [147]. The response drops during periods of LHC operation, and partially recovers during shutdown periods (or periods of low-luminosity data-taking). These observations correspond to changes in crystal transparency [146] and are used to correct the physics data. The response change observed in the ECAL channels is up to 6% in the barrel and it reaches up to 30% at $|\eta| \sim 2.5$, the limit of the tracker acceptance. The response change is up to 70% in the region closest to the beam pipe.

The ECAL light monitoring system is used to determine corrections, denoted $S(t)$, to response changes in the ECAL. The laser light is injected through optical fibers in each crystal. The spectral composition and the path for the collection of laser light at the photodetector are different from those

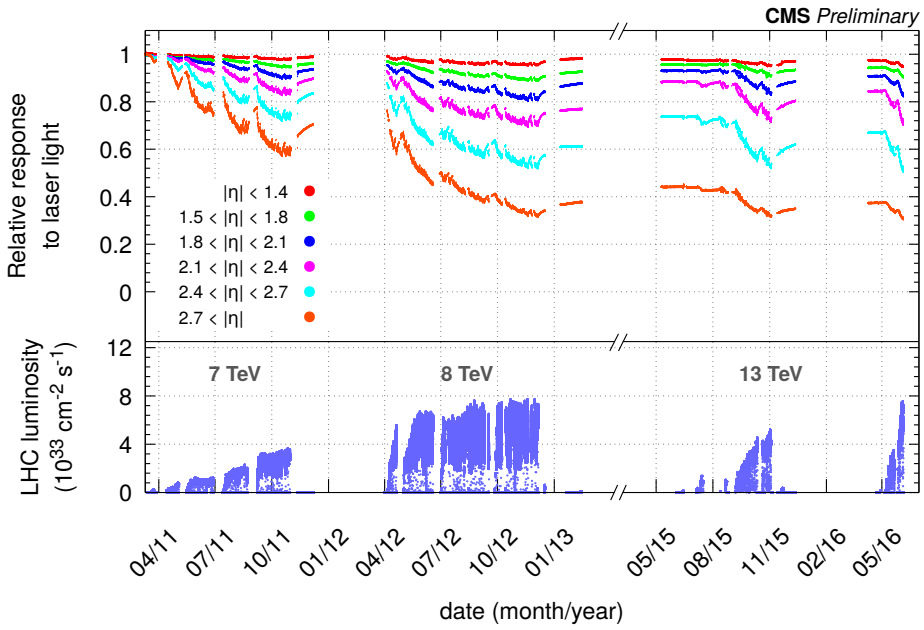

Figure 5.16: Relative response to laser light from 2011 to 2016, normalized to data at the start of 2011 [147]. An average is shown for each pseudorapidity range. The bottom plot shows the corresponding instantaneous luminosity. After each LHC technical stop, a recovery of crystal transparency is observed.

for scintillation light. A conversion factor is required to relate the changes in the ECAL response to laser light to the changes in the scintillation signal. The relationship is described by a power law [145]:

$$\frac{S(t)}{S_0} = \left(\frac{R(t)}{R_0}\right)^{\alpha}, \tag{5.9}$$

where $S(t)$ is the channel response to scintillation light at a particular time t, S_0 is the initial response, and $R(t)$ and R_0 are the corresponding response to laser light. The exponent α is independent of the loss for small transparency losses and was measured in test beams to be 1.52 and 1.0 for crystals from the two different producers, in Russia and China [148, 149, 150].

Alternative forms of these laser corrections, differing in time and spatial granularity, are utilized at different stages in the data processing: online at the HLT, during the prompt reconstruction, and during offline reprocessing of the data. At HLT, the laser corrections are updated once-per-week and are applied to 11 different η rings in each endcap and 17 different η rings in the barrel (the corrections are averaged over each ring). For the prompt

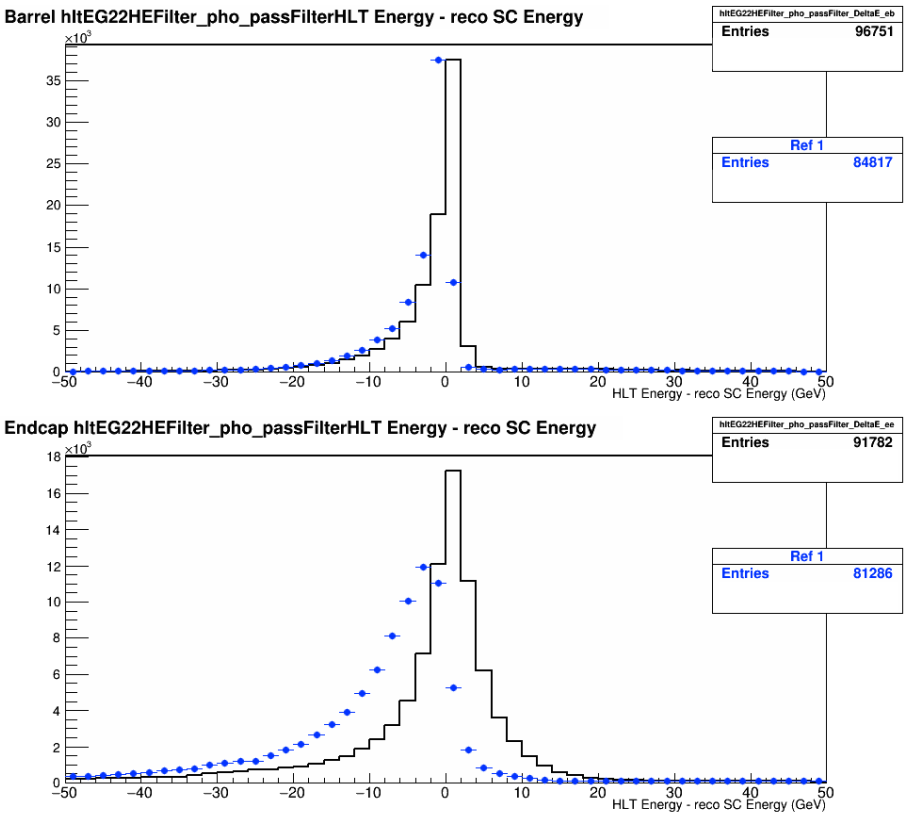

Figure 5.17: The top (bottom) plot shows the difference between the super-cluster energy reconstructed at HLT and a reference energy for the ECAL barrel (endcaps) for a particular week of data-taking in 2015. The blue data points show the difference using the week-old laser corrections, while the solid black histogram shows the reconstructed energy with the updated laser correction undergoing validation.

reconstruction and the offline reprocessing of the data, the laser corrections are updated every 40 minutes and are applied crystal-by-crystal.

The validation of the HLT laser corrections uses a custom workflow which re-runs the HLT reconstruction on recently collected data with two versions of laser corrections: the version currently online (and now out-of-date) and the version to be validated (and up-to-date). An example of a successfully validated HLT laser correction for a particular week of data-taking in 2015 is shown in Fig. 5.17 [151]. Unlike the outdated laser corrections (shown in blue), the updated laser corrections (shown in black) correct the energy response and improve the energy resolution for both the endcaps and the barrel.

The η and π^0 meson data are used to validate the laser corrections for

prompt reconstruction and to intercalibrate the energy of ECAL crystals. The events are selected online by a dedicated calibration trigger with a rate of 8 (2.5) kHz in the barrel (endcap), and recorded with reduced event content, including energy deposits in the ECAL crystals surrounding a possible π^0 candidate. A fit is carried out on the invariant mass distribution of the photon pairs in the mass range of the η or π^0 meson. The fit comprises a polynomial function to describe the background and a Gaussian distribution to describe the resonance peak. Fig. 5.18 shows an example of the π^0-meson peak with the fit superimposed, and the relative value of the fitted π^0 mass versus time in the barrel for a period of 8 hours [147]. The right plot shows the energy scale as a function of time, with (green points) and without (red points) the light monitoring corrections applied, over a period of 8 hours for data recorded on May 28, 2016 during LHC fill 4958. Each point is obtained from a fit to approximately 8 minutes of data taking. A number of measurements are possible for each LHC fill, owing to the high rate for recording π^0 and η events. This permits short-term changes in the ECAL response to be verified before the prompt reconstruction takes place.

Finally, isolated electrons from $W \to e\nu_e$ and $Z \to e^+e^-$ decays are used to provide an energy scale to validate the laser corrections over periods of days to weeks. The event selection is described in Ref. [152, 153, 120, 154]. The ratio of the electron energy, E, measured in the ECAL, to the electron momentum, p, measured in the tracker, is computed in each event, and a reference E/p distribution is obtained from the entire data set after applying laser corrections. The width of the E/p reference distribution is dominated by the energy and momentum resolution and is not biased by residual imperfections in the laser corrections. This reference distribution is then scaled to fit E/p distributions obtained by dividing the same data in groups of 12,000 (5,000) consecutive events for 8 TeV (13 TeV) data recorded in 2012 (2015). The scale factors provide a measure of the relative response and are shown in Fig. 5.19 for 2012 and 2015 data, as a function of time [120, 154]. The data are shown before (red open circles) and after (green filled circles) the laser monitoring corrections are applied. A stable response to electromagnetic showers is achieved throughout 2012 (2015) with an RMS of 0.09% (0.15%) in the barrel. This method does not require a knowledge of the absolute calibration of both the energy and the momentum.

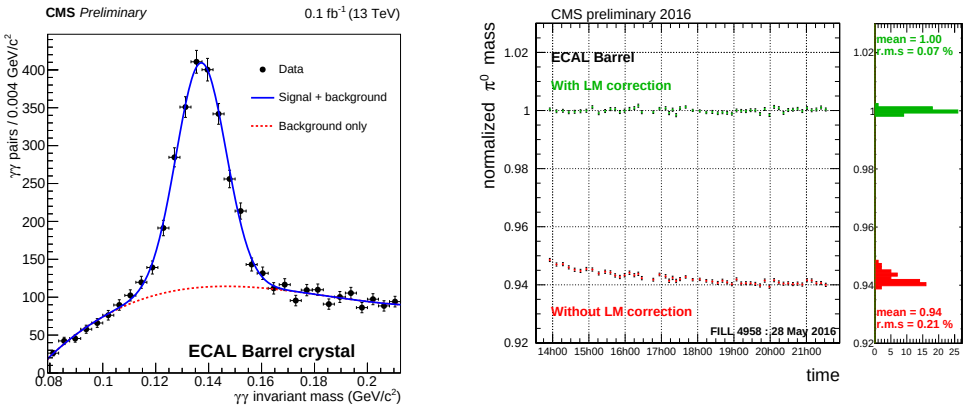

Figure 5.18: (Left) Invariant mass of photon pairs reconstructed in one crystal of the ECAL barrel, in the mass range of the π^0 meson, during the run 273730 taken in May 2016, corresponding to an integrated luminosity of approximately 100 pb^{-1}. (Right) The stability of the relative energy scale measured from the invariant mass distribution of π^0 decays in the ECAL barrel for a typical LHC fill in 2016. The energy scale is measured by fitting the invariant mass distribution of approximately 200,000 photon pairs in the mass range of the π^0 meson. Each point is obtained from a fit to approximately 8 minutes of data taking. The error bars represent the statistical errors on the fitted peak position. The energy scale is plotted as a function of time, over a period of 8 hours for data recorded on May 28, 2016 during LHC fill 4958. The plot shows the data with (green points) and without (red points) light monitoring corrections applied. The right-hand panel shows the projected relative energy scales [147].

5.8 Data scouting

An extension of the alignment/calibration data-taking strategy, referred to as *data scouting* [155], is based on reducing the event size from the default of $\sim$ 1 Megabyte (MB) in order to increase the recorded event rate and thus increase physics signal acceptance. This approach, first implemented at the LHC by the CMS experiment in 2011 [156], allows us to increase the physics signal acceptance of CMS even in the presence of backgrounds with large cross sections. This is particularly useful in the search for narrow resonances in the dijet mass spectrum, as described in Ch. B, where this strategy allows the search to be extended into a low-dijet-mass region previously only accessible at lower-energy colliders [157, 158].

Fig 5.20 schematically displays the H_T thresholds used for the different varieties of data scouting during the 2015 and 2016 runs and Fig 5.21 displays

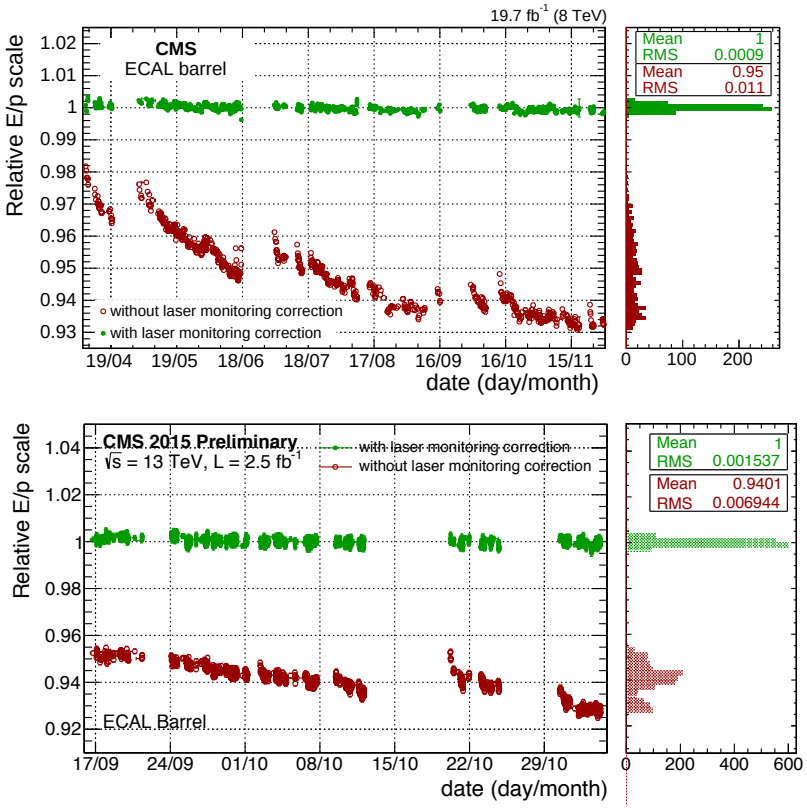

Figure 5.19: Ratio of the energy measured by the ECAL over the momentum measured by the tracker, E/p, for electrons selected from $W \to e\nu_e$ and $Z \to e^+e^-$ decays, as a function of the date at which they were recorded [120, 154]. The ratio is shown both before (red open circles) and after (green filled circles) the application of transparency corrections obtained from the laser monitoring system, and for the ECAL barrel in 2012 at 8 TeV (upper plot) and in 2015 at 13 TeV (lower plot). Histograms of the values of the measured points, together with their mean and RMS values are shown beside the main plots.

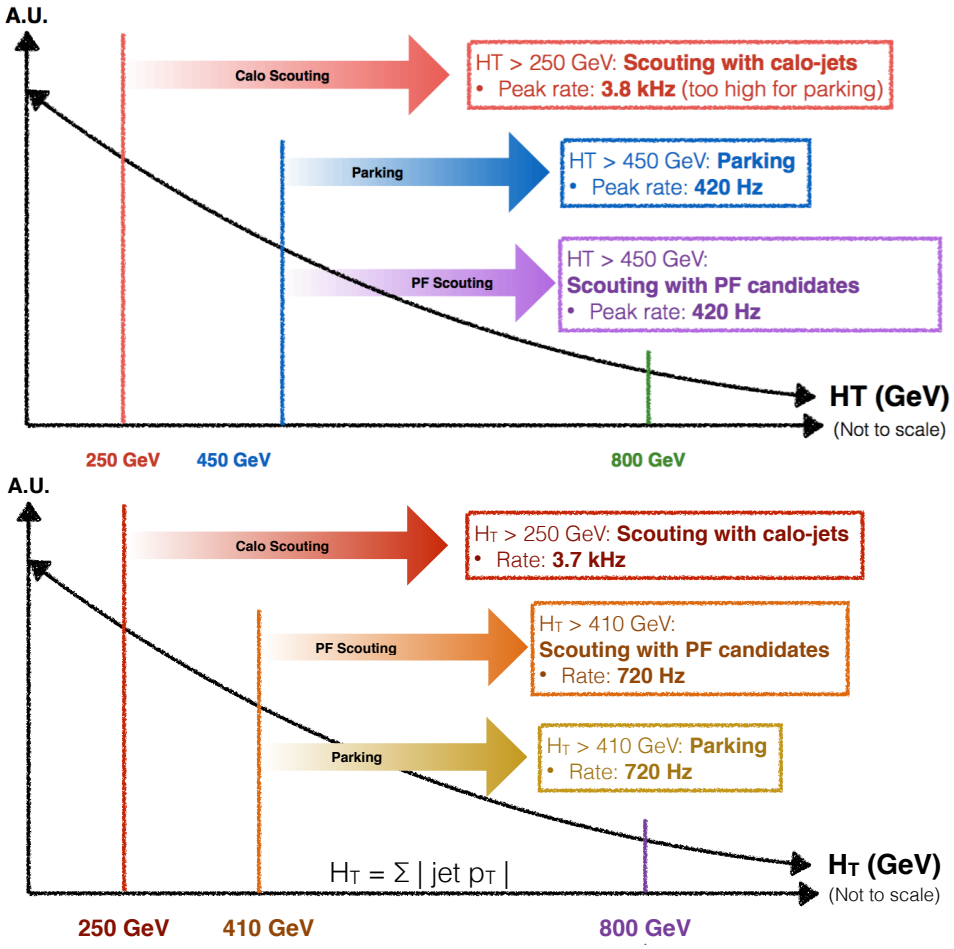

Figure 5.20: HLT H_T thresholds for Calo and PF scouting for 2015 (top) and 2016 (bottom) data-taking runs [155]. The rates for the 2015 (2016) are normalized to an instantaneous luminosity of 7×10^{33} cm^{-2} s^{-1} (10^{34} cm^{-2} s^{-1}).

the corresponding event content [155]. *Calo scouting*, which selects events based only on Calo jets and records only calorimetric information, has a very small event size of $\sim$ 1.5 kilobyte (kB), allowing the rate to go as a high as 3.8 kHz. Meanwhile, *PF scouting*, which runs the full PF algorithm and records all PF-reconstructed information, including leptons, photons, and jets with b-tagging information, has a larger event size $\sim$ 10 kB. In order to stay within the HLT timing budget, the maximum permissible rate is 720 Hz. Simultaneously, the *data parking* stream sends the full raw events from PF scouting directly to tape without reconstruction. This multifaceted approach is advantageous in the case that a signal is seen in the scouting data that warrants more investigation.

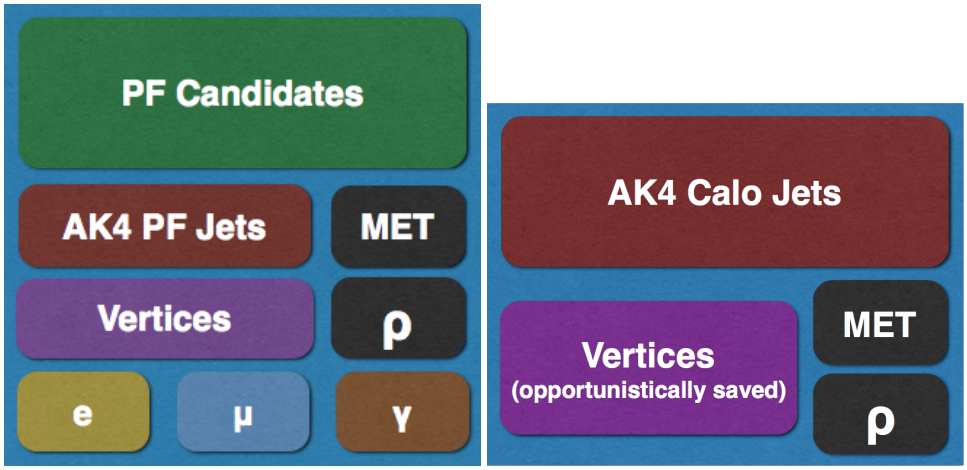

Figure 5.21: The event content for PF scouting (left) consists of PF candidates, anti-k_T $R = 0.4$ PF jets, PF E_T^{miss}, reconstructed vertices, PF-reconstructed electrons, muons, photons, and the median energy density in an event ρ, which amounts to ~ 10 kB. The event content for Calo scouting (right), consists of anti-k_T $R = 0.4$ Calo jets, Calo E_T^{miss}, vertices (if another trigger reconstructed them for this event), and the median energy density in an event ρ, which amounts to ~ 1.5 kB [155].

Chapter 6

TOPOLOGICAL HLT DEVELOPMENT AT $\sqrt{S} = 13\,\text{TEV}$

Traditionally, trigger algorithms employed at hadron colliders consisted of selecting events based on the presence of specific particles, such as leptons or photons, above some energy threshold and isolated from the rest of the event. In other trigger algorithms, global event properties (such as "sum" quantities like the hadronic transverse energy H_T or the missing transverse energy E_T^{miss}) were also used.

The event selection used in modern searches for BSM physics employ new techniques, such as kinematic variables like M_R and R^2, that no longer map on to these traditional trigger requirements. Fortunately, the flexibility of the software-based system allowed the development of dedicated trigger paths, based on sophisticated kinematic variables and specific event topologies.

To target a broad range of new physics possibilities, we designed four different types of triggers for use in $\sqrt{s} = 13\,\text{TeV}$ pp collisions:

- Dijet razor trigger with hyperbolic M_R and R^2 requirements targeting the squark pair production topology;
- Quadjet razor trigger with hyperbolic M_R and R^2 requirements targeting top-squark or gluino pair production topologies;
- High-R^2 trigger targeting dijet+invisible topologies with large transverse momentum imbalance; and
- Razor $H(b\bar{b})$ trigger targeting production of Higgs boson decaying to a bottom quark-antiquark pair ($H \to b\bar{b}$) in association with a jet and possibly some missing transverse energy, i.e. $H(b\bar{b}) + \text{jet} + \text{invisible}$.

The dijet and quadjet razor triggers are broadly motivated by SUSY pair production and represent an update and incremental improvement of the razor triggers used in previous searches at $\sqrt{s} = 8\,\text{TeV}$ [94]. Both sets of triggers are based on hyperbolic thresholds in the (M_R, R^2) plane, with the

2015 updated thresholds shown in Fig 6.1. The 2015 hyperbolic contours follow the iso-probability contours $(R^2 + 0.25)(M_R + 300\,\text{GeV}) = \text{constant}$, derived from the background-only fit to the MultiJet category in the 8 TeV razor search performed using 2012 data. This implies that these hyperbolic contours efficiently reject background, while maintaining a large acceptance for SUSY signal models with a large characteristic mass scale $M_\Delta \gtrsim 500\,\text{GeV}$ and sufficient transverse momentum imbalance. Another update is that the 13 TeV razor triggers are based on PF-reconstructed objects rather than Calo jets and muons, which means that the online R^2 variable is much more correlated with the offline R^2 variable, which is also PF-based. This leads to an improved trigger efficiency plateau of 97% for 2015 (compared to 95% in 2012), shown in Fig. 6.2.

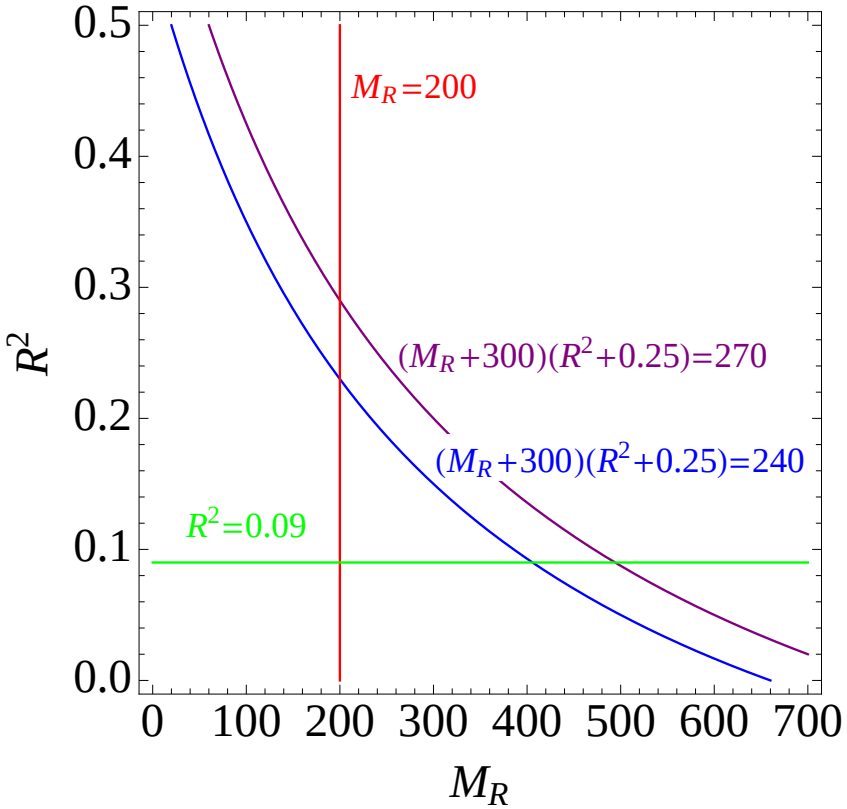

Figure 6.1: Hyperbolic and baseline thresholds in R^2 and M_R used in the dijet and quadjet razor triggers [44]. The hyperbolic thresholds are of the form $(R^2 + 0.25)(M_R + 300\,\text{GeV}) = \text{constant}$.

The high-R^2 trigger is motivated by the search for the direct production of dark matter (DM) particles at the LHC [159]. DM particles themselves would not leave a detectable signal in the detector, but if they were pro-

duced in association with high-energy quarks or gluons, they could produce signatures with jets and transverse momentum imbalance. The traditional approach, employed by both CMS and ATLAS, is to search in events with one high-p_T jet and large E_T^{miss} (so-called monojet searches) [160, 161]. A complementary approach is to search in events with at least two jets passing a looser event selection using the razor variables. The sensitivity of these variables to direct DM production was suggested in Ref. [162], and the search carried out by CMS demonstrates that the resulting sensitivity is comparable to that of monojet searches [162, 163, 159]. The hallmark of many direct DM production models in the razor plane is a peaking behavior near $R^2 \gtrsim 0.8$ and an exponentially falling M_R distribution with no special structure. For this reason, the high-R^2 trigger is designed with a threshold in R^2 but no requirement on M_R to allow for greater DM signal acceptance.

Finally, the razor $H(b\bar{b})$ trigger is motivated by an excess observed in Run 1 by CMS in events with a Higgs boson decaying to two photons ($H \to \gamma\gamma$) plus at least one extra jet [164]. The excess, corresponding to a local significance of 2.9σ, consists of five events observed with $400\,\text{GeV} < M_R < 1400\,\text{GeV}$, $R^2 > 0.05$, and $m_{\gamma\gamma}$ consistent with $m_H = 125\,\text{GeV}$ in a high-resolution diphoton category, compared to less than one expected background event. The general idea is to search for a similar signature in the $H \to b\bar{b}$ channel, which comes with a larger signal yield (90,000 times more assuming SM Higgs branching ratios), but a much larger background, resulting in a considerably worse signal-to-background ratio and a much larger background event rate. These final two features make the definition of an optimal trigger strategy much more challenging than in the $H \to \gamma\gamma$ decay channel. Given this, the trigger requirements of three jets, two b-jets, $M_R > 300\,\text{GeV}$, $R^2 > 0.02$, and $m_{b\bar{b}}$ roughly consistent with $m_H = 125\,\text{GeV}$ are chosen to (a) maintain signal acceptance based on the observed features, (b) accept additional events outside of the m_H window to permit a robust background estimation based on a fit, and (c) limit the rate and average CPU time of the trigger to an acceptable level.

For each trigger, we developed two different versions: a "main" version intended for $7 \times 10^{33}\ \text{cm}^{-2}\ \text{s}^{-1}$ and 20 average pileup interactions, and a "backup" version, with tighter thresholds intended for $1.4 \times 10^{34}\ \text{cm}^{-2}\ \text{s}^{-1}$ and 40 average pileup interactions. The correspondence between the pur-

pose of each trigger and its path name is shown in Tab. 6.1. Each trigger path name encodes the main selection criteria. For the dijet and quadjet triggers, "RsqMR240" denotes the hyperbolic threshold $(R^2 + 0.25)(M_R + 300\,\text{GeV}) = 240\,\text{GeV}$, "Rsq0p09_MR200" denotes the baseline thresholds $R^2 > 0.09$ and $M_R > 200\,\text{GeV}$, and "4jet" denotes a four-jet requirement where the two leading (remaining) jets are required to have a minimum p_T of 50 GeV (40 GeV). For the $H(b\bar{b})$ trigger, "TriPFJet80_60_40" denotes a three-jet requirement where the leading, subleading, and remaining jet is required have a minimium p_T of 80 GeV, 60 GeV, and 40 GeV, respectively, "DoublePFBTagCSV0p7_0p4" denotes a two q_b-tagged jet requirement, with CSV discriminator values above 0.7 and 0.4, respectively, and "Mbb60_200" denotes the $60 < m_{b\bar{b}} < 200\,\text{GeV}$ mass window.

Table 6.1: Correspondence between the purpose of each trigger and its path name.

Trigger path	Purpose
HLT_RsqMR240_Rsq0p09_MR200	main dijet trigger
HLT_RsqMR270_Rsq0p09_MR200	backup dijet trigger
HLT_RsqMR240_Rsq0p09_MR200_4jet	main quadjet trigger
HLT_RsqMR270_Rsq0p09_MR200_4jet	backup quadjet trigger
HLT_Rsq0p25	main high-R^2 trigger
HLT_Rsq0p30	backup high-R^2 trigger
HLT_Rsq0p02_MR300_TriPFJet80_60_40_ DoublePFBTagCSV0p7_0p4_Mbb60_200	main $H(b\bar{b})$ trigger
HLT_Rsq0p02_MR300_TriPFJet80_60_40_ DoublePFBTagCSV0p7_Mbb60_200	backup $H(b\bar{b})$ trigger

6.1 HLT path design

The design of the four main HLT paths in terms of producers (in purple) and filters (in blue) is shown in Fig. 6.3. The first step is always a filter, which rejects events with no hadronic activity above a certain threshold reconstructed by the L1 trigger. As detailed in Sec. 5.6, there are two main technical constraints an HLT path must satisfy: (a) the average CPU time required must be small enough so that the entire HLT menu fits within the timing budget of ~ 160 ms per event and (b) the rate must be small enough so that the entire HLT menu fits within the maximum allowable rate of ~ 1 kHz. To satisfy the timing requirement, all the paths are outfitted with calori-

metric prefilters. The aim of these prefilters is to reject events based only on information from the calorimeters, whose reconstruction algorithms are much faster than the PF algorithm. In other words, to keep the timing of the paths manageable, it is necessary to limit the input rate to the PF algorithm. Thus, all four triggers have a prefilter based on calorimeter-based versions of the razor variables.

6.2 HLT rate and average CPU time

The HLT rates and average CPU time consumed per event for the both the main and backup razor triggers, as measured in data collected in 2015, are presented in Tab. 6.2. The thresholds on the razor variables, jet p_T, and b-tag discriminator values, and were all optimized to achieve an acceptable level of added rate and added CPU time per event with respect to the rest of HLT menu (taking into account overlapping events and reused algorithms) for the full suite of razor triggers.

Table 6.2: HLT rates and average CPU time consumed for the main and backup razor triggers under different running conditions in 2015. Run 260627 had 5×10^{33} cm^{-2} s^{-1} peak instantaneous luminosity with 17 average pileup interactions, while run 259721 had 1.5×10^{33} cm^{-2} s^{-1} peak instantaneous luminosity with 23 average pileup interactions.

Trigger path	Data rate [Hz] Run 260627 5×10^{33} cm^{-2} s^{-1} 17 PU	CPU time [ms] Run 259721 1.5×10^{33} cm^{-2} s^{-1} 23 PU
HLT_RsqMR240_Rsq0p09_MR200	7.7	27
HLT_RsqMR270_Rsq0p09_MR200	2.3	17
HLT_RsqMR240_Rsq0p09_MR200_4jet	1.2	20
HLT_RsqMR270_Rsq0p09_MR200_4jet	0.5	15
HLT_Rsq0p25	0.7	14
HLT_Rsq0p30	0.4	14
HLT_Rsq0p02_MR300_TriPFJet80_60_40_DoublePFBTagCSV0p7_0p4_Mbb60_200	16.0	34
HLT_Rsq0p02_MR300_TriPFJet80_60_40_DoublePFBTagCSV0p7_Mbb60_200	8.0	26

6.3 Pileup dependence of HLT rate

The HLT rate, normalized by the number of colliding bunches, as a function of the number of pileup interactions for each razor trigger and for different data runs collected in 2015 is shown in Figures 6.5 and 6.6. Nominally, the dependence of the normalized HLT rate on pileup is expected to be linear,

as is the case for single-object triggers. In contrast, triggers based on sum quantities (such as H_T or E_T^{miss}) and multi-object triggers often demonstrate a nonlinear dependence on pileup, not due to a physical increase in the cross section of the selected physics processes, but rather due to the effects of pileup contamination [165]. To illustrate this, consider the case of a QCD dijet event with no true E_T^{miss}. Normally such an event would be rejected by E_T^{miss} triggers that require E_T^{miss} above some threshold, but if some jets from pileup interactions are misinterpreted as part of the event-of-interest then the HLT-reconstructed $\vec{p}_T^{miss}$ will be $-\sum_{j \in \text{pileup}} \vec{p}_T^{\,j}$, which may not perfectly balance to zero as illustrated in Fig. 6.4.

As the razor triggers are both based on sum quantities and multiple objects, they also exhibit some nonlinear dependence on pileup. This implies that as the pileup increases at the LHC in 2016 and beyond, either trigger thresholds will need to rise dramatically or more sophisticated methods to deal with pileup contamination will need to implemented. One such method is delineated in Ch. 9.

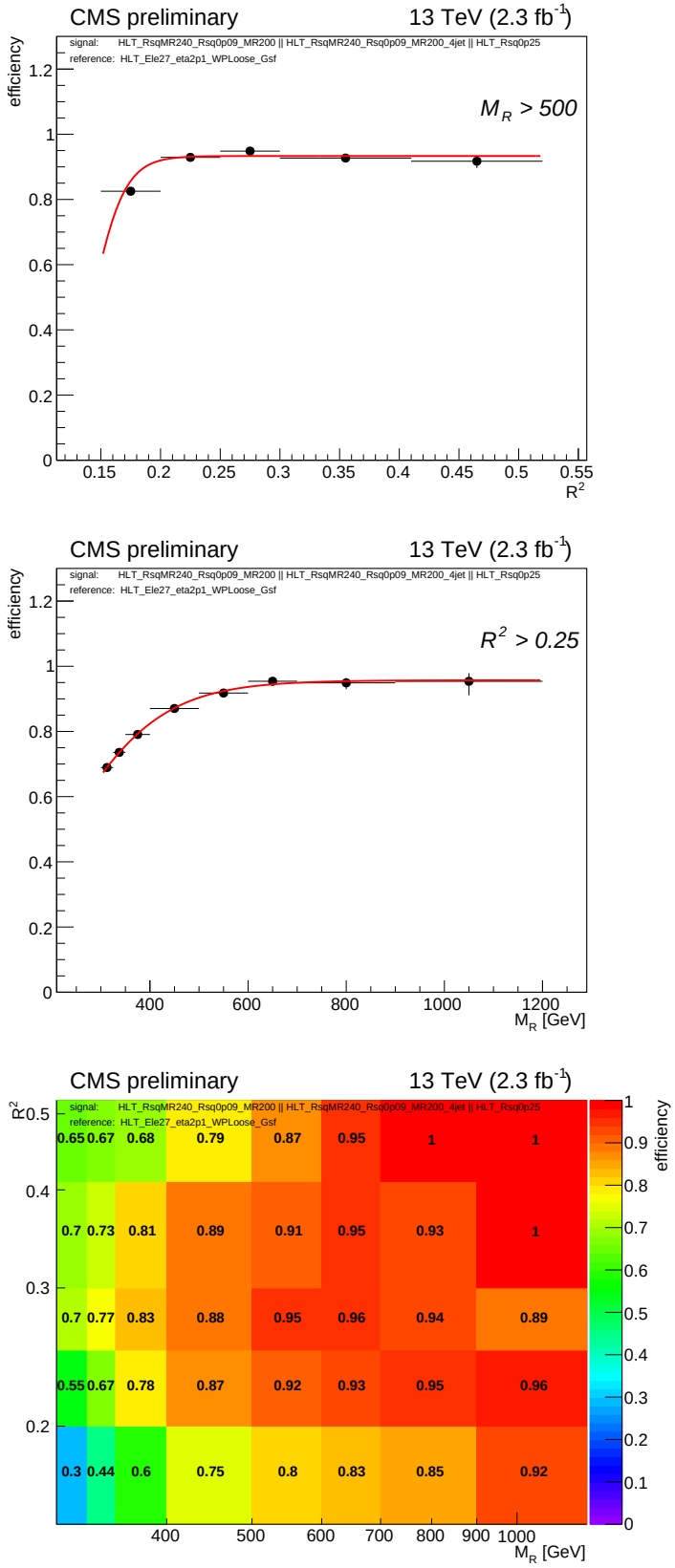

Figure 6.2: Trigger efficiency of the boolean "or" of the dijet, quadjet and high-R^2 triggers as used in the search of Ch. 8, measured in a data sample of single-electron events as a function of R^2 (top), M_R (middle), and as a function of (M_R, R^2) (bottom) [44].

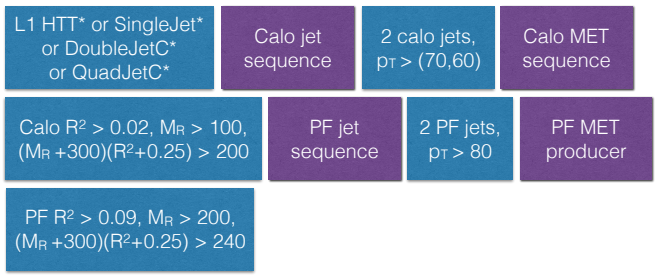

(a) HLT_RsqMR240_Rsq0p09_MR200

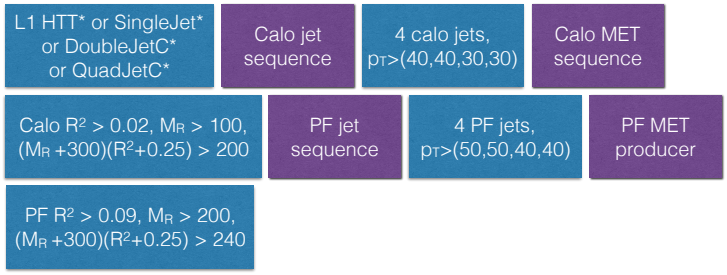

(b) HLT_RsqMR240_Rsq0p09_MR200_4jet

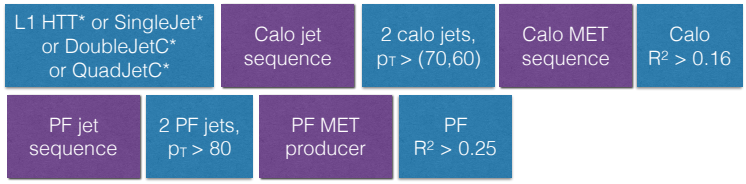

(c) HLT_Rsq0p25

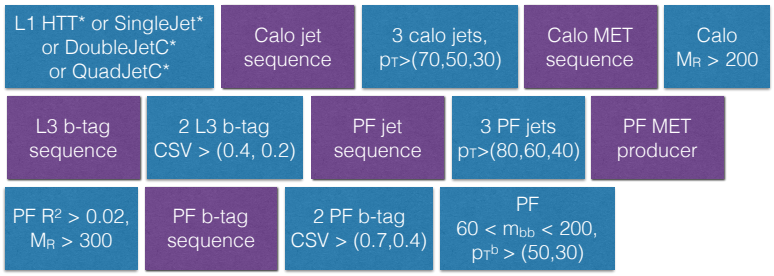

(d) HLT_Rsq0p02_MR300_TriPFJet80_60_40_ DoublePFBTagCSV0p7_0p4_Mbb60_200

Figure 6.3: Flow of the producer steps (in purple) and filter steps (in blue) in the razor triggers [44].

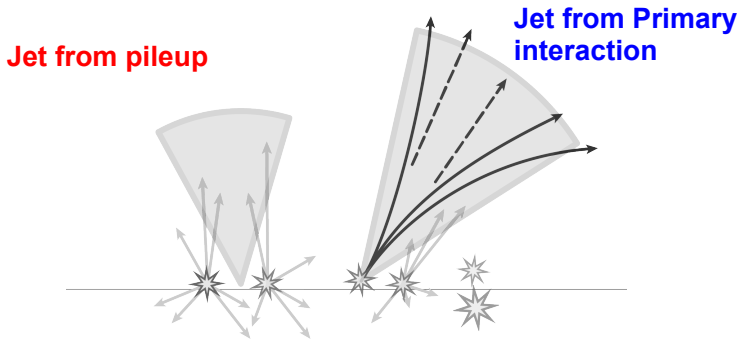

Figure 6.4: Pileup jet misinterpreted as part of the main interaction event [44].

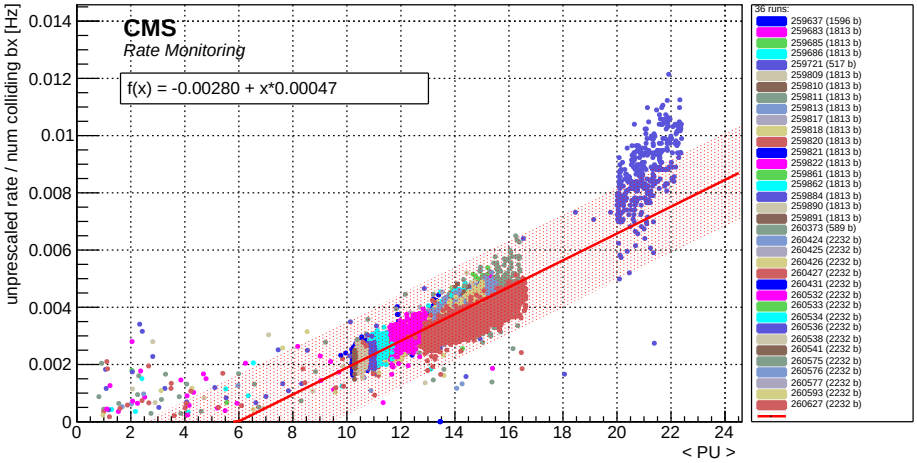

(a) HLT_RsqMR240_Rsq0p09_MR200

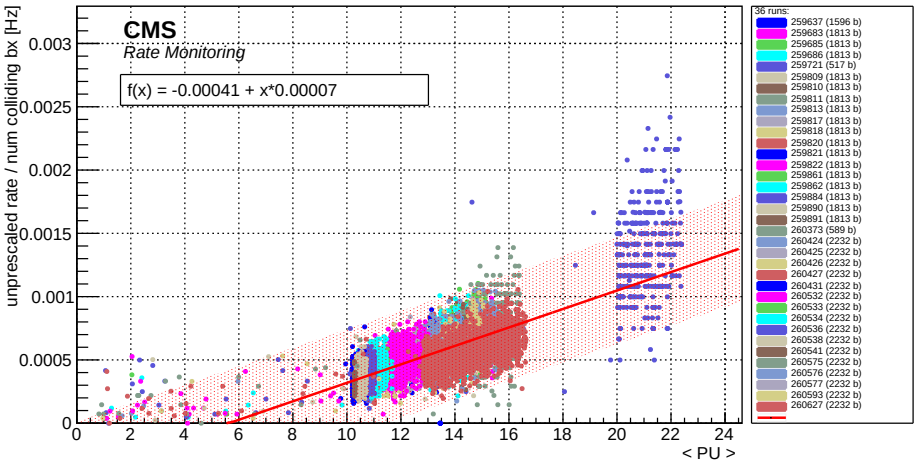

(b) HLT_RsqMR240_Rsq0p09_MR200_4jet

Figure 6.5: Pileup dependence of the dijet (a) and quadjet (b) razor triggers throughout 2015 [44]. Each data point corresponds to a different luminosity section (23.3 seconds of data-taking). The legend denotes the run number and number of colliding bunches in each run.

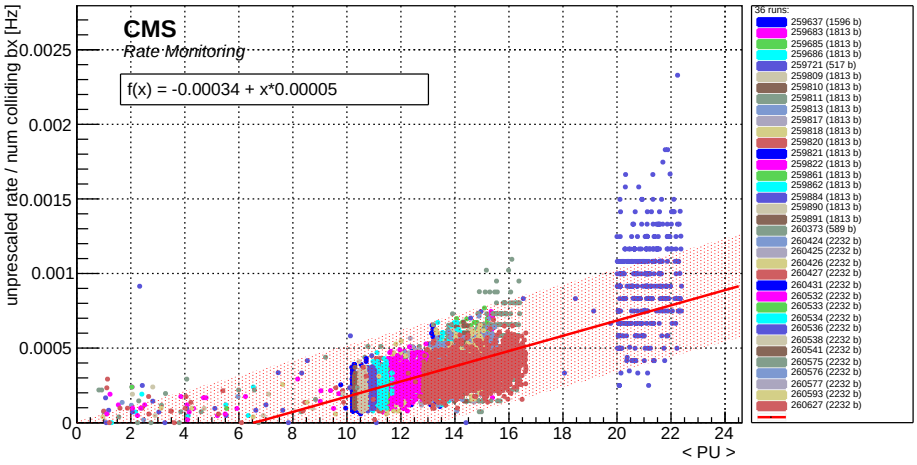

(c) HLT_Rsq0p25

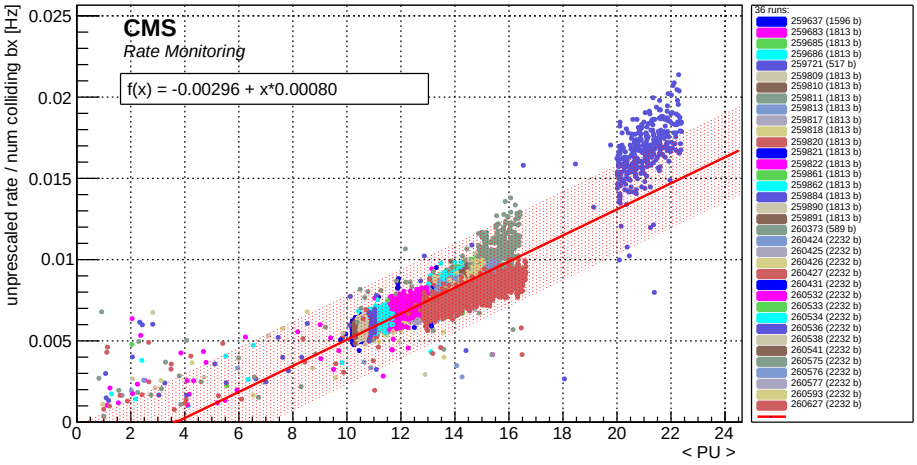

(d) HLT_Rsq0p02_MR300_TriPFJet80_60_40_
DoublePFBTagCSV0p7_0p4_Mbb60_200

Figure 6.6: Pileup dependence of the high-R^2 (c) and $H(b\bar{b})$ (d) razor triggers [44]. A detailed description of the graphs is given in Fig. 6.5

Part III

Searches for new physics at the LHC

Chapter 7

SEARCHES FOR SUPERSYMMETRY AT $\sqrt{S} = 8$ TEV

As discussed in Sec. 3.8, models of SUSY predict additional, undiscovered fundamental particles which correspond to the heavy superpartners of SM particles. Of particular interest is the production of top squarks, bottom squarks, and gluinos due to their role in taming the quadric divergence of the Higgs mass in the SM (see Sec. 3.5). The residual fine-tuning inherent in these models is dependent on the masses of these superpartners, with a preference for smaller masses to avoid large fine-tuning. These considerations have motivated searches for the lightest allowed top and bottom squarks, as well as gluinos that may couple to top/bottom squarks, whose decays would produce final states enriched in b-jets. Moreover, due to the possible presence of top quarks that produce leptons $\sim 30\%$ of the time in the decay chain, the presence of electrons or muons may be used as part of the event selection to enhance the signal-to-background ratio. We exploit both of these features (b-jets and leptons) in the event classification.

We classify events into different "boxes," or data categories, based on the jet multiplicity, b-jet multiplicity, and lepton (e or μ) multiplicity (see Fig. 7.1). The advantages of this classification are (i) by isolating different SM background processes, like $t\bar{t}$, we can better model them individually, and (ii) in the event of a discovery, we may be able to infer the values of certain SUSY branching fractions based on the boxes where the signal is present. The likelihood functions of the different boxes are statistically combined to exclude or discover particular SUSY models. In the following, this classification and statistical combination is referred to as the razor box approach.

In this chapter, we present an inclusive search for gluinos and top squarks[1] using pp collision data collected by CMS at $\sqrt{s} = 8$ TeV in the context of the minimal natural SUSY spectrum outlined in Sec. 3.8 [94]. Previous searches for natural SUSY by CMS [102, 103, 104, 105, 106] and ATLAS [97, 98, 99, 100, 101] at $\sqrt{s} = 7$ and 8 TeV have probed gluino masses up to 1.3 TeV

[1] Though we don't explicitly interpret our results in the context of bottom squark production, many of the conclusions regarding top squark production carry over.

and top squark masses up to 700 GeV under the assumptions of specific decay modes for the SUSY particles. One important feature that sets this search apart is that the SUSY parameter space of gluino and top squark branching ratios is explored for the first time at the LHC [94]. Notably, the razor box approach ensures good sensitivity to a wide range of branching ratios. In addition, we combine the results from the hadronic razor search with those from a previous search [102] for top-squark production in the single-lepton (eor μ) channel to obtain an improved bound on top-squark pair production.

The remainder of this chapter is organized as follows. The event selection and box definitions are detailed in Sections 7.1 and 7.2, respectively. The modeling of the SM backgrounds through a fit using an empirical function is explained in Sec. 7.3. In particular, the motivation for this empirical function and the properties that make it a suitable description are examined in Sec. 7.3. The results of the fits to data are presented and compared to the corresponding results in a signal injection scenario in Sec. 7.4. Finally, limits are derived in the context of the natural SUSY scenario of Sec. 3.8 and a summary is given in Sections 7.5 and 7.8, respectively.

7.1 Event selection

Events are selected at the L1 trigger level by requiring at least two jets with $|\eta| < 3$. At the HLT level, events are selected using dedicated razor algorithms, consisting of a loose selection on M_R and R^2. Razor-specific triggers, similar to those discussed in Ch. 6, are used in the HLT in order to avoid biases on the shapes of distributions from the SM background that are introduced by requirements on more traditional selection variables such as E_T^{miss}. The razor triggers reject the majority of the SM background, which mostly appears at low R^2 and low M_R, while retaining events in the signal-sensitive regions of the (M_R, R^2) plane. Two types of triggers are used: i) a hadronic razor trigger, which selects events that contain at least two PF jets with transverse momentum $p_T > 64$ GeV by applying threshold requirements on R^2, M_R, and their product; ii) a muon and electron razor trigger, which selects events with at least one isolated electron or muon with $p_T > 12$ GeV in combination with looser requirements on R^2, M_R, and their product. The trigger efficiency, evaluated using a dedicated trigger, is measured to be $(95 \pm 5)\%$ and is independent of R^2 and M_R for the events selected with the

baseline requirements described in Sec. 3.10.

Following the trigger selection, events are required to contain at least one reconstructed interaction vertex. If more than one vertex is found, the one with the highest p_T^2 sum of associated tracks is chosen as the interaction point for event reconstruction. Algorithms are used to remove events with detector- and beam-related noise that can mimic event topologies with high energy and large p_T imbalance [166, 167, 133].

The analysis uses a global event description based on the CMS particle flow (PF) algorithm [168, 169], described in Sec. 5.5.

A "tight" lepton identification is used for muons and electrons, consisting of requirements on isolation and track reconstruction quality. For electrons, the shape and position of the energy deposit in the electromagnetic calorimeter is used to further reduce the contamination from hadrons [170]. For events with one identified tight lepton, additional muons or electrons are identified through a "loose" lepton selection, characterized by a relaxed isolation requirement [171]. Tight leptons are required to have $p_T > 15\,\text{GeV}$ and loose leptons $p_T > 10\,\text{GeV}$.

Jets are reconstructed by clustering the PF candidates with the FastJet [132] implementation of the anti-k_T [131] algorithm with the distance parameter $R = 0.5$. We select events containing at least two jets with $p_T > 80\,\text{GeV}$ and $|\eta| < 2.4$, representing a tighter version of the L1 jet selection criterion. The p_T imbalance in the event, $\vec{p}_T^{\,\text{miss}}$, is the negative of the sum of the $\vec{p}_T$ of the PF candidates in the event. Its magnitude is referred to as E_T^{miss}. For each event, the $\vec{p}_T^{\,\text{miss}}$ and the four-momenta of all the jets with $p_T > 40\,\text{GeV}$ and $|\eta| < 2.4$ are used to compute the razor variables, as described in section 3.10.

The medium working point of the combined secondary vertex algorithm [134, 135], described in Sec. 5.5, is used for b-jet tagging. The b-tagging efficiency and mistag probability are measured from data control samples as a function of the jet p_T and η. For a p_T ¿60 GeV, the b-tag efficiency is approximately 68% and the mistag probability is approximately 1% [134]. Correction factors are derived for Monte Carlo (MC) simulations through comparison of the measured and simulated b-tagging efficiencies and mistag rates found in these control samples [135].

Events with no b-tagged jet are discarded, a criterion motivated by the nat-

ural SUSY signatures described in Sec. 3.8. A tighter requirement ($\geq$2 b-tagged jets) is imposed on events without an identified tight lepton and fewer than four jets. This requirement reduces the expected background from SM production of $Z(\rightarrow \nu\bar{\nu})$+jets events to a negligible level.

7.2 Box definitions

The selected events are categorized into the different, mutually exclusive razor boxes according to their event content as shown in Tab. 7.1. In the table, the boxes are listed according to the filling order, from the first (at the top of the table) to the last (at the bottom). If an event satisfies the requirements of two or more boxes, the event is assigned to the first listed box to ensure the boxes correspond to disjoint samples. A schematic flow chart is shown in Fig. 7.1.

The events in the single-lepton and two-lepton boxes are recorded using the electron and muon razor trigger. The remaining two boxes, generically referred to as "hadronic" boxes, contain events recorded using the hadronic razor trigger.

In the two-lepton boxes, the (M_R, R^2) distribution of events with at least one b-tagged jet is studied. For the other boxes, the data are binned according to the b-tagged jet multiplicity: 1 b-tag, 2 b-tags, and $\geq$3 b-tags.

Table 7.1: Kinematic and multiplicity requirements defining the nine razor boxes. Boxes are listed in order of event filling priority.

Box	Lepton	b-tag	Kinematic	Jet
Two-lepton boxes				
MuEle	$\geq$1 tight electron and $\geq$1 loose muon	$\geq$1 b-tag	($M_R > 300$ GeV and $R^2 > 0.15$) and ($M_R > 350$ GeV or $R^2 > 0.2$)	$\geq$2 jets
MuMu	$\geq$1 tight muon and $\geq$1 loose muon			
EleEle	$\geq$1 tight electron and $\geq$1 loose electron			
Single-lepton boxes				
MuMultiJet	1 tight muon	$\geq$1 b-tag	($M_R > 300$ GeV and $R^2 > 0.15$) and ($M_R > 350$ GeV or $R^2 > 0.2$)	$\geq$4 jets
EleMultiJet	1 tight electron			
MuJet	1 tight muon			2 or 3 jets
EleJet	1 tight electron			
Hadronic boxes				
MultiJet	none	$\geq$1 b-tag	($M_R > 400$ GeV and $R^2 > 0.25$) and ($M_R > 450$ GeV or $R^2 > 0.3$)	$\geq$4 jets
$\geq$2 b-tagged jet	none	$\geq$2 b-tag		2 or 3 jets

A baseline kinematic requirement is applied to define the region in which we search for a signal:

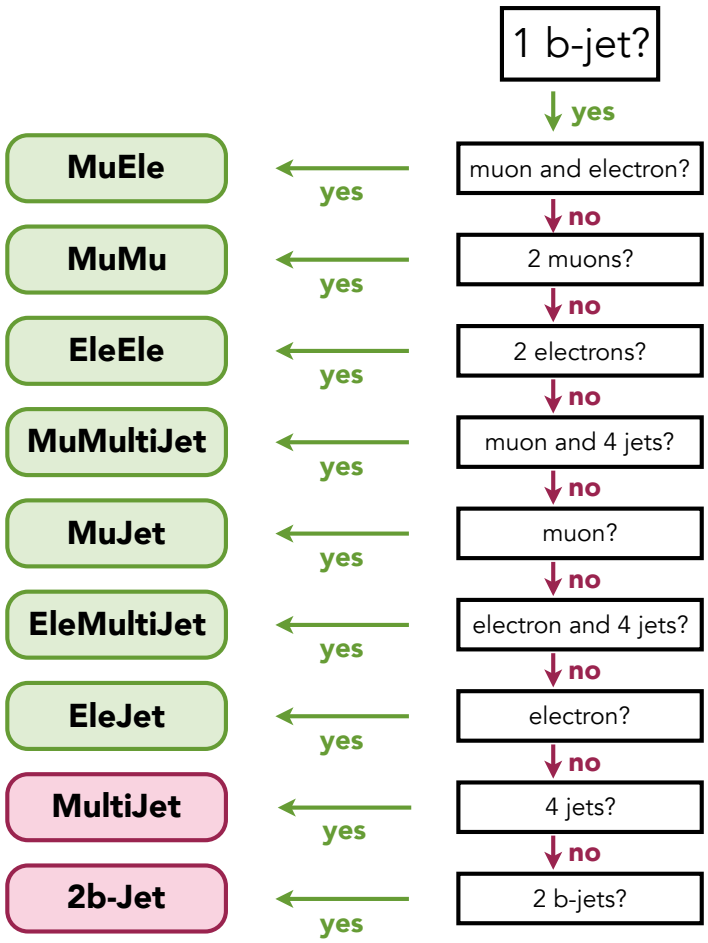

Figure 7.1: Schematic flow chart depicting how a data event is categorized into the different boxes based on its properties.

- $M_R > 400\,\text{GeV}$ and $R^2 > 0.25$ for the hadronic boxes;
- $M_R > 300\,\text{GeV}$ and $R^2 > 0.15$ for the other boxes.

The tighter baseline selection for the hadronic boxes is a consequence of the tighter threshold used for the hadronic razor trigger. The kinematic plane defined by the baseline selection is divided into three regions (see Fig. 7.2):

- Low M_R sideband: $400 < M_R < 550\,\text{GeV}$ and $R^2 > 0.30$ for the hadronic boxes; $300 < M_R < 450\,\text{GeV}$ and $R^2 > 0.20$ for the other boxes.
- Low R^2 sideband: $M_R > 450\,\text{GeV}$ and $0.25 < R^2 < 0.30$ for the hadronic boxes; $M_R > 350\,\text{GeV}$ and $0.15 < R^2 < 0.20$ for the other

boxes.

- Signal-sensitive region: $M_R > 550\,\text{GeV}$ and $R^2 > 0.30$ for the hadronic boxes; $M_R > 450\,\text{GeV}$ and $R^2 > 0.20$ for the other boxes.

The bottom left corner of the razor plane, not included in any of the three regions, is excluded from the analysis. Given this selection, the multijet background from quantum chromodynamics processes is reduced to a negligible level due to the fact that these processes typically peak at $R^2 \approx 0$ and fall exponentially for larger values of R^2 [82, 108].

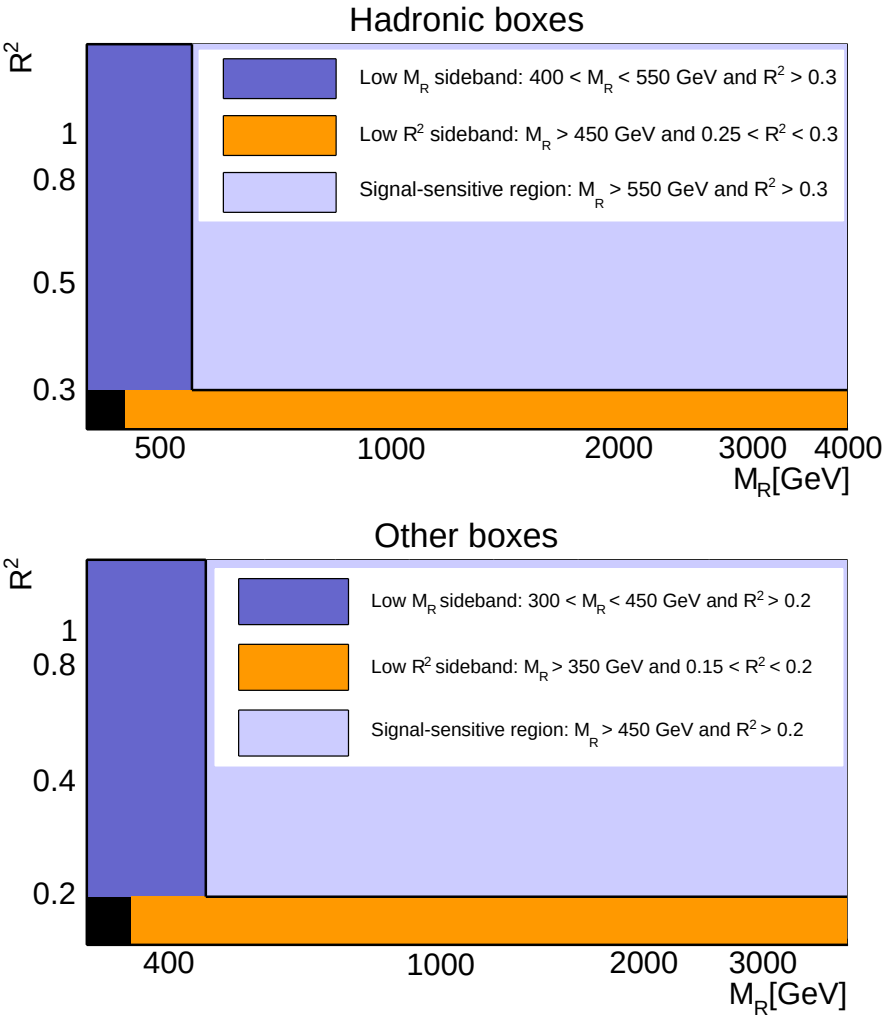

Figure 7.2: Definition of the sideband and the signal-sensitive regions used in the analysis for (top) the hadronic boxes and (bottom) the other boxes [94, 44].

An example of an event in data that passes the selection in the 2b-Jet box is shown in Fig. 7.3. The event has three b-tagged jets, $M_R = 602\,\text{GeV}$, and $R^2 = 0.55$.

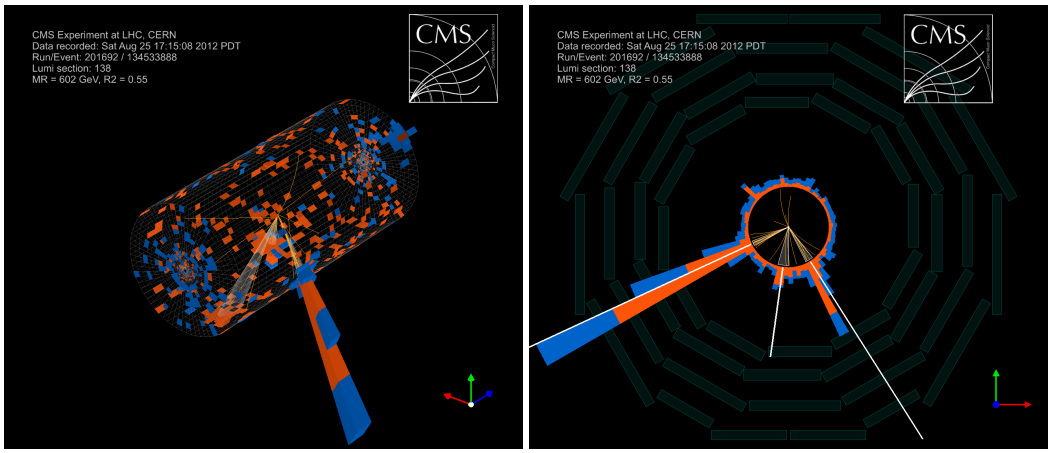

Figure 7.3: An event in the 2b-Jet box: three-dimensional view (left), 2D view in the (ρ,ϕ) plane (right) [44]. The event has three b-tagged jets, $M_R = 602\,\text{GeV}$, and $R^2 = 0.55$.

7.3 Background modeling

Under the hypothesis of no contribution from new-physics processes, the event distribution in the considered portion of the (M_R, R^2) plane can be described by the sum of the contributions from SM V+jets events (where V indicates a W or Z boson) and SM top quark-antiquark and single-top events, where the events with a top quark are generically referred to as the $t\bar{t}$ contribution. Based on MC studies, the contributions from other processes, such as the production of two or three electroweak bosons (diboson or triboson) and the production of $t\bar{t}$ in association with a W or Z boson ($t\bar{t}V$), are determined to be negligible.

We study each of these processes using MC samples, generated with the MADGRAPH v5 event generator [172, 173]. Parton shower and hadronization effects are included by matching events to the PYTHIA v6.4.26 simulation [174] using the MLM algorithm [175]. The events are processed by a GEANT-based [176] description of the CMS apparatus in order to account for the response of the detector.

Once normalized to the NLO inclusive cross section and the integrated luminosity, the absolute yield of the V+jets events contribution satisfying the

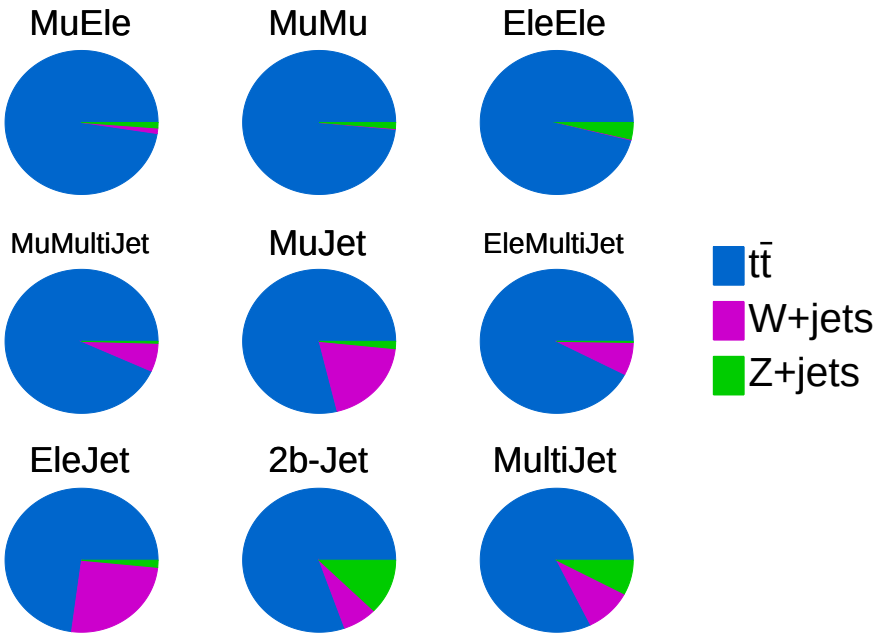

Figure 7.4: Graphical display of the breakdown of the different SM background contributions, estimated from MC simulated samples, in each box for the baseline event selection listed in Tab. 7.1 [44]. For these graphs, the V+jets background is broken down into the separate W+jets and Z+jets contributions.

event selection is found to be negligible in all of the two-lepton boxes. In the remaining boxes, its contribution to the total SM background is found to be approximately 25%. The contribution of V+jets events in the $\geq$2 b-tag and the $\geq$4 jet sample is found to be negligible. The remainder of the background in each box originates from $t\bar{t}$ events. Fig. 7.4 illustrates the breakdown of the different SM background contributions in each box for the baseline event selection listed in Tab. 7.1.

Empirical razor function

Based on the study of the data collected at $\sqrt{s} = 7\,\text{TeV}$ and the corresponding MC samples [82, 108], the two-dimensional probability density function $P_{\text{SM}}(M_{\text{R}}, \text{R}^2)$ for each SM process is found to be well described by the empirical function

$$f(M_{\text{R}}, \text{R}^2) = \left[b(M_{\text{R}} - M_{\text{R}}^0)^{1/n}(\text{R}^2 - \text{R}_0^2)^{1/n} - 1\right] \text{e}^{-bn(M_{\text{R}} - M_{\text{R}}^0)^{1/n}(\text{R}^2 - \text{R}_0^2)^{1/n}}, \tag{7.1}$$

where b, n, M_{R}^0, and R_0^2 are free parameters of the background model.

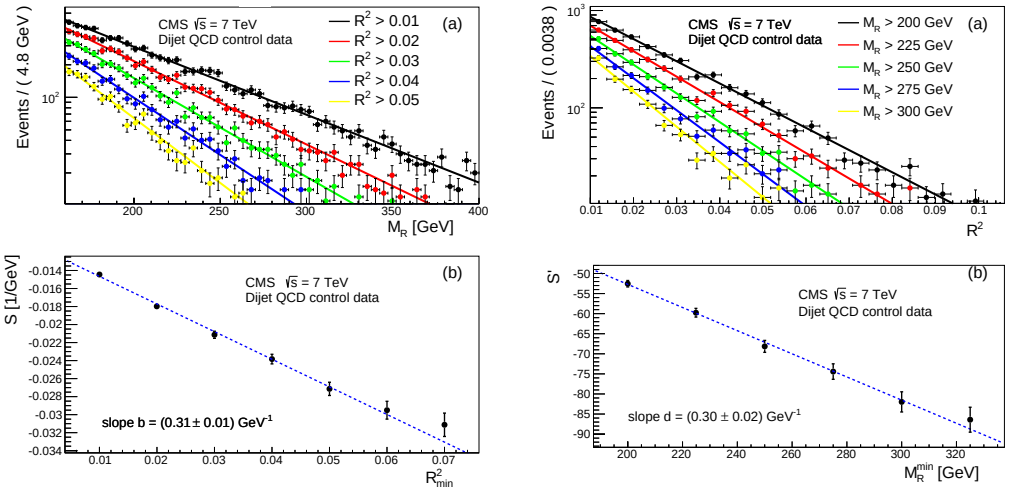

Figure 7.5: QCD multijet events collected by CMS at $\sqrt{s} = 7\,\text{TeV}$ demonstrate the two-dimensional correlation between M_R and R^2 that motivates the original functional form [108].

For $n = 1$, this function recovers the two-dimensional exponential function used for razor searches at $\sqrt{s} = 7\,\text{TeV}$ [82, 108]. The original motivation is detailed in the cited papers. A quick summary follows. There is an observed correlation between the two razor variables such that after a baseline selection $M_\text{R} > M_\text{R}^\text{min}$ and $\text{R}^2 > \text{R}^2_\text{min}$, the distributions of the SM backgrounds exhibit an exponential behavior in R^2 (M_R) when integrated over (M_R), (R^2):

$$\int_{\text{R}^2_\text{min}}^{\infty} P_\text{SM}(M_\text{R}, \text{R}^2)\text{d}\text{R}^2 \propto e^{-(r_0 + r_1 \text{R}^2_\text{min})M_R}\,, \tag{7.2}$$

$$\int_{M_\text{R}^\text{min}}^{\infty} P_\text{SM}(M_\text{R}, \text{R}^2)\text{d}M_\text{R} \propto e^{-(m_0 + m_1 M_\text{R}^\text{min})\text{R}^2}\,, \tag{7.3}$$

where r_0, r_1, m_0, and m_1 are interrelated exponential parameters. This behavior for QCD multijets background is illustrated in Fig. 7.5. The empirical function in Eqn. 7.1 with $n = 1$ perfectly replicates this behavior and the exponential parameters can be identified with the empirical function's parameters, namely $r_0 = -b\text{R}_0^2$, $m_0 = -bM_\text{R}^0$, and $r_1 = m_1 = b$.

To account for the possibility of non-exponential tails of the SM backgrounds, the $\sqrt{s} = 7\,\text{TeV}$ search invoked two copies of the empirical function with $n = 1$ to model each SM background. For the $\sqrt{s} = 8\,\text{TeV}$ search, we take a different approach by using only one instance of the function, but allowing the n parameter to deviate from 1. Fig. 7.6 illustrates the similarity between

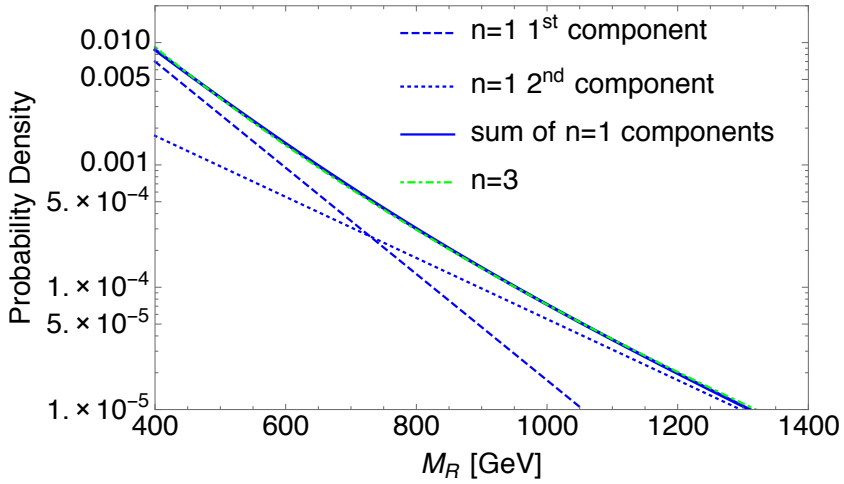

Figure 7.6: Two exponential components with $n = 1$ and their sum are shown in blue compared with a single modified exponential with $n = 3$ in green [44].

using two exponential components and using one instance of the generalized function.

One of the benefits of this functional form is that it is analytically integrable. By providing the analytical integral to RooFit, we avoid using RooFit's multi-dimensional numerical integration, which is costly in terms of function evaluations and may be inaccurate [177] [178]. In particular, the one-dimensional and two-dimensional integrals of the function are

$$\begin{aligned}\int_{\mathrm{R}^2_{\mathrm{min}}}^{\mathrm{R}^2_{\mathrm{max}}} f(M_{\mathrm{R}}, \mathrm{R}^2)\mathrm{d}\mathrm{R}^2 = &\exp\left(-bn(M_{\mathrm{R}} - M^0_{\mathrm{R}})^{1/n}(\mathrm{R}^2_{\mathrm{max}} - \mathrm{R}^2_0)^{1/n}\right) \\ &\times \exp\left(-bn(M_{\mathrm{R}} - M^0_{\mathrm{R}})^{1/n}(\mathrm{R}^2_{\mathrm{min}} - \mathrm{R}^2_0)^{1/n}\right) \\ &\times \left(\exp\left(-bn(M_{\mathrm{R}} - M^0_{\mathrm{R}})^{1/n}(\mathrm{R}^2_{\mathrm{max}} - \mathrm{R}^2_0)^{1/n}\right)(\mathrm{R}^2_{\mathrm{min}} - \mathrm{R}^2_0)\right. \\ &\left. - \exp\left(-bn(M_{\mathrm{R}} - M^0_{\mathrm{R}})^{1/n}(\mathrm{R}^2_{\mathrm{min}} - \mathrm{R}^2_0)^{1/n}\right)(\mathrm{R}^2_{\mathrm{max}} - \mathrm{R}^2_0)\right),\end{aligned} \tag{7.4}$$

and

$$\int_{M_{\mathrm{R}}^{\mathrm{min}}}^{M_{\mathrm{R}}^{\mathrm{max}}} \int_{\mathrm{R}^2_{\mathrm{min}}}^{\mathrm{R}^2_{\mathrm{max}}} f(M_{\mathrm{R}}, \mathrm{R}^2) \mathrm{d}\mathrm{R}^2 \mathrm{d}M_{\mathrm{R}} = n(bn)^{-n} \times \Big(\Gamma\left(n, bn(M_{\mathrm{R}}^0 - M_{\mathrm{R}}^{\mathrm{max}})^{1/n}(\mathrm{R}_0^2 - \mathrm{R}^2_{\mathrm{max}})^{1/n}\right) - \Gamma\left(n, bn(M_{\mathrm{R}}^{\mathrm{min}} - M_{\mathrm{R}}^0)^{1/n}(\mathrm{R}^2_{\mathrm{max}} - \mathrm{R}_0^2)^{1/n}\right) - \Gamma\left(n, bn(M_{\mathrm{R}}^{\mathrm{max}} - M_{\mathrm{R}}^0)^{1/n}(\mathrm{R}^2_{\mathrm{min}} - \mathrm{R}_0^2)^{1/n}\right) + \Gamma\left(n, bn(M_{\mathrm{R}}^{\mathrm{min}} - M_{\mathrm{R}}^0)^{1/n}(\mathrm{R}^2_{\mathrm{min}} - \mathrm{R}_0^2)^{1/n}\right) \Big) , \tag{7.5}$$

respectively, where $\Gamma(a, x)$ is the incomplete gamma function:

$$\Gamma(a, x) = \int_x^\infty t^{a-1} e^{-t} \mathrm{d}t \, . \tag{7.6}$$

7.4 Background fit results and signal injection

The shape of the empirical function in M_{R} and R^2 is determined through a ROOFIT-based [179], extended, maximum likelihood [180] fit to the data performed in one of two ways:

- A fit to the data in the sideband regions in M_{R} and R^2 as a model-independent way to look for excesses or discrepancies. The fit is performed using only the data in the sideband, and the functional form is extrapolated to the full M_{R} and R^2 plane.
- A fit to the data in the full search region in M_{R} and R^2 under background-only and signal-plus-background hypotheses, following a modified frequentist approach (LHC $\mathrm{CL_s}$) [181, 182, 183, 184] to interpret the data in the context of particular SUSY simplified models (Sec. 7.5).

fIn both cases, the empirical function is found to adequately describe the SM background in each of the boxes, for each b-tagged jet multiplicity value.

The SM background-only likelihood function for the two-lepton boxes is written as:

$$\mathcal{L}(\mathrm{data}|\boldsymbol{\theta}) = \frac{\mathrm{e}^{-N_{\mathrm{SM}}}}{N!} \prod_{i=1}^{N} N_{\mathrm{SM}} P_{\mathrm{SM}}(M_{\mathrm{R}(i)}, \mathrm{R}^2{}_{(i)}), \tag{7.7}$$

where $P_{\mathrm{SM}}(M_{\mathrm{R}}, \mathrm{R}^2)$ is the empirical function in Eqn. (7.1) normalized to unity, N_{SM} is the corresponding normalization factor, and $\boldsymbol{\theta}$ is the set of background shape and normalization parameters, and the product runs over the N events in the data set. This form of the likelihood is for one background process. The same form of the likelihood is used for the other boxes, for each b-tagged jet multiplicity. The total likelihood in these boxes is computed as the product of the likelihood functions for each b-tagged jet multiplicity.

The fits are performed independently for each box and simultaneously across the b-tagged jet multiplicity bins. Common background shape parameters (b, ${M_{\mathrm{R}}}^0$, R_0^2, and n) are used for the 2 b-tag and $\geq$3 b-tag bins, since no substantial difference between the two distributions is observed on large samples of $\mathrm{t\bar{t}}$ and V+jets MC events. A difference is observed between 1 b-tag and $\geq$2 b-tag samples, due to the observed dependence of the b-tagging efficiency on the jet p_{T}. Consequently, the shape parameters for the 1 b-tag bins are allowed to differ from the corresponding parameters for the $\geq$2 b-tag bins. The background normalization parameters for each b-tagged jet multiplicity bin are also treated as independent parameters.

The background shape parameters are estimated from the events in the two sidebands (Section 7.2). This shape is then used to derive a background prediction in the signal-sensitive region: 30 000 alternative sets of background shape parameters are generated from the covariance matrix returned by the fit. An ensemble of pseudo-experiment data sets is created, generating random (M_{R}, R^2) pairs distributed according to each of these alternative shapes. For each bin of the signal-sensitive region, the distribution of the predicted yields in each pseudo-experiment is compared to the observed yield in data in order to quantify the agreement between the background model and the observation. The agreement, described as a two-sided p-value, is then translated into the corresponding number of standard deviations for a normal distribution. The p-value is computed using the probability density as the ordering principle. The observed numbers of standard deviations in the two-lepton boxes are shown in Fig. 7.7, as a function of M_{R} and R^2. Positive and negative significance correspond to regions where the observed yield is respectively larger and smaller than the predicted one. Light gray areas correspond to empty bins with less than one event expected

on average. Similar results for the one-lepton and hadronic boxes are shown in Figs. 7.8–7.10. Figures 7.11–7.14 illustrate the extrapolation of the fit results to the full (M_{R}, R^2) plane, projected onto R^2 and M_{R} and summed over the b-tagged jet multiplicity bins. No significant deviation of the data from the SM background predictions is observed.

A goodness-of-fit (GOF) p-value may be computed for each fit using a mixed-sample method [185, 186]. In this method, a pseudo-experiment data set is generated with a factor of 10 more events than in data, $n_{\mathrm{MC}} = 10 n_{\mathrm{data}}$. The two data sets are mixed and for the mixed data set, a test statistic T, is calculated by finding the 10 nearest neighbors to each point in the mixed set and then counting how many of these neighbors are from the same sample:

$$T = \frac{1}{n_k(n_{\mathrm{data}} + n_{\mathrm{MC}})} \sum_{i=1}^{n_{\mathrm{data}}+n_{\mathrm{MC}}} \sum_{k=1}^{n_k} I(i,k) \,, \tag{7.8}$$

where $I(i,k) = 1$ if the i^{th} event and its k^{th} nearest neighbor belong to the same sample and $I(i,k) = 0$ otherwise, and $n_k = 10$ is the number of nearest-neighbor events being considered. A normalized Euclidean metric is used to quantify distances,

$$|\vec{x}_i - \vec{x}_j|^2 = \sum_{\nu}^{D} \left(\frac{x_i^\nu - x_j^\nu}{\sigma_\nu} \right) \,, \tag{7.9}$$

where D is the dimensionality of the dataset, $\vec{x}_i = (x_i^1, \ldots, x_i^D)$ is a random point, and σ_ν is the root mean square of the ν^{th} variate in the dataset. If the two samples, the pseudo-experiment data set and the real data set, have the same parent distribution, then there is a quantity $(T - \mu_T)/\sigma_T$ that has a limiting standard normal distribution. The quantities μ_T and σ_T are given by

$$\mu_T = \frac{n_{\mathrm{data}}(n_{\mathrm{data}} - 1) + n_{\mathrm{MC}}(n_{\mathrm{MC}} - 1)}{n(n-1)} \,, \tag{7.10}$$

$$\lim_{n, n_k, D \to \infty} \sigma_T^2 = \frac{1}{n n_k} \left(\frac{n_{\mathrm{data}} n_{\mathrm{MC}}}{n^2} + 4 \frac{n_{\mathrm{data}}^2 n_{\mathrm{MC}}^2}{n^4} \right) \,, \tag{7.11}$$

where $n = n_{\mathrm{data}} + n_{\mathrm{MC}}$. The convergence to this limit for σ_T is fast enough that it is acceptable to use even for $D = 2$, $n_k = 10$, and $n_{\mathrm{MC}} = 10 n_{\mathrm{data}}$.

The values of the modified test statistic $(T - \mu_T)/\sigma_T$ and the corresponding one-sided p-value for each of the sideband fits are tabulated in Tab. 7.2.

Table 7.2: Goodness-of-fit test statistic and one-sided p-values for each of sideband fits. The mixed-sample method [185, 186] used to derive these measures is described in text. To evalute the test statistic, all of the data in the sidebands and the signal-sensitive region is used. Therefore, these measures quantify both the agreement between the sideband data and the fit and the agreement between the signal-sensitive-region data and the extrapolation.

Box	b-tags	$(T-\mu_T)/\sigma_T$	p-value
Two-lepton boxes			
MuEle	≥ 1	0.74	23%
MuMu	≥ 1	-0.34	63%
EleEle	≥ 1	-0.73	77%
Single-lepton boxes			
MuMultiJet	1	0.43	33%
	2	1.61	5%
	≥ 3	-0.62	73%
MuJet	1	0.82	21%
	2	-0.26	60%
	≥ 3	1.04	15%
EleMultiJet	1	-1.39	92%
	2	0.46	32%
	≥ 3	0.49	31%
EleJet	1	0.25	40%
	2	0.55	29%
	≥ 3	1.05	15%
Hadronic boxes			
2b-Jet	2	1.96	2%
	≥ 3	-0.60	73%
MultiJet	1	0.68	25%
	2	-0.77	78%
	≥ 3	-0.47	68%

To evalute the test statistic, all of the data in the sidebands and the signal-sensitive region is used. Therefore, these measures quantify both the agreement between the sideband data and the fit and the agreement between the signal-sensitive-region data and the extrapolation. We find GOF p-values that are consistent with a uniform distribution and suggest a high-level of agreement between the data and the fit plus the extrapolation.

To demonstrate the discovery potential of this analysis, we apply the background-prediction procedure to a simulated signal-plus-background MC sample. Fig. 7.15 shows the M_{R} and R^2 distributions of SM background events and

T1bbbb events (Section 3.8). The gluino and LSP masses are set respectively to 1.3 TeV and 50 GeV, representing a new-physics scenario near the expected sensitivity of the analysis. A signal-plus-background sample is obtained by adding the two distributions of Fig. 7.15, assuming an integrated luminosity of 19.3 fb^{-1} and a gluino-gluino production cross section of 0.02 pb, corresponding to 78 expected signal events in the signal-sensitive region. The agreement between the background prediction from the sideband fit and the yield of the signal-plus-background pseudo-experiments is displayed in Fig. 7.16-7.18 for different values of the gluino-gluino production cross section, including 0.003, 0.01, and 0.02 pb. The contribution of signal events to the sideband region has a negligible impact on the determination of the background shape, while a disagreement is observed in the signal-sensitive region, characterized as an excess of events clustered around $M_{\text{R}} \approx 1.3$ TeV. The excess indicates the presence of a signal in this simulated MC sample, and the position of the excess in the M_{R} variable provides information about the underlying SUSY mass spectrum.

7.5 Modified frequentist statistical procedure

We interpret the results of the searches by determining the 95% confidence level (CL) upper limits on the production cross sections of the SUSY models presented in Section 3.8, using the LHC CL_{s} procedure [184] and a global likelihood determined by combining the likelihoods of the different search boxes and sidebands. To reduce computational requirements, a binned likelihood is used,

$$\mathcal{L}(\text{data}|\mu,\boldsymbol{\theta}) = \prod_{i=1}^{n_b} \text{Poisson}(x_i|s_i(\mu,\boldsymbol{\theta}) + b_i(\boldsymbol{\theta})) \cdot \text{Constraint}(\boldsymbol{\theta}|\bar{\boldsymbol{\theta}},\boldsymbol{\delta\theta}) \ , \quad (7.12)$$

where μ is the signal strength (parameter of interest), $\boldsymbol{\theta}$ is the vector of nuisance parameters, x_i is the data yield in the ith bin, $s_i(\mu,\boldsymbol{\theta})$ the corresponding signal yield, and $b_i(\boldsymbol{\theta})$ the corresponding background yield, computed as

$$b_i(\boldsymbol{\theta}) = N_{\text{SM}} \int_{M_{\text{R}}^{\text{min},i}}^{M_{\text{R}}^{\text{max},i}} \int_{\text{R}^2_{\text{min},i}}^{\text{R}^2_{\text{max},i}} P_{\text{SM}}(M_{\text{R}},\text{R}^2)\text{d}\text{R}^2\text{d}M_{\text{R}} \ , \quad (7.13)$$

and the product runs over the number of bins n_b. Finally, this is used to define the test statistic following the LHC CL_{s} procedure [184],

$$\tilde{q}_\mu = -2\log\frac{\mathcal{L}(\text{data}|\mu,\hat{\boldsymbol{\theta}}_\mu)}{\mathcal{L}(\text{data}|\hat{\mu},\hat{\boldsymbol{\theta}})} \ , \ \ 0 \leq \hat{\mu} \leq \mu \ , \quad (7.14)$$

where $\hat{\boldsymbol{\theta}}_\mu$ refers to the conditional maximum likelihood estimators of $\boldsymbol{\theta}$ assuming a given value μ, and $\hat{\mu}$ and $\hat{\boldsymbol{\mu}}$ correspond to the global maximum of the likelihood.

Systematic uncertainties are related to nuisance parameters $\boldsymbol{\theta}$ that are incorporated into the model. Then the dependence of the test statistic on these nuisance parameters is removed through "profiling" (maximizing the likelihood by varying the nuisance parameters). That is the uncertainty is propagated by allowing the nuisance parameters to vary in determining the profile likelihood test statistic. This profiling broadens the test statistic distribution thus increasing the uncertainty on the parameter-of-interest μ.

Typically, the distribution of the test statistic is built by performing many MC pseudoexperiments, and then this distribution is used to evaluate the upper limits on μ. This procedure may become very computationally intensive especially if there are many nuisance parameters that must be fit in each pseudoexperiment. Based on the theorems of Wald [187] and Wilks [188], there is an approximate method to compute upper limits based on the asymptotic behavior at large N (where N is the size of the data sample) of the test statistic [183]. In this asymptotic regime, the distribution of $\tilde{q}_\mu$ approaches a chi-square distribution for one degree of freedom [188]. Based on this asymptotic approximation, we may derive the observed 95% CL upper limit on the signal strength without any MC pseudoexperiments by computing the value of μ that satisfies,

$$\mathrm{CL_s} \equiv \frac{\mathrm{CL_{s+b}}}{\mathrm{CL_b}} = \frac{1-\Phi(\sqrt{\tilde{q}_\mu})}{\Phi(\sqrt{\tilde{q}_{\mu,\mathrm{A}}}-\sqrt{\tilde{q}_\mu})} = \alpha\,, \tag{7.15}$$

where $\alpha = 0.05$, $\tilde{q}_{\mu,\mathrm{A}}$[2] is the test statistic evaluated on the Asimov dataset [189] corresponding exactly to the expected background and the nominal nuisance parameters (setting all statistical fluctuations to zero) [183, 184], and $\Phi(x)$ is the cumulative distribution function of the standard normal distribution,

$$\Phi(x) = \frac{1}{\sqrt{2\pi}}\int_{-\infty}^{x} e^{-t^2/2}\mathrm{d}t\,. \tag{7.16}$$

Similar expressions may be used to derive the median expected 95% CL upper limit,

$$\frac{1-\Phi(\sqrt{\tilde{q}_{\mu,\mathrm{A}}})}{0.5} = \alpha\,, \tag{7.17}$$

[2]Note $\tilde{q}_{\mu,\mathrm{A}} = \frac{\mu^2}{\sigma_\mathrm{A}^2}$ where σ_A is an estimator for the variance of μ.

and to find the $\pm N\sigma$ uncertainty band about the expected limit,

$$\frac{1-\Phi(\sqrt{\tilde{q}_{\mu,\mathrm{A}}}\mp N)}{\Phi(\pm N)}=\alpha\,, \tag{7.18}$$

Importantly, for situations with small numbers of events, the asymptotic result is known to give biased (over-optimistic) results [184].

Conversely, in the case of a discovery, one tests $\mu = 0$ and measures the "local significance" using a modified test statistic,

$$q_0=-2\log\frac{\mathcal{L}(\text{data}|0,\hat{\hat{\boldsymbol{\theta}}}_0)}{\mathcal{L}(\text{data}|\hat{\mu},\hat{\boldsymbol{\theta}})}\,,\quad \hat{\mu}\geq 0\,. \tag{7.19}$$

The observed local significance is then simply,

$$Z=\sqrt{q_0}\,. \tag{7.20}$$

To claim a discovery, the modern (sociological) standard in experimental high energy physics is a global p-value of 2.9×10^{-7} corresponding to global significance of 5σ, after taking into account the look-elsewhere effect [190, 191, 192].

These asymptotic formulae are used in the searches conducted at $\sqrt{s} = 13\,\text{TeV}$ described in Chapter 8 and Appendix B of this thesis. However, for the search described in this chapter, the final limits are based on MC pseudoexperiments.

7.6 Systematic uncertainties

For the razor search boxes, the signal contribution is modeled by a template function, for a given signal hypothesis in a specific box and a given b-tagged jet multiplicity. The template function, normalized to unit probability, is multiplied by the expected signal yield and the signal strength parameter in each bin ($\mu\sigma_{\mathrm{NLO+NLL}}L\epsilon^{\mathrm{box}}_{\text{b-tag}}$). Here $\sigma_{\mathrm{NLO+NLL}}$ is the SUSY signal cross section calculated to next-to-leading order (NLO) plus next-to-leading-logarithm (NLL) accuracy [63, 64, 65, 66, 67, 68], L is the integrated luminosity corresponding to the size of the data set, and $\epsilon^{\mathrm{box}}_{\text{b-tag}}$ is the signal selection efficiency for a given box and, in case of the single-lepton and hadronic boxes, for a given b-tagged jet multiplicity.

Each systematic uncertainty is incorporated in the likelihood with a dedicated nuisance parameter, whose value is not known a priori but rather

must be estimated from the data. The set of nuisance parameters may be divided into three distinct classes (though their statistical treatment is the same): those related to the signal normalization, those related to the signal shape, and those related to the background normalization and shape.

We consider the following systematic uncertainties associated with the signal normalization, with the size of the uncertainty indicated in parentheses:

- integrated luminosity (2.6%) [193];
- trigger efficiency (5%);
- lepton reconstruction and identification efficiencies (3% per lepton), measured from an inclusive $Z \to \ell^+\ell^-$ event sample ($\ell = e, \mu$) as a function of the lepton p_T and η values [170, 171].

In addition, four signal-shape systematic uncertainties are considered, whose sizes vary with R^2, M_R, and the b-tagged jet multiplicity:

- The uncertainty in the jet b-tagging and mistagging efficiencies (up to 20% depending on the signal model), evaluated for each (M_R, R^2) and b-tagged jet multiplicity bin. The uncertainty is evaluated by propagating the uncertainty in data-to-simulation scale factors [135].
- the uncertainty in the modeling of the parton distribution functions (PDFs) (up to 10% depending on the signal model), evaluated for each bin in the (M_R, R^2) plane and for each box and b-tag multiplicity following the PDF4LHC [194, 195, 196] prescription, using the CTEQ-6.6 [197] and MRST-2006-NNLO [198] PDF sets.
- The uncertainty in the jet energy scale and resolution (up to 5% depending on the signal model), evaluated from a set of data control samples and MC simulations [126].
- The uncertainty in the modeling of the associated jet production by the MADGRAPH simulation (up to 20% depending on the signal model), studied using Z+jets and $t\bar{t}$ data events and parameterized by an MC-to-data scale factor as a function of the magnitude of the vector sum of the p_T values of the two produced SUSY particles [102].

The impact of each of these uncertainties on the SUSY signal shape is taken into account by varying each effect up or down by one standard deviation.

The uncertainty in the knowledge of the background distributions is taken into account by maximizing the likelihood with respect to the background shape and normalization parameters using the data in the two sidebands and the signal-sensitive region. The background parameterization is able to accommodate several sources of systematic uncertainties defined below:

- dependence of the background shape on the b-tag multiplicity;
- dependence of the background shape on the lepton and jet multiplicities;
- deviation of the two-dimensional shape from an exponentially falling distribution, through the background empirical function parameter n, which modifies the tail in M_{R} and R^2;
- shape bias induced by the dependence of the b-tagging efficiency and mistag rate on the jet p_{T};
- deviation of the b-tagging and mistagging efficiencies from the MC prediction, through independent normalization factors in each b-tagged jet multiplicity bin.

The combination of razor and exclusive single-lepton [102] searches is performed using the same procedure, taking into account the systematic uncertainties associated with the five following effects:

- the PDFs;
- the jet energy scale correction;
- the integrated luminosity;
- the b-jet tagging efficiency;
- the associated jet production.

The uncertainties in the background predictions are taken to be uncorrelated, being derived from independent data control samples with different

techniques. We verified that the correlation model for the systematics has a negligible impact on the combination, since similar results are obtained when neglecting any correlation between the systematic uncertainties of the two searches.

7.7 Interpretation

The results of this search are interpreted in the context of the natural SUSY simplified models presented in Section 3.8.

Limits on gluino pair production

The derived limits on gluino pair production for different gluino branching fraction scenarios (discussed in Sec. 3.8) are presented in Fig. 7.19. A comparison of the simplified natural SUSY gluino-gluino exclusions, obtained for the different decay-mode combinations of third generation quarks, is shown in Fig. 7.20. The limits corresponding to gluino-gluino topologies with mixed branching fractions lie within the band defined by the 100% $\tilde{g} \to b\bar{b}\tilde{\chi}_1^0$ and the 100% $\tilde{g} \to t\bar{t}\tilde{\chi}_1^0$ contours. Gluino masses smaller than 1.2 TeV for 100% $\tilde{g} \to t\bar{t}\tilde{\chi}_1^0$ and 1.3 TeV for 100% $\tilde{g} \to b\bar{b}\tilde{\chi}_1^0$ are excluded, for an LSP mass of 100 GeV. For any LSP mass value, a larger number of top quarks in the decay topology corresponds to a weaker limit, mainly due to a reduced total signal efficiency with respect to the four-bottom-quark final state and a worse M_R and R^2 resolution for events with higher jet multiplicity in the final state. Given this fact and the inclusive nature of the analysis, the 100% $\tilde{g} \to t\bar{t}\tilde{\chi}_1^0$ limit can be considered to represent a conservative estimate of a branching-fraction-independent limit, generically valid for gluino-gluino production within the context of the natural SUSY spectrum shown in Fig. 3.7.

Limits on top-squark pair production

The derived limits on top squark pair production from the razor search in the 100% $\tilde{t} \to b\tilde{\chi}_1^{\pm}$, 50% $\tilde{t} \to b\tilde{\chi}_1^{\pm}$ and 50% $\tilde{t} \to t\tilde{\chi}_1^0$, and 100% $\tilde{t} \to t\tilde{\chi}_1^0$ scenarios are presented in Fig. 7.21 and compared in Fig. 7.22. As in the case of the gluino interpretation, the expected limit from the razor search improves as the number of top quarks in the decay topology decreases. For an LSP mass of 100 GeV, top-squark mass values larger than 400 GeV and smaller than 650 GeV are excluded in all three top-squark branching fraction

scenarios.

Within the considered scenarios, a top-squark decay to a chargino (neutralino) is topologically similar to a bottom-squark decay to a neutralino (chargino). In the limit of degenerate charginos and neutralinos, the decay products of the chargino are generically too soft to be detected and this correspondence is exact. However, for large mass differences between the squarks and the chargino, the chargino decay products may be boosted enough to become observable, breaking the correspondence. For the models with the intermediate decay to charginos, there is a migration of reconstructed events from the low-background 2b-Jet box to the high-background MultiJet box and a consequently weaker limit with respect to the simplified model without decays to charginos.

A stronger limit on top-squark pair production is derived by combining the hadronic boxes of the razor search with the results of the exclusive single-lepton analysis [102]. The exclusive single-lepton search is conservatively assumed to only have sensitivity when both top squarks decay to a top quark and a neutralino. Fig. 7.23 (top) presents the combined result obtained for the scenario where the top squark only decays to a top quark and the lightest neutralino. For an LSP mass of 100 GeV, the combination improves the constraint on the top-squark mass from 660 to 730 GeV. This result provides the most stringent limit on this specific simplified model.

Fig. 7.23 (bottom) presents a more generic limit on the top-squark mass. We consider two decay modes for the top squark, as indicated in Fig. 3.7. We scan the relative branching fractions, assuming that no other decay mode is allowed. The largest excluded cross section (that is, the worst upper limit) is found for each choice of the top-squark and neutralino mass. A branching-fraction-independent limit is derived by comparing the worst-case exclusion to the corresponding top-squark pair production cross section. In this manner, top squarks decaying to the two considered decay modes are excluded at a 95% confidence level for mass values >400 GeV and <645 GeV, assuming a neutralino mass of 100 GeV. Unlike other simplified model interpretations, this interpretation is not based on a specific choice of branching fractions. While a residual model dependence is present because only two decay modes are considered, this result is more general than previous constraints.

7.8 Summary

In this chapter, we presented the search for supersymmetric particles using proton-proton collision data collected by CMS in 2012 at $\sqrt{s} = 8\,\text{TeV}$. The data set size corresponds to an integrated luminosity of $19.3\,\text{fb}^{-1}$. We consider events with at least two jets, at least one of which is identified as a b-tagged jet, and study the event distribution in the razor variables (M_R, R^2). The data are classified according to the muon, electron, jet, and b-tagged jet multiplicities. No significant excess is observed with respect to the standard model background expectations, derived from a fit to the data distribution in low-M_R and low-R^2 sidebands.

The inclusive razor search is translated into 95% confidence level exclusion limits on the masses of the gluino and the top squark, in the context of simplified natural SUSY models. For a neutralino mass of 100 GeV and depending on the branching fractions, the pair production of gluinos and top squarks in multi-bottom, multi-top, and mixed top-plus-bottom quark topologies is excluded for gluino masses up to 1.3 TeV and top-squark masses up to 660 GeV. Using the combined likelihood of the hadronic boxes of the razor search and the single-lepton channels of the exclusive top-squark search [102], the exclusion bound on the top-squark mass is extended to 730 GeV for a top squark decaying to a top quark and to a neutralino of mass 100 GeV. Again assuming the neutralino mass to be 100 GeV, top squarks decaying to the two considered decay modes are excluded at a 95% confidence level for mass values between 400 and 645 GeV, independent of the branching fractions.

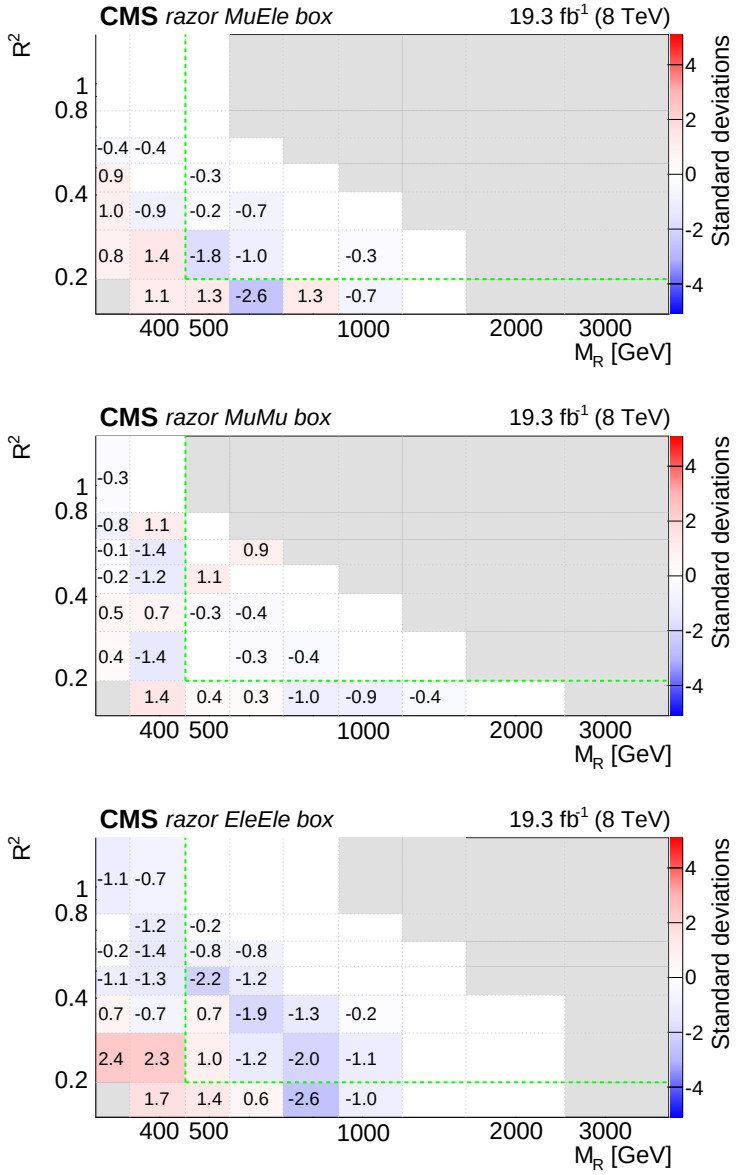

Figure 7.7: Comparison of the expected background and the observed yield in data in the (top) MuEle, (middle) MuMu, and (bottom) EleEle boxes [94, 44]. A probability density function is derived for the bin-by-bin yield using pseudo-experiments, sampled from the output of the corresponding sideband fit. A two sided p-value is computed comparing the observed yield to the distribution of background yield from pseudo-experiments. The p-value is translated into the corresponding number of standard deviations, quoted in each bin and represented by the bin-filling color. Positive and negative significance correspond to regions where the observed yield is respectively larger and smaller than the predicted one. The white areas correspond to bins in which a difference smaller than 0.1 standard deviations is observed. The gray areas correspond to empty bins with less than one background event expected on average. The dashed lines represent the boundaries between the sideband and the signal regions.

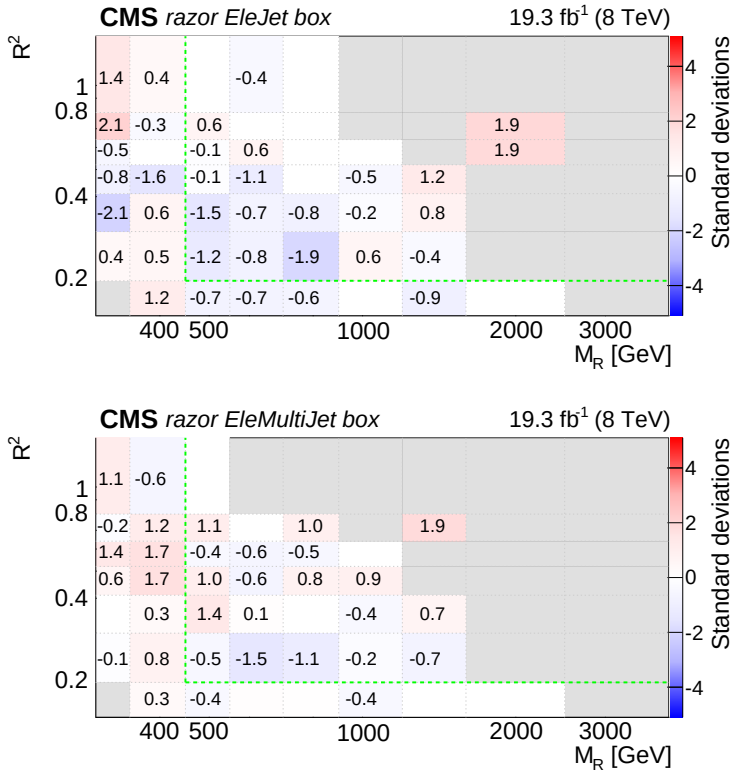

Figure 7.8: Comparison of the expected background and the observed yield in (top) the EleJet and (bottom) the EleMultiJet boxes [94, 44]. A detailed explanation is given in the caption of Fig. 7.7.

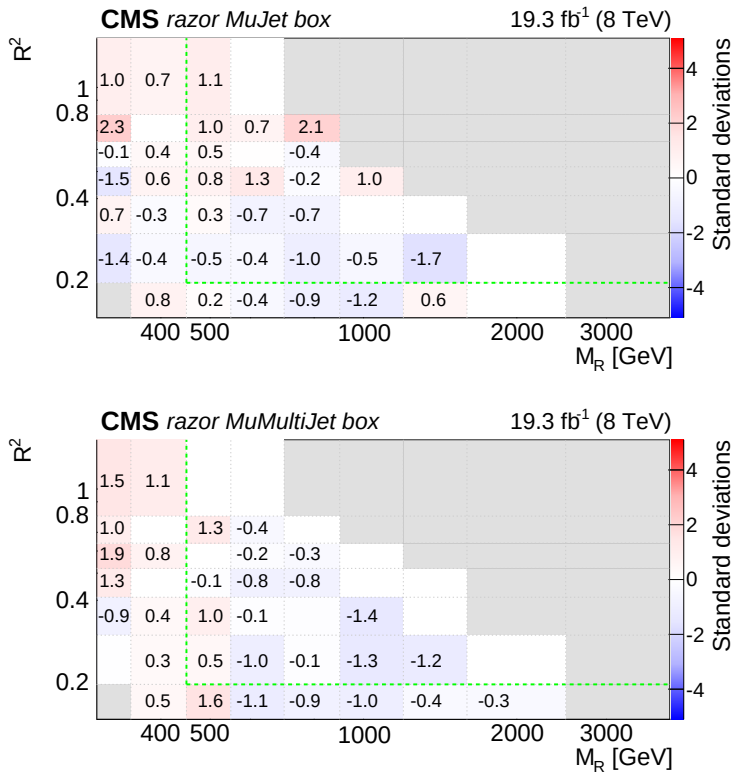

Figure 7.9: Comparison of the expected background and the observed yield in (top) the MuJet and (bottom) the MuMultiJet boxes [94, 44]. A detailed explanation is given in the caption of Fig. 7.7.

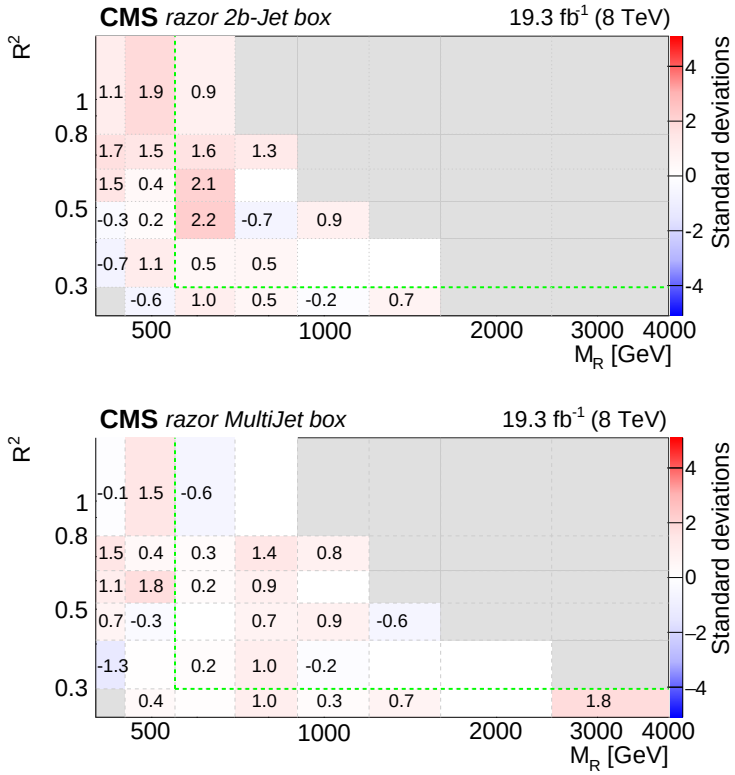

Figure 7.10: Comparison of the expected background and the observed yield in the $\geq$2 b-tagged jet box (left) and the MultiJet box (right) [94, 44]. A detailed explanation is given in the caption of Fig. 7.7.

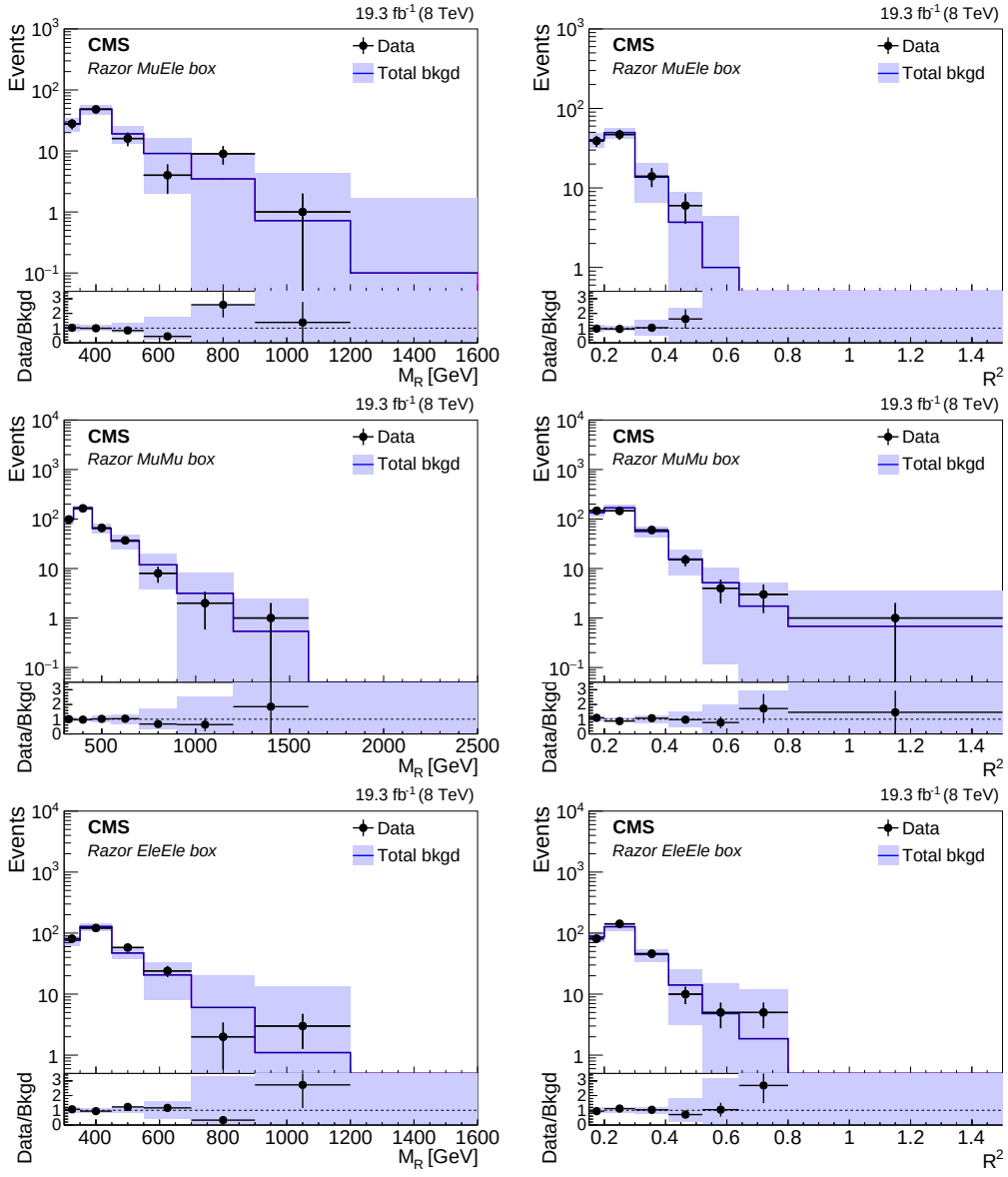

Figure 7.11: Projection of the sideband fit result in the (upper row) MuEle, (middle row) MuMu, and (lower row) EleEle boxes on M_R (left) and R^2 (right), respectively [94, 44]. The fit is performed in the sideband regions and extrapolated to the signal-sensitive region. The solid line and the filled band represent the total background prediction and its uncertainty. The points and the band in the bottom panel represent the data-to-prediction ratio and the prediction uncertainty, respectively.

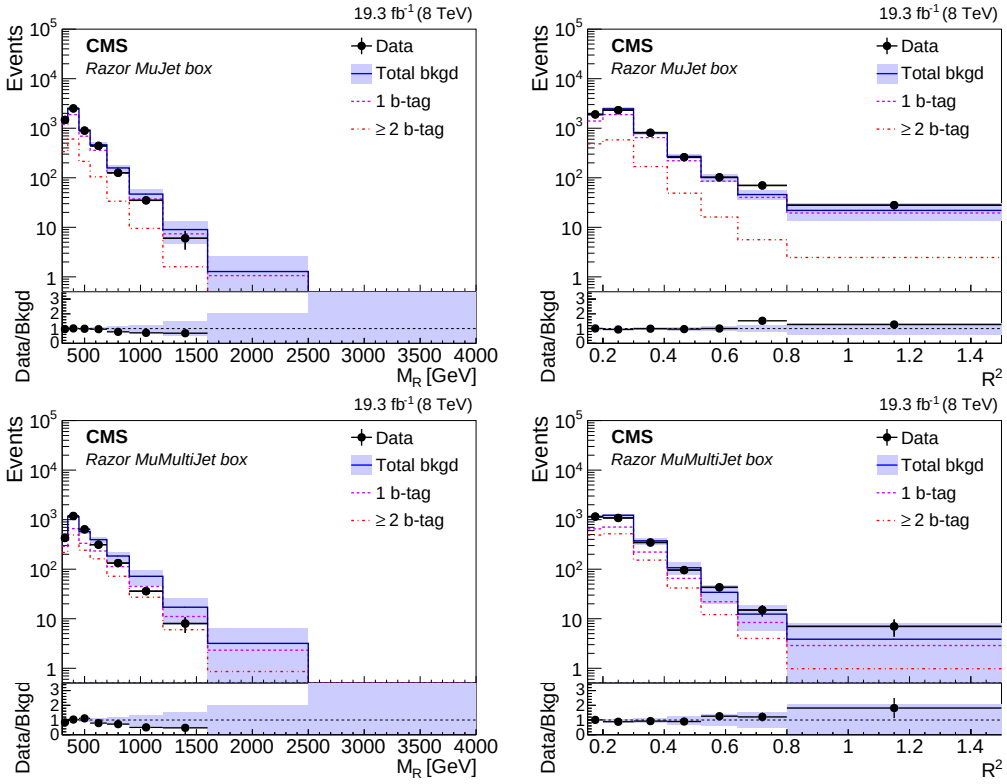

Figure 7.12: Projection of the sideband fit result in the MuJet box on (upper left) M_R and (upper right) R^2, and of the sideband fit result in the MuMultiJet box on (lower left) M_R and (lower right) R^2 [94, 44]. The fit is performed in the sideband regions and extrapolated to the signal-sensitive region. The solid line and the filled band represent the total background prediction and its uncertainty. The dashed and dot-dashed lines represent the background shape for 1 b-tag and $\geq$2 b-tag events, respectively. The points and the band in the bottom panel represent the data-to-prediction ratio and the prediction uncertainty, respectively.

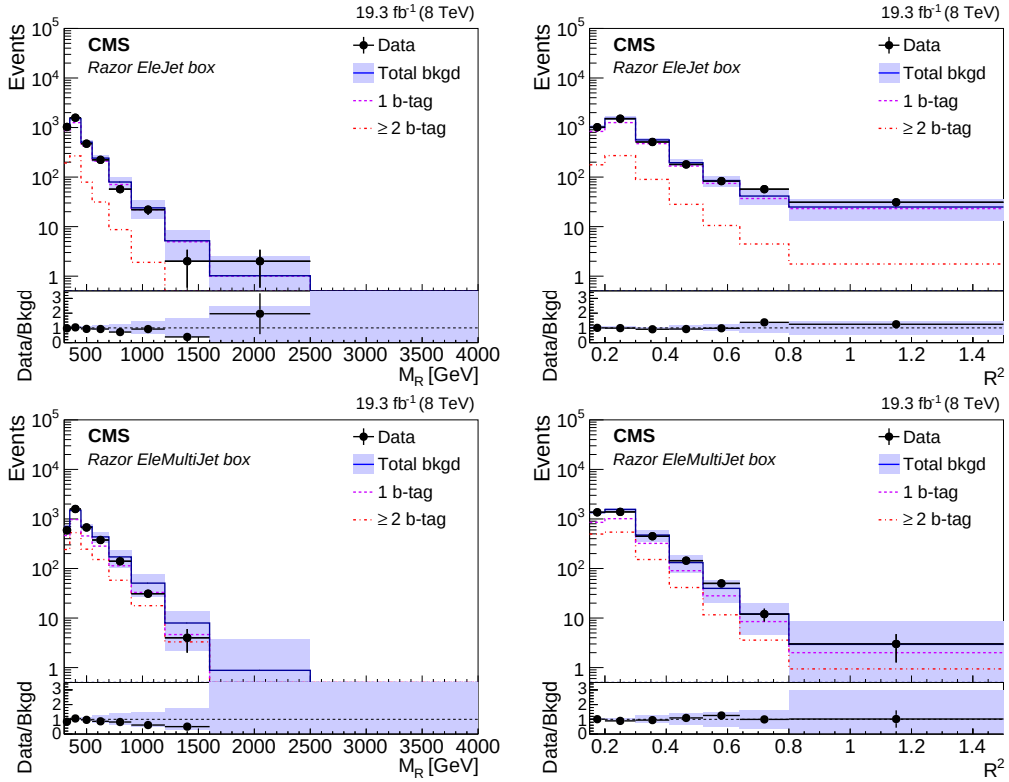

Figure 7.13: Projection of the sideband fit result in the EleJet box on (upper left) M_R and (upper right) R^2, and projection of the sideband fit result in the EleMultiJet box on (lower left) M_R and (lower right) R^2 [94, 44]. A detailed explanation is given in the caption of Fig. 7.12.

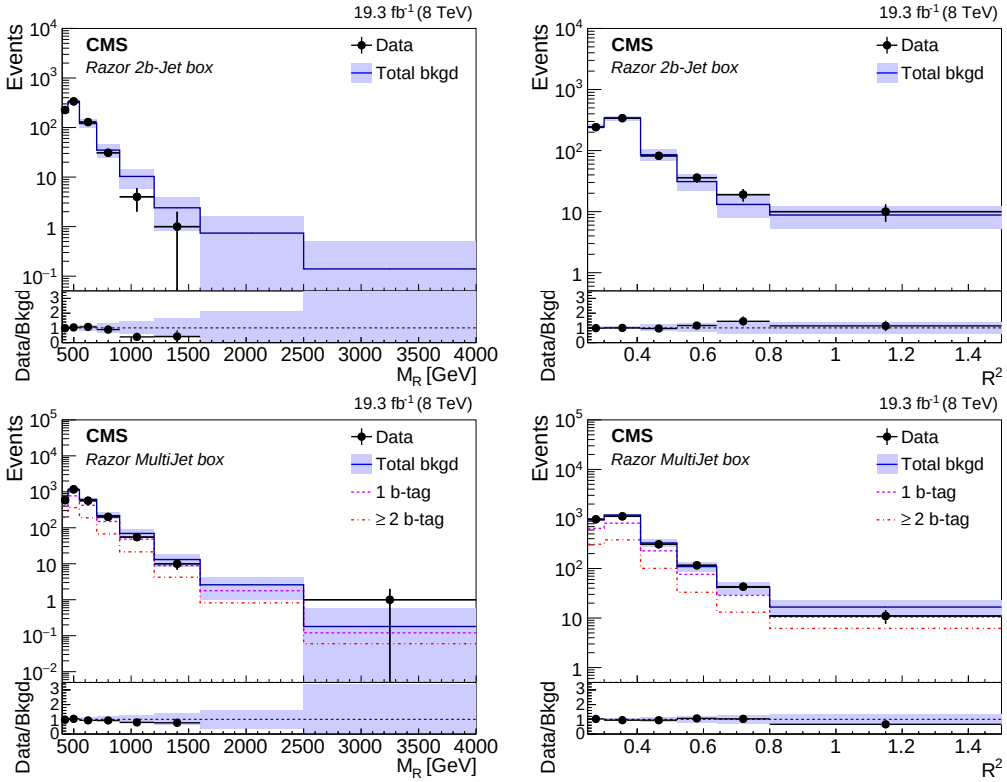

Figure 7.14: Projection of the sideband fit result in the $\geq$2 b-tagged jet box on (upper left) M_R and (upper right) R^2, and projection of the sideband fit result in the MultiJet box on (lower left) M_R and (lower right) R^2 [94, 44]. A detailed explanation is given in the caption of Fig. 7.12.

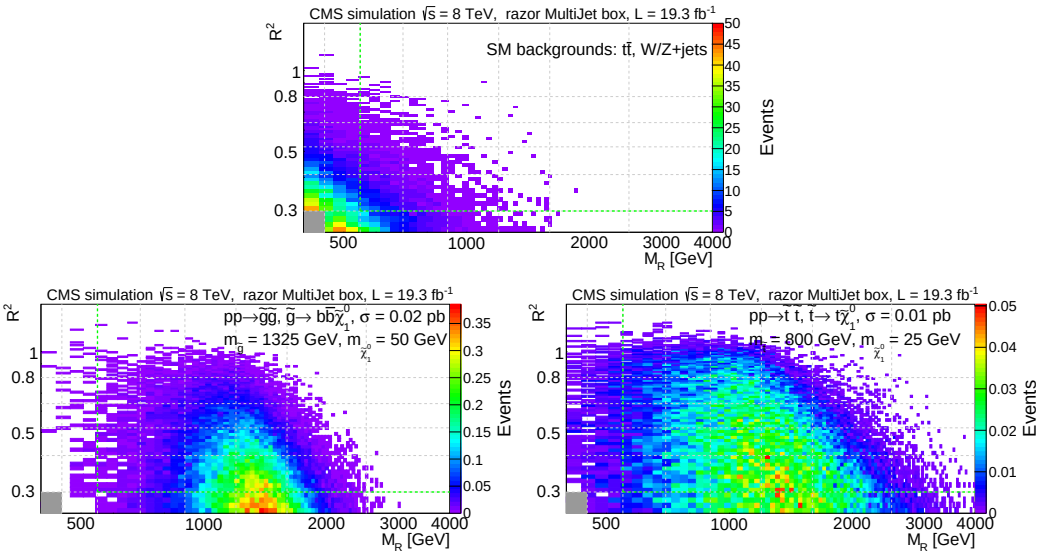

Figure 7.15: Distribution of (top) simulated SM background events, (bottom left) $\widetilde{g}\widetilde{g}$ events, and (bottom right) $\widetilde{t}\widetilde{t}$ events in the MultiJet box. Each gluino has a mass of 1.3 TeV and decays to a bottom quark-antiquark pair and the LSP with a mass of 50 GeV [94, 44]. Similarly, each top squark has a mass of 800 GeV and decays to a top quark and the LSP with a mass of 25 GeV [44].

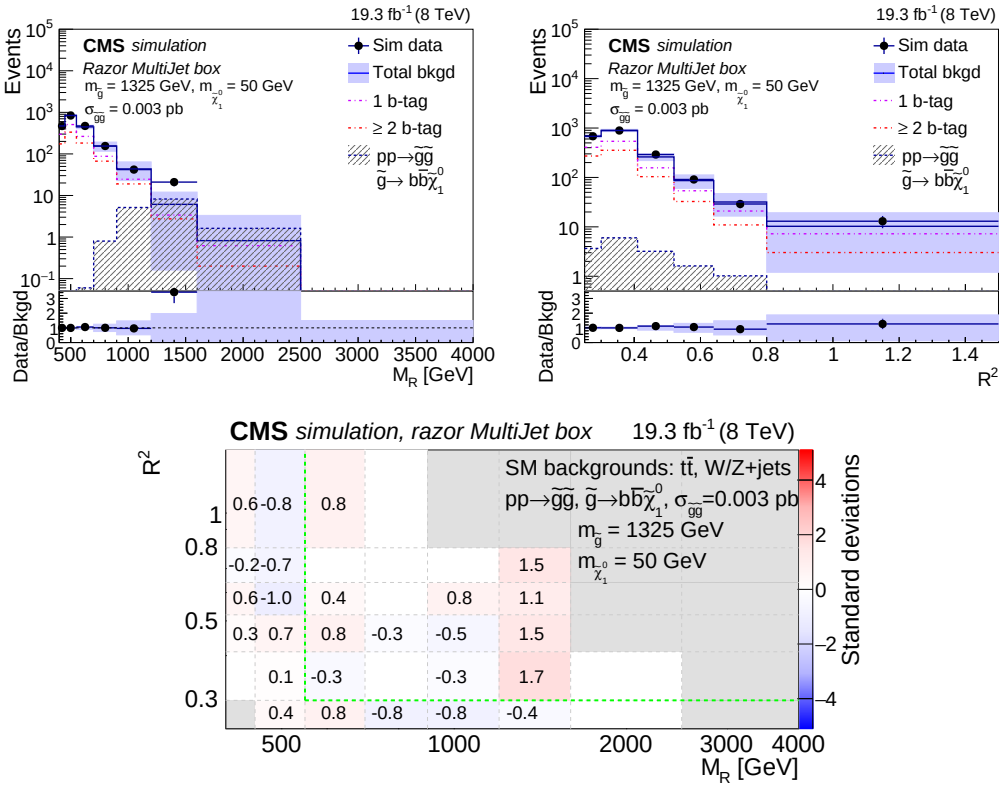

Figure 7.16: Result of the fit to the sideband events of a signal-plus-background MC sample, corresponding to the gluino model whose distribution is shown in Fig. 7.15 [94, 44]. A gluino-gluino production cross section of 0.003 pb is assumed. The one-dimensional projections on (upper left) M_R and (upper right) R^2 are shown, together with (bottom) the agreement between the observed yield and the prediction from the sideband fit as a function of R^2 and M_R. This agreement is evaluated from a two-sided p-value using an ensemble of background-only pseudo-experiments as described in Sec. 7.3.

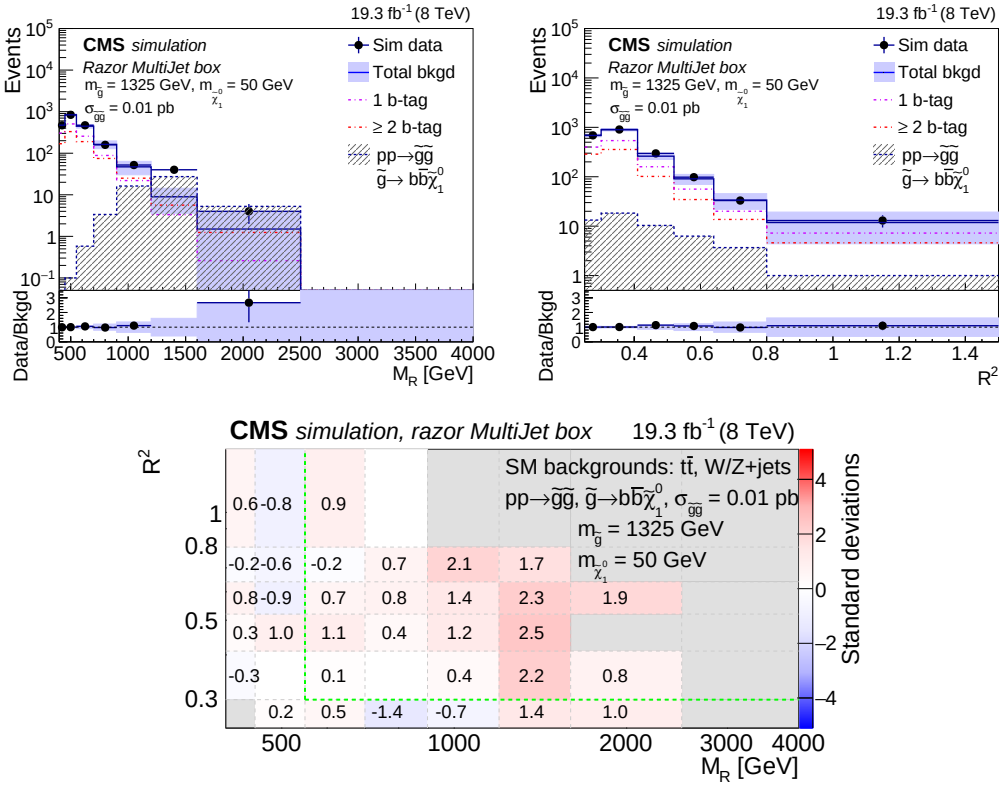

Figure 7.17: Result of the fit to the sideband events of a signal-plus-background MC sample, corresponding to the gluino model shown in Fig. 7.15, with a gluino-gluino production cross section of 0.01 pb [44]. A detailed explanation is given in the caption of Fig. 7.16.

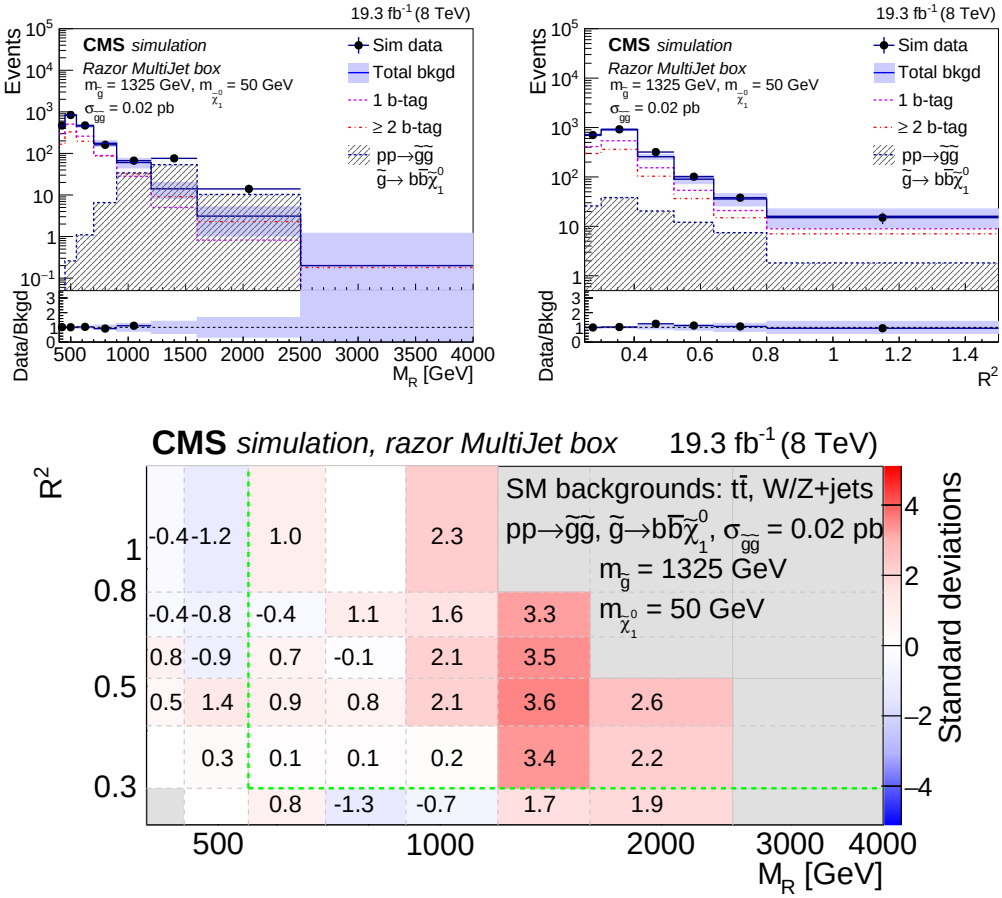

Figure 7.18: Result of the fit to the sideband events of a signal-plus-background MC sample, corresponding to the gluino model shown in Fig. 7.15, with a gluino-gluino production cross section of 0.02 pb [44]. A detailed explanation is given in the caption of Fig. 7.16.

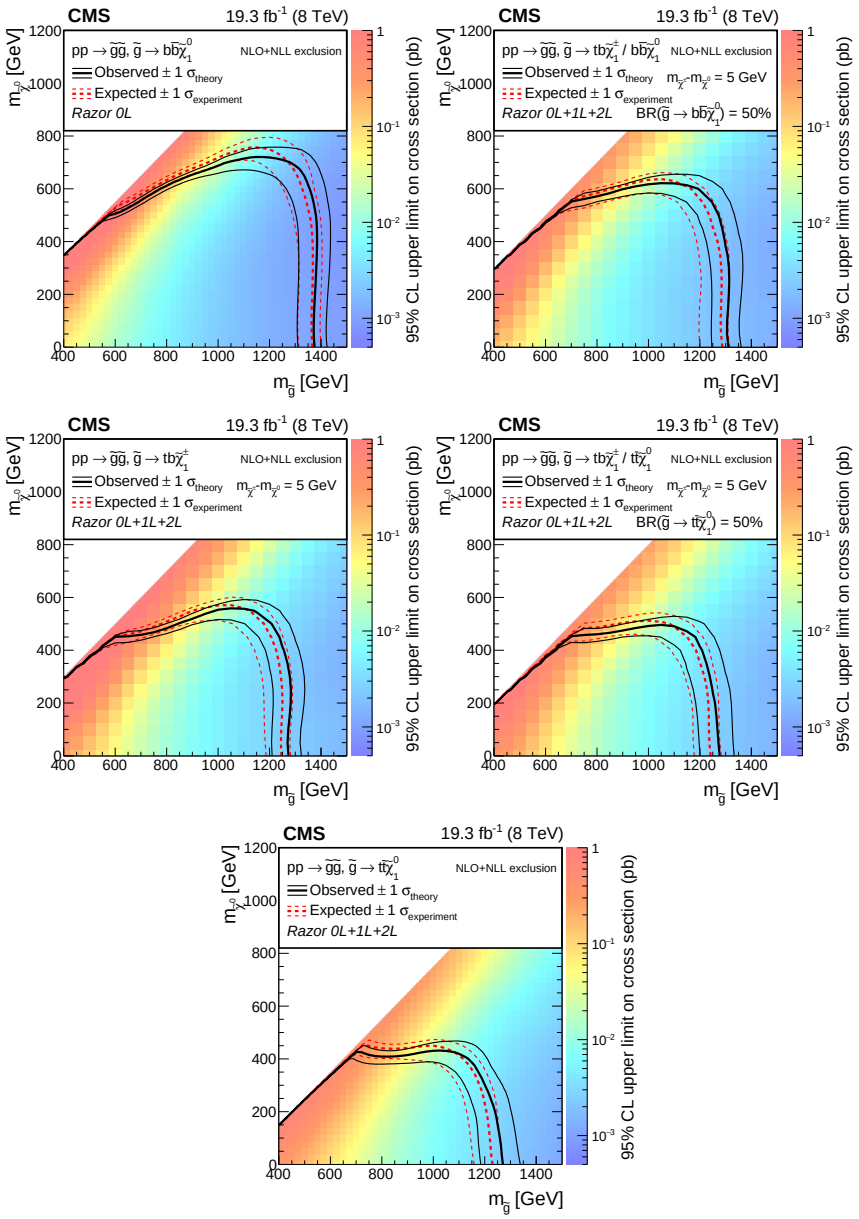

Figure 7.19: Interpretation of the inclusive search with razor variables in the context of gluino pair production models: (upper left) 100% $\tilde{g} \to b\bar{b}\tilde{\chi}_1^0$, (upper right) 50% $\tilde{g} \to b\bar{b}\tilde{\chi}_1^0$ and 50% $\tilde{g} \to tb\tilde{\chi}_1^\pm$ (middle left) 100% $\tilde{g} \to tb\tilde{\chi}_1^\pm$, (middle right) 50% $\tilde{g} \to t\bar{t}\tilde{\chi}_1^0$ and 50% $\tilde{g} \to tb\tilde{\chi}_1^\pm$, and (bottom) 100% $\tilde{g} \to t\bar{t}\tilde{\chi}_1^0$ [94, 44]. The limit for 100% $\tilde{g} \to b\bar{b}\tilde{\chi}_1^0$ is derived using only the hadronic boxes, while the limits for the remaining models are derived using all nine boxes. The color coding indicates the observed 95% CL upper limit on the signal cross section. The dashed and solid lines represent the expected and observed exclusion contours at a 95% CL, respectively. The dashed contours around the expected limit and the solid contours around the observed one represent the one standard deviation theoretical uncertainties in the cross section and the combination of the statistical and experimental systematic uncertainties, respectively.

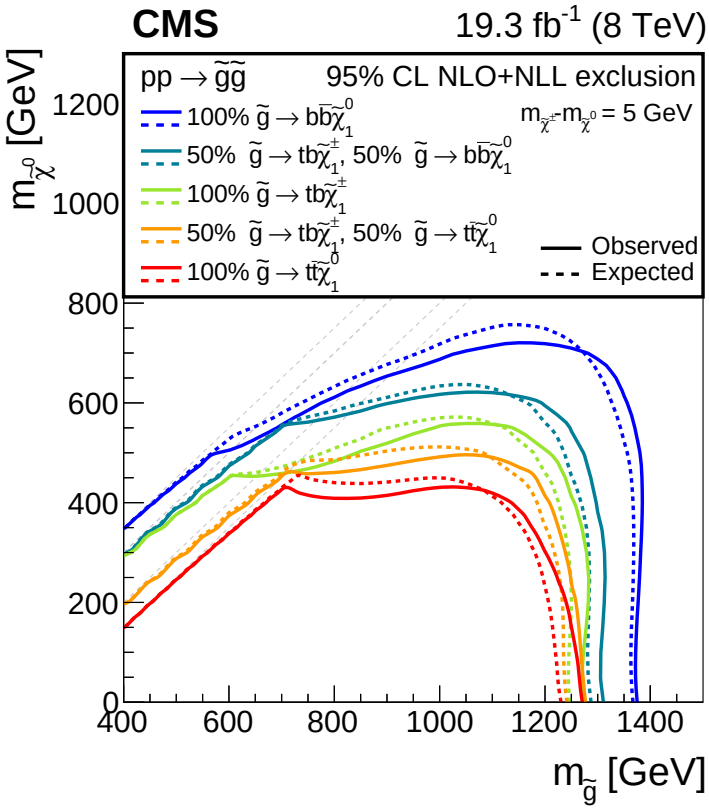

Figure 7.20: Gluino mass limit at a 95% CL, obtained for different gluino pair production models with the inclusive razor analysis in the context of the natural SUSY spectrum of Fig. 3.7 [94, 44].

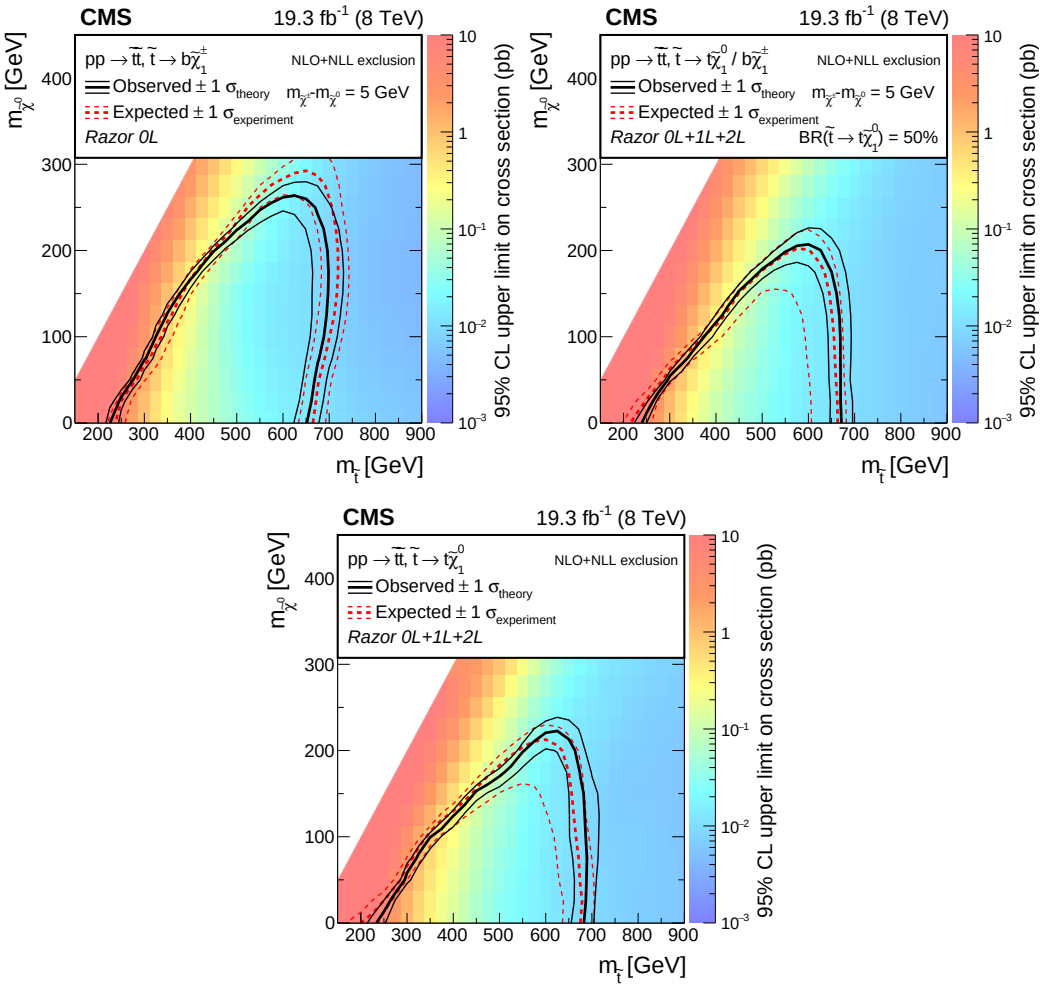

Figure 7.21: Interpretation of the inclusive search with razor variables in the context of top-squark pair production models: (top) 100% $\tilde{t} \to b\tilde{\chi}_1^{\pm}$, (middle) 50% $\tilde{t} \to b\tilde{\chi}_1^{\pm}$ and 50% $\tilde{t} \to t\tilde{\chi}_1^0$, and (bottom) 100% $\tilde{t} \to t\tilde{\chi}_1^0$ [94, 44]. The limit for 100% $\tilde{t} \to b\tilde{\chi}_1^{\pm}$ is derived using only the hadronic boxes, while the limits for the remaining models are derived using all nine boxes. The meaning of the color coding and the displayed contours is explained in the caption of Fig. 7.19.

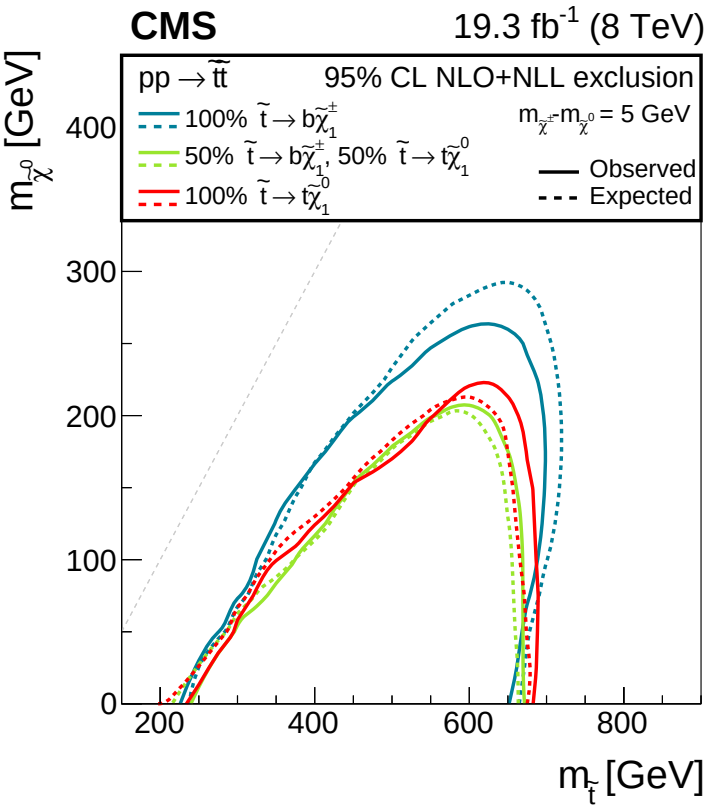

Figure 7.22: Top-squark mass limit at a 95% CL, obtained for different squark pair production models with the inclusive razor analysis in the context of the natural SUSY spectrum of Fig. 3.7 [94, 44].

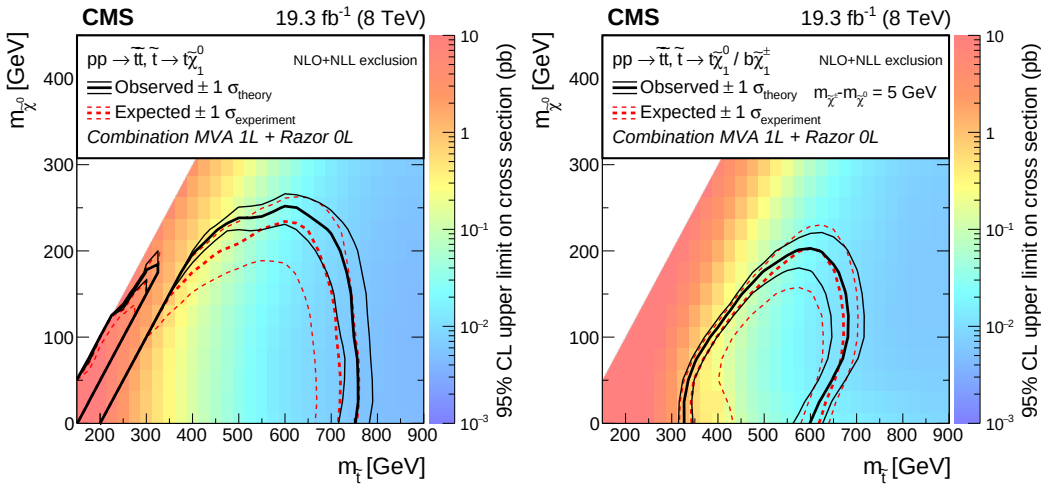

Figure 7.23: Top-squark mass limit at a 95% CL, obtained combining the result of the hadronic razor boxes with the result of Ref. [102] for (top) 100% $\tilde{t} \to t\tilde{\chi}_1^0$ and (bottom) independent of the branching fraction choice [94, 44]. The meaning of the color coding and the displayed contours is explained in the caption of Fig. 7.19.

Chapter 8

SEARCHES FOR SUPERSYMMETRY AT $\sqrt{S} = 13\,\text{TEV}$

Searches for SUSY performed using pp collision data collected in 2012 at $\sqrt{s} = 8\,\text{TeV}$ by ATLAS [97, 98, 99, 100, 101, 199, 200, 201] and CMS [102, 103, 104, 105, 106, 202, 203], including the inclusive razor search described in Ch. 7 [94], have probed SUSY particle masses near the TeV scale.

In early 2015, the LHC restarted pp collisions at a collision energy of 13 TeV after two years of maintenance and upgrades. The increase in center-of-mass energy from 8 to 13 TeV provides an opportunity to significantly extend the sensitivity of LHC searches to higher SUSY particle masses [204, 205, 96, 206, 207, 208, 209, 210, 211, 212, 213, 214, 215, 216]. In particular, the largest gain in sensitivity is expected for gluinos, which would be produced almost 50 times more often at 13 TeV than at 8 TeV for a gluino mass of 1.6 TeV. Top squarks, on the other hand would only be produced at a rate 10 times larger for a top squark mass of 800 GeV. Fig. 8.1 shows the pair production cross sections for gluinos and top squarks at 8 and 13 TeV as well as their ratio.

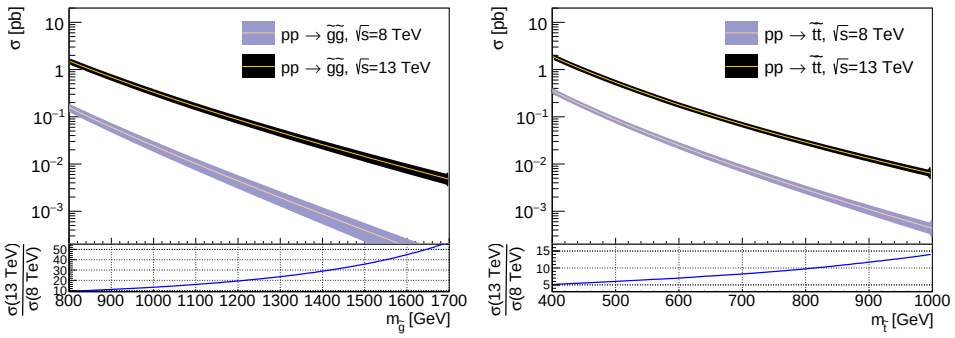

Figure 8.1: The NLO+NLL pair production cross sections for gluinos (left) and top squarks (right) in pp collisions at $\sqrt{s} = 8$ and 13 TeV [63, 64, 65, 66, 67, 68, 69, 44]. The bottom panel shows the ratio of the cross sections.

In this chapter, we interpret the results of the inclusive search at 13 TeV using the simplified natural SUSY scenarios for pair production of gluinos and top squarks detailed in Sec. 3.8 of this thesis. We follow a similar strategy as

the search performed at 8 TeV, with some changes and improvements. The modifications are the following

- We utilize two independent background estimation methods: one based on control regions in data, and assisted by the simulation, and one based on the fit with the empirical function.
- Only three separate data categories – Multijet, EleMultijet, and MuMultijet – all of which target gluino production, are considered in the 13 TeV search.
- The anti-k_{T} algorithm with radius parameter $R = 0.4$ is used to cluster jets.
- The selection of muons and electrons is updated, and in particular, uses a new isolation variable with a lepton p_{T} dependent cone size that corrects for the effects of pileup.
- We reject hadronically decaying τ leptons in the zero-lepton event categories.
- The binned form of the maximum likelihood fit to the (M_{R},R^2) is used in all cases.
- The sideband region used in the model-independent search for excesses or discrepancies is redefined with a tighter M_{R} threshold, as shown in Fig. 8.7.
- A new subcategory of events with zero b-tagged jets in each category is included in the 13 TeV search.
- Rather than constraining the (M_{R},R^2) shape of $\geq$ 3b-jet category category to be exactly the same as the 2b-jet category, the shapes of the two categories are allowed to differ with one additional nuisance parameter describing the deviation.

Each of these changes is described in greater detail below.

The remainder of this chapter is organized as follows. A description of simulated signal and background samples is given in Sec. 8.1. Sec. 8.2 describes physics object reconstruction and event selection. Sec. 8.3 describes

the analysis strategy, and the background estimation techniques used in this analysis are described in Sec. 8.4. Sec. 8.5 covers the systematic uncertainties. Finally, our results and their interpretation are presented in Sec. 8.6, followed by a summary in Sec. 8.7.

8.1 Simulated event samples

Simulated Monte Carlo (MC) samples are used for modeling of the SM backgrounds in the search regions and for calculating the selection efficiencies for SUSY signal models. The production of $t\bar{t}$+jets, W+jets, Z+jets, γ+jets, and QCD multijet events, as well as production of gluino and top squark pairs, is simulated with the MC generator MADGRAPH v5 [172]. Single top quark events are modeled at next-to-leading order (NLO) with MADGRAPH_aMC@NLO v2.2 [173] for the s-channel, and with POWHEG v2 [217, 218] for the t-channel and W-associated production. Contributions from $t\bar{t}W$, $t\bar{t}Z$ are also simulated with MADGRAPH_aMC@NLO v2.2. Simulated events are interfaced with PYTHIA v8.2 [219] for fragmentation and parton showering. The NNPDF3.0LO and NNPDF3.0NLO [220] parton distribution functions (PDF) are used, respectively, with MADGRAPH, and with POWHEG and MADGRAPH_aMC@NLO.

The SM background events are simulated using a GEANT4-based model [176] of the CMS detector. The simulation of SUSY signal model events is performed using the CMS fast simulation package [221]. All simulated events include the effects of pileup, i.e. multiple pp collisions within the same or neighboring bunch crossings, and are processed with the same chain of reconstruction programs as is used for collision data. Simulated events are weighted to reproduce the observed distribution of pileup vertices in the data set, calculated based on the measured instantaneous luminosity.

The SUSY signal production cross sections are calculated to next-to-leading order (NLO) plus next-to-leading-logarithm (NLL) accuracy [63, 64, 65, 66, 67, 68, 69], assuming all SUSY particles other than those in the relevant diagram to be too heavy to participate in the interaction. The NLO+NLL cross sections and their associated uncertainties [69] are used to derive the exclusion limit on the masses of the SUSY particles. The hard scattering is generated with MADGRAPH up to two extra partons to model initial-state radiation at the matrix element level, and simulated events were interfaced

to PYTHIA for the showering, fragmentation and hadronization steps.

8.2 Object reconstruction and selection

Physics objects are defined using the particle-flow (PF) algorithm [168, 169], described in Sec. 5.5. The reconstructed PF candidates are clustered into jets using the anti-k_t algorithm [131, 132] with a distance parameter of 0.4 for 13 TeV instead of 0.5 used at 8 TeV. As in the 8 TeV search, we consider jets with transverse momentum $p_T > 40$ GeV and $|\eta| < 3.0$.

Electrons are reconstructed by associating a cluster of energy deposited in the ECAL with a reconstructed track [222], and are required to have $p_T > 5$ GeV and $|\eta| < 2.5$. A "tight" selection used to identify prompt electrons is based on requirements on the electromagnetic shower shape, the geometric matching of the track to the calorimeter cluster, the track quality and impact parameter, and isolation. The isolation of electrons and muons is defined as the scalar sum of the transverse momenta of all neutral and charged PF candidates within a cone $\Delta R = \sqrt{(\Delta\eta)^2 + (\Delta\phi)^2}$ along the lepton direction. The variable is corrected for the effects of pileup using an effective area correction [223], and the cone size ΔR shrinks with increasing lepton p_T according to

$$\Delta R = \begin{cases} 0.2, & p_T \leq 50 \text{ GeV} \\ \frac{10\,\text{GeV}}{p_T}, & 50 < p_T \leq 200 \text{ GeV} \\ 0.05, & p_T > 200 \text{ GeV}. \end{cases} \tag{8.1}$$

The use of the lepton p_T dependent isolation cone enhances the efficiency of identifying leptons in events containing a large amount of hadronic energy, such as those with $t\bar{t}$ production. For tight electrons, the isolation is required to be less than 10% of the electron p_T. The selection efficiency for tight electrons increases from 60% for p_T around 20 GeV to 70% for p_T around 40 GeV and to 80% for p_T above 50 GeV.

To improve the purity of all-hadronic signals in the zero-lepton event categories, a looser "veto" selection is also defined. For this selection, electrons are required to have $p_T > 5$ GeV. The output of a boosted decision tree is used to identify electrons based on shower shape and track information [222]. For electrons with $p_T > 20$ GeV, the isolation is required to be less than 20% of the electron p_T. For electrons with p_T between 5 and 20 GeV, the value of the absolute isolation, computed by summing the p_T's of all

particle flow candidates within a ΔR cone of 0.3, is required to be less than 5 GeV. For the veto electron selection, the efficiency increases from 60% for p_T around 5 GeV to 80% for p_T around 15 GeV and 90% for p_T above 20 GeV.

Muons are reconstructed by combining tracks found in the muon system with corresponding tracks in the silicon detectors [224], and are required to have $p_T > 5$ GeV and $|\eta| < 2.4$. Muons are identified based on the quality of the track fit, the number of detector hits used in the tracking algorithm, and the compatibility between track segments. The absolute value of the 3D impact parameter significance of the muon track, which is defined as the ratio of the impact parameter to its estimated uncertainty, is required to be less than 4. As for electrons, we define a "tight" selection for muons with $p_T > 20$ GeV and a "veto" selection for muons with $p_T > 5$ GeV. For both tight and veto muons with $p_T > 20$ GeV the isolation is required to be less than 20% of the muon p_T, while for veto muons with p_T between 5 and 20 GeV the isolation computed using a ΔR cone of 0.4 is required to be less than 10 GeV. For tight muons we require $d_0 < 0.2$ cm, where d_0 is the transverse impact parameter of the muon track, while this selection is not applied for veto muons. The selection efficiency for tight muons increases from 65% for p_T around 20 GeV to 75% for p_T around 40 GeV and to 80% for p_T above 50 GeV. For the veto muon selection, the efficiency increases from 85% for p_T around 5 GeV to 95% for p_T above 20 GeV.

We additionally reconstruct and identify hadronically decaying τ leptons (τ_h) to further enhance the all-hadronic purity of the zero-lepton event categories, using the hadron-plus-strips algorithm [225], which identifies τ decay modes with one charged hadron and up to two neutral pions, or three charged hadrons. The τ_h candidate is required to have $p_T > 20$ GeV, and the isolation, defined as the p_T sum of other nearby PF candidates, must be below a certain threshold. The loose cutoff-based selection [225] is used and results in an efficiency of about 50% for successfully reconstructed τ_h decays.

To identify jets originating from b-hadron decays, we use the updated CSVv2 b-jet tagger (see Sec. 5.5), which uses the inclusive vertex finder to select b-jets [226, 135, 134]. The "medium" working point is used to define the event categories for the search signal regions. For jets with p_T between 40 and 200 GeV the b jet tagging efficiency is approximately 70% and the prob-

ability of misidentifying a light-flavor quark or gluon as a b jet is 1.5% in typical background events relevant for this search.

Photon candidates are reconstructed from clusters of energy deposits in the ECAL. They are identified using selections on the hadronic to electromagnetic energy ratio (H/E) and the transverse shower width $\sigma_{\eta\eta}$, measured in terms of the energy weighted spread within the 5×5 crystal matrix centered on the crystal with the largest energy deposit in the supercluster [120],

$$(\sigma_{\eta\eta})^2 = \frac{\left(\sum_{5\times5}(\eta_i - \bar{\eta})^2 w_i\right)}{\sum_{5\times5} w_i}\,, \tag{8.2}$$

where w_i is a weight that depends logarithmically on the energy. Photon isolation, defined as the scalar p_{T} sum of charged particles within a cone of $\Delta R < 0.3$, must be less than 2.5 GeV. Finally, photon candidates that share the same energy cluster as an identified electron are vetoed.

8.3 Analysis strategy and event selection

We employ an event classification approach similar to the one used in the 8 TeV search in Sec. 7.2. We select events with four or more jets, using search categories defined by the number of leptons and b-tagged jets in the event. Events in the zero lepton category, denoted as the Multijet category, are required to have no electrons or muons passing the tight or veto selection, and no selected τ_{h}. The Multijet category consists of events with no electrons or muons passing the tight or veto selection, and no selected τ_{h}. Events in the one electron (muon) category, denoted as the Electron Multijet (Muon Multijet) category, are required to have one and only one electron (muon) passing the tight selection. Within these three event classes, we divide the events further into categories depending on whether the events have zero, one, two, or more than two b-tagged jets.

Each event in the above categories is treated as a dijet-like event by grouping selected leptons and jets in the event into two megajets in order to compute the razor variables M_{R} and R^2 defined in Sec. 3.10.

The events of interest are triggered either by the presence of a high-p_{T} electron or muon, or through dedicated hadronic triggers requiring the presence of at least two highly energetic jets and with loose thresholds on the razor variables M_{R} and R^2. The single-electron (single-muon) triggers require at least one isolated electron (muon) with $p_{\mathrm{T}} > 23\,(20)$ GeV. The isola-

tion requirement is dropped for electrons (muons) with $p_T > 105$ (50) GeV. The efficiencies for the single electron (muon) triggers are above 70% for p_T around 25 (20) GeV, and reach a plateau above 97% for $p_T > 40\,\text{GeV}$. The efficiencies for the single electron trigger were measured in data and simulation and found to be in good agreement, as were the corresponding efficiencies for muons. Corrections for residual difference of trigger efficiency between data and MC simulation are applied to simulated samples. The hadronic razor trigger requires at least two jets with $p_T > 80\,\text{GeV}$ or at least four jets with $p_T > 40\,\text{GeV}$. The events are also required to pass selections on the razor variables $M_R > 200\,\text{GeV}$ and $R^2 > 0.09$ and on the product $(M_R + 300\,\text{GeV}) \times (R^2 + 0.25) > 240\,\text{GeV}$. The efficiency of the hadronic razor trigger for events passing the baseline M_R and R^2 selections described below is 97% and is consistent with the prediction from MC simulation.

For events in the Electron or Muon Multijet categories, the search region is defined by the selections $M_R > 400\,\text{GeV}$ and $R^2 > 0.15$. The p_T of the electron (muon) is required to be larger than 25 (20 GeV). To suppress backgrounds from the $W(\ell\nu)$+jets and $t\bar{t}$ processes, we require that the transverse mass M_T formed by the lepton and $\vec{p}_T^{\,\text{miss}}$ be larger than 120 GeV.

For events in the Multijet category, the search uses a region defined by the selections $M_R > 500\,\text{GeV}$ and $R^2 > 0.25$ and requires the presence of at least two jets with $p_T > 80\,\text{GeV}$ within $|\eta| < 3.0$, for compatibility with the requirements imposed by the hadronic razor triggers. For QCD multijet background events, the E_T^{miss} arises mainly from mismeasurement of the energy of one of the leading jets. In such cases, the two razor megajets tend to lie in a back-to-back configuration. Therefore, to suppress the QCD multijet background we require that the azimuthal angle $\Delta\phi_R$ between the two razor megajets be less than 2.8 radians.

Finally, events containing signatures consistent with beam-induced background or anomalous noise in the calorimeters are rejected using dedicated filters [166, 133].

8.4 Background modeling

The main background processes in the search regions considered are $W(\ell\nu)$+jets (with $\ell = e, \mu, \tau$), $Z(\nu\bar{\nu})$+jets, $t\bar{t}$, and QCD multijet production. For event categories with zero b-tagged jets, the background is primarily composed

of the W($\ell\nu$)+jets and Z($\nu\bar{\nu}$)+jets processes, while for categories with two or more b-tagged jets it is dominated by the $t\bar{t}$ process. There are also very small contributions from the production of two (VV) or three electroweak bosons (VVV) and from the production of $t\bar{t}$ in association with a W or Z boson ($t\bar{t}V$). These contributions are summed and labeled "Other" in Fig. 8.2-8.5.

We model the background using two independent methods based on control samples in data with entirely independent sets of systematic assumptions. The first method (A) is based on the use of dedicated control regions that isolate a specific background processes in order to control and correct the predictions of the MC simulation. The second method (B) is based on a fit to an assumed functional form for the shape of the observed data distribution in the two-dimensional (M_R,R^2) plane as in the 8 TeV search. These two background predictions are compared to and cross-checked against each other in order to significantly enhance the robustness of the background estimate.

Method A: simulation-assisted background prediction

The simulation-assisted method defines dedicated control regions that isolate each of the main background processes. Data in these control regions are used to control and correct the accuracy of the MC prediction for each of the background processes. Corrections for the jet energy response and lepton momentum response are applied to the MC, as are corrections for the trigger efficiency and the selection efficiency of electrons, muons, and b-tagged jets. Any disagreement observed in these control regions is then interpreted as an inaccuracy of the MC in predicting the hadronic recoil spectrum and jet multiplicity.

Two alternative formulations of the method are typically used in searches for new physics [103, 203, 97]. In the first formulation, the data control region yields are extrapolated to the search regions via translation factors derived from simulation. In the second formulation, simulation to data correction factors are derived in bins of the razor variables M_R and R^2 and are then applied to the simulation prediction of the search region yields. The two formulations are identical and the choice of which formulation is used depends primarily on the convenience of the given data processing

sequence. In both cases, the contributions from background processes other than the one under study are subtracted using the MC prediction. We employ the first formulation of the method for the estimate of the QCD background, while the second formulation is used for modeling all other major backgrounds. Details of the control regions used for each of the dominant background processes are described in the subsections below.

Finally, the small contribution from rare background processes such as $t\bar{t}V$ is modeled using simulation. Systematic uncertainties on the cross sections of these processes are propagated to the final result.

The $t\bar{t}$ and $W(\ell\nu)$+jets background

The control region to isolate the $t\bar{t}$ and $W(\ell\nu)$+jets processes is defined by requiring at least one tight electron or muon. To suppress QCD multijet background, the quantities E_T^{miss} and M_T are both required to be larger than 30 GeV. To minimize contamination from potential SUSY processes and to explicitly separate the control region from the search regions, we require $M_T < 100$ GeV. The $t\bar{t}$ enhanced control region is defined by requiring that there be at least one b-tagged jet, and the $W(\ell\nu)$+jets enhanced control region is defined by requiring no such b-tagged jets. Other than these b-tagged jet requirements, we place no explicit requirement on the number of jets in the event, in order to benefit from significantly larger control samples.

We first derive corrections for the $t\bar{t}$ background, and then measure corrections for the $W(\ell\nu)$+jets process after first applying the corrections already obtained for the $t\bar{t}$ background in the $W(\ell\nu)$+jets control region. As discussed above, the corrections to the MC prediction are derived in two-dimensional bins of the (M_R,R^2) plane. We observe that the M_R spectrum predicted by the simulation falls off more steeply than the control region data for both the $t\bar{t}$ and $W(\ell\nu)$+jets processes, as shown in Fig. 8.2. In Fig. 8.3, we show the two-dimensional (M_R,R^2) distributions for data and simulation in the $W(\ell\nu)$+jets control region. The statistical uncertainties in the correction factors due to limited event yields in the control region bins are propagated and dominate the total uncertainty of the background prediction. For bins at large M_R (near 1000 GeV), the statistical uncertainties range between 15% and 50%.

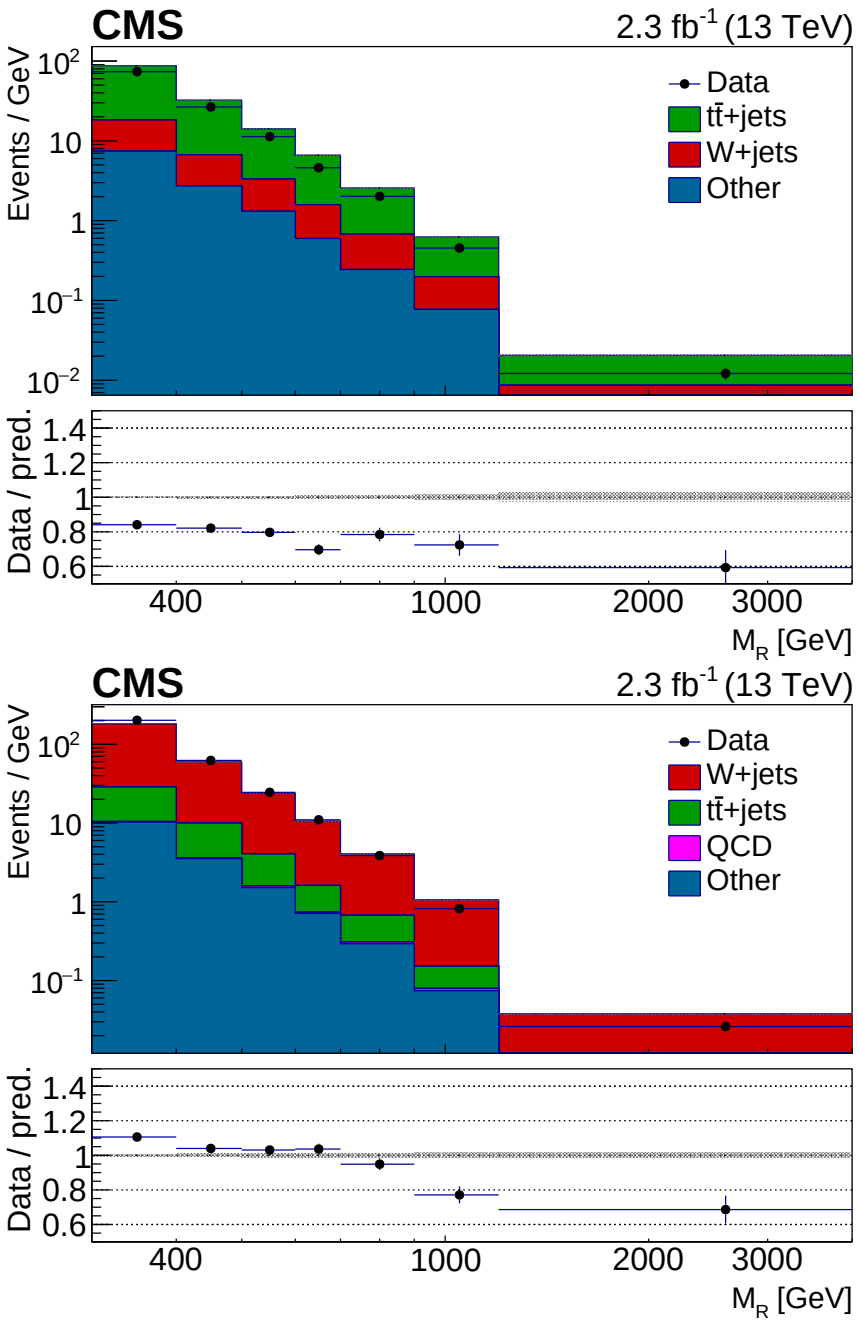

Figure 8.2: The M_R distributions for events in the $t\bar{t}$ (upper) and $W(\ell\nu)$+jets (lower) control regions are shown, comparing data with the MC prediction [227]. The ratio of data to the background prediction is shown on the bottom panel, with the statistical uncertainty expressed through the data point error bars and the systematic uncertainty of the background prediction represented by the shaded region. In the right-hand plot, the $t\bar{t}$ MC events have been reweighted according to the corrections derived in the $t\bar{t}$-enhanced control region.

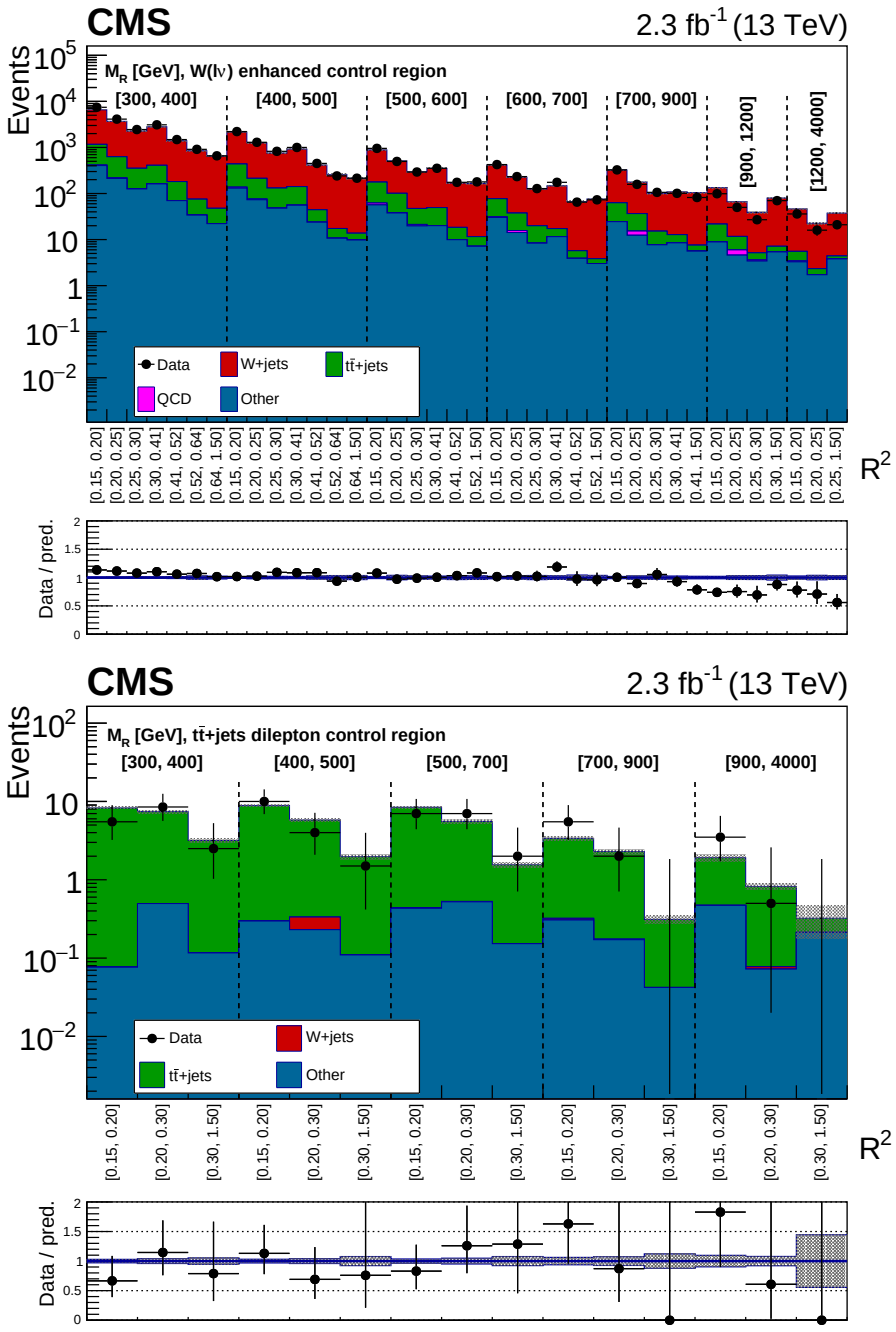

Figure 8.3: The two-dimensional M_R-R^2 distribution for the W($\ell\nu$)+jets enhanced (upper) and the $t\bar{t}$ dilepton (lower) control regions are shown, comparing data with the MC prediction [227]. The $t\bar{t}$ MC events have been reweighted according to the correction factors derived in the $t\bar{t}$-enhanced control region. The two-dimensional M_R-R^2 distribution is shown in a one dimensional representation, with each M_R bin marked by the dashed lines and labeled near the top , and each R^2 bin labeled below. The bottom panel shows the ratio of data to the background prediction, with uncertainties displayed as in Fig. 8.2.

Corrections to the MC simulation are first measured and applied as a function of M_R and R^2, inclusively in the number of selected jets. As our search region requires a higher multiplicity of jets, an additional correction factor is required to accurately model the jet multiplicity. We measure this additional correction factor to be 0.90 ± 0.03 by comparing the data and the MC prediction in the W($\ell\nu$)+jets and $t\bar{t}$ control region for events with four or more jets. To control for possible simulation mismodeling that is correlated between the number of jets and the razor variables, we perform additional cross-checks of the M_R and R^2 distributions in bins of the number of b-tagged jets in the $t\bar{t}$ and W($\ell\nu$)+jets control regions for events with four or more jets. For bins which show statistically significant disagreement, the size of the disagreement is propagated as a systematic uncertainty. The typical range of these additional systematic uncertainties is between 10% and 30%.

The $t\bar{t}$ and W($\ell\nu$)+jets backgrounds in the zero-lepton Multijet event category are composed of *lost lepton events* with at least one lepton in the final state, which is either out of acceptance or fails the veto electron, veto muon, or τ_h selection. To ensure a good understanding of the rate of lost lepton events in data and the MC simulation, two additional control regions are defined to evaluate accuracy of the modeling of the acceptance and efficiency for selecting veto electrons, veto muons, and τ_h. We require events in the veto lepton (τ_h candidate) control region to have at least one veto electron or muon (τ_h candidate) selected. The M_T is required to be between 30 and 100 GeV in order to suppress QCD multijet background and contamination from potential new physics processes. At least two jets with $p_T > 80$ GeV and at least four jets with $p_T > 40$ GeV are required, consistent with the search region requirements. Finally, we consider events with $M_R > 400$ GeV and $R^2 > 0.25$. The distribution of the veto lepton p_T for events in the veto lepton and veto τ_h control regions are shown in Fig. 8.4, and demonstrate that the MC models describe well the observed data. The observed discrepancies in any bin are propagated as systematic uncertainties in the prediction of the $t\bar{t}$ and W($\ell\nu$)+jets in the Multijet category search region.

The $t\bar{t}$ background in the Electron and Muon Multijet categories is primarily from the dilepton decay mode as the M_T requirement highly suppresses

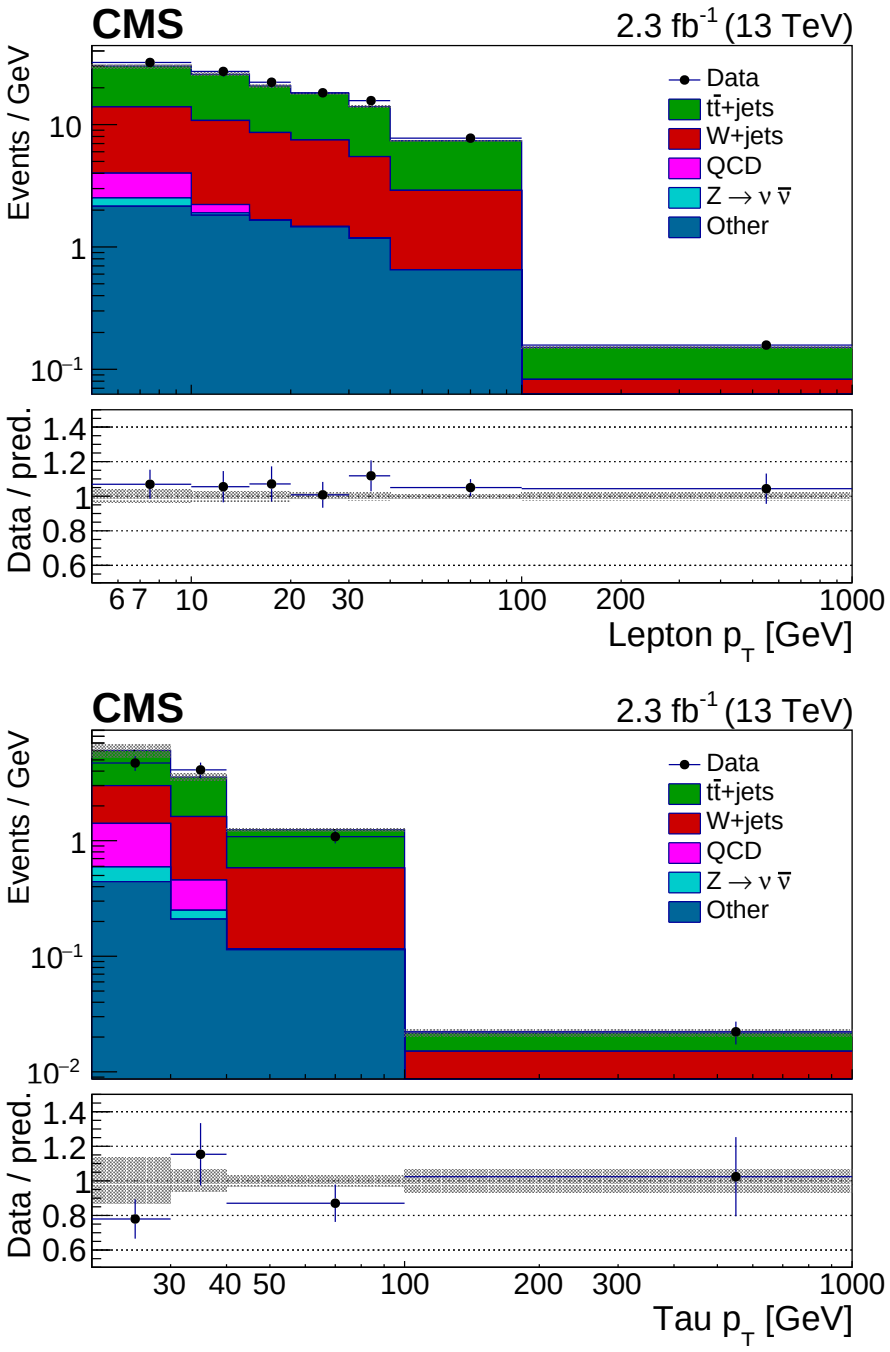

Figure 8.4: The p_T distribution of the veto electron or muon (upper) and the veto τ_h (lower) is shown for events in the veto lepton control regions, comparing data with the MC prediction [227]. The $t\bar{t}$ and $W(\ell\nu)$+jets MC events have been reweighted according to the correction factors derived in the $t\bar{t}$ enhanced and $W(\ell\nu)$+jets enhanced control regions, respectively. The bottom panel shows the ratio of data to the background prediction, with uncertainties displayed as in Fig. 8.2.

the semi-leptonic decay mode. Corrections to the MC simulation derived from the $t\bar{t}$ control region primarily arise from semi-leptonic decays. We define an additional control region enhanced in dilepton $t\bar{t}$ decays to confirm that the MC corrections derived from a region dominated by semi-leptonic decays also apply to dilepton decays. We select events with two tight leptons, both with $p_T > 30\,\text{GeV}$, $E_T^{\text{miss}} > 40\,\text{GeV}$, and dilepton mass larger than 20 GeV. For events with two leptons of the same flavor, we additionally veto events with a dilepton mass between 76 and 106 GeV in order to suppress background from Z boson decays. At least one b-tagged jet is required to enhance the purity for the $t\bar{t}$ process. Finally, we mimic the phase space region similar to our search region in the Electron and Muon Multijet categories by treating one lepton as having failed the identification criteria and applying the M_T requirement using the other lepton. The correction factors measured in the $t\bar{t}$ control region are applied to the MC prediction of the dilepton $t\bar{t}$ cross-check region in bins of M_R and R^2. In Fig. 8.3 we show the (M_R,R^2) distribution for the dilepton $t\bar{t}$ cross-check region in events with four or more jets, and we observe no significant mismodeling by the simulation, indicating that the measured corrections are accurate.

The $Z \to \nu\bar{\nu}$ background

Three independent control regions are used to predict the $Z(\nu\bar{\nu})$+jets background, relying on the assumption that Monte Carlo simulation mismodeling of the hadronic recoil spectrum and the jet multiplicity distribution of the $Z(\nu\bar{\nu})$+jets process are similar to those of the $W(\ell\nu)$+jets and γ+jets processes. The primary and most populated control region is the γ+jets control region, defined by selecting events with at least one photon passing loose identification and isolation requirements. The events are triggered using single-photon triggers, and the photon is required to have $p_T > 50\,\text{GeV}$. The momentum of the photon candidate in the transverse plane is added vectorially to $\vec{p}_T^{\,\text{miss}}$ in order to simulate an invisible particle, as one would have in the case of a $Z \to \nu\bar{\nu}$ decay, and the M_R and R^2 variables are computed according to this invisible decay scenario. A template fit to the distribution of $\sigma_{\eta\eta}$ is performed to determine the contribution from misidentified photons to the γ+jets control region and is found to be about 5%, independent of the M_R and R^2. Events from the γ+jets process where the photon is produced within the cone of a jet (labeled as γ+jets fragmentation) are considered to be background and subtracted using the MC prediction. Backgrounds from rarer processes such as $W\gamma$, $Z\gamma$, and $t\bar{t}\gamma$ are also subtracted similarly. In Fig. 8.5, we show the M_R distribution as well as the two-dimensional (M_R,R^2) distribution for the γ+jets control region, where we again observe a steeper M_R falloff in the data compared to the simulation. Correction factors are derived in bins of M_R and R^2 and applied to the MC prediction for the $Z \to \nu\bar{\nu}$ background in the search region. The statistical uncertainties for the correction factors range between 10% and 30% and are among the dominant uncertainties for the $Z \to \nu\bar{\nu}$ background prediction. Analogous to the procedure for the $t\bar{t}$ and $W(\ell\nu)$+jets control region, we derive an additional correction factor of 0.87 ± 0.05 to accurately describe the yield in events with four or more jets. Additional cross-checks are performed in bins of the number of b-tagged jets and systematic uncertainties ranging from 4% for events with zero b-tagged jets to 58% for events with three or more b-tagged jets are derived.

The second control region, enhanced in the $W(\ell\nu)$+jets, is defined identically to the $W(\ell\nu)$+jets control region described in Section 8.4, except that the lepton is treated as invisible by adding its momentum vectorially to

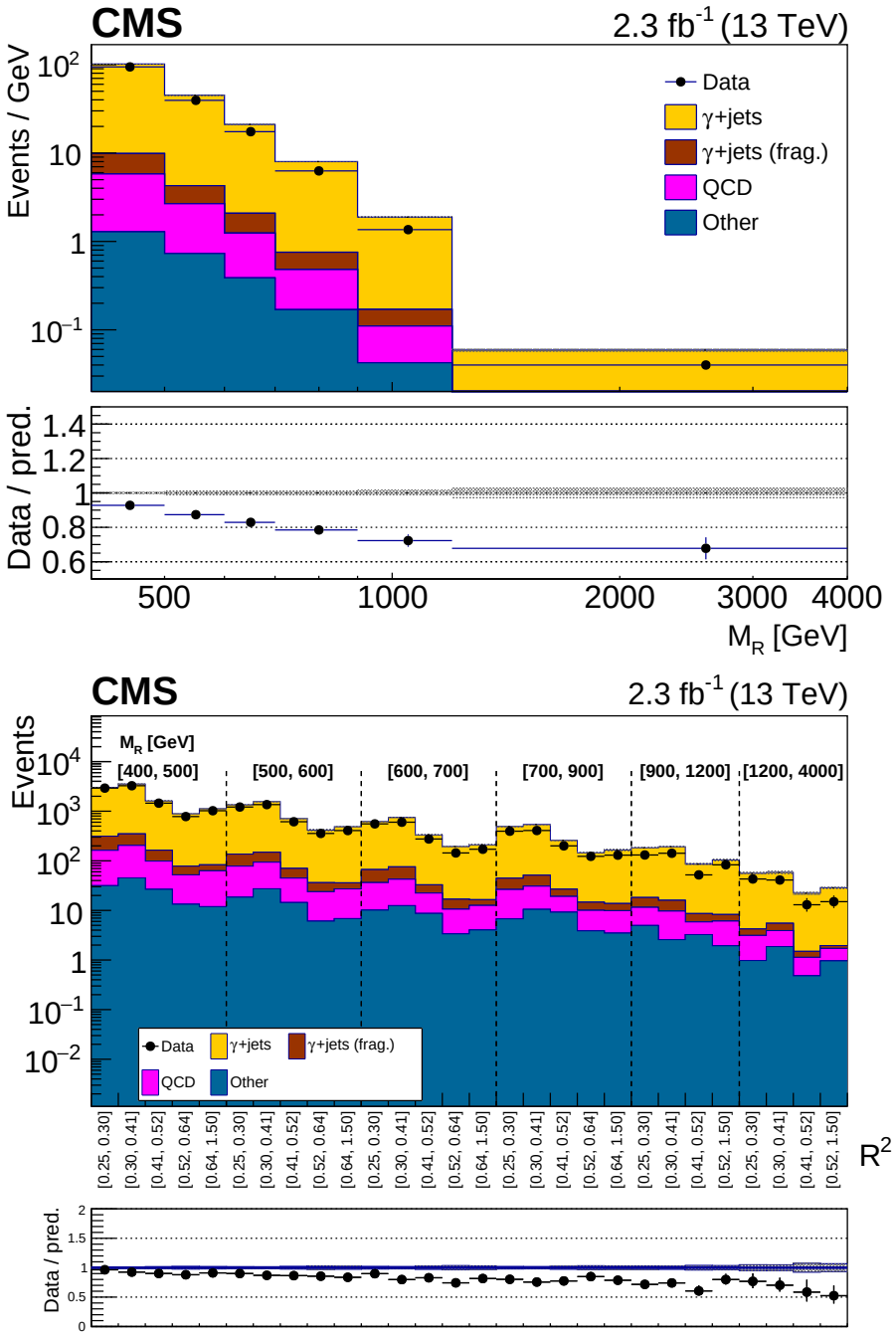

Figure 8.5: The one-dimensional distribution of M_R in the γ+jets control region (upper) and the two-dimensional M_R-R^2 distribution in the γ+jets control region (lower) are shown. The two-dimensional M_R-R^2 distribution is shown in a one-dimensional representation as in Fig. 8.3. The bottom panel shows the ratio of data to the background prediction, with uncertainties displayed as in Fig. 8.2.

$\vec{p}_{\mathrm{T}}^{\,\mathrm{miss}}$, and the M_{R} and R^2 variables are computed accordingly. Correction factors computed using events from this control region are compared to those computed from the γ+jets control region and exhibit differences ranging between 10% and 40% depending on the M_{R}-R^2 bin. These differences are propagated as a systematic uncertainty.

The third control region, enhanced in $\mathrm{Z} \to \ell^+\ell^-$ decays, is defined by selecting events with two tight electrons or two tight muons, and requiring that the dilepton mass is between 76 and 106 GeV. Events are required to have no b-tagged jets in order to suppress $\mathrm{t\bar{t}}$ background. The two leptons are treated as invisible by adding their momenta vectorially to $\vec{p}_{\mathrm{T}}^{\,\mathrm{miss}}$. We apply the correction factors obtained from the γ+jet control region to the $\mathrm{Z} \to \ell^+\ell^-$ MC prediction and perform a cross-check against data in this control region. No significant discrepancy between the data and the prediction is observed.

The QCD multijet background

The QCD multijet processes contribute about 10% of the total background in the zero-lepton Multijet event category for bins with zero or one b-tagged jets. Such events enter the search regions in the tails of the $E_{\mathrm{T}}^{\mathrm{miss}}$ distribution when the energy of one of the jets in the event is significantly under- or over-measured. In most such situations, the $\vec{p}_{\mathrm{T}}^{\,\mathrm{miss}}$ points either toward or away from the leading jets and therefore the two megajets tend to be in a back-to-back configuration. The search region is defined by requiring that the azimuthal angle between the two megajets $\Delta\phi_R$ be less than 2.8, which was found to be an optimal selection based on studies of QCD multijet and signal simulated samples. We define the control region for the QCD background process to be events with $\Delta\phi_{\mathrm{R}} > 2.8$, keeping all other selection requirements identical to those for the search region. The purity of the QCD multijet process in the control region is more than 70%.

After subtracting the non-QCD background, we project the observed data yield in the control region to the search region using the translation factor ζ:

$$\zeta = \frac{N(|\Delta\phi_{\mathrm{R}}| < 2.8)}{N(|\Delta\phi_{\mathrm{R}}| > 2.8)}, \tag{8.3}$$

where the numerator and denominator are the number of events passing

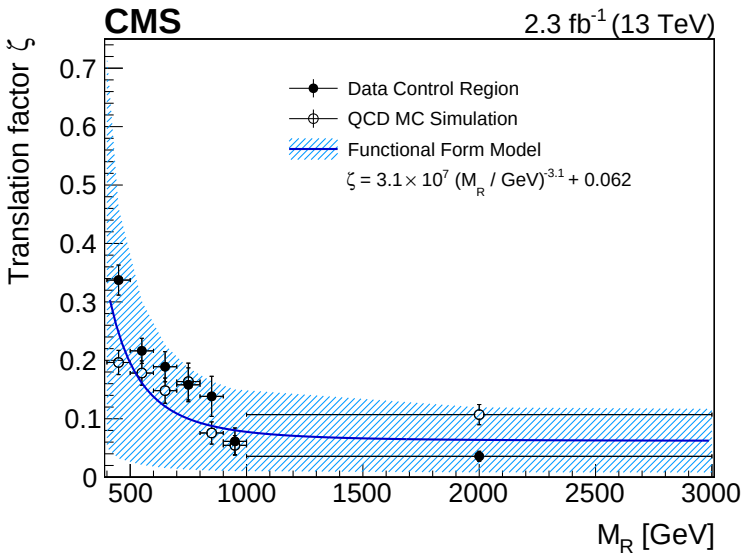

Figure 8.6: The translation factor ζ is shown as a function of M_R [227]. The curve shows the functional form used to model the M_R dependence, and the open circle and black dot data points are the values of ζ measured in the low-R^2 data control region and the QCD MC simulation, respectively. The hashed region indicates the size of the systematic uncertainty in ζ.

and failing the selection on $|\Delta\phi_R| < 2.8$, respectively. We find that the translation factor calculated from the MC simulation decreases as a function of M_R and is, to a large degree, constant as a function of R^2. Using data events in the low R^2 region (0.15 to 0.25), dominated by QCD multijet background, we measure the translation factor ζ as a function of M_R to cross-check the values obtained from the simulation. The M_R dependence of ζ is modeled as the sum of a power law and a constant. This functional shape is fitted to the values of ζ calculated from the MC. A systematic uncertainty of 87% is propagated, covering both the spread around the fitted model as a function of M_R and R^2 in simulation, and the difference between the values measured in simulation and data. The function used for ζ and the values measured in data and simulation are shown in Fig. 8.6.

We perform two additional cross-checks on the accuracy of the MC prediction for ζ in control regions dominated by processes similar to the QCD multijet background with no invisible neutrinos in the final state. The first cross-check is performed on a dimuon control region enhanced in $Z \to \mu^+\mu^-$ decays, and the second cross-check is performed on a dijet control region enhanced in QCD dijet events. In both cases, the events at large R^2 result

from cases similar to our search region where the energy of a leading jet is severely mismeasured. We compare the values of ζ measured in these data control regions to the values predicted by the simulation and observe agreement within 20%, well within the systematic uncertainty of 87% assigned to the QCD background estimate.

Method B: fit-based background prediction

The second background prediction method is based the same methodology as the 8 TeV search described in Sec. 7.3 along with the modifications detailed above.

The sideband region is defined to be 100 GeV in width in M_R and 0.05 in R^2. Explicitly, for the Multijet event category, it comprises the region 500 GeV $< M_R <$ 600 GeV and $R^2 > 0.3$, plus the region $M_R >$ 500 GeV and $0.25 < R^2 < 0.3$. For the Muon and Electron Multijet event categories, it comprises the region 400 GeV $< M_R <$ 500 GeV and $R^2 > 0.2$, plus the region $M_R >$ 400 GeV and $0.15 < R^2 < 0.2$. The updated sideband regions for the 13 TeV search are shown in Fig. 8.7.

For each event category, we fit the two-dimensional distribution of M_R and R^2 in the sideband region using the above functional form, separately for events with zero, one, two, and three or more b-tagged jets. The normalization in each event category and each b-tagged jet bin is independently varied in the fit. Due to the lack of data events in the category with three or more b-tagged jets, we constrain the shape in this category to be related to the shape for events with two b-tagged jets as follows:

$$f_{SM}^{\geq 3b}(M_R, R^2) = (1 + m_{M_R}(M_R - M_R^{offset}))f_{SM}^{2b}(M_R, R^2), \tag{8.4}$$

where $f_{SM}^{2b}(M_R, R^2)$ and $f_{SM}^{\geq 3b}(M_R, R^2)$ are the probability density functions for events with two and with three or more b-tagged jets, respectively; M_R^{offset} is the lowest M_R value in a particular event category; and m_{M_R} is an additional nuisance parameter constrained by a Gaussian distribution centered at the value measured using the simulation and with a 100% uncertainty. The above form for the shape of the background events with three or more b-tagged jets is verified in simulation.

Numerous tests are performed to establish the robustness of the fit model in adequately describing the underlying distributions. To demonstrate that

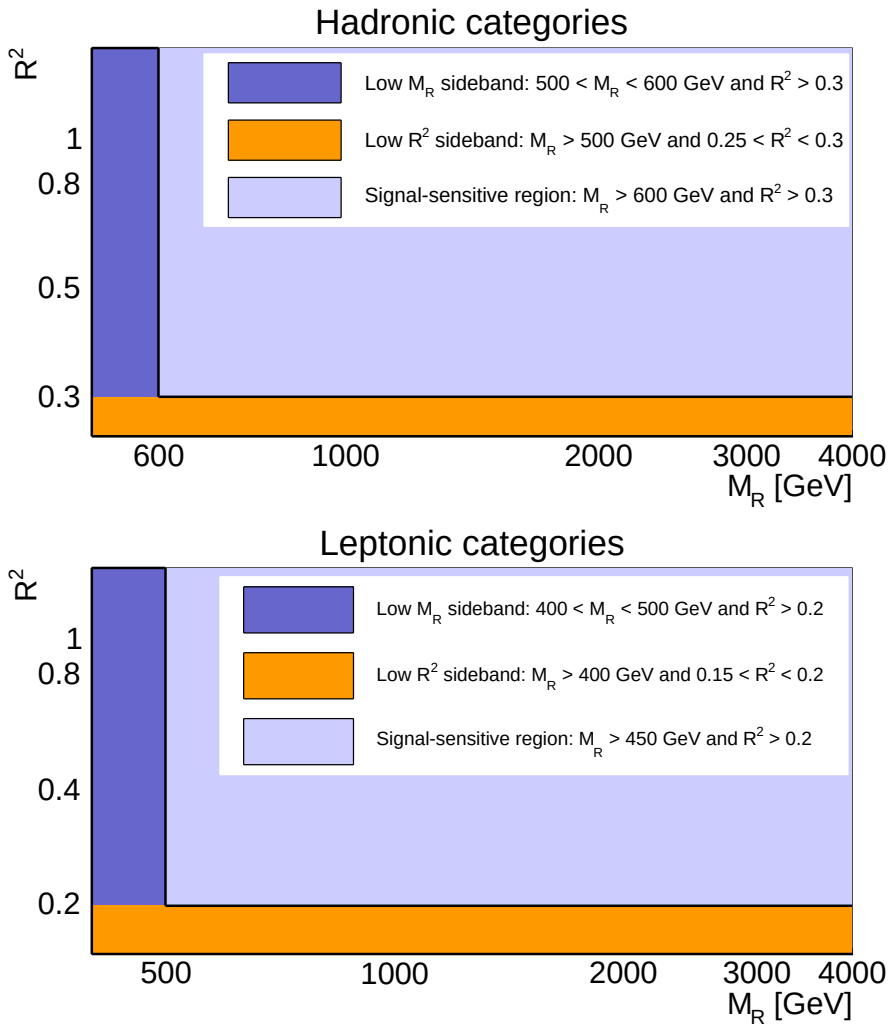

Figure 8.7: Updated definition of the sideband and the signal-sensitive regions used in the analysis, for (top) the Multijet category and (bottom) the other categories for the 13 TeV search [44].

the background model gives an accurate description of the background distributions, we construct a representative data set using MC samples, and perform the background fit using the form given by Eqn. (7.1). Goodness of fit is evaluated by comparing the background prediction from the fit with the prediction from the simulation. This procedure is performed separately for each of the search categories and we find that the fit function yields an accurate representation of the background predicted by the simulation.

We also observe that the accuracy of the fit model is insensitive to variations of the background composition predicted by the simulation in each event category by altering relative contributions of the dominant backgrounds,

performing a new fit with the alternative background composition, and comparing the new fit results to the nominal fit result. The contributions of the main $t\bar{t}$, $W(\ell\nu)$+jets, and $Z(\nu\bar{\nu})$ backgrounds are varied by 30%, and the rare backgrounds from QCD multijet and $t\bar{t}Z$ processes are varied by 100%. For the Muon and Electron Multijet event categories, we also vary the contributions from the dileptonic and semi-leptonic decays of the $t\bar{t}$ background separately by 30%. In each of these tests, we observe that the chosen functional form can adequately describe the shapes of the M_R and R^2 distributions as predicted by the modified MC simulation.

Additional pseudoexperiment studies are performed comparing the background prediction from the sideband fit and the full region fit to evaluate the average deviation between the two fit predictions. We observe that the sideband fit and the full region fit predictions in the signal-sensitive region differ by up to 15% and we propagate an additional systematic uncertainty to the sideband fit background prediction to cover this average difference.

To illustrate method B, we present the data and fit-based background predictions in Fig. 8.8, for events in the 2 b-tag and $\geq$ 3 b-tag Multijet categories. The number of events observed in data is compared to the prediction from the sideband fit in the M_R and R^2 bins. To quantify the agreement between the background model and the observation, we generate alternative sets of background shape parameters from the covariance matrix calculated by the fit. An ensemble of pseudoexperiment data sets is created, generating random (M_R, R^2) pairs distributed according to each of these alternative shapes. For each (M_R,R^2) bin, the distribution of the predicted yields from the ensemble of pseudoexperiments is compared to the observed yield in data. The agreement between the predicted and the observed yields is described as a two-sided p-value and translated into the corresponding number of standard deviations for a normal distribution. Positive (negative) significance indicates the observed yield is larger (smaller) than the predicted one. We find that the pattern of differences between data and background predictions in the different bins considered is consistent with statistical fluctuations.

To demonstrate that the model-independent sideband fit procedure used in the analysis would be sensitive to the presence of a signal, we perform a signal injection test. We sample a signal-plus-background pseudo-data set and

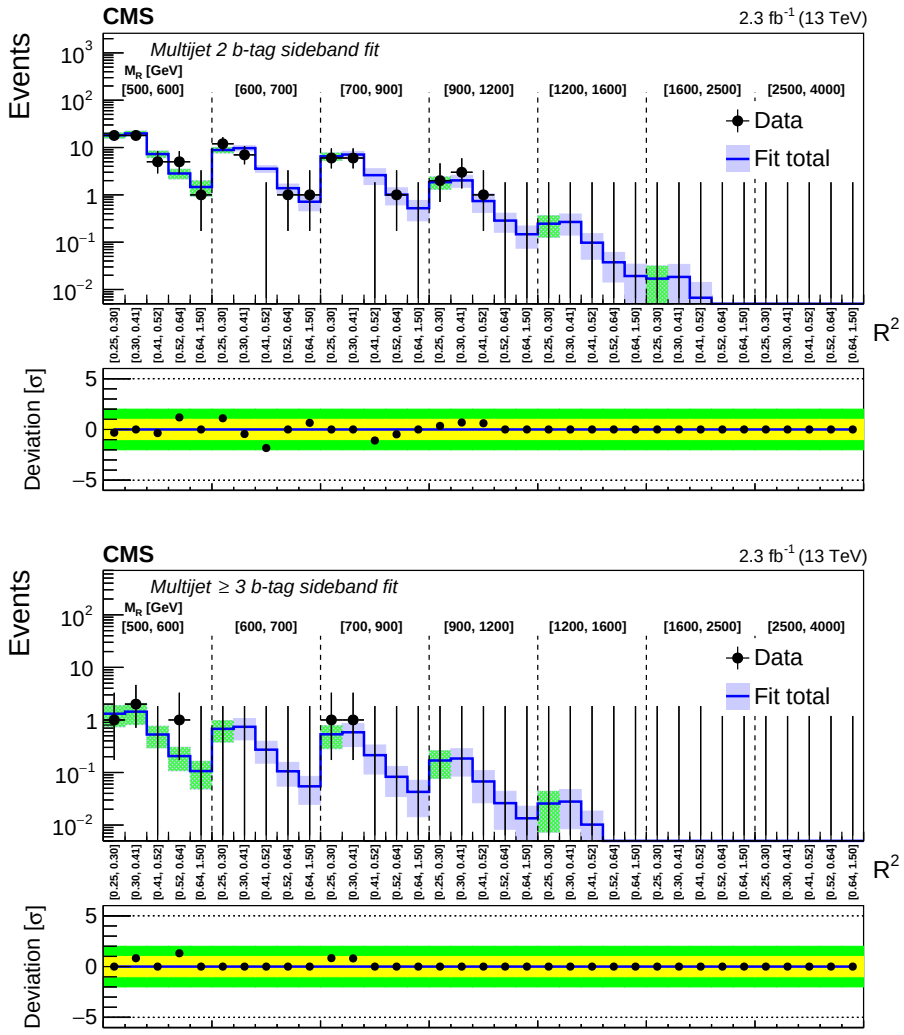

Figure 8.8: Comparison of the sideband fit background prediction with the observed data in bins of M_R and R^2 variables in the Multijet category for the 2 b-tag (upper) and ≥ 3 b-tag (lower) bins [227, 44]. Vertical dashed lines denote the boundaries of different M_R bins. On the upper panels, the colored bands represent the systematic uncertainties in the background prediction, and the uncertainty bands for the sideband bins are shown in green. On the bottom panels, the deviations between the observed data and the background prediction are plotted in units of standard deviation (σ), taking into account both statistical and systematic uncertainties. The green and yellow horizontal bands show the boundaries of 1 and 2 σ.

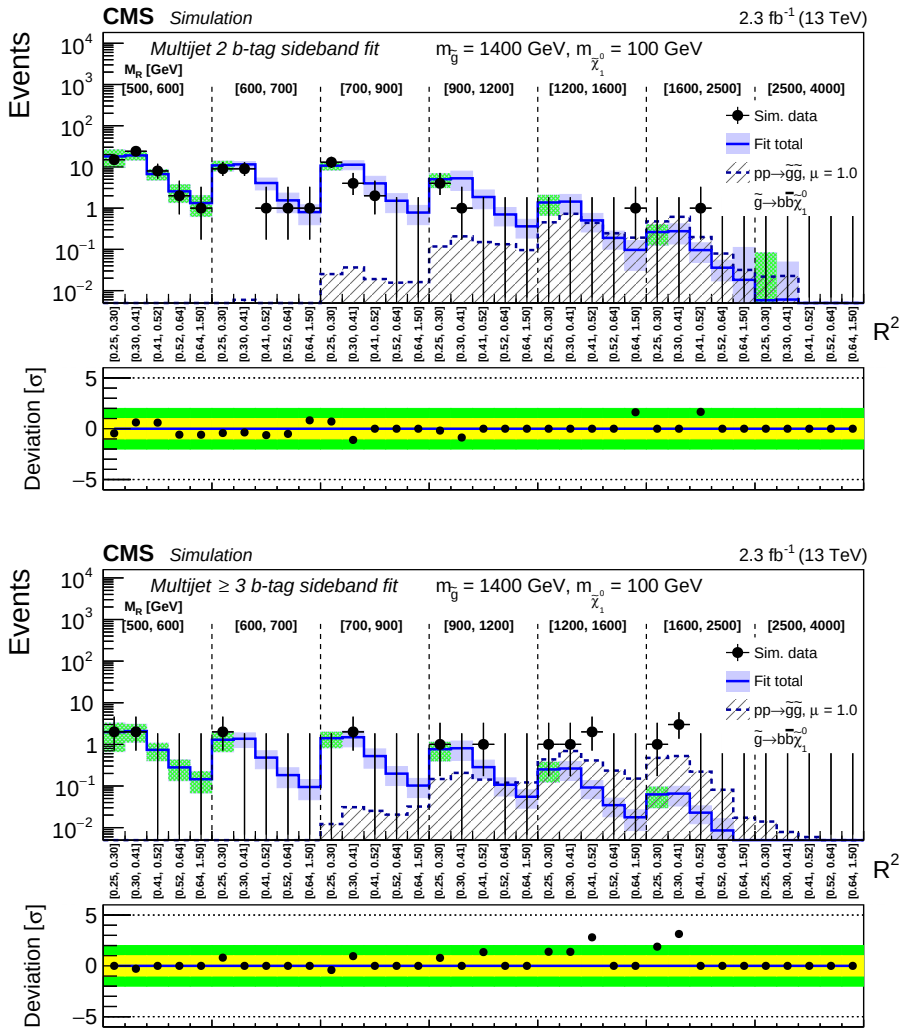

Figure 8.9: The result of the background-only fit performed in the sideband of the 2 b-tag (upper) and ≥ 3 b-tag (lower) bins of the Multijet category on a signal-plus-background pseudodata set assuming a gluino pair production simplified model signal, where gluinos decay with a 100% branching fraction to a $b\bar{b}$ pair and the LSP, with $m_{\tilde{g}} = 1.4\,\text{TeV}$ and $m_{\tilde{\chi}_1^0} = 100\,\text{GeV}$, at nominal signal strength [227, 44]. A detailed explanation of the figure format is given in the caption of Fig. 8.8.

perform a background-only fit in the sideband. We show one illustrative example of such a test in Fig. 8.9, where we inject a signal corresponding to gluino pair production, in which each gluino decays to a neutralino and a $b\bar{b}$ pair with $m_{\tilde{g}} = 1.4\,\text{TeV}$ and $m_{\tilde{\chi}_1^0} = 100\,\text{GeV}$. The deviations with respect to the fit predictions are shown for the 2 b-tag and ≥ 3 b-tag Multijet categories. We observe characteristic patterns of excesses in two adjacent groups of bins neighboring in M_R.

For completeness, in Figs. 8.10-8.14, we present the results of the search for SUSY signal events in the remaining categories, namely the 0 b-tag and 1 b-tag bins of the Multijet category, the four b-tag bins of the Muon Multijet category, and the four b-tag bins of the Electron Multijet category. No statistically significant deviations from the expected background predictions are observed in these categories in data.

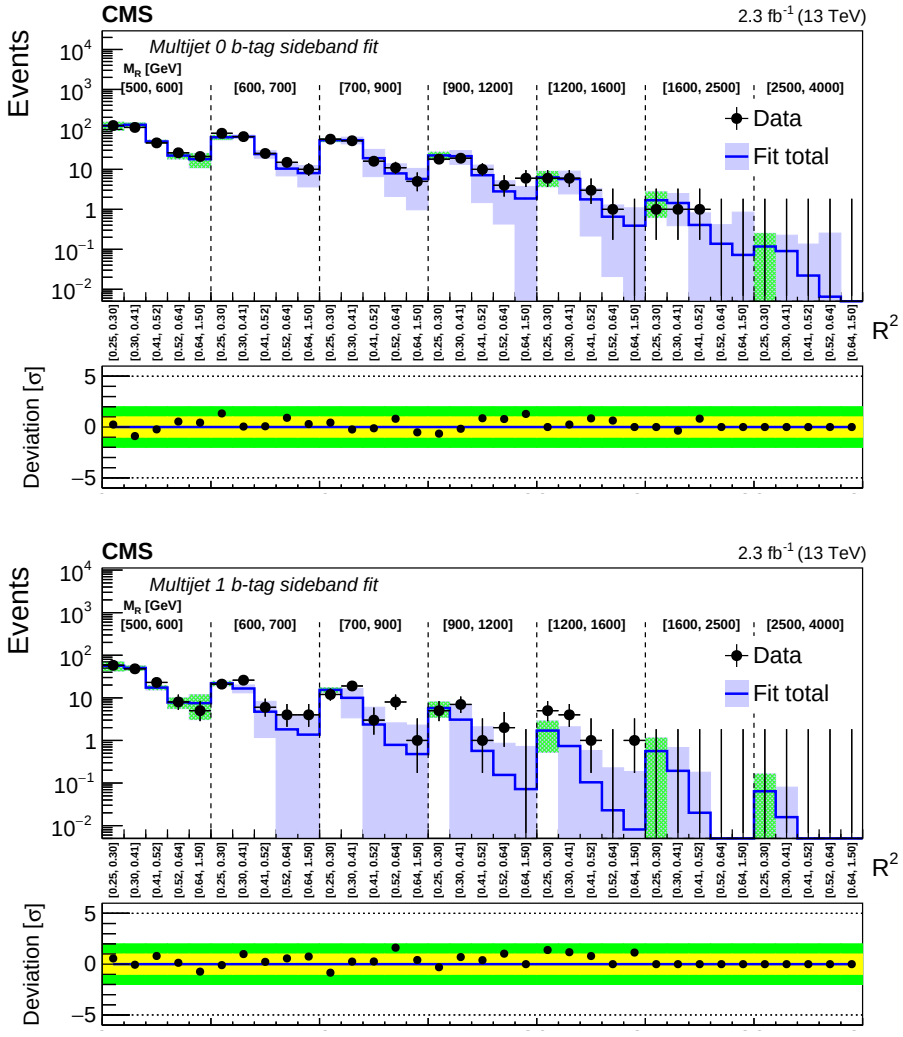

Figure 8.10: Comparison of the predicted background with the observed data in bins of M_R and R^2 variables in the Multijet category for the 0 b-tag (upper) and 1 b-tag (lower) bins [227, 44]. A detailed explanation of the panels is given in the caption of Fig. 8.8.

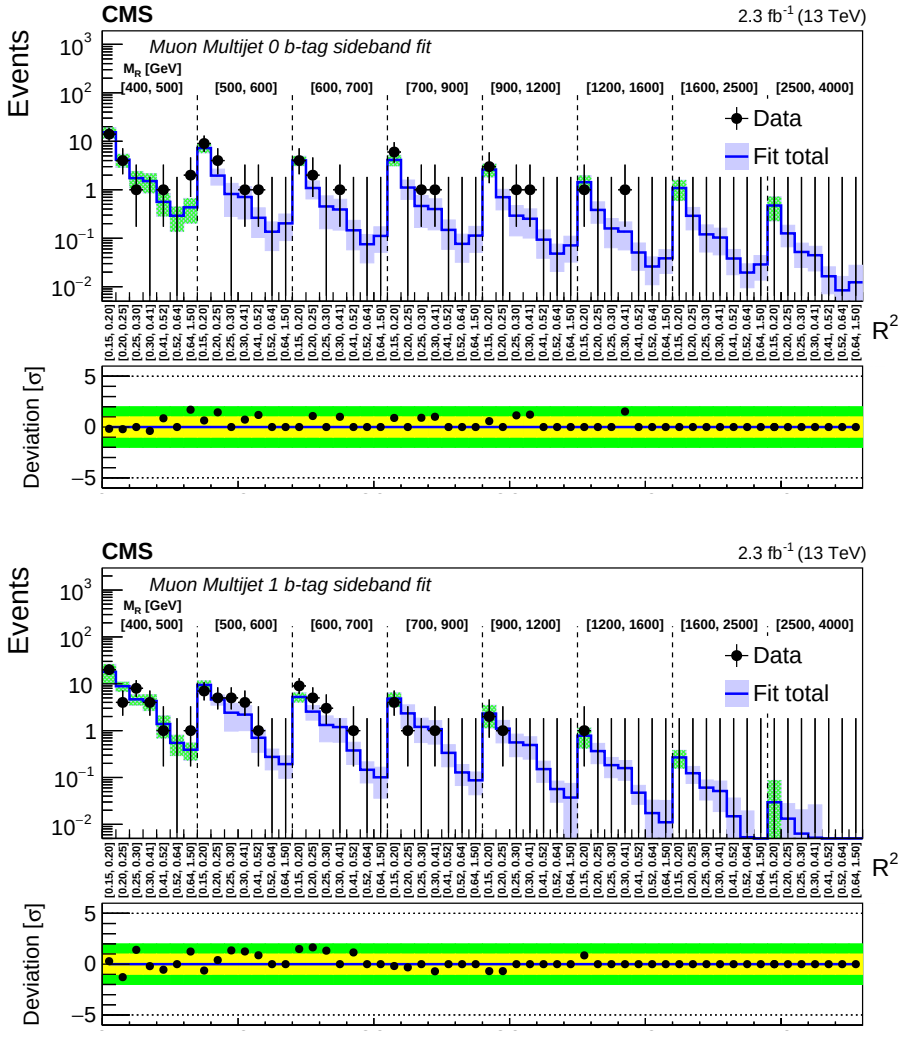

Figure 8.11: Comparison of the predicted background with the observed data in bins of M_R and R^2 variables in the Muon Multijet category for the 0 b-tag (upper) and 1 b-tag (lower) bins [227, 44]. A detailed explanation of the panels is given in the caption of Fig. 8.8.

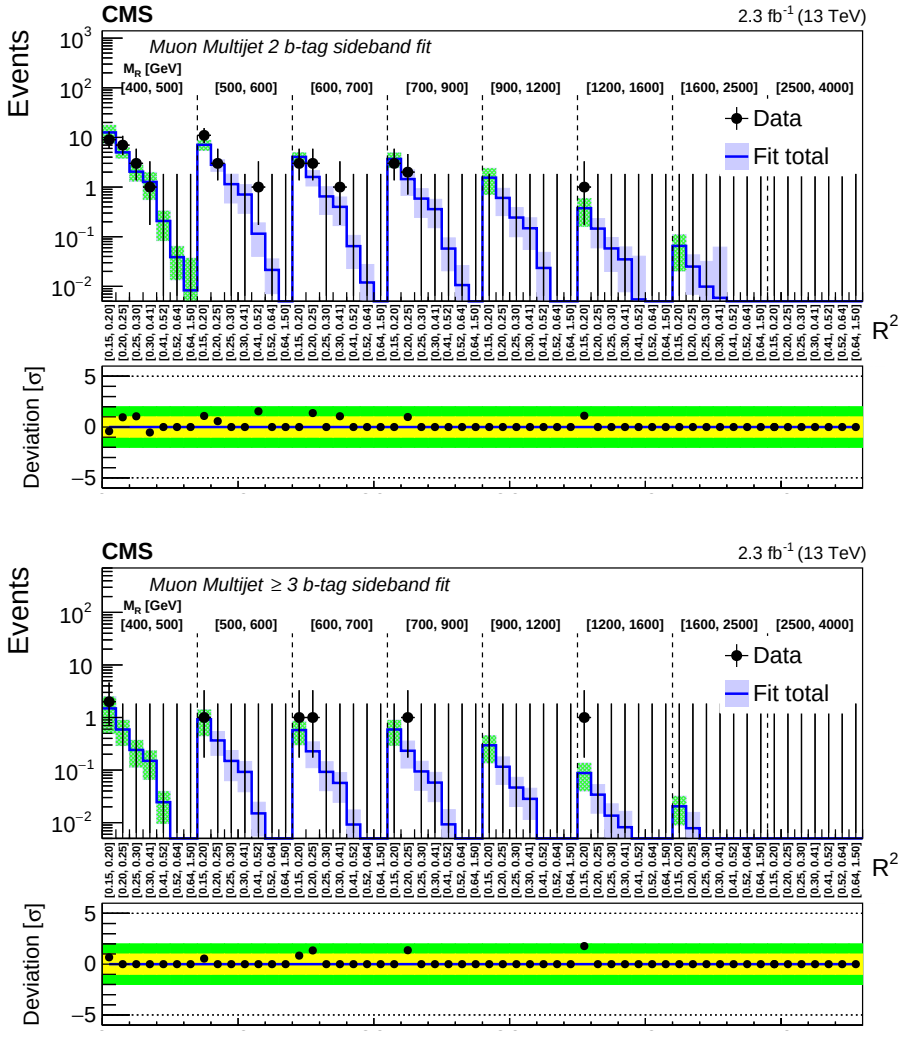

Figure 8.12: Comparison of the predicted background with the observed data in bins of M_R and R^2 variables in the Muon Multijet category for the 2 b-tag (upper) and $\geq$ 3 b-tag (lower) bins [227, 44]. A detailed explanation of the panels is given in the caption of Fig. 8.8.

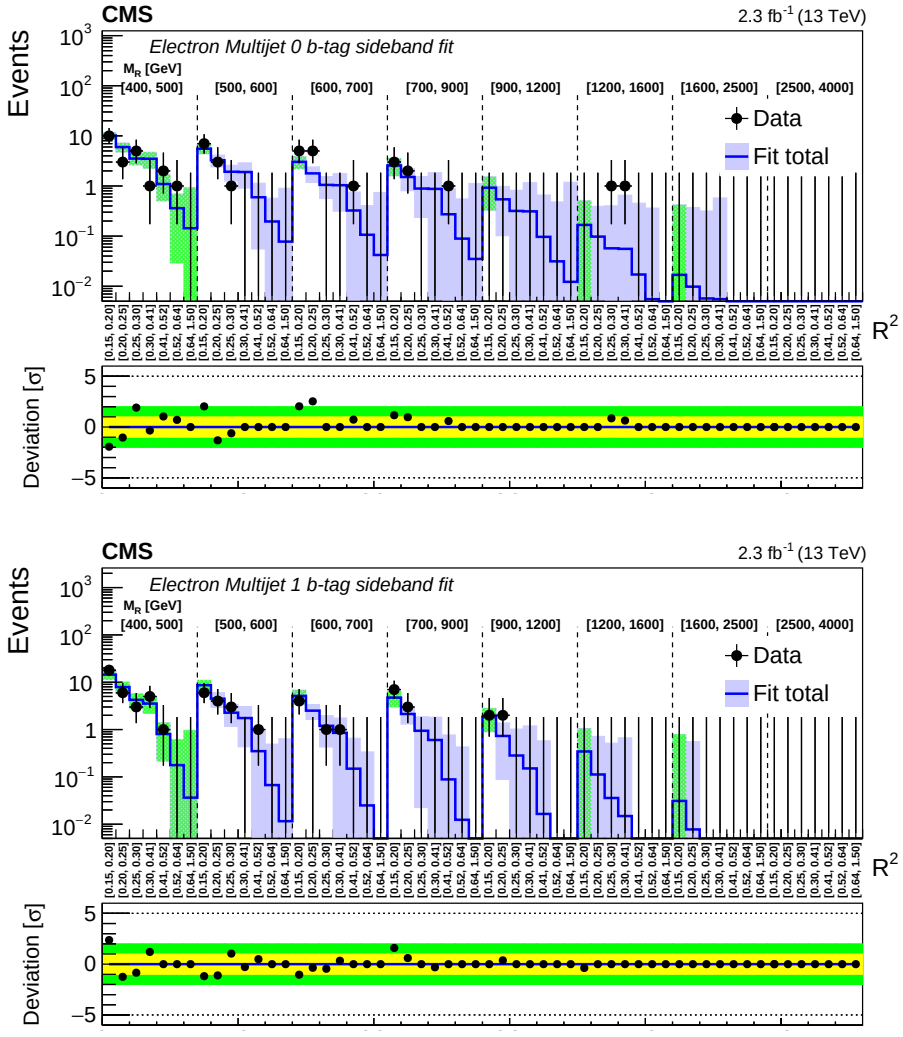

Figure 8.13: Comparison of the predicted background with the observed data in bins of M_R and R^2 variables in the Electron Multijet category for the 0 b-tag (upper) and 1 b-tag (lower) bins [227, 44]. A detailed explanation of the panels is given in the caption of Fig. 8.8.

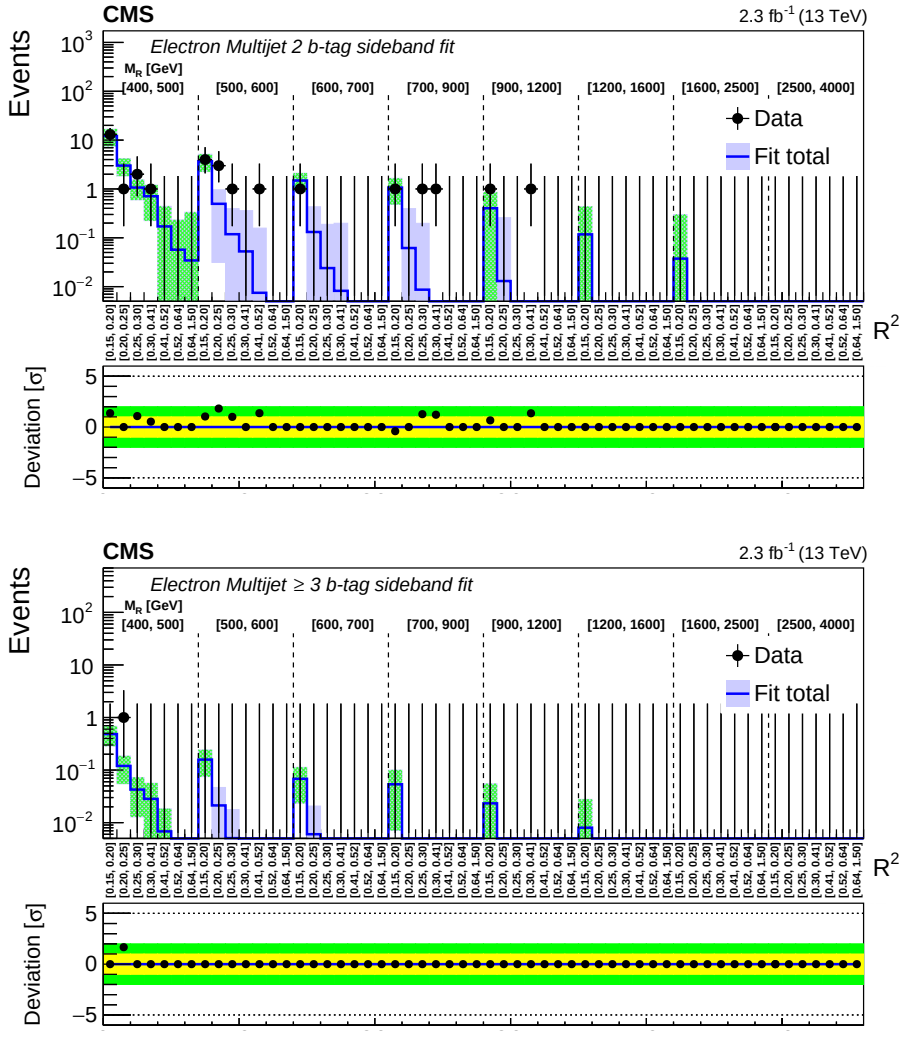

Figure 8.14: Comparison of the predicted background with the observed data in bins of M_R and R^2 variables in the Electron Multijet category for the 2 b-tag (upper) and ≥ 3 b-tag (lower) bins [227, 44]. A detailed explanation of the panels is given in the caption of Fig. 8.8.

Comparison of the two methods

The background predictions obtained from methods A and B are systematically compared in all of the search region categories. For method B, the model-independent fit to the sideband is used for this comparison. In Fig. 8.15, we show the comparison of the two background predictions for two example event categories. The predictions from the two methods agree within the uncertainties of each method. The uncertainty from the fit-based method tends to be slightly larger at high M_R and R^2 due to the additional uncertainty in the exact shape of the tail of the distribution, as the n and b parameters are not strongly constrained by the sideband data.

The two background predictions use methods based on data that make very different systematic assumptions. Method A assumes that corrections to the simulation prediction measured in control regions apply also to the signal regions, while method B assumes that the shape of the background distribution in M_R and R^2 is well described by a particular exponentially falling functional form. The agreement observed between predictions obtained using these two very different methods significantly enhances the confidence of the background modeling, and also validates the respective assumptions.

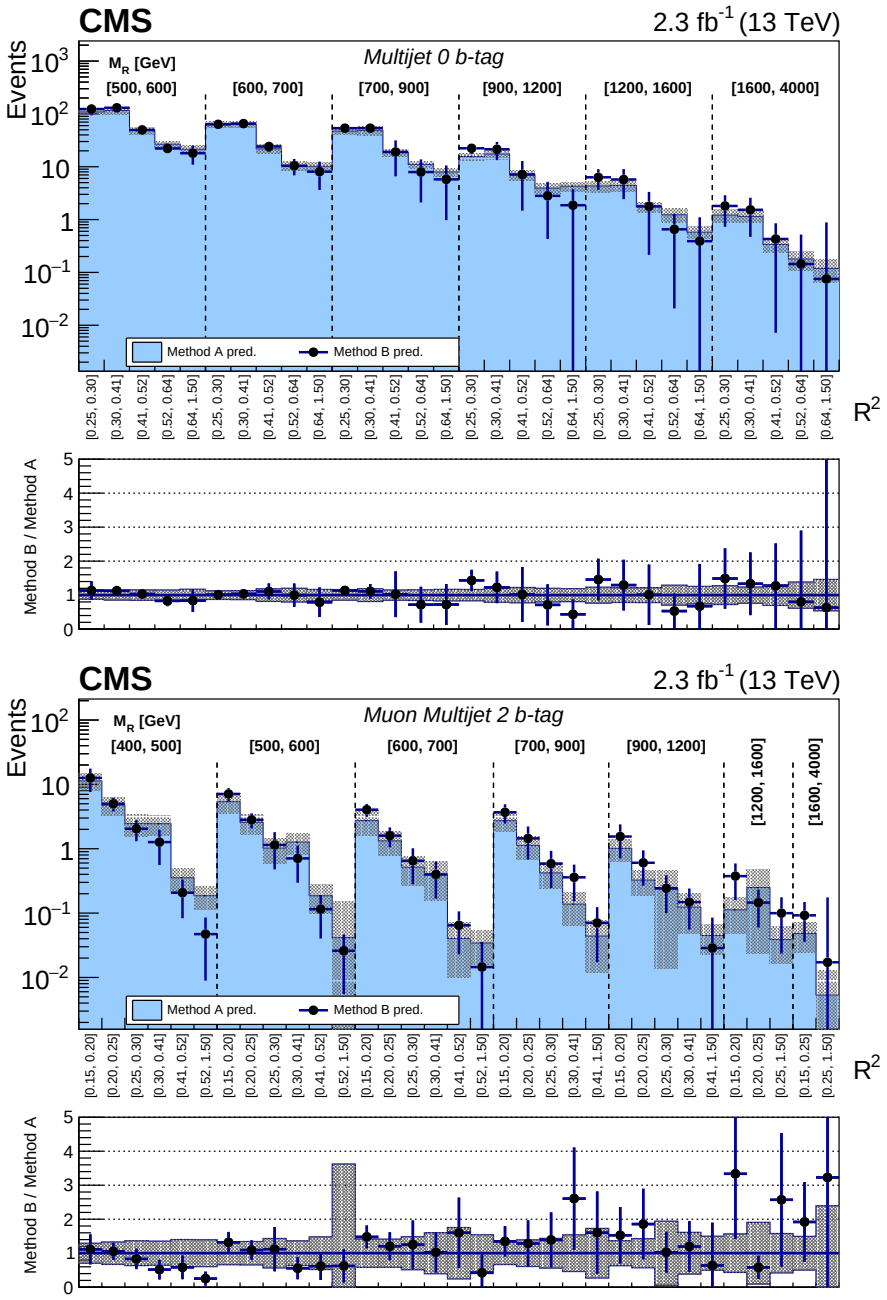

Figure 8.15: Comparisons of the two alternative background predictions for the (M_R,R^2) distribution for the 0 b-tag bin of the Multijet category (upper) and the 2 b-tag bin of the Muon Multijet category (lower) [227]. The two-dimensional (M_R,R^2) distribution is shown in a one-dimensional representation, with each M_R bin marked by the dashed lines and labeled near the top and each R^2 bin labeled below. The ratios of the method B fit-based predictions to the method A simulation-assisted predictions are shown on the bottom panels. The method B uncertainty is represented by the error bars on the data points and the method A uncertainty is represented by the shaded region.

8.5 Systematic uncertainties

Various systematic uncertainties are considered in the evaluation of the signal and background predictions. Different types of systematic uncertainties are considered for the two different background models.

For method A, the largest uncertainties arise from the precision with which the MC corrections are measured. The dominant uncertainties in the correction factors result from statistical uncertainties due to the limited size of the control region event sample. We also propagate systematic uncertainties in the theoretical cross-section for the small residual backgrounds present in the control regions, and they contribute $2-5\%$ to the correction factor uncertainty. Additional systematic uncertainties are computed from the procedure that tests that the accuracy of the MC corrections as a function of (M_R, R^2), and the number of b-tagged jets in events with four or more jets. The total uncertainty from this procedure ranges from 10% for the most populated bins to 50% and 100% for the least populated bins. For the $Z \to \nu\bar{\nu}$ process, we also propagate the difference in the correction factors measured in the three alternative control regions as a systematic uncertainty, intended to estimate the possible differences in the simulation mismodeling of the hadronic recoil for the γ+jets process and the $Z(\nu\bar{\nu})$+jets process. These systematic uncertainties range from 10 to 40%. For the QCD multijet background prediction the statistical uncertainty due to limited event counts in the $\Delta\phi_R > 2.8$ control regions and the systematic uncertainty of 87% in the translation factor ζ are propagated.

For method B, the systematic uncertainties in the background are propagated as part of the maximum likelihood fit procedure. For each event category, the background shape in M_R and R^2 is described by four independent parameters: two that control the exponential fall off and two that control the behavior of the nonexponential tail. Systematic uncertainties in the background are propagated through the freedom of these unconstrained shape parameters in the fit model. For more populated bins, such as the 0 b-tag and 1 b-tag bins in the Multijet category, the systematic uncertainties range from about 30% at low M_R and R^2 to about 70% at high M_R and R^2. For sparsely populated bins such as the 3-or-more b-tag bin in the Muon Multijet or Electron Multijet categories, the systematic uncertainties range from about 60% at low M_R and R^2 to more than 200% at high M_R and R^2.

Table 8.1: Summary of the main instrumental and theoretical systematic uncertainties. The systematic uncertainty associated to the modeling of the initial-state radition is only applied for events with recoil above 400 GeV.

Source	On signal and/or bkg	Typical values [%]
Jet energy scale	Both	$2-15$
Electron energy scale	Both	$7-9$
Muon momentum scale	Both	$7-9$
Muon efficiency	Both	$7-8$
Electron efficiency	Both	$7-8$
Trigger efficiency	Both	3
b-tagging efficiency	Both	$6-15$
b mistagging efficiency	Both	$4-7$
Missing higher orders	Both	$10-25$
Integrated luminosity	Both	2.7
Fast simulation corrections	Signal only	$0-10$
Initial-state radiation	Signal only	$15-30$

Systematic uncertainties due to instrumental and theoretical effects are propagated as shape uncertainties in the signal predictions for methods A and B, and on the background predictions for method A. The background prediction from method B is not affected by these uncertainties as the shape and normalization are measured from data. Uncertainties in the trigger and lepton selection efficiency, and the integrated luminosity [228] primarily affect the total normalization. Uncertainties in the b-tagging efficiency affect the relative yields between different b-tag categories. The uncertainties from missing higher-order corrections and the uncertainties in the jet energy and lepton momentum scale affect the shapes of the M_R and R^2 distributions.

For the signal predictions, we also propagate systematic uncertainties due to possible inaccuracies of the fast simulation in modeling the lepton selection and b tagging efficiencies. These uncertainties were evaluated by comparing the $t\bar{t}$ and signal GEANT based MC samples with those that used fast simulation. Finally, we propagate an uncertainty in the modeling of initial-state radiation for signal predictions, that ranges from 15% for signal events with recoil between 400 and 600 GeV to 30% for events with recoil above 600 GeV. The systematic uncertainties and their typical impact on the background and signal predictions are summarized in Table 8.1.

8.6 Interpretation

We present results of the search using method A as it provides slightly better sensitivity. The two-dimensional (M_R,R^2) distributions for the search regions in the Multijet, Electron Multijet, and Muon Multijet categories observed in data are shown in Figures 8.16-8.21, along with the background prediction from method A. We observe no statistically significant discrepancies and interpret the null search result using method A by determining the 95% confidence level (CL) upper limits on the production cross sections of the SUSY models presented in Sec. 3.8 using a global likelihood determined by combining the likelihoods of the different search boxes and sidebands. Following the LHC CL_s procedure [184] precisely defined in Sec. 7.5, we use the profile likelihood ratio test statistic and the asymptotic formula to evaluate the 95% CL observed and expected limits on the SUSY cross section $\sigma_{\text{NLO+NLL}}$. Systematic uncertainties are taken into account by incorporating nuisance parameters $\boldsymbol{\theta}$, representing different sources of systematic uncertainty, into the likelihood function $\mathcal{L}(\text{data}|\mu, \boldsymbol{\theta})$. For each signal model the simulated SUSY events are used to estimate the effect of possible signal contamination in the analysis control regions, and the method A background prediction is corrected accordingly. As before, the template probability density for the signal, normalized to unit probability, is multiplied by $\mu\sigma_{\text{NLO+NLL}}L\epsilon^{\text{box}}_{\text{b-tag}}$, where μ is the signal strength parameter, $\sigma_{\text{NLO+NLL}}$ is the SUSY signal cross section, L is the integrated luminosity corresponding to the size of the data set, and $\epsilon^{\text{box}}_{\text{b-tag}}$ is the signal selection efficiency for a given category and b-tagged jet multiplicity. To determine a confidence interval for μ, we construct the profile likelihood ratio test statistic $\tilde{q}_\mu$ of Eqn. 7.14 as a function of μ. Then for example, a 68% confidence interval for μ can be taken as the region for which the test statistic is less than 1. By allowing each nuisance parameter to vary, the test statistic curve is wider, reflecting the systematic uncertainty arising from each source, and resulting in a larger confidence interval for μ.

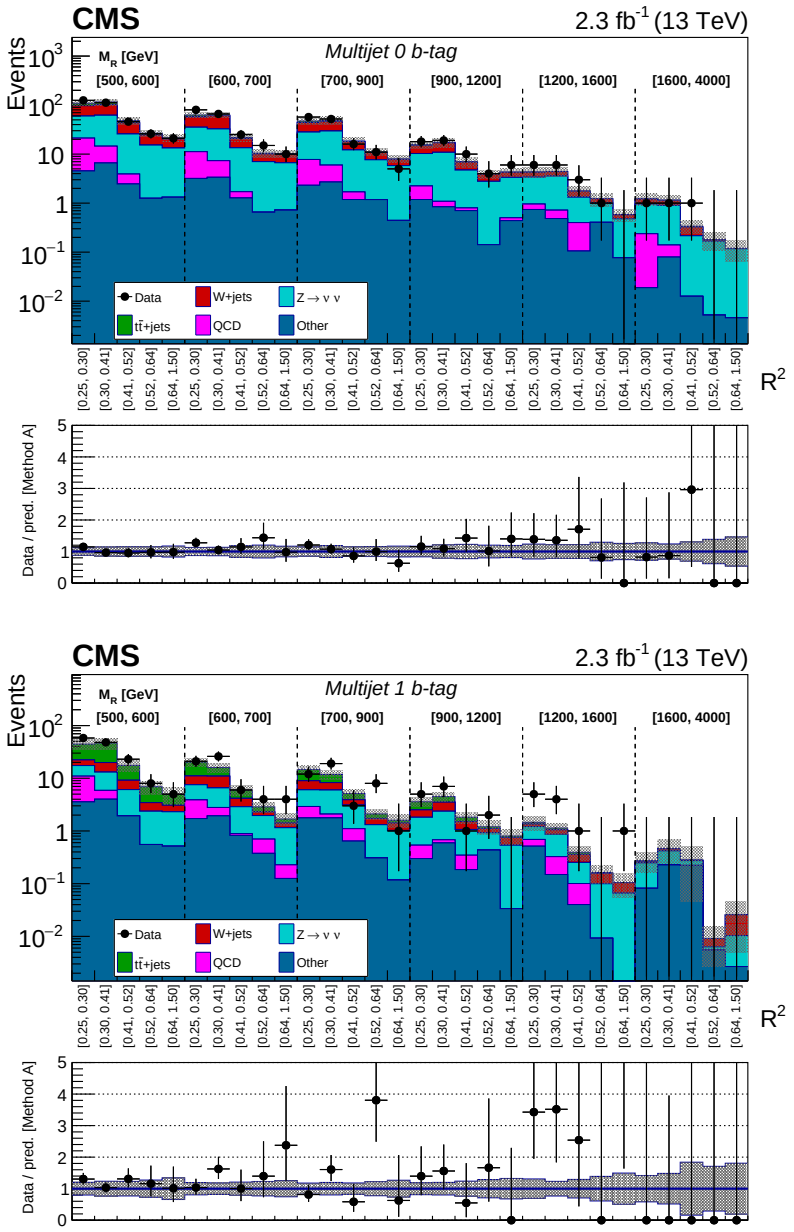

Figure 8.16: The (M_R,R^2) distribution observed in data is shown along with the background prediction obtained from method A for the Multijet event category in the 0 b-tag (upper) and 1 b-tag (lower) bins [227]. The two-dimensional (M_R,R^2) distribution is shown in a one-dimensional representation, with each M_R bin marked by the dashed lines and labeled near the top, and each R^2 bin labeled below. The ratio of data to the background prediction is shown on the bottom panels, with the statistical uncertainty expressed through the data point error bars and the systematic uncertainty of the background prediction represented by the shaded region.

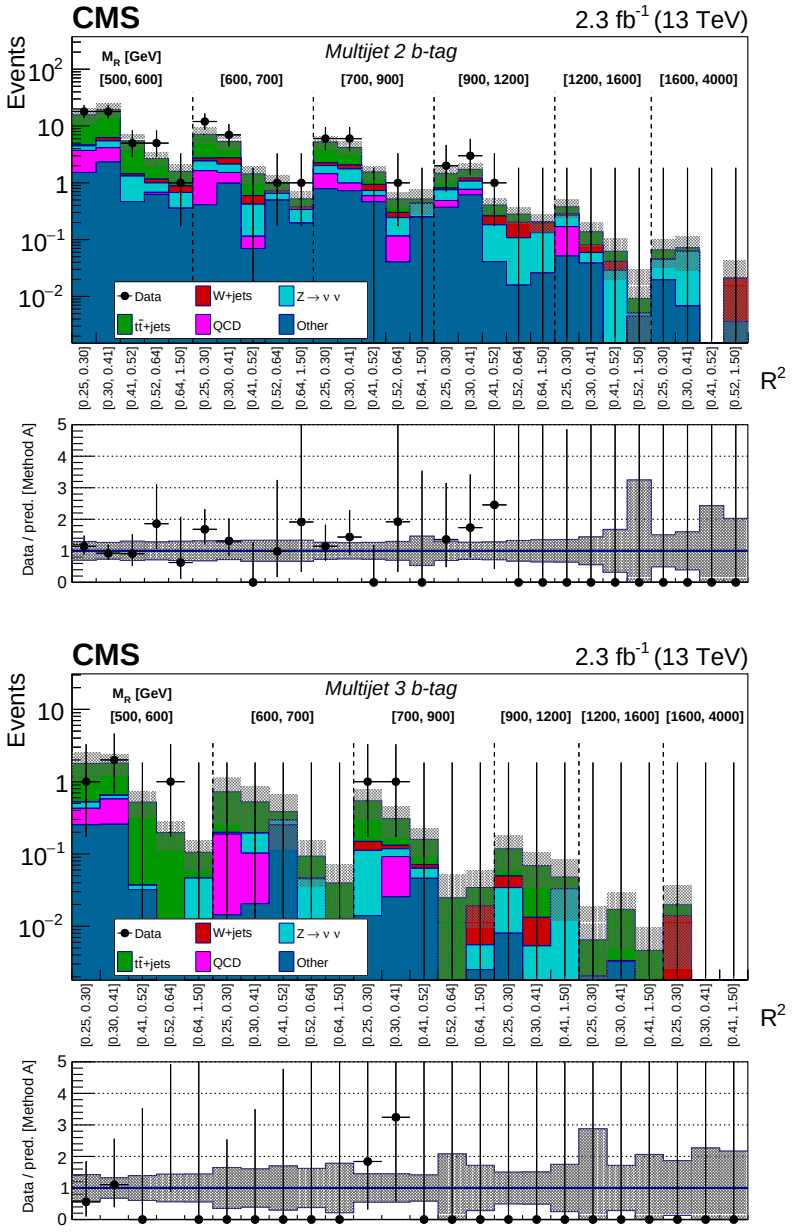

Figure 8.17: The (M_R,R^2) distribution observed in data is shown along with the background prediction obtained from method A for the Multijet event category in the 2 b-tag (upper) and $\geq$ 3 b-tag (lower) bins [227]. A detailed explanation of the panels is given in the caption of Fig. 8.16.

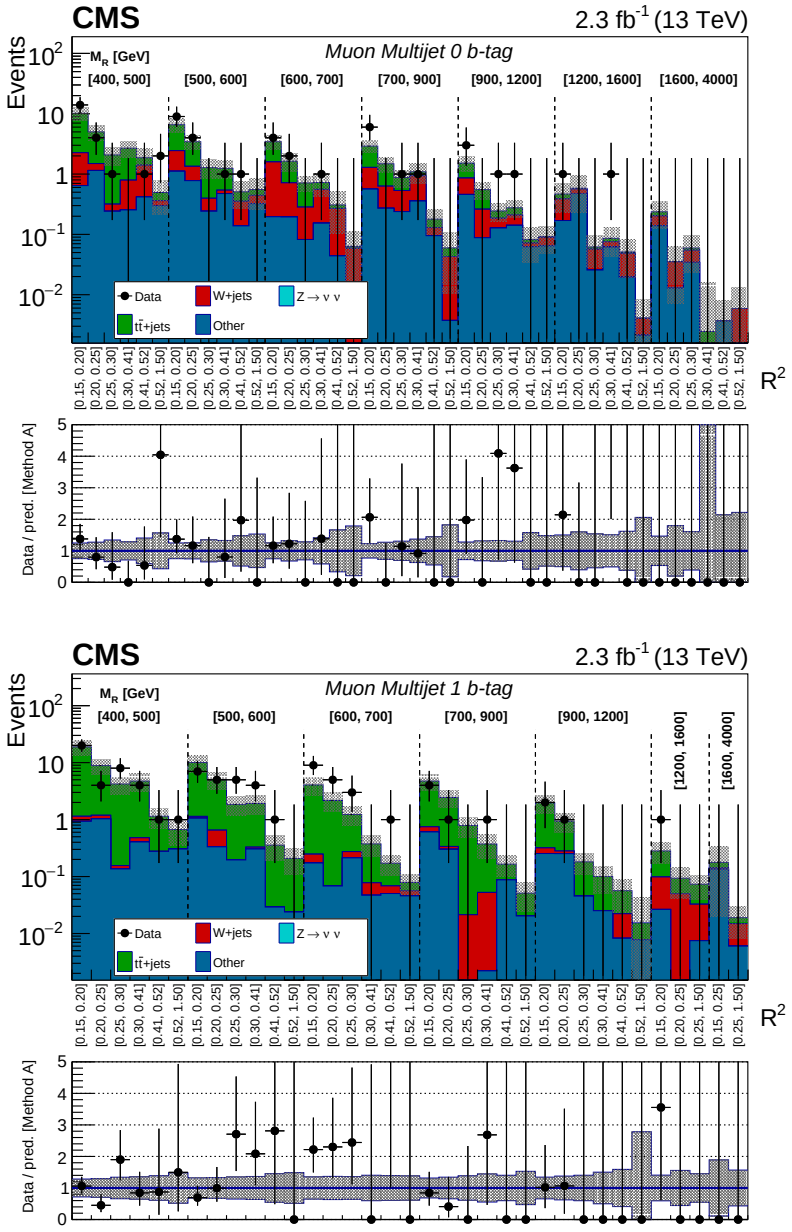

Figure 8.18: The (M_R,R^2) distribution observed in data is shown along with the background prediction obtained from method A for the Muon Multijet event category in the 0 b-tag (upper) and 1 b-tag (lower) bins [227]. A detailed explanation of the panels is given in the caption of Fig. 8.16.

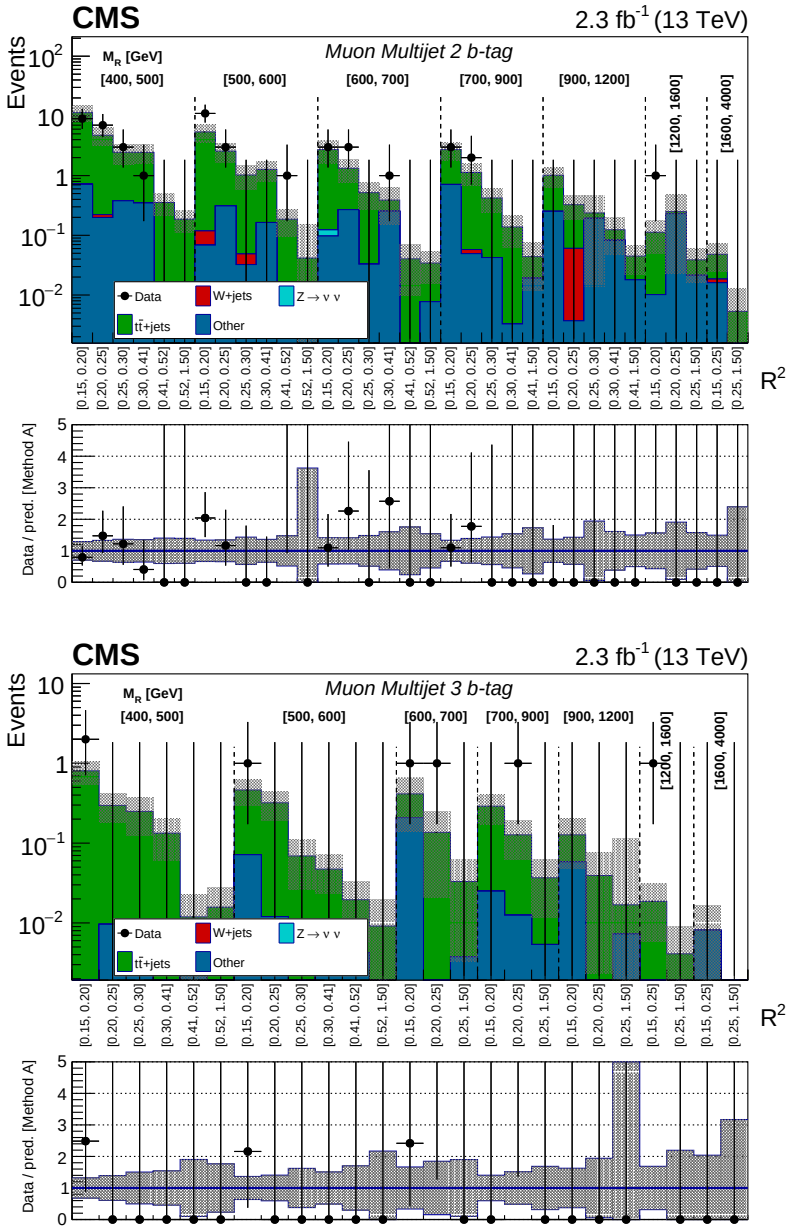

Figure 8.19: The (M_R,R^2) distribution observed in data is shown along with the background prediction obtained from method A for the Muon Multijet event category in the 2 b-tag (upper) and $\geq$ 3 b-tag (lower) bins [227]. A detailed explanation of the panels is given in the caption of Fig. 8.16.

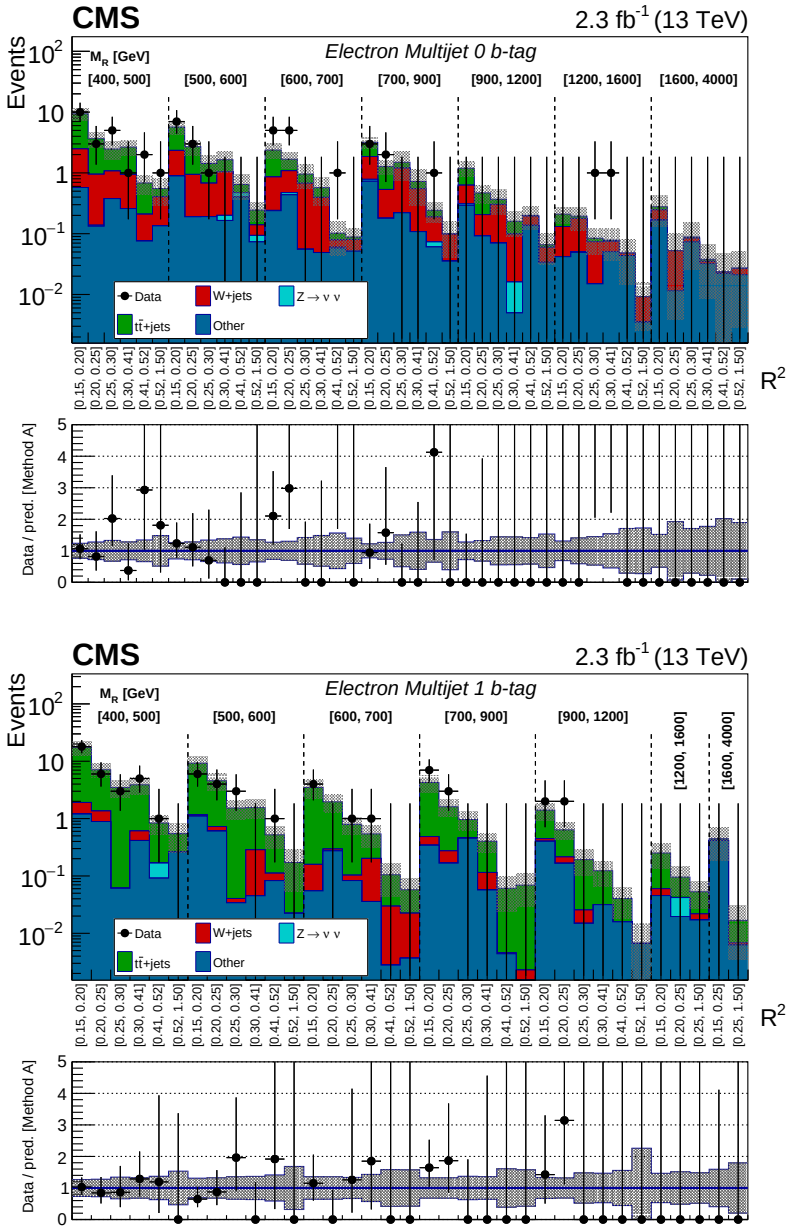

Figure 8.20: The (M_R,R^2) distribution observed in data is shown along with the background prediction obtained from method A for the Electron Multijet event category in the 0 b-tag (upper) and 1 b-tag (lower) bins. A detailed explanation of the panels is given in the caption of Fig. 8.16.

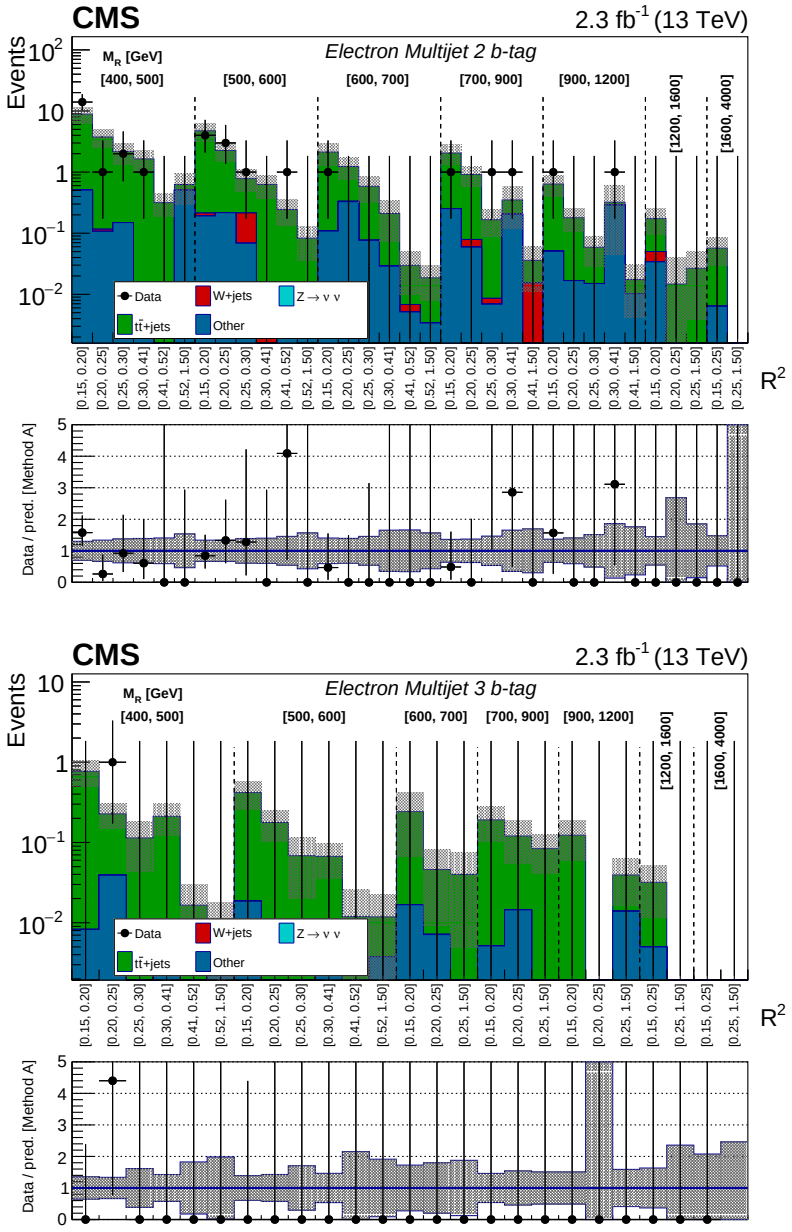

Figure 8.21: The (M_R,R^2) distribution observed in data is shown along with the background prediction obtained from method A for the Electron Multijet event category in the 2 b-tag (upper) and $\geq$ 3 b-tag (lower) bins [227]. A detailed explanation of the panels is given in the caption of Fig. 8.16.

First, we consider the scenario of gluino pair production decaying to third-generation quarks. Gluino decays to the third-generation are enhanced if the masses of the third-generation squarks are significantly lighter than those of the first two generations, a scenario that is strongly motivated in natural SUSY models [74, 119, 229, 230] discussed in Sec. 3.8. Prompted by this, we consider the three decay modes:

- $\tilde{g} \to b\bar{b}\tilde{\chi}^0$;
- $\tilde{g} \to t\bar{t}\tilde{\chi}^0$;
- $\tilde{g} \to b\bar{t}\tilde{\chi}_1^+ \to b\bar{t}W^{*+}\tilde{\chi}_1^0$ or charge conjugate,

where W^* denotes a virtual W boson. Due to a technical limitation inherent in the event generator, we consider these three decay modes for $|m_{\tilde{g}} - m_{\tilde{\chi}_1^0}| \geq 225\,\text{GeV}$. For $|m_{\tilde{g}} - m_{\tilde{\chi}_1^0}| < 225\,\text{GeV}$, we only consider the $\tilde{g} \to b\bar{b}\tilde{\chi}^0$ decay mode.

We perform a scan over all possible branching fractions to these three decay modes and compute limits on the production cross section under each such scenario. The production cross section limits for a few characteristic branching fraction scan points are shown on the left of Fig. 8.22 as a function of the gluino and neutralino masses. We find a range of excluded regions for different branching fraction assumptions and generally observe the strongest limits for the $\tilde{g} \to b\bar{b}\tilde{\chi}_1^0$ decay mode over the full two-dimensional mass plane and the weakest limits for the $\tilde{g} \to t\bar{t}\tilde{\chi}_1^0$ decay mode. For scenarios that include the intermediate decay $\tilde{\chi}_1^\pm \to W^{*\pm}\tilde{\chi}_1^0$ and small values of $m_{\tilde{\chi}_1^0}$ the sensitivity is reduced because the LSP carries very little momentum in both the NLSP rest frame and the laboratory frame, resulting in small values of E_T^{miss} and R^2. By considering the most conservative limit obtained for all scanned branching fractions, we calculate an exclusion limit valid for any assumption on the branching fractions, presented on the right of Fig. 8.22. For an LSP with mass of a few hundred GeV, we exclude pair production of gluinos decaying to third-generation quarks for mass below about 1.6 TeV. This result is a unique attempt at deriving a branching fraction independent limit on gluino pair production at the LHC for the scenario in which gluino decays are dominated by three-body decays to third-generation quarks and a neutralino LSP.

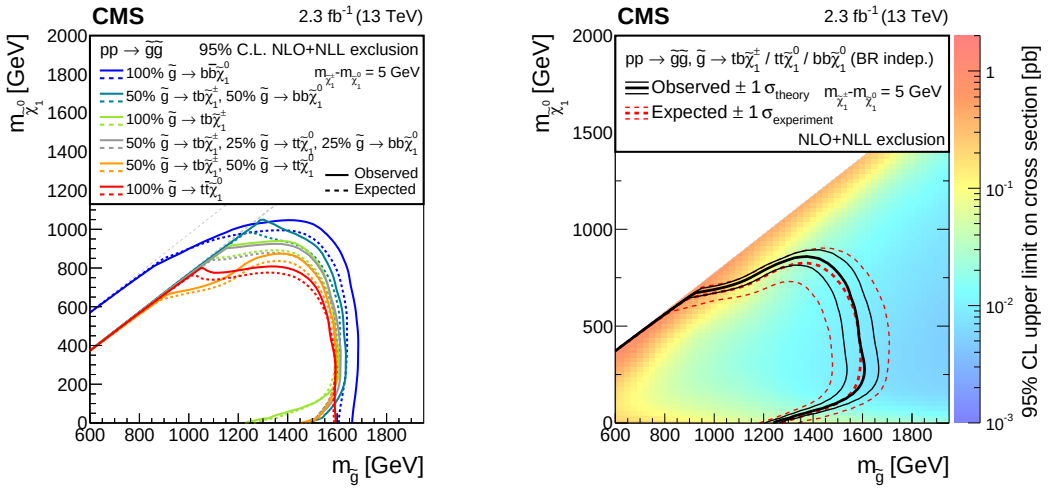

Figure 8.22: (Left) the expected and observed 95% confidence level (CL) upper limits on the production cross section for gluino pair production decaying to third-generation quarks under various assumptions of the branching fractions. The two gray dashed diagonal lines correspond to $|m_{\tilde{g}} - m_{\tilde{\chi}_1^0}| = 25\,\text{GeV}$, which is where the scan ends for the $\tilde{g} \to b\bar{b}\tilde{\chi}_1^0$ decay mode, and $|m_{\tilde{g}} - m_{\tilde{\chi}_1^0}| = 225\,\text{GeV}$, which is where the scan ends for the remaining modes due to a technical limitation inherent in the event generator. For $|m_{\tilde{g}} - m_{\tilde{\chi}_1^0}| < 225\,\text{GeV}$, we only consider the $\tilde{g} \to b\bar{b}\tilde{\chi}_1^0$ decay mode. (Right) the analogous upper limits on the gluino pair production cross section valid for any values of the gluino decay branching fractions [227].

In Fig. 8.23, we present additional interpretations for simplified model scenarios of interest. On the left, we show the production cross section limits on gluino pair production where the gluino decays to two light-flavored quarks and the LSP, and on the right we show the production cross section limits on top squark pair production where the top squark decays to a top quark and the LSP. For a very light LSP, we exclude top squark production with mass below 750 GeV.

8.7 Summary

We have presented an inclusive search for supersymmetry in events with no more than one lepton, a large multiplicity of energetic jets, and missing transverse energy. The search is sensitive to a broad range of SUSY scenarios including pair production of gluinos and top squarks. The event categorization in the number of leptons and the number of b-tagged jets enhances the search sensitivity for a variety of different SUSY signal scenar-

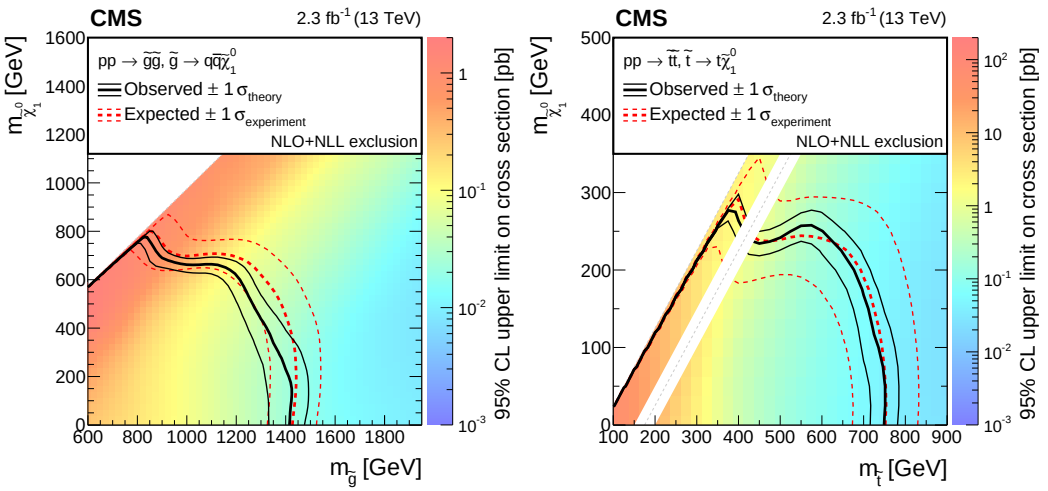

Figure 8.23: Expected and observed 95% confidence level (CL) upper limits on the production cross section for (left) gluino pair production decaying to two light-flavored quarks and the LSP and (right) top squark pair production decaying to a top quark and the LSP. The white diagonal band in the right plot corresponds to the region $|m_{\tilde{t}} - m_t - m_{\tilde{\chi}_1^0}| < 25\,\text{GeV}$, where the signal efficiency is a strong function of $m_{\tilde{t}} - m_{\tilde{\chi}_1^0}$, and as a result the precise determination of the cross section upper limit is uncertain because of the finite granularity of the available MC samples in this region of the $(m_{\tilde{t}}, m_{\tilde{\chi}_1^0})$ plane [227].

ios. Two alternative background estimation methods are presented, both based on transfer factors between data control regions and the search regions, but having very different systematic assumptions: one relying on the simulation and associated corrections derived in the control regions, and the other relying on the accuracy of an assumed functional form for the shape of background distribution in the M_R and R^2 variables. The two predictions agree within their uncertainties, thereby demonstrating the robustness of the background modeling.

No significant deviations from the predicted standard model background are observed in any of the search regions, and this result is interpreted in the context of simplified models of gluino or top squark pair production. For decays to a top quark and an LSP with a mass of 100 GeV, we exclude top squarks with masses below 750 GeV. Considering separately the decays to bottom quarks and the LSP or first- and second-generation quarks and the LSP, gluino masses up to 1.65 TeV or 1.4 TeV are excluded, respectively. Furthermore, this search goes beyond the existing simplified model paradigm

by interpreting results in a broader context inspired by natural SUSY, with multiple gluino decay modes considered simultaneously. By scanning over all possible branching fractions for three-body gluino decays to third generation quarks, exclusion limits are derived on gluino pair production that are valid for any values of the gluino decay branching fractions. For a chargino NLSP nearly degenerate in mass with the LSP and LSP masses in the range between 200 and 600 GeV, we exclude gluinos with mass below 1.55 to 1.6 TeV, regardless of their decays. This result is a more generic constraint on gluino production than previously reported at the LHC.

8.8 LHC coverage of natural supersymmetry

Although the results of the Ch. 7 and 8 represent the most generic constaints on the gluino and top squark from the LHC in terms of constraining multiple decay modes simultaneously, more stringent constraints for particular decay modes have been derived. Fig. 8.24 shows the most stringent limits on the gluino and top squark from ATLAS and CMS using 13 TeV data collected in 2016.

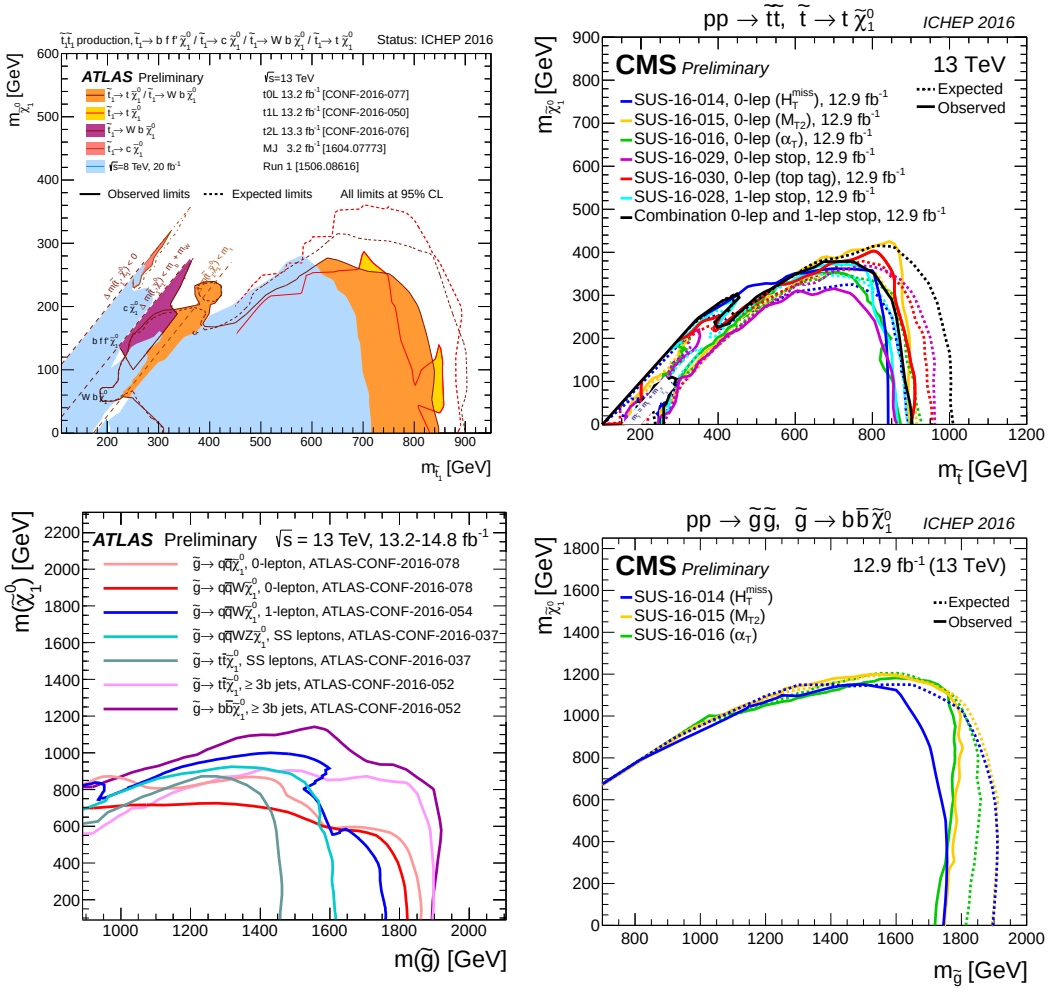

Figure 8.24: ATLAS (left) and CMS (right) 13 TeV limits presented at ICHEP 2016 for top squark (top) and gluino (bottom) pair production.

Part IV

Beyond the LHC: calorimeters with precision timing

Chapter 9

FAST TIMING FOR THE HIGH-LUMINOSITY LHC

To significantly extend the discovery reach of colliders to natural SUSY, it is necessary to go to higher energies and higher luminosities. Studies based on current search strategies [231, 232], project discovery-level sensitivity up to $\sim$ 2 TeV gluinos and $\sim$ 1 TeV top squarks for an integrated luminosity of 3000 fb^{-1} at an upgraded high-luminosity LHC (HL-LHC) with $\sqrt{s} = 14$ TeV. In order to produce this enormous dataset, the HL-LHC [233] is expected to provide instantaneous luminosities of 5×10^{34} $\text{cm}^{-2}\text{s}^{-1}$. The enhanced data rates will provide the datasets necessary to perform precision measurements of the Higgs couplings, probe rare Higgs processes, study the scattering of longitudinally polarized W bosons, and search for physics beyond the SM.

The rate of simultaneous interactions per bunch crossing (known as pileup) is projected to reach an average of 140. The large amount of pileup increases the likelihood of confusion in the reconstruction of events of interest, due to the contamination from particles produced in different pileup interactions. The ability to discriminate between jets produced in the events of interests – especially those associated with the vector boson fusion processes – and jets produced by pileup interactions will be degraded, the missing transverse energy resolution will deteriorate, and several other physics objects performance metrics will suffer.

One way to mitigate pileup confusion effects, complementary to precision tracking methods, is to perform a time-of-arrival measurement associated with a particular layer of the calorimeter, allowing for a time assignment for both charged particles and photons. Such a measurement with a precision of about 20 to 30 ps, when unambiguously associated to the corresponding energy measurement, will significantly reduce the inclusion of pileup particles in the reconstruction of the event of interest given that the spread in collision time of pileup interactions is about 200 ps. The association of the time measurement to the energy measurement is crucial, leading to a prototype design that calls for the time and energy measurements to

be performed in the same active detector element. It is in this context that we study the possibility of measuring the time of arrival of particles with a calorimetric device.

We focus our studies on measurements of the time of flight using sampling calorimeters based on LYSO crystals. Due to its very high light yield ($\sim$ 30 K photons/ MeV) [234], and radiation tolerance [235, 236, 237, 238], LYSO is the active element of one of the options originally considered for the upgrade of the CMS detector for the HL-LHC [239].

In Fig. 9.1 we present a simplified illustration of the major time scales associated to the timing measurement using a monolithic crystal calorimeter. Upon entering the crystal the photon or electron travels at the speed of light, interacts, and begins to shower, producing scintillation light in the crystal. The time between the entry of the photon into the crystal and the first interaction is denoted by t_{I} and for high energy impinging particles it is the shower development time. The time associated with the conversion of the incident photon to scintillation light is denoted by t_{S}. The scintillation light travels from the point of interaction to the photodetector at the velocity $c/\hat{n}$, where $\hat{n}$ is the effective index of refraction of the crystal [240]. The time associated with the propagation of the scintillation light to the photodetector is denoted by t_{P}. Once the scintillation light reaches the photodetector, the photons are converted into an electrical signal. The time associated with this process is known as the photodetector signal transit time, t_{T}. Finally, the data acquisition (DAQ) system has a characteristic time constant t_{D}. Each of these time intervals will fluctuate or jitter on an event-by-event basis, contributing to the time resolution.

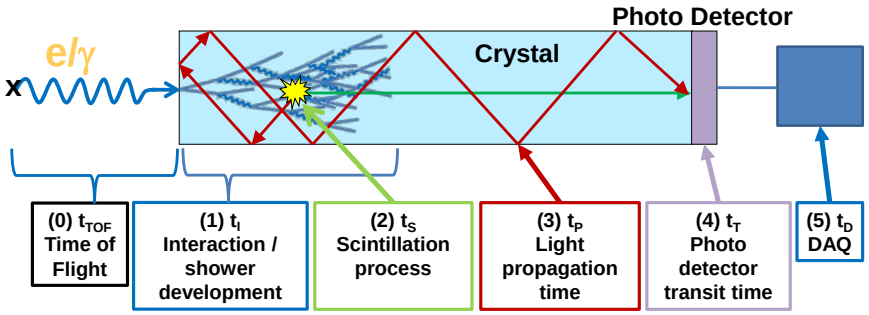

Figure 9.1: Timing measurement schematic breakdown using a monolithic, large scintillating crystal [241]. The incident particle impinges on the crystal face from the left. The characteristic time intervals are discussed in the text.

Previous studies [242], measured the time resolution at different absorber thickness for electron beams with energies varying from 12 to 32 GeV, and showed that the time of arrival of the front of an electromagnetic shower can be determined with a precision better than 20 ps. The electronic time resolution of the DAQ system was measured to be about 6 ps. Using the same techniques, we measure the time resolution of the MCP-PMT photodetectors used in the studies presented in this chapter to be between 11 ps and 14 ps, depending on the exact device.

To characterize the time resolution of an inorganic crystal scintillator calorimeter we study the contributions due to fluctuations in the shower development, scintillation process, and light propagation to the photodetector. We take advantage of the very large number of scintillation photons in a LYSO crystal which result in modest fluctuations associated with the creation and transit of each particular scintillation photon for a LYSO-based detector.

9.1 Experimental setup

A schematic diagram of a typical time of flight measurement setup is shown in Fig. 9.2. All measurements involve a fast photodetector, typically a micro-channel-plate photo-multiplier-tube (MCP-PMT) with a time resolution around 20-30 ps [242], which measures the reference (t_0) timestamp, and a photodetector further downstream that detects the signal associated with the electromagnetic shower and provides a simultaneous energy and time (t_1) measurement.

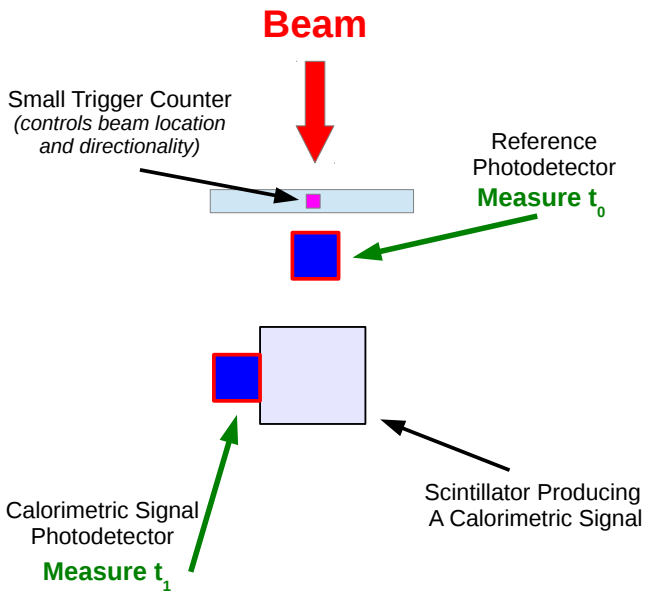

Figure 9.2: The basic schematic diagram of the experimental setup for a typical time of flight measurement is shown to illustrate the basic detector elements [241]. One photodetector is used as a time reference and the second measures energy and time simultaneously.

In our study we used two types of MCP-PMT photodetectors, one produced by Hamamatsu (model R3809-52) [243], and one produced by Photek (model PMT240) [244]. A DRS4 waveform digitizer V4 evaluation board [245] was used as the primary DAQ system, connected to a laptop via USB interface. The DRS chip contains a switched capacitor array (SCA) with 1024 cells, capable of digitizing eight analog signals with high speed (5 GSPS) and high accuracy (11.5 bit SNR). All experimental beam studies were performed at the Fermilab Test Beam Facility (FTBF), which provided proton beams from the Fermilab Main Injector accelerator at 120 GeV, and secondary electron beams of energies ranging from 4 to 32 GeV. All detector elements were placed inside of a dark box lined with copper foil, providing RF shielding. A 2×2 mm^2 scintillator was placed inside the box at the upstream extremity and used to trigger the DAQ readout, providing a strict constraint on the location and directionality of the beam particles used in the time of flight studies. A differential Čerenkov counter (not shown in

the schematic) provided by the FTBF facility and located upstream of our experimental hall, was used for electron identification.

9.2 Event selection and data analysis

Our primary goal is to reconstruct the time of flight of beam particles between different detector elements. Different time reconstruction algorithms are used for different detector elements, and all involve the assignment of a timestamp using specific features of each corresponding signal pulse. The signal pulse for the reference time detector is very sharp and symmetric around its maximum amplitude, as shown in Fig. 9.3. Thus for the reference detector we determine the time position of the pulse peak by fitting a Gaussian function to the peak of the pulse, using three sampling points before the pulse maximum and four sampling points after. The fitted mean parameter of the Gaussian function is assigned as the timestamp t_0. The signal pulse for the downstream time measurement is the result of scintillation light, and exhibits a fast rising edge and a significantly slower decay. Therefore, we assign the timestamp t_1 using a constant fraction of the rising edge. A linear function is fit to the sampling points between 10% and 60% of the pulse maximum and the timestamp is assigned as the time at which the fitted linear function rises to 20% of the pulse maximum. Examples of fits performed to assign a time stamp from each pulse are shown in Fig. 9.4. The impact from the choice of the functional forms is studied by using a set of alternative functions in the fits, and choosing the one that results in the best time resolution. Among the functions that we tested, the difference between the best and worst performing functions was about 8 ps.

Event selection and pulse cleaning procedures are used to eliminate abnormal pulses in the readout, as described in Ref. [242]. Large signals above 500 mV are rejected because they saturate the DRS4 inputs. Only pulses with amplitude larger than 20 mV are used for time of flight measurements, in order to reduce the impact of noise from the DRS waveform digitizer DAQ system. Events containing more than one pulse within the 200 ns readout window are not used. Attenuators were used to extend the dynamic range of the DRS4 waveform digitizer in cases when a large fraction of signal pulses are saturated.

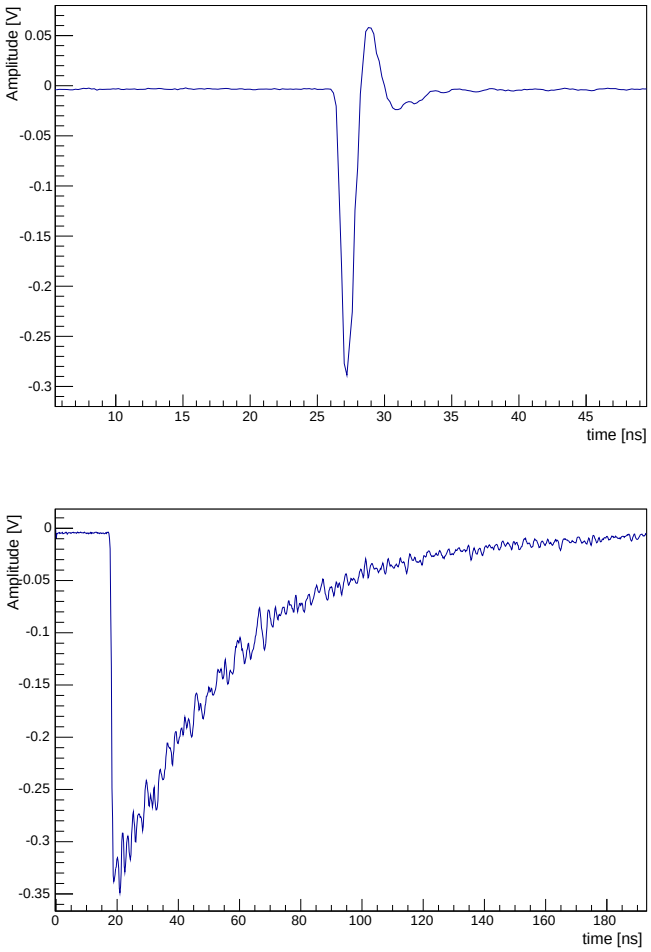

Figure 9.3: Sample pulses as digitized by the DRS4 board. Pulses are shown from the reference Hamamatsu R3809 MCP-PMT (top) and from the Hamamatsu R3809 MCP-PMT optically coupled to a $(1.7\,\mathrm{cm})^3$ LYSO crystal cube (bottom) recorded using 8 GeV electron beam [241].

9.3 Timing in LYSO-based calorimeters

The timing measurement in LYSO-based calorimeters is driven by three main factors – other than the intrinsic transit time of the photodetector itself and the DAQ electronics: (a) the shower profile fluctuations, (b) the scintillation time, and (c) the light propagation time. Stochastic processes during the development of an electromagnetic shower affect the time of observed signals, as both the transverse size and the depth of the shower can fluctuate event-by-event. Random processes in the scintillation mechanism and the randomization of the optical paths for the scintillation light affect both the speed of the signal formation and the time jitter. We study these effects

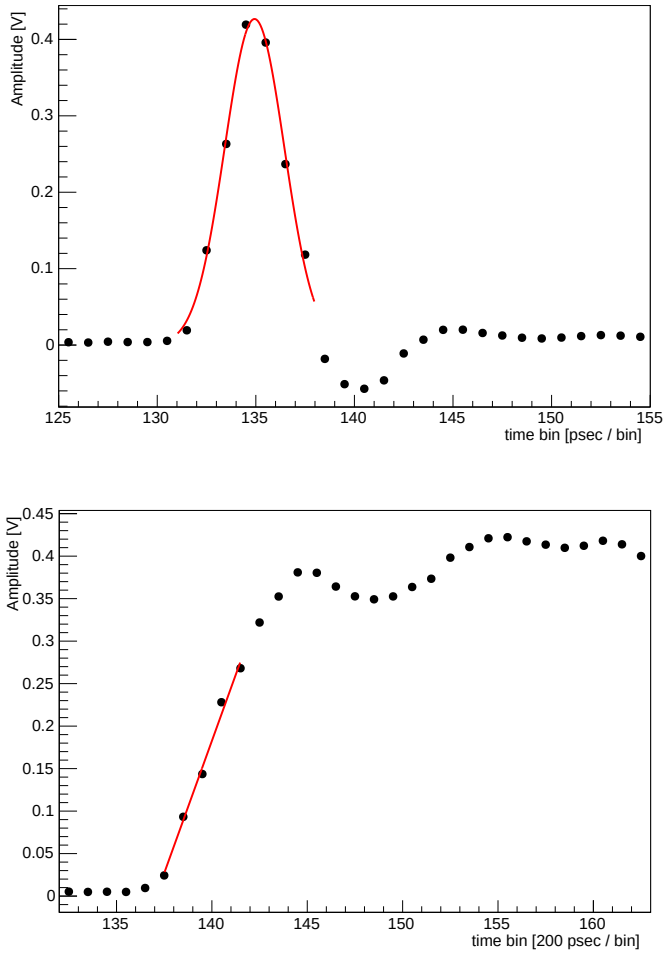

Figure 9.4: Sample fits used to assign timestamps to digitized MCP-PMT pulses [241]. Pulses are shown from the reference Hamamatsu R3809 MCP-PMT (top) and from the Hamamatsu R3809 MCP-PMT optically coupled to a $(1.7\,\mathrm{cm})^3$ LYSO crystal (bottom) recorded during an 8 GeV electron run.

using two independent experimental setups.

For a homogeneous crystal calorimeter, we are interested in the characterization and optimization of the light propagation time, i.e. the time the scintillation light travels down the length of the crystal. Our setup uses a small LYSO cube with linear dimensions of 17mm as the active scintillation element. The size of this element reduces the effect of the light propagation time and jitter. The LYSO cube is placed behind about 4.5 X_0 radiation lengths of lead. Using this LYSO-based sampling calorimeter, we measure the time resolution of electrons.

We also study a shashlik calorimeter composed of alternating layers of tungsten and LYSO, in which scintillation light is extracted through wavelength shifting (WLS) fibers. In this setup, the light propagation time through the fiber is the dominant factor of the timing measurement. We study as a baseline an alternate version of this calorimeter where the light is extracted through direct optical coupling of the photodetectors at the edges of a few LYSO layers to minimize the light propagation time.

Timing studies of the LYSO-based sampling calorimeter

We study the combined impact of the shower profile fluctuations, the scintillation mechanism in LYSO, and the light propagation time resolution using a sampling calorimeter with a $(1.7\ \text{cm})^3$ LYSO cube as active element. The LYSO crystal is wrapped in Tyvek and attached to the Hamamatsu R3809 MCP-PMT (HAMB) with optical coupling [246]. A second Hamamatsu MCP-PMT photodetector (HAMA) is placed upstream of the calorimeter and is used to measure the reference time. A schematic diagram and a photograph of the experimental setup are shown in Fig. 9.5.

To ensure that the electron beam is constrained to within a $2 \times 2\ \text{mm}^2$ region, a plastic scintillator placed upstream and approximately 2 mm by 2 mm in cross sectional area is used to trigger the DAQ readout on the DRS digitizer. Electron events are identified by requiring a signal with amplitude larger than 10 mV in a Čerenkov counter located upstream. Large lead bricks are placed upstream of the Hamamatsu R3809 MCP-PMT (HAMB), out of the path of the beam. These shield the photodetector from stray particles produced in events where an electromagnetic shower occurs upstream of the lead radiator. Such stray shower particles yield very fast signals which can significantly contaminate the scintillation signal. Using the same experimental setup without the LYSO active element in place, we find that stray shower type events yield less than 10% contamination and give a negligible effect on the scintillation signal.

The thickness of the LYSO active element is relatively small and captures only a fraction of the total energy of the electron, but yields a reasonable energy measurement as it is close to the shower maximum.

The time of flight measurement is performed using the LYSO sampling calorimeter for electron beams with energies varying from 4 GeV to 32 GeV.

The corresponding measured time of flight distributions are shown in Fig. 9.6. We achieve the best time resolution of 34 ps for electrons with beam energy of 32 GeV.

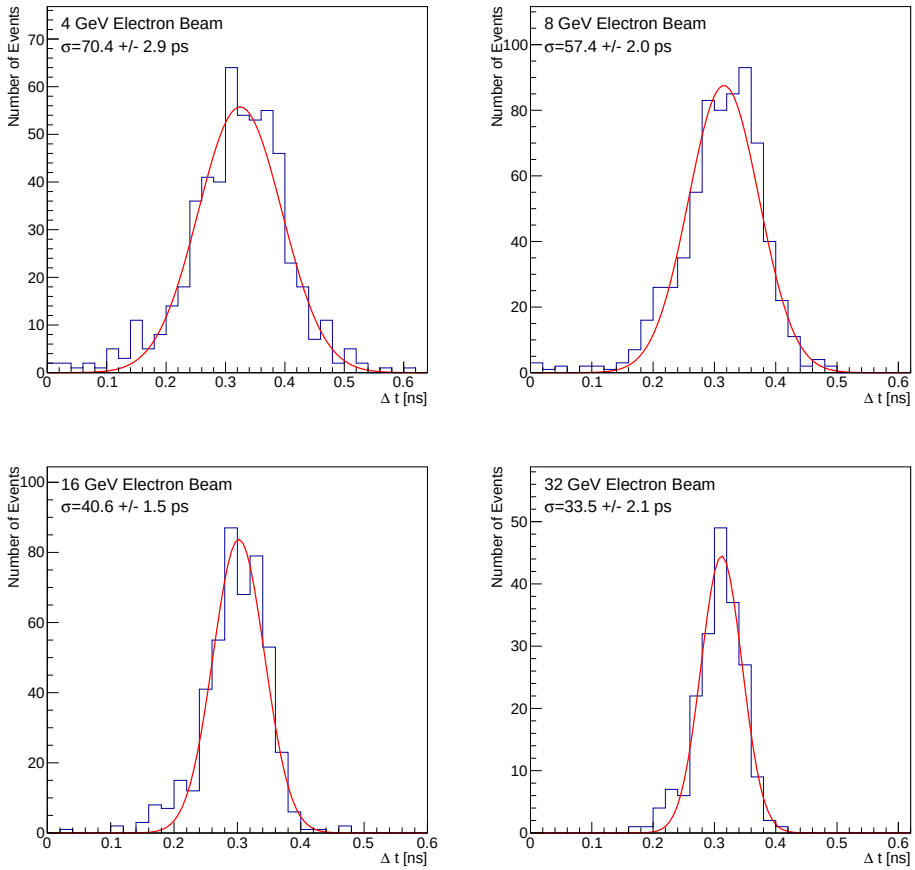

Figure 9.6: Time of flight distributions for the LYSO cube sampling calorimeter for 4 GeV (top left), 8 GeV (top right), 16 GeV (bottom left), and 32 GeV (bottom right) electron beam energy [241].

The time resolution measurement is plotted as a function of the beam energy in Fig. 9.15 (left). We fit the result to the sum of a $1/\sqrt{E}$ term and a constant term of about 11 ps. Given that we measure the contribution to the intrinsic time resolution of the photodetector and the DAQ electronics to be about 20 ps [242], using the results from the 32 GeV electron beam, we infer that the combined contribution to the time resolution from the shower profile fluctuations, the scintillation mechanism, and the light propagation time inside the LYSO cube is about 27 ps.

Timing studies of the LYSO-tungsten shashlik calorimeter
Wavelength shifting fibers readout (WLS Y11 & DSB1)

We study the time resolution of a LYSO-tungsten Shashlik calorimeter, one of the options originally proposed for the Phase 2 upgrade of the CMS end-cap calorimeter system [239]. We compare the time resolution performance for two alternative light propagation schemes.

In our setup the scintillation light is collected by WLS fibers that pass through a set of four holes in the LYSO and tungsten layers. In Fig. 9.7, a shashlik cell and the light extraction scheme is illustrated. A schematic diagram and a photograph showing this experimental setup are shown in Fig. 9.8. Two MCP-PMTs by Hamamatsu (R3809) are used to collect the scintillation light, while a Photek 240 MCP-PMT is used as a reference time detector.

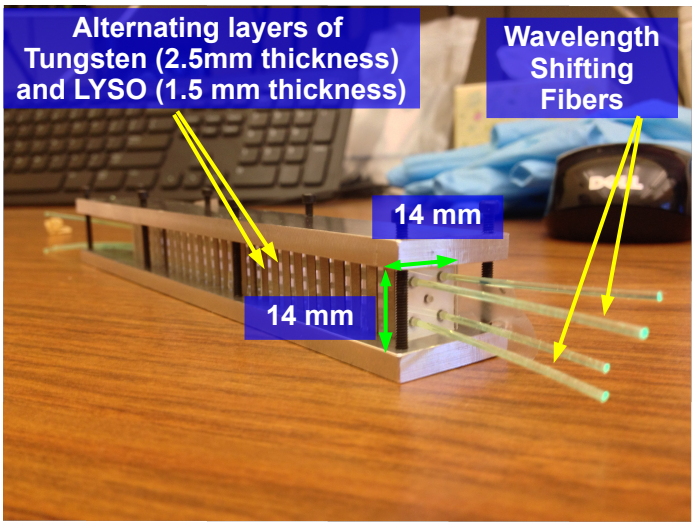

Figure 9.7: The shashlik configuration based upon interleaved W and LYSO layers. Twenty-eight LYSO crystal plates and twenty-seven W plates comprise the module. Four WLS fibers are used to read out the scintillation light from the tiles [241].

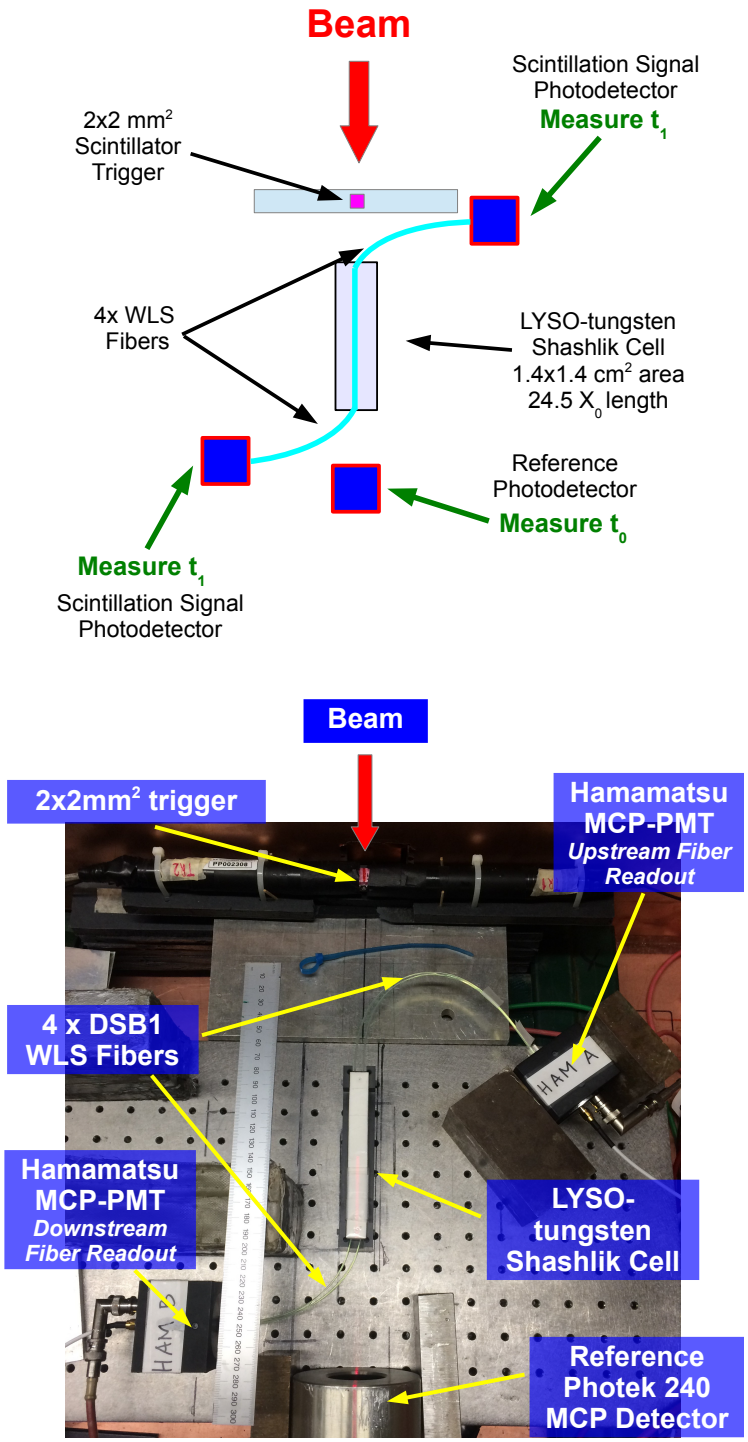

Figure 9.8: A schematic diagram of the experimental setup for the time of flight measurement using the LYSO-tungsten shashlik calorimeter with fiber signal extraction, along with a photograph of the experimental setup [241].

We compare the signal pulses obtained using two different types of WLS fiber in the same LYSO-tungsten shashlik calorimeter. In Fig. 9.9 (a) and (b) and we show the pulse shapes averaged over a few hundred events obtained using DSB1 fibers [247] and Y11 fibers, plotted in blue and red respectively. We find that the rise time of the pulse obtained using the DSB1 fibers, about 2.4 ns, is significantly faster than the rise time of the pulse obtained using the Y11 fibers, which is about 7.1 ns. To optimize the time resolution of this type of calorimeter the DSB1 fiber provides a better choice than Y11 if only this parameter is considered. The signal rise times we observe are comparable to the measured decay times of the corresponding WLS fibers [247].

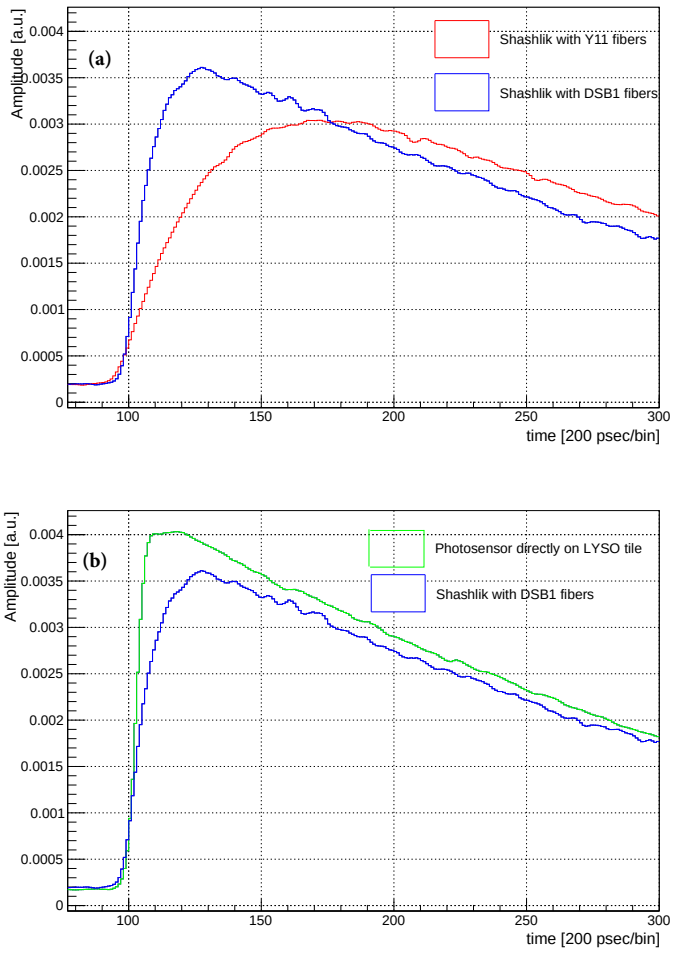

Figure 9.9: (Top) Pulse shapes digitized by the DRS4 board and averaged over several hundred events obtained from the LYSO-tungsten shashlik calorimeter with light extracted using DSB1 (blue) and Y11 (red) WLS fibers. (Bottom) DSB1(blue) shashlik average light pulse shape compared with the averaged pulse shape obtained from direct optical coupling of the photodetector to one edge of a LYSO tile in the shashlik calorimeter. (green)

Using the shashlik calorimeter cell with DSB1 fibers, we measure the time resolution for electron beams with energy varying between 4 GeV and 32 GeV. In Fig. 9.10(b) we show the distribution of the pulse integral which is proportional to the total collected charge, for the 32 GeV beam, and observe an energy resolution of about 5% while for the small LYSO cube shown in Fig. 9.10(a), the energy resolution was about 20%. For this particular run in the Shashlik setup, no electron identification requirements could be made

due to a misconfiguration of the upstream Čerenkov counter, so the background is visible.

Time of flight distributions, fitted to Gaussian functions, are shown in Fig. 9.11, and the σ parameter of the Gaussian fit is plotted as a function of the beam energy in Fig. 9.15. We find that the dependence of the time resolution on beam energy follows a $1/\sqrt{E}$ functional form, indicating that the current calorimeter setup remains in the photostatistics limited regime. The best time resolution we obtain with this setup is 104 ps. As the measurements are photostatistics limited, the result can be improved in the future if the light collection efficiency is increased.

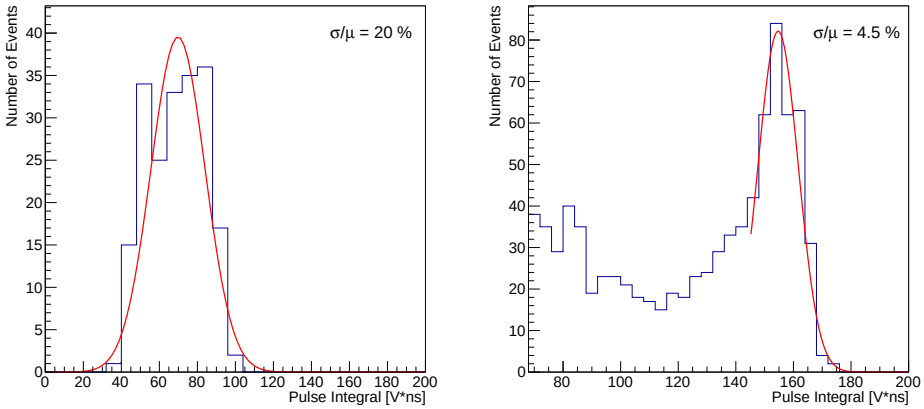

Figure 9.10: (Left) Histogram of the pulse integral which is proportional to the total collected charge is shown for events recorded using the LYSO cube sampling calorimeter for a 32 GeV electron beam. (Right) Histogram of the pulse integral for events recorded using the LYSO-tungsten shashlik calorimeter using DSB1 fibers, for a 32 GeV electron beam. The background is included due to a misconfiguration of the Čerenkov counter [241].

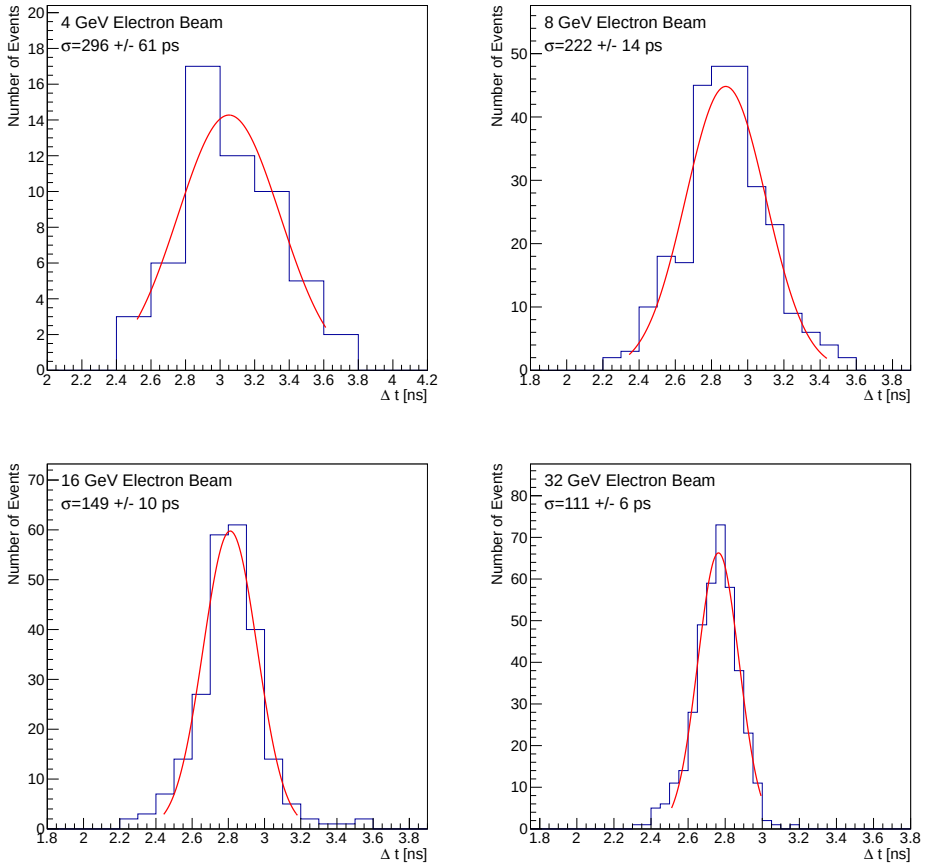

Figure 9.11: Time of flight distributions for the LYSO-tungsten shashlik calorimeter using DSB1 fibers for 4 GeV (top left), 8 GeV (top right), 16 GeV (bottom left), and 32 GeV (bottom right) electron beam energy [241].

Directly coupled MCP-PMTs to LYSO shashlik plates

In this setup the MCP-PMT photodetectors are directly coupled to the edges of two adjacent LYSO layers in the shashlik calorimeter and scintillation light is directly transported to the photodetector through the edges of the tile layers. A schematic diagram and corresponding picture of the experimental setup are shown in Fig. 9.12. In Fig. 9.13, we show a zoomed-in photograph of the exposed LYSO plates from which the scintillation light signal is extracted.

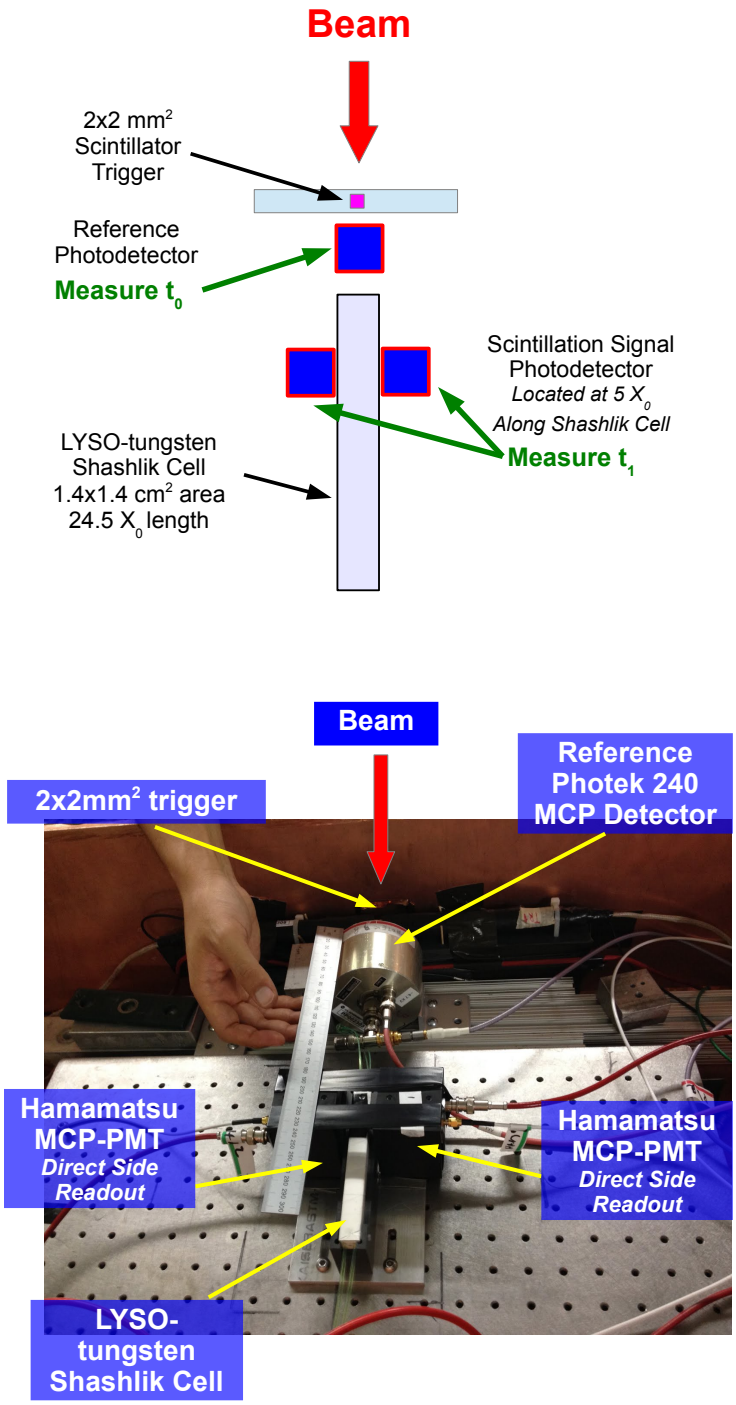

Figure 9.12: A schematic diagram of the experimental setup for the time of flight measurement using the LYSO-tungsten shashlik calorimeter with signal extraction from the edges of two LYSO plates, along with a picture of the experimental setup [241].

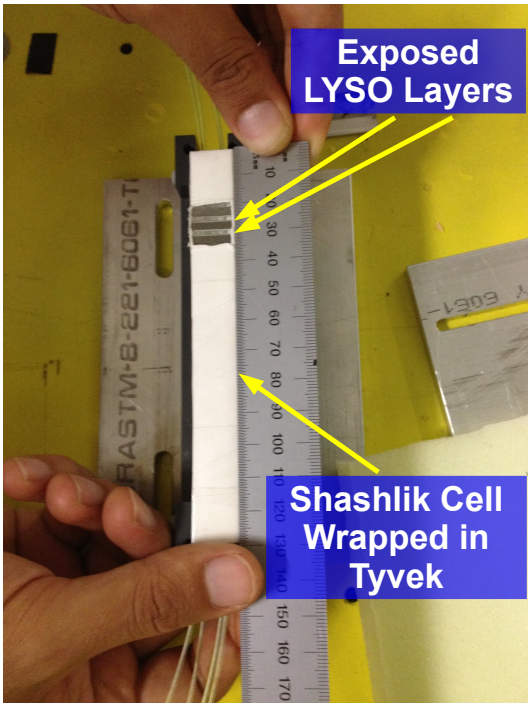

Figure 9.13: A photograph of the two exposed LYSO layers in the shashlik cell. The scintillation light signal is extracted by optically coupling the edges of these two exposed LYSO layers to MCP-PMT photodetectors [241].

With this setup we invoke an interplay between the light propagation jitter and the limited photostatistics. By placing the photodetectors in direct contact with the edges of two LYSO layers, we minimize the distance the scintillation light travels to reach the photodetectors, and reduce the impact of light propagation jitter on the time measurement resolution. However in this setup we have also reduced the available photostatistics, as we collect light from only a small fraction of the shashlik cell. In Fig. 9.14, we show the time of flight distributions for electron beams at various energies, fitted to Gaussian functions. The width of the best-fit Gaussian is plotted as a function of the beam energy in Fig. 9.15. The best time resolution that we obtain is about 55 ps, and fitting the result to the sum of a $1/\sqrt{E}$ term and a constant term, we find a constant term of about 30 ps.

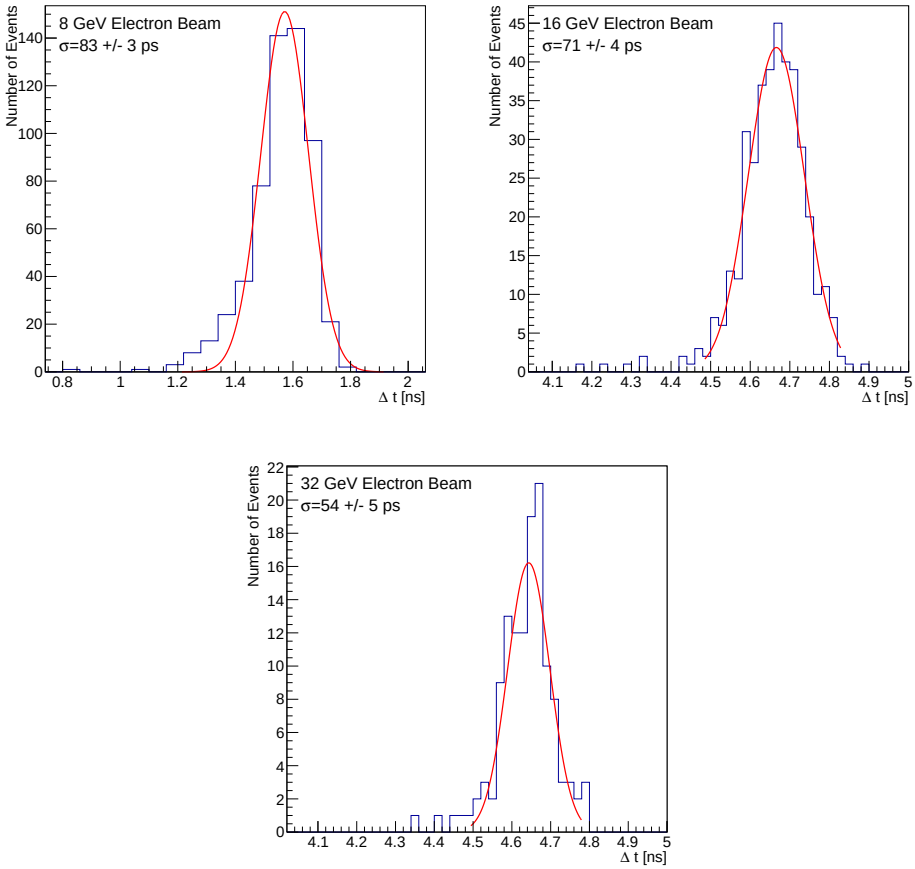

Figure 9.14: Time of flight distributions for the LYSO-tungsten shashlik calorimeter with signal extracted from the edges of two LYSO layers for 8 GeV (top left), 16 GeV (top right), and 32 GeV (bottom) electron beam energy [241].

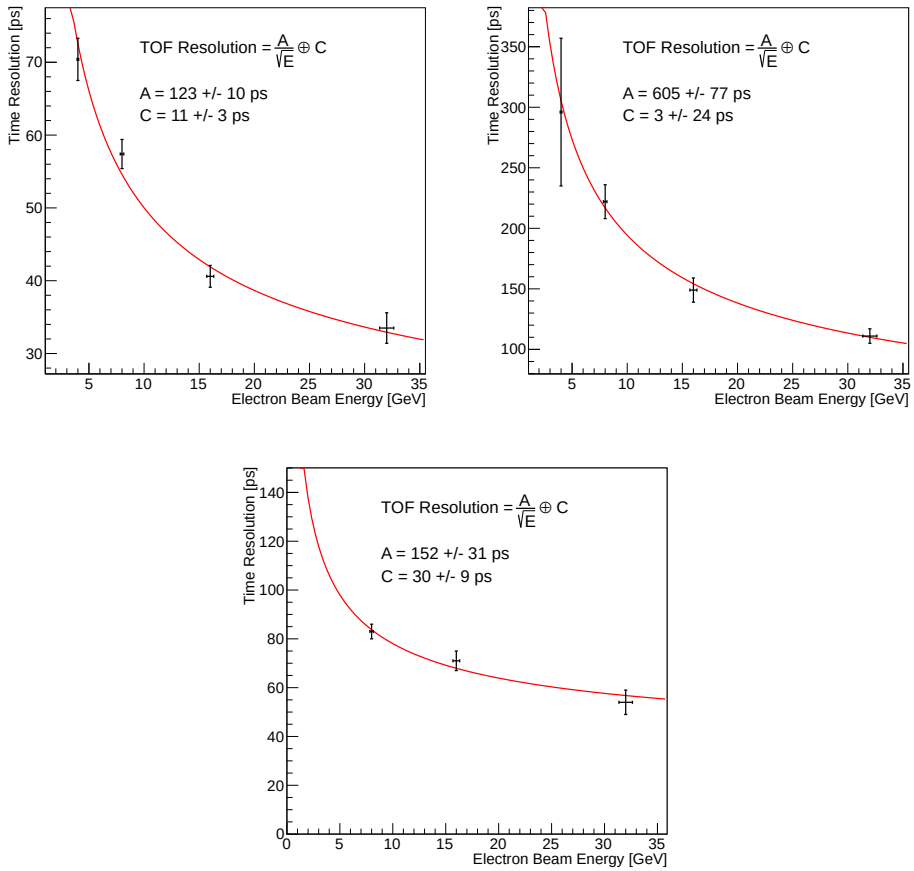

Figure 9.15: Timing resolution measurement as a function of the electron beam energy for (top left) the LYSO cube sampling calorimeter, (top right) the LYSO-tungsten shashlik calorimeter read-out with DSB1 fibers, and (bottom) the LYSO-tungsten shashlik calorimeter read-out directly by optically coupling to the edges of two LYSO layers. In all cases we fit the data with a function of $1/\sqrt{E}$ and a constant term.

In summary, we find that removing the impact of the wavelength shifting mechanism and minimizing the impact of optical transit does indeed improve the time resolution, but at a cost in photostatistics. Results obtained in this experiment suggest that a LYSO-tungsten shashlik calorimeter with edge readout can likely achieve 30 ps resolution provided some improvement to the light collection efficiency is achieved.

9.4 Summary

In this chapter we have described studies characterizing the timing performance of LYSO-based calorimeters. Using a $(1.7\,\mathrm{cm})^3$ LYSO crystal that samples the electromagnetic showers created by electrons of various energies ranging from 4 GeV to 32 GeV at about $4.5X_0$, we infer that the contribution to the time resolution from event-by-event fluctuations of the shower profile, the scintillation process, and the light propagation is less than 30 ps. Studies using different wavelength shifting fibers in a LYSO-tungsten shashlik calorimeter demonstrates that the choice of the fiber affects the timing performance. Besides the absorption and re-emission processes in the fibers, we found that another important factor influencing the timing performance is the light extraction efficiency. Using DSB1 fibers, despite being photostatistics limited, we obtained a best time resolution of about 100 ps. A future development of such a detector will be focused on increasing the light collection efficiency. In a setup where the scintillation light from the LYSO-tungsten shashlik calorimeter is extracted via the edges of two LYSO layers, thereby removing completely the wavelength shifting mechanism and long light propagation distance, we achieve a best time resolution of 55 ps. The result indicates that such a calorimeter design can achieve the 30 ps time resolution benchmark obtained with the LYSO cube provided some improvement to the light collection efficiency.

In comparing results using different light extraction schemes, we find that at a given light yield the time resolution depends significantly on the light propagation fluctuations. As the light yield increases the dependence on the light propagation fluctuations is reduced. The effect can be seen in the summary Fig. 9.16, where we show the dependence of the time resolution on the average pulse height for the shashlik cell with light extracted through the DSB1 fibers and for the sampling calorimeter with the LYSO cube. For the same average pulse height of 500 mV, the LYSO cube time resolution is about half of the shashlik using the DSB1 fibers which have also twice the rise time. As the pulse height increases the time resolution improves. Extrapolating to the regime of very large light yield, we should be able to reach asymptotically the best resolution without limitations from the light propagation fluctuations.

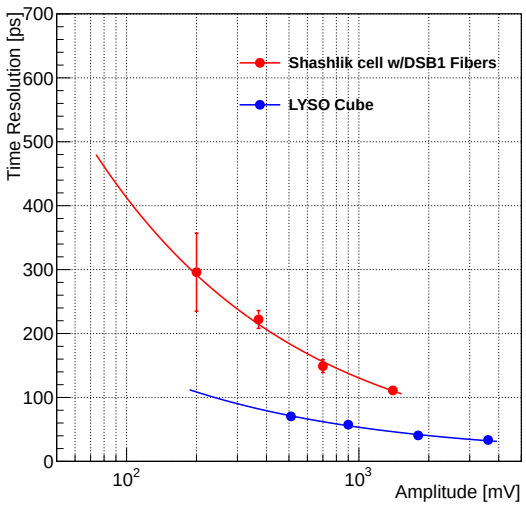

Figure 9.16: Comparison of time resolutions obtained with the $(1.7\text{ cm})^3$ LYSO cube (blue), and the LYSO-tungsten shashlik calorimeter with light extracted using DSB1 fibers (red) [241]. The x-axis in this figure displays the amplitude of the signal, corrected for the attenuation factors.

In summary, using a LYSO-based calorimeter and different light propagation experimental setups we obtain about 30 ps resolution time measurement for the maximum light yield achieved.

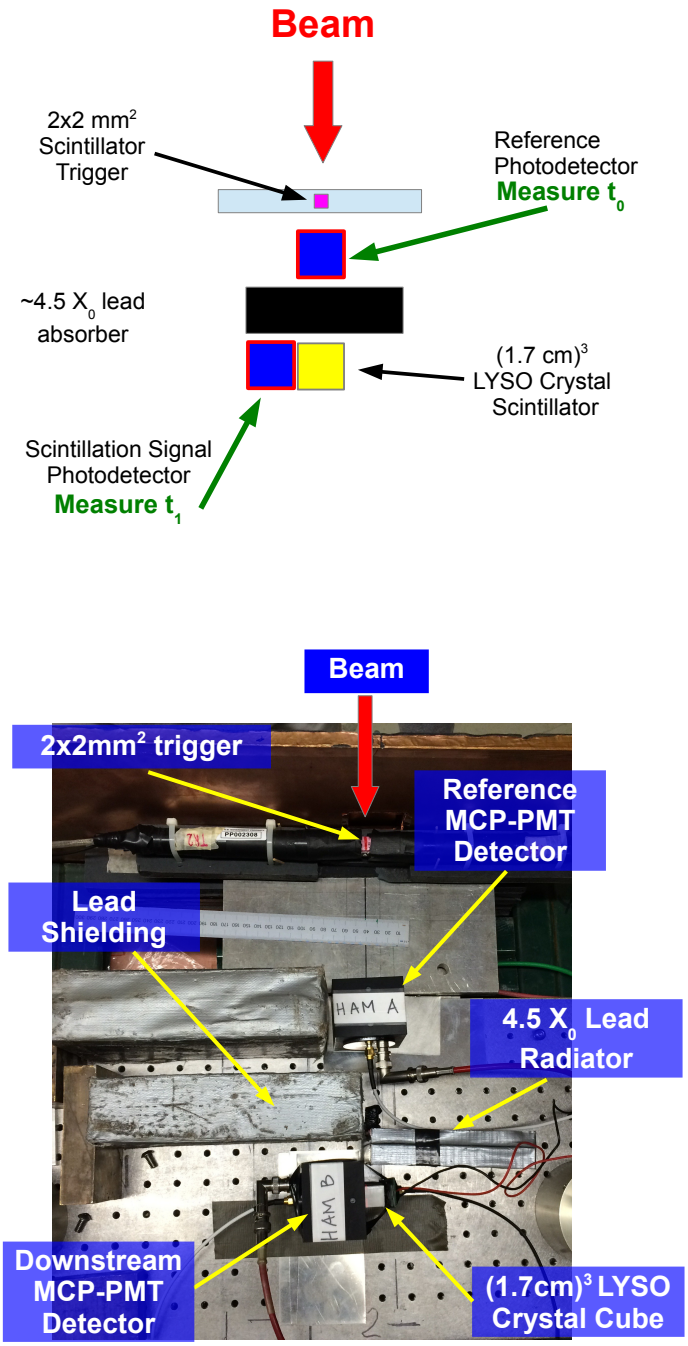

Figure 9.5: A schematic diagram of the experimental setup for the time of flight measurement using the LYSO sampling calorimeter is shown on the left, along with a picture of the experimental setup shown on the right [241].

Part V

Conclusion

Chapter 10

CONCLUSION AND OUTLOOK

In this thesis, we first presented the theoretical motivations for a specific supersymmetric extension of the standard model in which the quadratic divergence of the Higgs mass is tamed to merely a logarithmic one. One interpretation of this resulting sensitivity is that the fundamental Higgs mass parameter no longer needs to be finely-tuned for the physical Higgs mass to match the observed value of 125 GeV, yielding a more natural theory. The particle spectrum of this scenario includes light higgsino-like neutralinos and charginos, a light bottom and top squark, and a light gluino, all accessible at the current LHC energy of 13 TeV.

We reviewed the LHC and the CMS detector. In particular, we focused on the aspects of CMS important for the natural SUSY searches, including the silicon tracker, the electromagnetic and hardon calorimeters, the high-level trigger, the alignment and calibration, the particle-flow reconstruction of jets and missing transverse momentum, and the identification of jets originating from b-quarks. We also discussed the topological HLT paths based on razor variables developed for 13 TeV searches in hadronic final states.

We then described two inclusive searches for natural SUSY using the razor variables performed at $\sqrt{s} = 8$ and 13 TeV, respectively. These searches go beyond the "simplified model" paradigm by interpreting results in a broader natural SUSY context, with multiple gluino or top squark decay modes considered simultaneously. The analyses exclude a top squark below ~ 700 TeV and a gluino below ~ 1.6 TeV for a low-mass neutralino LSP and independent of the branching ratios. This sensitivity to different gluino and top squark decay modes is a consequence of the inclusive approach of the searches, which consider events with 0, 1, and ≥ 2 leptons, and 0, 1, 2, and ≥ 3 b-tagged jets.

As continuing the search for natural SUSY requires colliders going to higher luminosities and therefore pileup, we discussed the possibility of using calorimeters with precision timing capabilities to mitigate to the problems associated with the higher pileup anticipated after the HL-LHC upgrade. In

dedicated experiments at the FNAL test beam facility, we obtained a time resolution of $\sim$ 30 ps using a LYSO-based calorimeter and different light propagation experimental setups in an electron test beam. The achieved time resolution corresponds to the precision needed to significantly reduce (by about a factor of ten) the inclusion of pileup particles in the reconstruction of the event of interest at the HL-LHC.

In an appendix, we proposed two simplified model topologies for searches for SUSY in H($\gamma\gamma$)+jet events. We reinterpreted the results of an 8 TeV CMS search for SUSY using razor variables, and found both models to be consistent with the excess observed in data at a $\sim 2\sigma$-level. An updated 13 TeV search from CMS used one of the models proposed and also found an excess in data consistent with one of the model topologies at the $\sim 2\sigma$-level at the same mass values.

Finally, in another appendix, we discussed a search for narrow resonances in the dijet mass spectrum at 13 TeV using the data-scouting technique at CMS, which records a smaller event format to increase the maximum recordable rate. This search has far-reaching implications for many models of new physics, including models with a vector or axial-vector mediator that couples to quarks and dark matter particles. For the benchmark choice of mediator couplings, the dijet search excludes mediator masses from 0.5 TeV up to $\sim$ 2.7 TeV largely independent of the dark matter particle mass, which constitutes a larger exclusion than traditional $E_{\mathrm{T}}^{\mathrm{miss}} + \mathrm{X}$ (mono-X) searches at the LHC. In the plane of the dark matter-nucleon interaction cross section versus dark matter mass, the dijet search is also more sensitive than direct detection experiments for spin-dependent cross sections.

Despite the null results in the search for physics beyond the standard model described in this thesis, the LHC continues to be the most exciting discovery machine in the world. It remains the best place to seek answers the most pressing theoretical questions of the day: How is the Higgs mass 125 GeV, a value too small for the standard model without SUSY but too large for many SUSY scenarios? Are the couplings of the Higgs boson exactly as predicted by the standard model? Are there weak-scale SUSY particles? Does dark matter couple (indirectly) to quarks? Because of these unanswered questions, I believe we are on the precipice of a paradigm-shifting discovery, which will usher in an era of characterization and measurement of new

particles and couplings, rather than exclusions.

Chapter 11

ATTRIBUTION

Ch. 2 and Ch. 3 lays out the theoretical foundations of particle physics, supersymmetry, and naturalness, and represents the work of theoretical physicists cited therein. Sec. 3.8 presents a framework for interpretation proposed and established by myself in collaboration the CMS SUSY group, especially Maurizio Pierini and Frank Wuerthwein. Ch. 4 gives an overview of the LHC and represents the work of many engineers and physicists cited therein.

Ch. 5 recounts work done by my CMS collaborators on the CMS detector. An exception is the discussion of the alignment and calibration triggers and the HLT conditions validation in Sec. 5.7, which I coordinated for the start of Run 2 in 2015. In collaboration with Alex Mott, Si Xie, Dustin Anderson, and Maurizio Pierini, Ch. 6 presents my work on the development of the 13 TeV razor triggers. Ch. 7 presents the 8 TeV inclusive razor search for SUSY, in which I was the lead analyst in collaboration with Maurizio Pierini and Maria Spiropulu. The combination of the hadronic razor search with the exclusive single-lepton top squark search in Sec. 7.7 was performed in collaboration with Frank Golf and Ryan Ward Kelley. Ch. 8 describes the 13 TeV inclusive razor search for SUSY and represents my work for the fit-based background estimation method B, the work of Dustin Anderson for the simulation-based background estimation method A, as well as the work of Jay Lawhorn, Cristián Peña, Si Xie, Artur Apresyan, Maurizio Pierini, and Maria Spiropulu. Ch. 9 discusses test beam studies of the timing performance of LYSO-based calorimeters, done by myself in collaboration with Adi Bornheim, Cristián Peña, Dustin Anderson, Si Xie, Artur Apresyan, Anatoly Ronzhin, Jason Trevor, and Maria Spiropulu.

App. A represents the work done by myself, Cristián Peña, Maurizio Pierini, and Maria Spiropulu. Finally, I was the lead analyst in the 13 TeV search for narrow resonances in the dijet mass spectrum presented in App. B, although I collaborated closely with colleagues in the CMS Exotica group, including Dustin Anderson, Si Xie, Artur Apresyan, Maurizio Pierini, David Sheffield,

Juska Pekkanen, Robert Harris, and Francesco Santanastasio. In preparing the Z'_B and dark matter interpretation of the dijet searches, I also collaborated with Bora Isildak, Zhixing "Tyler" Wang, Phil Harris, Nhan Tran, Tristan Du Pree, and others.

Part VI

Other searches for exotic new physics at the LHC

Appendix A

PHENOMENOLOGY OF SQUARK-MEDIATED H+JETS PRODUCTION AT THE LHC

Much of the focus of the ATLAS and CMS collaborations has been on searching for strongly-produced SUSY partners, which have large production cross sections at the LHC and are needed to protect the mass of the Higgs (H) boson from large quantum corrections: the gluino, the bottom squark, and the top squark. As presented in Chapters 7 and 8, no evidence for the production of such particles was found, pushing the allowed mass range for gluinos and top squarks above $\sim 1600\,\text{GeV}$ and $\sim 700\,\text{GeV}$, respectively, for a low-mass neutralino LSP and largely independent of the top squark and gluino branching ratios [94, 227].

In a few cases, a data yield above the expected background was observed for certain signal regions, for example, in the case of the dilepton edge analysis by CMS [248] and the SUSY search in Z+jets events by ATLAS [249]. These excesses correspond to, respectively, $\sim 2.4\sigma$ and $\sim 3.0\sigma$ of local significance, which are reduced after accounting for the look-elsewhere effect (LEE). Several interpretations of these results were given in the literature [250, 251, 252, 253, 254, 255], mainly related to the electroweak production of SUSY particles with long decay chains.

Here we discuss another interesting excess, observed in a search for electroweak SUSY partners in $\text{H}(\gamma\gamma)+\,\geq 1$ jet events by the CMS collaboration performed at 8 TeV [164]. The analysis uses the diphoton invariant mass $m_{\gamma\gamma}$ to select events with a H-like candidate. The nonresonant (mostly QCD diphoton production) and resonant (standard model $\text{H}(\gamma\gamma)$ production) backgrounds are estimated using the $m_{\gamma\gamma}$ sidebands in data and the Monte Carlo simulation, respectively. The background prediction is performed as a function of the razor variables M_R and R^2 in five mutually exclusive *boxes*, targeting different final states: high-p_T $\text{H}(\gamma\gamma)$ (`HighPt` box), $\text{H}(\gamma\gamma)+\text{H}(\text{b}\bar{\text{b}})$ (`Hbb` box), $\text{H}(\gamma\gamma)+\text{Z}(\text{b}\bar{\text{b}})$ (`Zbb` box), and low-p_T $\text{H}(\gamma\gamma)$ with high- and low-resolution photons (`HighRes` and `LowRes` boxes, respectively). Five events are observed in one (M_R, R^2) bin of the `HighRes`

box, compared to less than one expected background event. This corresponds to a local significance of 2.9σ, reduced to 1.6σ after the LEE.

In this paper, we discuss a possible interpretation of this search in terms of SUSY models with light quarks. We emulate this CMS analysis to derive bounds on squark production. Since the analysis does not require or veto jets originating from b-quarks (b-jets), the results apply to bottom-squark production in natural SUSY models.

Recently, an updated search was performed with data collected at 13 TeV [256], which exhibits a similar excess of 2.5σ local significance, reduced to 1.4σ after the LEE. Model B proposed in this thesis was also used for the interpretation of the results.

A.1 Benchmark signal models

We consider two simplified models with bottom squark pair production, both resulting in a H+jets final state.

In the first model, hereafter referred to as model A, we consider the asymmetric production of a $\widetilde{b}_2\widetilde{b}_1$ pair, where $\widetilde{b}_2$ and $\widetilde{b}_1$ are the heaviest and the lightest bottom squarks, respectively. The $\widetilde{b}_2$ decays to $b\widetilde{\chi}_2^0$, with $\widetilde{\chi}_2^0 \rightarrow H\widetilde{\chi}_1^0$. The lightest neutralino $\widetilde{\chi}_1^0$ is assumed to be the LSP. The $\widetilde{b}_1$, close in mass to the LSP, decays to $b\widetilde{\chi}_1^0$. All the other SUSY partners are assumed to be too heavy to be produced at the LHC and are ignored in this analysis. This model represents a new mechanism for the production of $H + 2b\text{-jets} + \text{invisible}$, with one of the associated b-jets typically having low momentum.

In the second model, hereafter referred to as model B [257], two bottom squarks $\widetilde{b}_1\widetilde{b}_1$ are produced, each decaying as $\widetilde{b}_1 \rightarrow b\widetilde{\chi}_2^0$. The $\widetilde{\chi}_2^0$ then decays to $H\widetilde{\chi}_1^0$, the $\widetilde{\chi}_1^0$ being the LSP. As for model A, the other SUSY partners are ignored. This simplified model corresponds to a final state consisting of $2H + 2b\text{-jets} + \text{invisible}$.

The mass spectrum for each model is shown in Fig. A.1. We fix the $\widetilde{\chi}_2^0$ and $\widetilde{\chi}_1^0$ masses to 230 GeV and 100 GeV, respectively. In model A, we fix the $\widetilde{b}_1$ mass to 130 GeV as varying its mass in between the limits of the $\widetilde{\chi}_1^0$ and $\widetilde{\chi}_2^0$ masses has little effect. Finally, we scan the $\widetilde{b}_2$ ($\widetilde{b}_1$) mass between 250 GeV and 800 GeV for model A (B). These assumptions do not limit the conclusions derived on the squark production cross section. In fact, the analysis is

sensitive to mass differences and not to the absolute mass of SUSY partners. On the other hand, the chosen LSP and NLSP masses does play a role when the cross section limits are translated in terms of mass exclusion bounds.

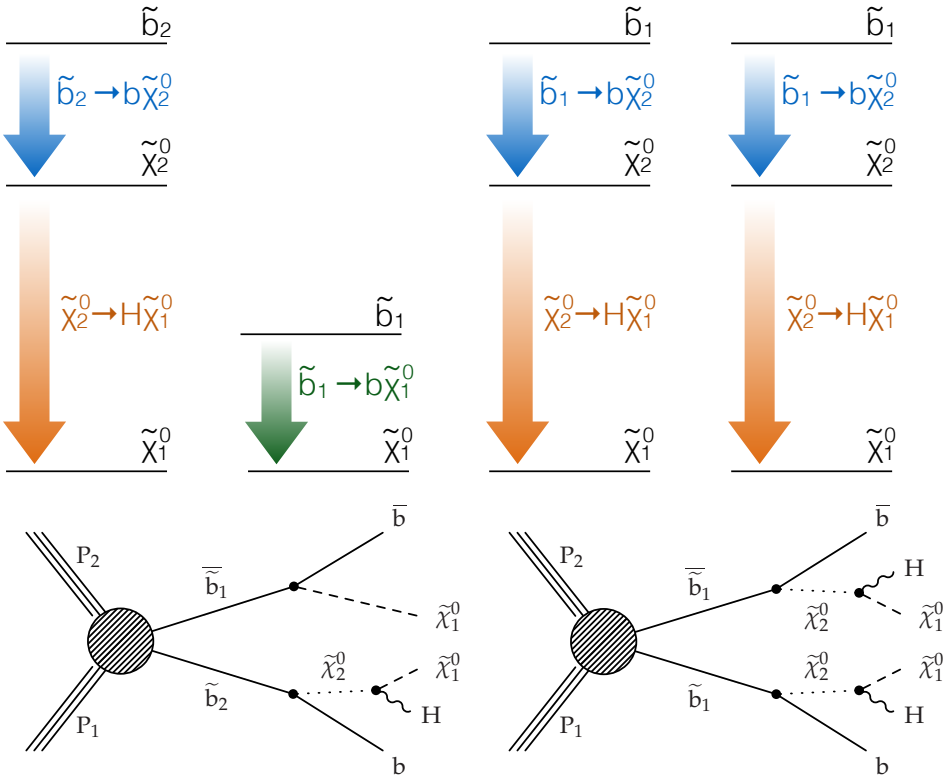

Figure A.1: Pictorial representation of the decay chains and event topologies associated with model A (left) and model B (right), as described in the text [44].

A.2 Event generation and detector emulation

The study is performed using samples of Monte Carlo events. The event generation is performed in PYTHIA 8.210 [258, 259]. The default parton density function set is NNPDF 2.3 QCD+QED LO (with $\alpha_s(m_Z) = 0.130$) [260, 261, 262]. Fast simulation of the CMS detector is performed in DELPHES 3.3.2 [263]. The default description of CMS as provided in the release is used, except for a modification to the photon isolation and efficiency, described in the next section. Jet clustering is performed using FASTJET 3.1.3 [132]. As in CMS, the anti-k_T jet clustering algorithm is used with jet-size parameter $R = 0.5$ [131].

Table A.1: Photon isolation requirements, as in Ref [120]. The photon isolation variables, I_γ, I_n, and I_π, are computed by summing the transverse momenta of photons, neutral hadrons, and charged hadrons, respectively, inside an isolation cone of radius $\Delta R = 0.3$ around the selected photon.

I_γ	barrel	$1.3\,\mathrm{GeV} + 0.005 p_\mathrm{T}^\gamma$
	endcap	–
I_n	barrel	$3.5\,\mathrm{GeV} + 0.04 p_\mathrm{T}^\gamma$
	endcap	$2.9\,\mathrm{GeV} + 0.04 p_\mathrm{T}^\gamma$
I_π	barrel	2.6 GeV
	endcap	2.3 GeV

A.3 Emulation of the CMS search

The emulated event selection is summarized as follows,

- Events with two isolated photons with $p_\mathrm{T} > 25\,\mathrm{GeV}$ and $|\eta| < 1.44$ are selected. As in Ref. [120], the photon isolation variables, I_γ, I_n, and I_π, are computed by summing the transverse momenta of photons, neutral hadrons, and charged hadrons, respectively, inside an isolation cone of radius $\Delta R = 0.3$ around the selected photon. The photon isolation requirements on these variables are shown in Tab A.1. An additional photon selection efficiency is applied in DELPHES such that isolated photons with $p_\mathrm{T} < 10\,\mathrm{GeV}$ ($p_\mathrm{T} \geq 10\,\mathrm{GeV}$) are randomly selected with 94% (98%) efficiency.

- Events with one H candidate with $p_\mathrm{T} > 20\,\mathrm{GeV}$ are selected. A pair of selected photons is considered an H candidate if at least one photon has $p_\mathrm{T} > 40\,\mathrm{GeV}$ and the diphoton mass $m_{\gamma\gamma} > 100\,\mathrm{GeV}$. If the event contains more than one H candidate, the one with the highest scalar sum p_T of the two photons is selected.

- Jets are reconstructed using the FASTJET [132] implementation of the anti-k_T [131] algorithm with jet radius parameter $R = 0.5$.

- Events with at least one jet with $p_\mathrm{T} > 30$ GeV and $|\eta| < 3.0$ are selected.

- An emulation of the "medium" requirement (mistag probability of 1% and b-tag efficiency of $\sim$ 68%) of the combined secondary vertex (CSV) b-tagging algorithm is used to identify b-jets [135].

- A $b\bar{b}$ candidate pair is identified if both jets satisfy the medium requirement of the b-tagging algorithm (note: the CMS analysis requires only one to satisfy the medium requirement, while both are required to satisfy the loose requirement).
- The $b\bar{b}$ candidate pair with the mass closest to 125 GeV or 91.2 GeV is chosen as the $H \to b\bar{b}$ or $Z \to b\bar{b}$ candidate, respectively.
- The razor variable M_R, calculated from two megajets [108] is required to be greater than 150 GeV. All possible combinations of the reconstructed jets and the $H(\gamma\gamma)$ candidate are clustered to form megajets. The pair of megajets that minimizes the sum in quadrature of the invariant masses of the two megajets is selected.

After this baseline selection, events are categorized according to the following requirements,

- `HighPt`: all events with an $H \to \gamma\gamma$ candidate with $p_T > 110$ GeV.
- `Hbb`: remaining events with a $H \to b\bar{b}$ candidate with mass $110 \geq m_{b\bar{b}} \geq 140$ GeV.
- `Zbb`: remaining events with a $Z \to b\bar{b}$ candidate with mass $76 \geq m_{b\bar{b}} \geq 106$ GeV.
- `HighRes`: 70% of remaining events after the `Zbb` selection (emulating the efficiency of the "high-resolution photon" selection).
- `LowRes`: all remaining events.

We assume the breakdown of events between the `HighRes` box and `LowRes` box is 70%-to-30% after the `Zbb` selection. This is based on the following observations: (i) CMS categorizes events in the `HighRes` box if both photons in the event satisfy $\sigma_E/E < 0.015$, where σ_E/E is the estimated relative energy resolution, and categorizes events in the `LowRes` box otherwise, (ii) CMS observes a similar 70%-to-30% breakdown for both SM Higgs production and electroweak SUSY processes in Monte Carlo simulation [164], and (iii) we expect this breakdown to be model-independent assuming both photons are real and come from the decay of a Higgs boson, as it is based

on the properties of such photons detected in CMS and not on the details of the model.

Finally, the search region selection is as follows,

- The search region in the $m_{\gamma\gamma}$ distribution is defined by $(125 - 2\sigma_{\text{eff}}, 126 + 2\sigma_{\text{eff}})$ in each event category, where σ_{eff} is defined such that $\sim 68\%$ of Higgs boson events fall in an interval of $\pm\sigma_{\text{eff}}$ around the nominal m_{H} value. Following this procedure using our generated and simulated signal samples, we derive σ_{eff} to be 3.8 GeV in the `HighPt` box and 2.2 GeV in the `HighRes` and `LowRes` boxes. For the `Hbb` and `Zbb` boxes, due to the low number of selected signal events, we use the overall average value of 2.8 GeV.

We note that these σ_{eff} values are larger than the corresponding ones in Ref. [164]. This is due to the larger width observed for the diphoton mass distribution in Higgs boson events simulated and reconstructed with DELPHES, compared to official CMS software. This implies the effective diphoton mass resolution when using DELPHES is larger than in the real CMS detector. We attempt to account for this with a modification explained in Sec.A.5.

A.4 Bayesian statistical procedure

We model the likelihood according to a Poisson density, considering the expected background yield (with associated uncertainty), the expected signal yield (for a given signal cross section), and the observed yield. The background uncertainty is modeled with a gamma density. The background yields and the corresponding uncertainties are taken from the tables provided in Ref. [164]. To take into account systematic uncertainties on the signal, we assign a 30% uncertainty (assuming a log-normal density) on the signal strength, a multiplicative factor modifying the signal cross section. We then derive the posterior density for the signal cross section σ as:

$$p(\sigma|\text{data}) \propto \mathcal{L}(\text{data}|\sigma)\, p_0(\sigma)\,, \tag{A.1}$$

where $\mathcal{L}(\text{data}|\sigma)$ is the likelihood and $p_0(\sigma)$ is the prior density taken to be uniform. The likelihood is then

$$\mathcal{L}(\text{data}|\sigma) = \int_0^\infty \mathrm{d}\mu \; \text{Ln}(\mu|\bar{\mu}, \delta\mu) \prod_{i=0}^{n_{\text{bins}}} \int_0^\infty \mathrm{d}b_i \text{Poisson}(n_i|L\mu\sigma\epsilon_i + b_i) \times \Gamma(b_i|\bar{b}_i, \delta b_i) \; , \tag{A.2}$$

where the product runs over the number of bins n_{bins}; n_i is the observed yield in the i^{th} bin, L is the integrated luminosity, b_i is the assumed value of the background yield in the i^{th} bin and $\bar{b}_i \pm \delta b_i$ is its expected value and the associated uncertainty; ϵ_i is the nominal value of the signal efficiency times acceptance in the i^{th} bin; μ is the signal strength, a nuisance parameter modifying the signal cross section (nominally equal to $\bar{\mu} = 1$ with a $\delta\mu = 30\%$ uncertainty); $\text{Ln}(x|m, \delta)$ is the log-normal distribution for x, parameterized such that $\log(m)$ is the mean and $\log(1 + m\delta)$ is the standard deviation of the log of the distribution; $\Gamma(x|m, \delta)$ is the gamma distribution for x, parameterized such that m is the mode and δ^2 is the variance of the distribution. The 95% credibility level (CL) upper limit on the signal cross section σ_{up} is obtained from the posterior, such that

$$\frac{\int_0^{\sigma_{\text{up}}} \mathrm{d}\sigma \; p(\sigma|\text{data})}{\int_0^\infty \mathrm{d}\sigma \; p(\sigma|\text{data})} = 0.95 \; . \tag{A.3}$$

We also utilize a signal significance measure defined by

$$Z(\sigma) = \text{sign}[\log B_{10}(\text{data}, \sigma)] \sqrt{2|\log B_{10}(\text{data}, \sigma)|} \; , \tag{A.4}$$

where

$$B_{10}(\text{data}, \sigma) = \frac{\mathcal{L}(\text{data}|\sigma, H_1)}{\mathcal{L}(\text{data}|H_0)} \tag{A.5}$$

is the *local* Bayes factor for the data for a given signal cross section σ, and $\mathcal{L}(\text{data}|\sigma, H_1)$ and $\mathcal{L}(\text{data}|H_0)$ are the likelihoods for the signal-plus-background (H_1) and background-only (H_0) hypotheses, respectively. As described in Ref. [264], this measured is a signed Bayesian analog of the frequentist "n-sigma." For each signal model with specified masses, we scan the signal cross section σ to find the maximum significance, which occurs at the mode of the posterior.

A.5 Correction and validation

As explained Sec. A.3, we find differences in the performance of the emulated CMS detector and the real CMS detector, e.g. the larger diphoton mass resolution. To take into account this and other differences in the detector simulation and reconstruction performed by DELPHES and official CMS software, we conservatively double the background uncertainties in each bin reported by CMS in Ref. [164] when evaluating the likelihood in Eqn. A.2. We find this conservative approach better reproduces the observed and expected limits on a benchmark simplified model.

To validate our emulation result, we produced 95% CL limits on the production cross section of an electroweak simplified model of $\widetilde{\chi}_1^{\pm}\widetilde{\chi}_2^0$ production, followed by the decays $\widetilde{\chi}_1^{\pm} \to W^{\pm}\widetilde{\chi}_1^0$, $\widetilde{\chi}_2^0 \to H\widetilde{\chi}_1^0$. For this model, CMS provided the 95% confidence level upper limits on the cross section assuming an LSP mass of $m_{\widetilde{\chi}_1^0} = 1\,\text{GeV}$ and equal chargino and second neutralino masses, $m_{\widetilde{\chi}_1^{\pm}} = m_{\widetilde{\chi}_2^0}$. The comparison between our result and the CMS result for this model is shown in figure A.2 as a function of $m_{\widetilde{\chi}_1^{\pm}}$.

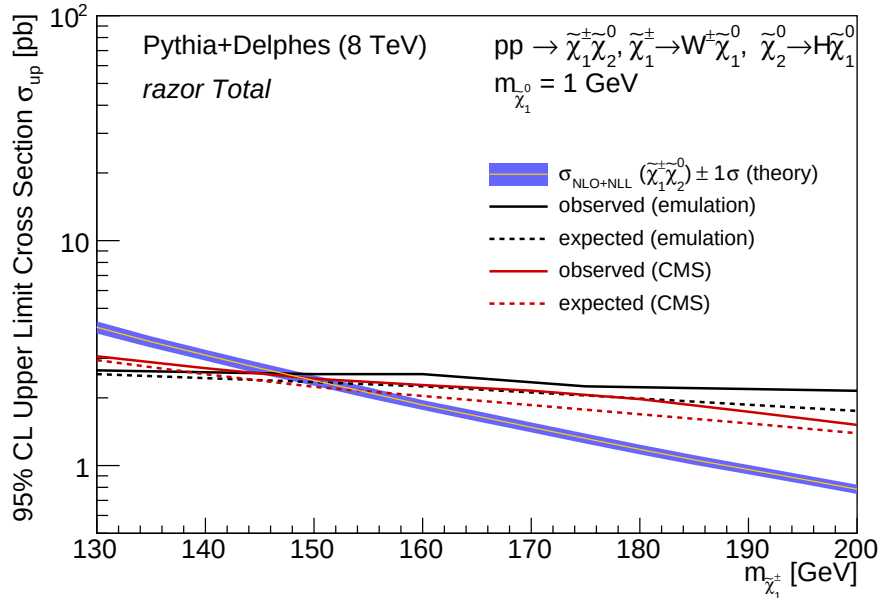

Figure A.2: Comparison between the CMS result (red) and our emulation (black). Note, this scan assumes $m_{\widetilde{\chi}_1^0} = 1\,\text{GeV}$ and $m_{\widetilde{\chi}_1^{\pm}} = m_{\widetilde{\chi}_2^0}$.

A.6 Results and reinterpretation

Figures A.3-A.5 contain the results of the reinterpretation of the CMS data for both models. To show how well signal model A agrees with the excess observed by CMS, Fig. A.3 (top) displays the expected SM background distribution and uncertainty taken from the CMS result compared to the distribution of the signal events for $m_{\tilde{b}_2} = 500\,\text{GeV}$ and $m_{\tilde{b}_2} = 800\,\text{GeV}$, with other mass parameters set as $m_{\tilde{b}_2} = 130\,\text{GeV}$, $m_{\tilde{\chi}_2^0} = 230\,\text{GeV}$, and $m_{\tilde{\chi}_1^0} = 100\,\text{GeV}$. The bin numbers correspond to the order of the signal regions in the yield tables in Ref. [164] and are reproduced in Tab. A.2. The

Table A.2: `HighRes` bin numbering scheme as in Ref. [164].

Bin	M_R range	R^2 range
0	[150, 250]	[0.00, 0.05]
1	[150, 250]	[0.05, 0.10]
2	[150, 250]	[0.10, 0.15]
3	[150, 250]	[0.15, 1.00]
4	[250, 400	[0.00, 0.05]
5	[250, 400]	[0.05, 0.10]
6	[250, 400]	[0.10, 1.00]
7	[400, 1400]	[0.00, 0.05]
8	[400, 1400]	[0.05, 1.00]
9	[1400, 3000]	[0.00, 1.00]

normalization for each signal model is taken from the mode (i.e. "best-fit") signal cross section of the posterior density in the `HighRes` box. Fig. A.4 (top), shows the 95% CL combined upper limit on the cross section for model A. Finally, Fig. A.5 (top) shows the maximum significance Z as well as the best fit signal cross section for model A as a function of $m_{\tilde{b}_2}$.

The bottom of Fig. A.3-A.5 are the analogous results for model B. The chosen model B mass points in Fig. A.3 are $m_{\tilde{b}_1} = 500\,\text{GeV}$ or $m_{\tilde{b}_1} = 800\,\text{GeV}$, $m_{\tilde{\chi}_2^0} = 230\,\text{GeV}$, and $m_{\tilde{\chi}_1^0} = 100\,\text{GeV}$. The limit and significance scans in Fig. A.4 and A.5 are performed as a function of the $\tilde{b}_1$ mass. For model B, we also compare both the excluded cross section at 95% CL and the best-fit cross section as a function of the $\tilde{b}_1$ mass to the NLO+NLL predicted cross section at $\sqrt{s} = 8\,\text{TeV}$ [63, 64, 65, 66, 67, 69]. We find the 8 TeV data excludes bottom squark pair prodction below $m_{\tilde{b}_1} = 330\,\text{GeV}$ for the chosen neutralino masses of $m_{\tilde{\chi}_2^0} = 230\,\text{GeV}$ and $m_{\tilde{\chi}_1^0} = 100\,\text{GeV}$. More interestingly, the largest combined significance is 1.8σ for $m_{\tilde{b}_1} = 500\,\text{GeV}$ and the

best-fit cross section is 0.4 pb, which is of the same order of magnitude as the predicted cross section.

A.7 Discussion and summary

In this appendix, we proposed two simplified models of bottom squark pair production for use in the interpretation of an excess observed by CMS in a search for SUSY in H+jets events using razor variables at $\sqrt{s} = 8\,\text{TeV}$ [164]. In model A, we considered the asymmetric production of a $\widetilde{b}_2\widetilde{b}_1$ pair, with the $\widetilde{b}_1 \to \widetilde{\chi}_1^0$, $\widetilde{b}_2 \to b\widetilde{\chi}_2^0$, and $\widetilde{\chi}_2^0 \to H\widetilde{\chi}_1^0$, where $\widetilde{\chi}_1^0$ is a neutralino LSP and we fix the mass splitting $m_{\widetilde{\chi}_2^0} - m_{\widetilde{\chi}_1^0} = 130\,\text{GeV}$. In model B, we considered the symmetric production of a $\widetilde{b}_1\widetilde{b}_1$ pair, with $\widetilde{b}_1 \to b\widetilde{\chi}_2^0$, $\widetilde{\chi}_2^0 \to H\widetilde{\chi}_1^0$, and $m_{\widetilde{\chi}_2^0} - m_{\widetilde{\chi}_1^0} = 130\,\text{GeV}$.

We scanned the bottom squark masses for a fixed LSP mass of $m_{\widetilde{\chi}_1^0} = 100\,\text{GeV}$ for both models and quantified the agreement with the data. We found the excess observed in data is broadly consistent with both models, with the largest signal significance being 1.8σ corresponding to model B with $m_{\widetilde{b}_1} = 500\,\text{GeV}$, $m_{\widetilde{\chi}_2^0} = 230\,\text{GeV}$, and $m_{\widetilde{\chi}_1^0} = 100\,\text{GeV}$. Interestingly, following this study, model B used by the CMS collaboration to interpret the results of the updated 13 TeV search for SUSY in the same channel [256], where the largest signal significance was found to be 2.1σ for the same masses of $m_{\widetilde{b}_1} = 500\,\text{GeV}$, $m_{\widetilde{\chi}_2^0} = 230\,\text{GeV}$, and $m_{\widetilde{\chi}_1^0} = 100\,\text{GeV}$.

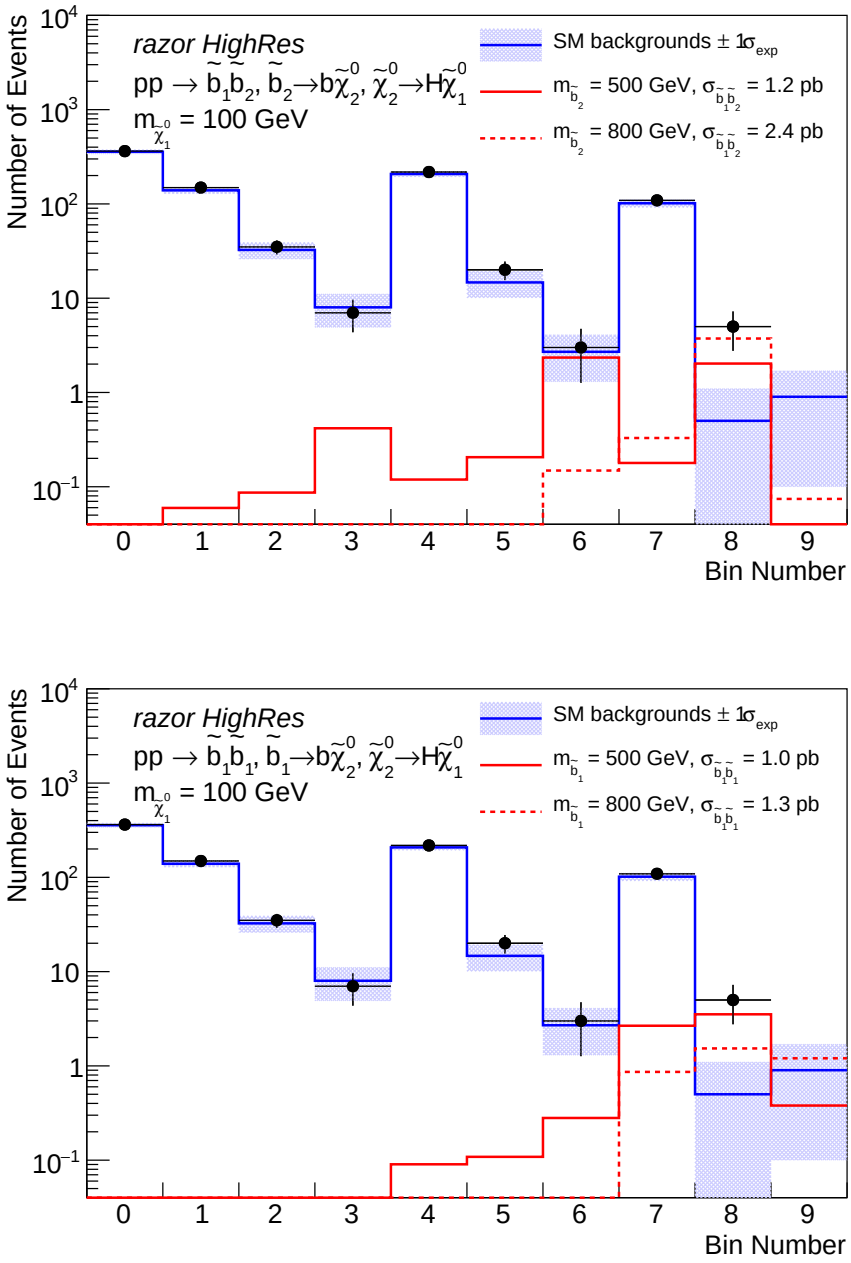

Figure A.3: (Top) The expected background and its uncertainty (multiplied by a factor of two as explained in the text) compared to the best-fit signal distribution in the `HighRes` box for two particular mass points, $m_{\tilde{b}_2} = 500\,\text{GeV}$ and $m_{\tilde{b}_2} = 800\,\text{GeV}$, in model A. (Bottom) The expected background and its uncertainty (multiplied by a factor of two as explained in the text) compared to the best-fit signal distribution in the `HighRes` box for two particular mass points, $m_{\tilde{b}_1} = 500\,\text{GeV}$ and $m_{\tilde{b}_1} = 800\,\text{GeV}$, in model B [44]. The bin numbers correspond to the order of the signal regions in the yield tables in Ref. [164] and are reproduced in Tab. A.2.

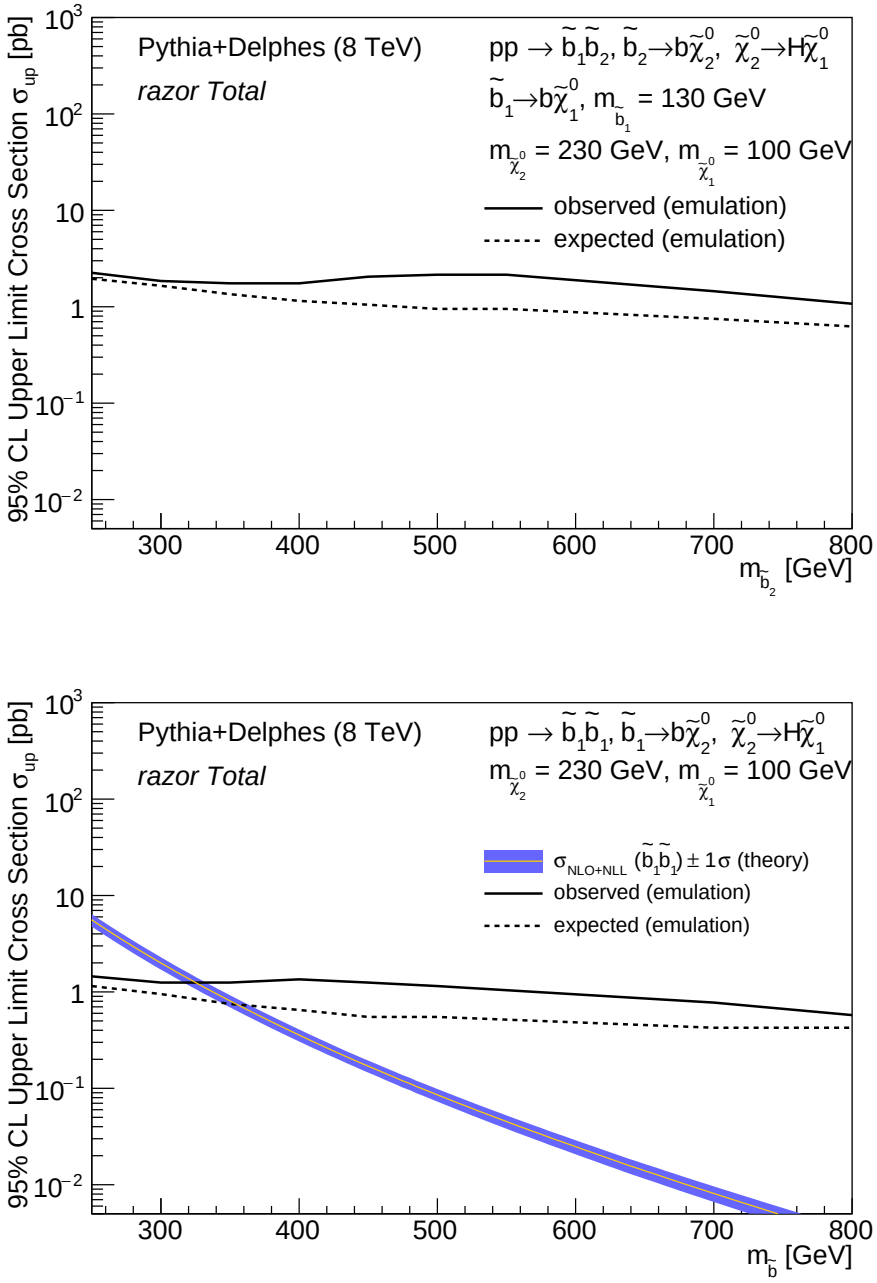

Figure A.4: (Top) The 95% CL upper limit on the cross section on $\tilde{b}_1\tilde{b}_2$ production in model A as a function of $m_{\tilde{b}_2}$ (black). (Bottom) The 95% CL upper limit on the cross section on $\tilde{b}_1\tilde{b}_1$ production in model B as a function of $m_{\tilde{b}_1}$ (black) compared to the NLO+NLL predicted cross section (yellow). Note, these scans assume $m_{\tilde{\chi}_1^0} = 100\,\text{GeV}$, $m_{\tilde{\chi}_2^0} = 230\,\text{GeV}$, and for model A $m_{\tilde{b}_1} = 130\,\text{GeV}$ [44].

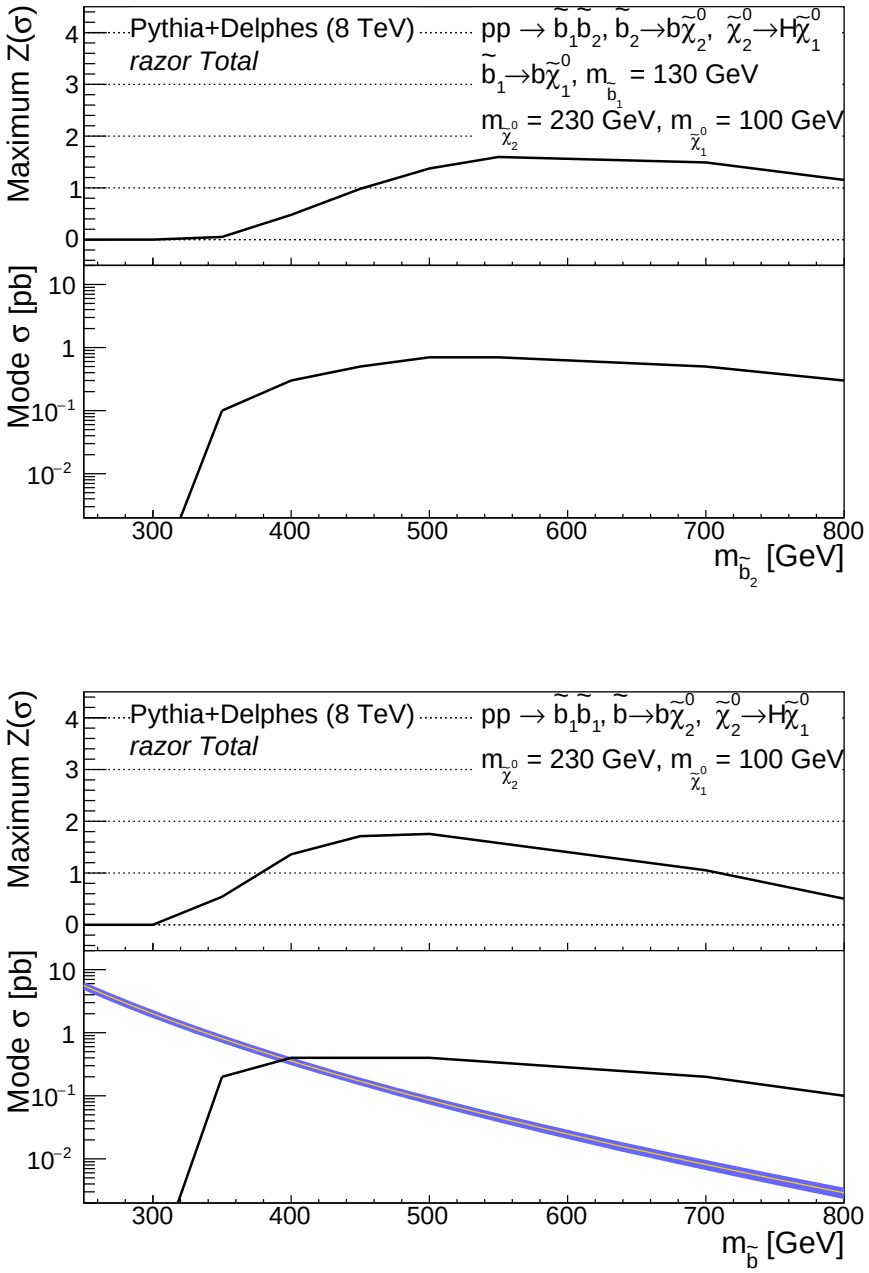

Figure A.5: (Top) The maximum significance $Z(\sigma)$ for a given $m_{\tilde{b}_2}$ in the top panel and the "best fit" signal cross section σ in the bottom panel for model A. (Bottom) The maximum significance $Z(\sigma)$ for a given $m_{\tilde{b}_1}$ in the top panel and the "best fit" signal cross section σ in the bottom panel for model B. Note, these scans assume $m_{\tilde{\chi}_1^0} = 100\,\text{GeV}$, $m_{\tilde{\chi}_2^0} = 230\,\text{GeV}$, and for model A $m_{\tilde{b}_1} = 130\,\text{GeV}$ [44].

Appendix B

SEARCHES FOR NEW PHYSICS IN THE DIJET MASS SPECTRUM AT $\sqrt{S} = 13\,\text{TEV}$

Deep inelastic proton-proton (pp) collisions often produce two or more energetic jets when the constituent partons are scattered with large transverse momenta (p_T). The invariant mass m_jj of the pair of jets having the largest values of p_T in the event (the dijet) has a spectrum that is predicted by quantum chromodynamics (QCD) to fall steeply and smoothly with increasing dijet mass. Many extensions of the standard model predict the existence of new massive particles that couple to quarks (q) and gluons (g) and can be detected as resonances in the dijet mass spectrum. One example is a model in which dark matter (DM) couples to standard model particles through a DM mediator that is also a dijet resonance [265]. Here we report a search for narrow resonances, those with natural widths that are small compared to the experimental resolution (up to $\sim 10\%$ of the resonance mass).

This appendix presents the results of two searches for dijet resonances, using data collected with the CMS detector in pp collisions at $\sqrt{s} = 13\,\text{TeV}$ with an integrated luminosity of $12.9\,\text{fb}^{-1}$. First, a *low-mass* search, for resonances with mass between 0.6 and 1.6 TeV, is performed using dijets that are reconstructed in the high-level trigger in a process called *data scouting* [155]. Data scouting was previously used for a low-mass search by CMS at $\sqrt{s} = 8\,\text{TeV}$ [157], and a similar trigger-level search was recently reported by ATLAS at $\sqrt{s} = 13\,\text{TeV}$ [266]. Second, a *high-mass* search, for resonances with mass above 1.6 TeV, is performed using dijets from the normal reconstruction chain. Similar high-mass searches were published many times by CMS and ATLAS at $\sqrt{s} = 13\,\text{TeV}$ [267, 268], 8 TeV [269, 270, 271] and 7 TeV [272, 273, 274, 275, 276, 277, 278] using strategies reviewed in Ref. [279].

The low-mass search was partially motivated by the excess at 750 GeV in both the CMS [25] and ATLAS [26] diphoton mass spectra in 2015 13 TeV data. To effectively search in this mass range with minimal systematic uncertainty due to the trigger, it is necessary to use the data scouting tech-

nique with Calo jets, as it allows the dijet resonance search to begin at $m_{jj} \gtrsim 450\,\text{GeV}$ with full trigger efficiency. Due to tighter trigger thresholds (explained in Sec.5.8), the corresponding data scouting technique using jets reconstructed with the particle-flow algorithm (PF jets) [168, 169] requires $m_{jj} \gtrsim 750\,\text{GeV}$ for full trigger efficiency, which does not permit a robust background estimation at 750 GeV. Unfortunately, more recent results using additional 13 TeV data collected in 2016 by CMS [27] and ATLAS [28] suggest the diphoton excess at $m_{\gamma\gamma} = 750\,\text{GeV}$ is most likely a statistical fluctuation.

We present model-independent searches and, in addition, consider the following models of s-channel dijet resonances: string resonances [280, 281], scalar diquarks [282], axigluons [283, 284], colorons [285, 284], excited quarks (q^*) [286, 287], color-octet scalars [288], new gauge bosons (W' and Z') with SM-like or leptophobic couplings [289], and Randall–Sundrum (RS) gravitons (G) [290]. We note that the anomalous coupling of the color-octet scalar model used is $k_s^2 = 1/2$ [291], reducing the width and cross section of this model by a factor of $1/2$ compared to previous CMS searches, and otherwise the specific choices of parameters for the models are the same as in Ref. [272].

We also interpret the results of the searches in the context of a simplified model of dark matter (DM) production with a vector or axial-vector mediator that couples to DM particles and quarks [292, 293, 294]. This is the first DM-centric interpretation of a dijet search performed by CMS.

B.1 Measurement of the invariant mass spectra

Reconstruction and trigger

The particle-flow (PF) algorithm [168, 169] is used to reconstruct the particles in an event and to identify them as muons, electrons, photons, and either charged or neutral hadrons.

Jets are reconstructed from either particles, giving PF jets, or from calorimeter towers, giving Calo jets. To reconstruct both types of jets we use the anti-k_T algorithm [131] with a distance parameter of 0.4, implemented in the FastJet package [295]. For PF jets, charged PF candidates not originating from the primary vertex are removed prior to the jet finding. For both types of jets, an event-by-event jet-area-based correction [124, 125, 296] is applied

to the jets to remove the estimated energy from additional collisions in the same or adjacent bunch crossings (pileup).

Events are selected using a two-tier trigger system. Events satisfying loose jet requirements at the first level (L1) are examined by the high-level trigger (HLT). The high-level triggers use H_T, the scalar sum of the jet p_T from all jets in the event with $p_T > 40\,\text{GeV}$ and $|\eta| < 3$. For the high-mass search PF jets are used to compute H_T, and events are accepted if they pass the HLT requiring $H_T > 800\,\text{GeV}$. For the high-mass search we select events with $m_{jj} > 1058\,\text{GeV}$ for which the combined L1 trigger and HLT are found to be fully efficient. For the low-mass search, when an event passes the HLT trigger the jets reconstructed at the HLT are directly saved, along with a few other necessary objects reconstructed at HLT. The shorter time for event reconstruction and the reduced event size saved at HLT allows a reduced H_T threshold compared to the high-mass search. For the low-mass search Calo jets are used to compute H_T, the threshold is $H_T > 250\,\text{GeV}$, and we select events with $m_{jj} > 453\,\text{GeV}$ for which the trigger is fully efficient.

Event preselection

At least one reconstructed vertex is required with $|z| < 24\,\text{cm}$. The primary vertex is defined as the vertex with the highest sum of p_T^2 of the associated tracks. The jet momenta and energies are corrected using calibration constants obtained from simulation, test beam results, and pp collision data at $\sqrt{s} = 13\,\text{TeV}$, using methods described in Ref. [296] with all *in situ* calibrations obtained from the current data. All jets are required to have $p_T > 30\,\text{GeV}$ and $|\eta| < 2.5$. The two jets with largest p_T are defined as the leading jets. Jet identification (ID) criteria are applied to remove spurious jets associated with calorimeter noise. The jet ID for PF jets is described in Ref. [297]. The jet ID for Calo jets requires that the fraction of jet energy deposited within the electromagnetic calorimeter be between 5% and 95% of the total jet energy. An event is rejected if either of the two leading jets fails the jet ID criteria.

Wide jet reconstruction and event selection

Geometrically close jets are combined into "wide jets" and used to determine the dijet mass, as in the previous CMS searches [275, 272, 271, 269]. The wide-jet algorithm, designed for dijet resonance event reconstruction,

reduces the analysis sensitivity to gluon radiation from the final-state partons. The two leading jets are used as seeds and the four-vectors of all other jets, if within $\Delta R = \sqrt{(\Delta\eta)^2 + (\Delta\phi)^2} < 1.1$, are added to the nearest leading jet to obtain two wide jets, which then form the dijet system. The background from t-channel dijet events peaks at large values of $|\Delta\eta_{jj}|$ and is suppressed by requiring the pseudorapidity separation of the two wide jets to satisfy $|\Delta\eta_{jj}| < 1.3$. The above requirements maximize the search sensitivity for isotropic decays of dijet resonances in the presence of QCD dijet background. For the low-mass search, after wide jet reconstruction and event selection, we use a correction derived from a smaller sample of dijet data to calibrate the wide jets reconstructed from Calo jets at HLT. With this correction, based on a dijet balance tag-and-probe method similar to that discussed in Ref. [127], the wide jets from Calo jets have the same response as those reconstructed from PF jets.

Dijet mass spectra and fits

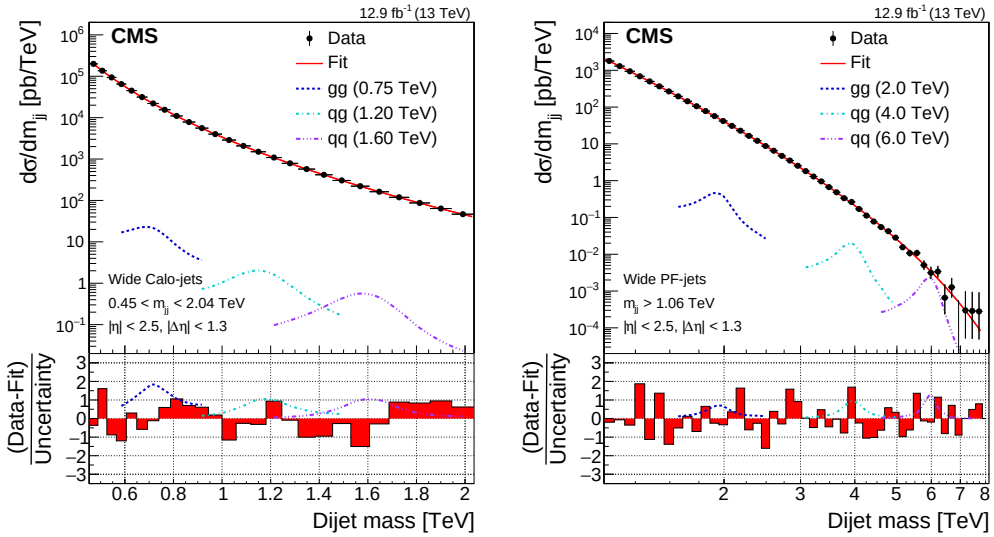

Figure B.1: Dijet mass spectra (points) compared to a fitted parameterization of the background (solid curve) for the low-mass search (left) and the high-mass search (right) [158, 44]. The lower panel in each plot shows the difference between the data and the fitted parametrization, divided by the statistical uncertainty of the data. Predicted signals from narrow gluon-gluon, quark-gluon, and quark-quark resonances are shown with cross section equal to the observed upper limit at 95% CL.

Fig. B.1 shows the dijet mass spectra, defined as the observed number of events in each bin divided by the integrated luminosity and bin width, with predefined bins of width corresponding to the dijet mass resolution [277]. The highest mass event has a dijet mass of 7.7 TeV and is shown in Fig. B.2. The dijet mass spectra for the high-mass search and for the low-mass search

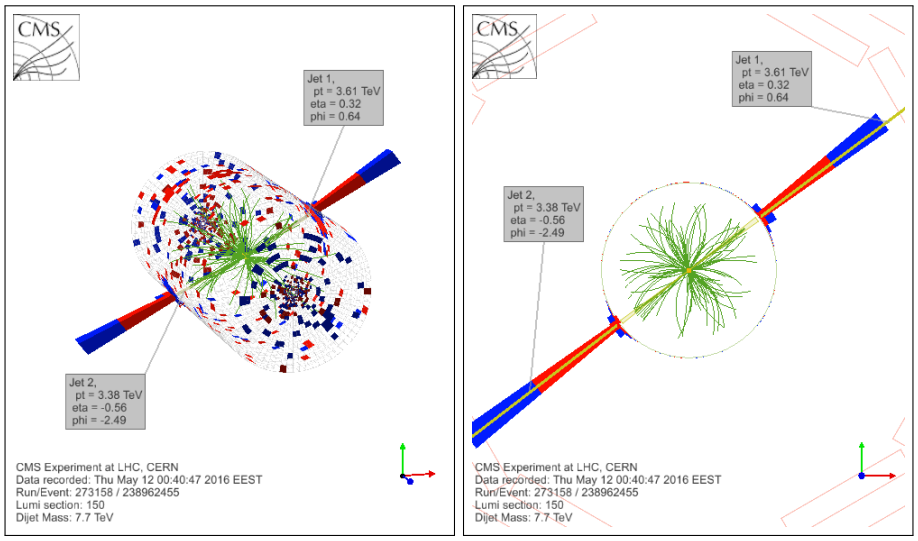

Figure B.2: The event with the highest dijet invariant mass: three dimensional view (left), 2D view in the (ρ,ϕ) plane (right) [158]. The p_{T}, η, and ϕ values of the two wide jets are indicated. The invariant mass of the two wide jets is 7.7 TeV.

are fit with the following parameterization:

$$\frac{\mathrm{d}\sigma}{\mathrm{d}m_{\mathrm{jj}}} = \frac{p_0(1-x)^{p_1}}{x^{p_2+p_3\log(x)}}\,, \tag{B.1}$$

where $x = m_{\mathrm{jj}}/\sqrt{s}$ and p_0, p_1, p_2, and p_3 are four fitted parameters. The functional form in Eqn. B.1 was also used in previous searches [157, 267, 277, 275, 272, 271, 269, 268, 278, 276, 273, 274, 270, 298] to describe the data. In Fig. B.1 we show the result of binned maximum likelihood fits, which yields the following chi-squared per number of degrees of freedom: $\chi^2/\mathrm{NDF} = 33.3/42$ for the high-mass search, $\chi^2/\mathrm{NDF} = 17.3/22$ for the low-mass search. The dijet mass spectra are well modeled by the background fits. In the lower panels of Fig. B.1, in the region of dijet mass between 1.1 and 2 TeV, the bin-by-bin differences between the data and the background fit are not identical in the two searches because fluctuations in

reconstructed dijet mass for Calo jets and PF jets are not completely correlated.

B.2 Search

We search in the dijet mass spectrum for narrow resonances. Fig. B.3 shows examples of dijet mass distributions for simulated signal events generated with the PYTHIA 8 [299] program. The predicted mass distributions have

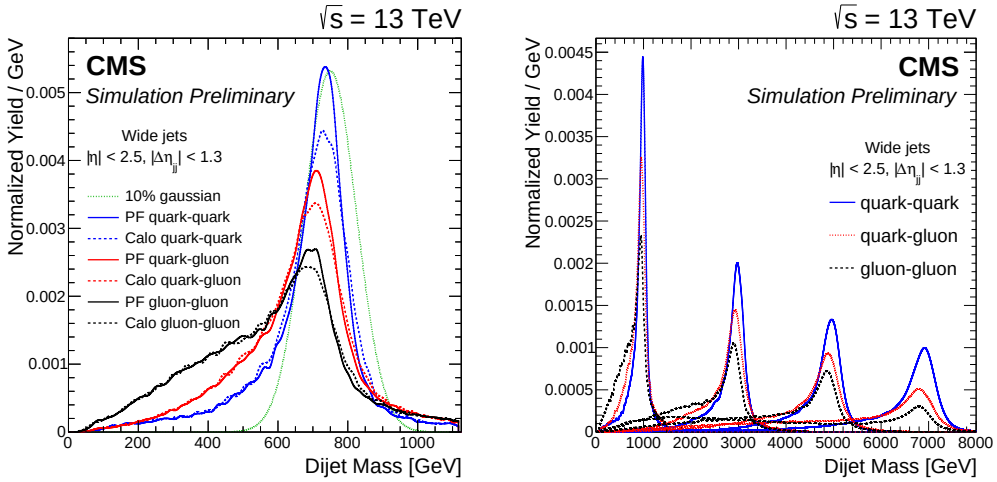

Figure B.3: The reconstructed resonance mass spectrum predicted by the PYTHIA 8 MC event generator including simulation of the detector [158]. Resonances from quark-quark processes modeled by $q\bar{q} \to G \to q\bar{q}$ (blue), quark-gluon processes modeled by $qg \to q^* \to qg$ (red), and gluon-gluon processes modeled by $gg \to G \to gg$ (black), where G is an RS graviton and q^* is an excited quark. (left) Resonances generated with a mass of 750 GeV are shown for wide jets from PF jet reconstruction (solid) and Calo jet reconstruction (dashed). Also shown is a hypothetical Gaussian shape (dotted green) with a mean mass of 750 GeV and an RMS width equal to 10% of the mean mass. (right) Resonances generated with a mass of 1, 3, 5, and 7 TeV are shown for wide jets from PF jet reconstruction.

Gaussian cores from the jet energy resolution, and tails towards lower mass values primarily from QCD radiation. The contribution of this low-mass tail to the lineshape depends on the parton content of the resonance (qq, qg, or gg). Resonances containing gluons, which emit QCD radiation more strongly than quarks, have a more pronounced tail. In Fig. B.3, for a resonance mass of 750 GeV, we also show a hypothetical Gaussian shape with an RMS width of 10%, which is one of the widths used by the ATLAS experiment for their generic limits on Gaussian resonances. Fitting the core

of the CMS qq resonance lineshape for Calo jets to a truncated Gaussian also gives an RMS width of approximately 10% at the resonance mass value of 750 GeV. Note that the expected distributions of dijet resonances from PYTHIA differ from a Gaussian shape centered at the resonance mass. This is primarily because of QCD radiation which produces significant tails and shifts the peak to a lower value of dijet mass. These real physical effects in the PYTHIA resonance shapes result in lower search sensitivity compared to hypothetical Gaussian shapes which neglect these effects.

Fig. B.1 includes the signal distributions of quark-quark, quark-gluon and gluon-gluon resonances with signal cross sections excluded at 95% CL by this analysis, as described below. There is no evidence for a narrow resonance in the data, as seen in Fig. B.1. The most significant excess in the data relative to the background fit occurs in the low-mass search around 800 GeV in dijet mass. Fitting this data to a gluon-gluon resonance with a mass of 850 GeV yields a significance of 2.6 standard deviations.

B.3 Model-independent interpretation

We use the dijet mass spectrum from wide jets, the background parameterization, and the dijet resonance shapes to set limits on new particles decaying to the parton pairs qq (or $q\bar{q}$), qg, and gg. A separate limit is determined for each final state (qq, qg and gg) because of the dependence of the dijet resonance shape on the type of the two final-state partons.

The dominant sources of systematic uncertainty are the jet energy scale, jet energy resolution, integrated luminosity, and the estimation of background. The uncertainty in the jet energy scale is 2%, determined from Run 2 data using the methods described in Ref. [296]. This uncertainty is propagated to the limits by shifting the dijet mass shape for signal by $\pm 2\%$. The uncertainty in the jet energy resolution translates into an uncertainty of 10% in the resolution of the dijet mass [296], and is propagated to the limits by increasing and decreasing by 10% the reconstructed width of the dijet mass shape for signal. The uncertainty in the integrated luminosity is 6.2%, and is propagated to the normalization of the signal. Changes in the values of the parameters describing the background introduce a change in the signal strength that is accounted for as a systematic uncertainty.

The modified frequentist method [181, 300] is utilized to set upper limits on

signal cross sections, following the prescription described in Ref. [184] and Sec. 7.5 of this thesis. We use a multi-bin counting experiment likelihood, which is a product of Poisson distributions corresponding to different bins. We evaluate the likelihood independently at each value of resonance pole mass from 600 GeV to 1600 GeV in 50 GeV steps in the low-mass search, and from 1.6 TeV to 7.5 TeV in 100 GeV steps in the high-mass search. Gaussian distributions are used to model systematic uncertainties in the jet energy scale and jet energy resolution, and log normal distributions are used to model uncertainties in the integrated luminosity, treated as nuisance parameters within a constraint placed on the likelihood. For this methodology, the systematic uncertainty on the background is automatically evaluated via profiling, effectively refitting for the optimal values of the background parameters for each value of resonance cross section. The procedure gives the same limits as the Bayesian procedure used previously for dijet resonance searches at CMS [269]. For both the Bayesian and modified frequentist statistical procedures we find that the background systematic uncertainty has the largest effect on the limit. The amount the background uncertainty affects the limit depends significantly on the signal shape and the resonance mass, with the largest effect for the gluon-gluon resonances and the smallest effect for the hypothetical Gaussian resonances in the low-mass search, and the effect decreases as the resonance mass increases.

The potential bias introduced through the choice of background parameterization was investigated using signal injection and extraction tests with two background parameterization choices. First, we generated pseudo-data with injected signal of strength μ using an alternative background parameterization

$$\frac{\mathrm{d}\sigma}{\mathrm{d}m_{\mathrm{jj}}} = p_0 \exp\left(p_1 x^{p_2} + p_1(1-x)^{p_3}\right) . \tag{B.2}$$

Then, we fit these data with the nominal background parameterization of Eqn. B.1 in order to extract the measured signal strength $\hat{\mu}$ and its uncertainty σ_μ. The resulting bias $(\hat{\mu} - \mu)/\sigma_\mu$ was found to be negligible as illustrated in Fig. B.4.

Figures B.5-B.7 and Tables B.2-B.3 show the model-independent observed upper limits at 95% confidence level (CL) on $\sigma \times B \times A$, i.e., the product of the cross section (σ), the branching fraction (B), and the acceptance (A) for the kinematic requirements $|\Delta\eta_{\mathrm{jj}}| < 1.3$ and $|\eta| < 2.5$, for narrow res-

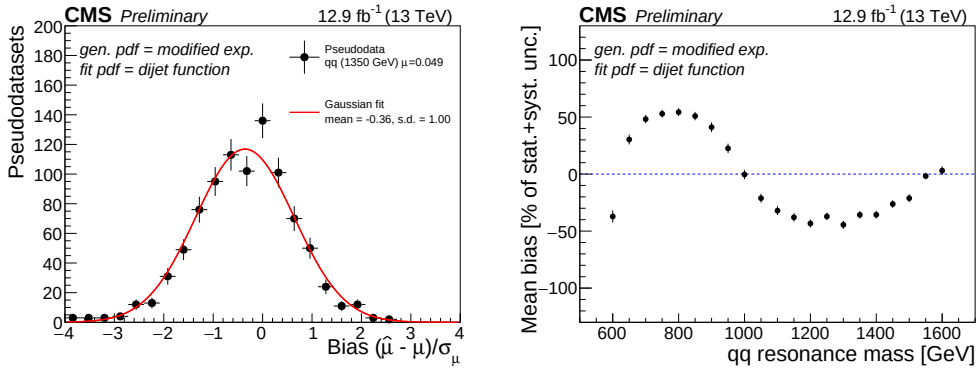

Figure B.4: Bias $(\hat{\mu} - \mu)/\sigma_\mu$ when generating pseudodata with the alternative parameterization of Eqn. B.2 and fitting with the nominal background parameterization of Eqn. B.1 for a qq resonance of mass 1350 GeV with a signal strength $\mu = 0.049$ corresponding to the 95% CL limit on $\sigma \times B \times A$ of 0.49 pb (left). Bias for qq resonances as a function of mass from 600 GeV to 1600 GeV (right) [44].

onances. In Fig. B.5, for comparison purposes only, limits are also shown from Gaussian shapes with an RMS width equal to 10% of the mass. The acceptance of the minimum dijet mass requirement in each search has been taken into account by correcting the limits. The acceptance of the minimum dijet mass requirement in each search has been evaluated separately for qq, qg, and gg resonances, and has been taken into account by correcting the limits, and therefore does not appear in the acceptance A. The corrections are independent of the spin and coupling of the narrow resonance at the one percent level. Figures B.5-B.7 also show the expected limits on the cross section and their bands of uncertainty. The difference in the limits for qq, qg, and gg, and Gaussian resonances at the same resonance mass originates from the difference in their lineshapes. We note that the limits from Gaussian resonances are smaller than can be expected from any physical model, as they do not have any tails due to radiation, and consequently they are narrower and located closer to the resonance pole than any combination of two partons can produce.

Figures B.8 and B.9 also show the observed signal significance as a function of resonance mass for both searches. No sizeable significance is found, with the largest being 2.6σ for an 850 GeV gg resonance.

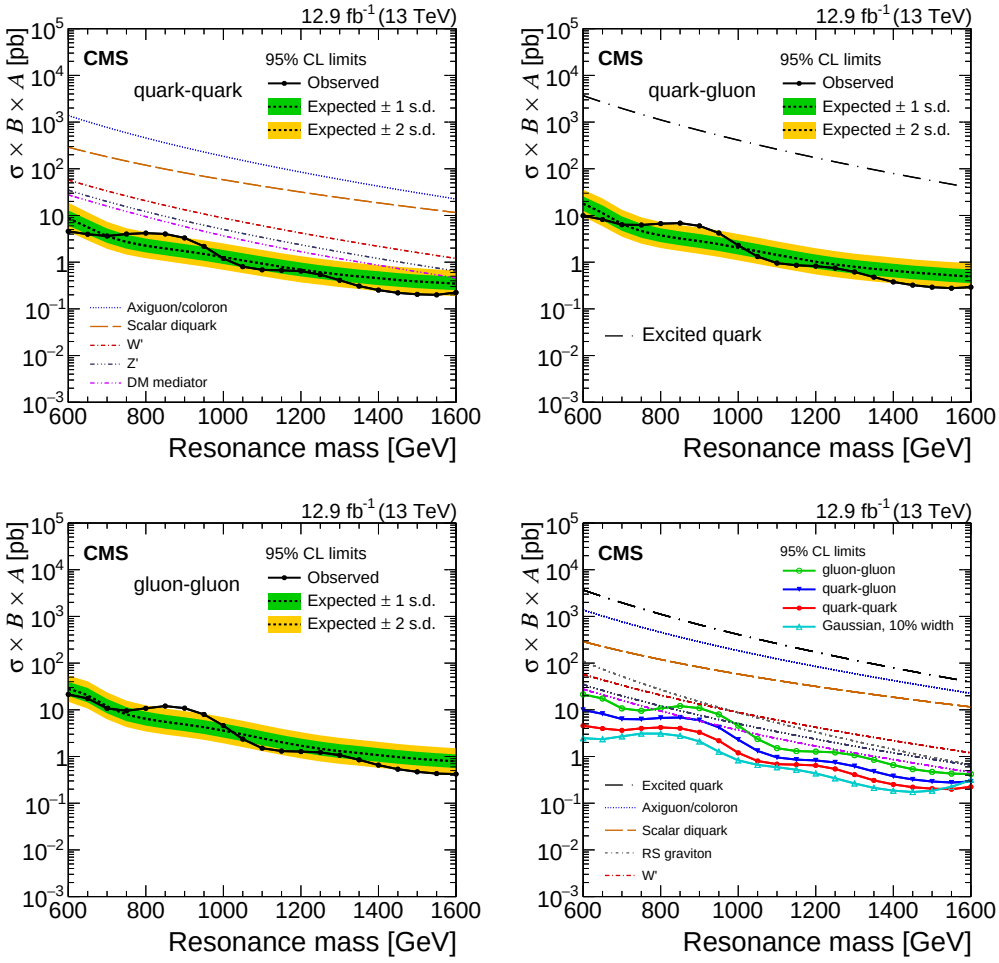

Figure B.5: Limits from the low-mass search [158, 44]. The observed 95% CL upper limits on the product of the cross section, branching fraction, and acceptance for quark-quark (top left), quark-gluon (top right), and gluon-gluon (bottom left) type dijet resonances. The corresponding expected limits (dashed) and their variation at the 1 and 2 standard deviation levels (shaded bands) are also shown. (bottom right) The observed limits (solid) are summarized for fully simulated shapes from all three physical types of resonances along with the limit for a hypothetical Gaussian shape with RMS width equal to 10% of the mean mass. Limits are compared to the predicted cross sections of excited quarks [286, 287], axigluons [283], colorons [285], scalar diquarks [282], new gauge bosons W′ and Z′ with SM-like couplings [289], a dark matter mediator for $m_{\mathrm{DM}} = 1\,\mathrm{GeV}$ [292, 301], and RS gravitons [290].

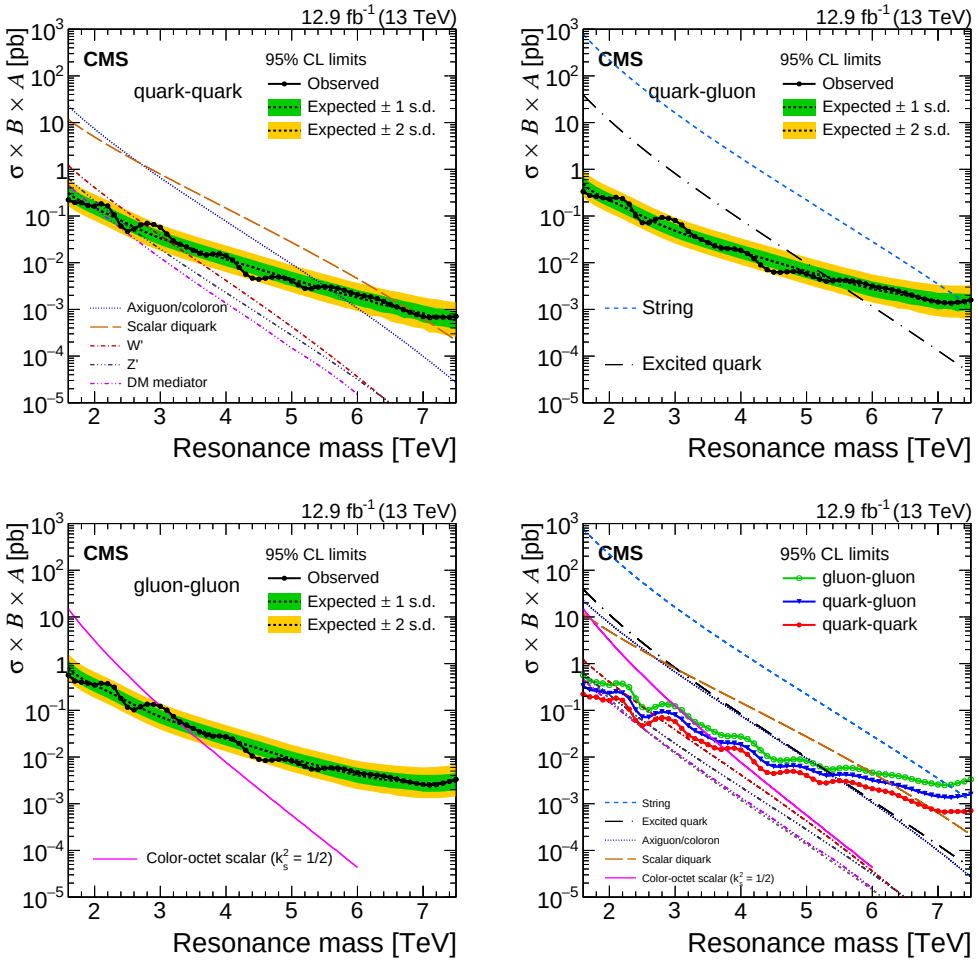

Figure B.6: Limits from the high-mass search [158, 44]. The observed 95% CL upper limits on the product of the cross section, branching fraction, and acceptance for quark-quark (top left), quark-gluon (top right), and gluon-gluon (bottom left) type dijet resonances. The corresponding expected limits (dashed) and their variation at the 1 and 2 standard deviation levels (shaded bands) are also shown. (bottom right) The observed limits (solid) are summarized. Limits are compared to the predicted cross sections of string resonances [280, 281], excited quarks [286, 287], axigluons [283], colorons [285], scalar diquarks [282], color-octet scalars [288], new gauge bosons W′ and Z′ with SM-like or leptophobic couplings [289], a dark matter mediator for $m_{\mathrm{DM}} = 1\,\mathrm{GeV}$ [292, 301], and RS gravitons [290].

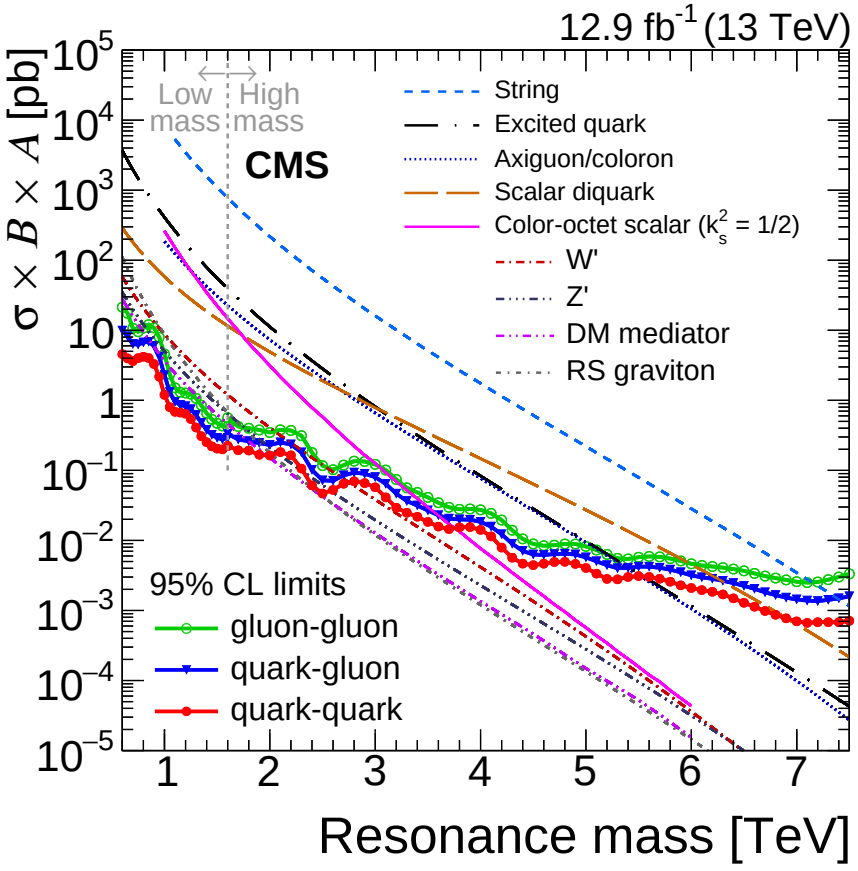

Figure B.7: Limits from both the low-mass and high-mass search [158, 44]. The observed 95% CL upper limits on the product of the cross section, branching fraction, and acceptance for quark-quark, quark-gluon, and gluon-gluon type dijet resonances. The observed limits (solid) are presented from the low-mass search, for resonance masses between 0.6 TeV and 1.6 TeV, and from the high-mass search for resonance masses greater than or equal to 1.6 TeV. Limits are compared to the predicted cross sections of string resonances [280, 281], excited quarks [286, 287], axigluons [283], colorons [285], scalar diquarks [282], color-octet scalars [288], new gauge bosons W′ and Z′ with SM-like or leptophobic couplings [289], a dark matter mediator for $m_{\mathrm{DM}} = 1$ GeV [292, 301], and RS gravitons [290].

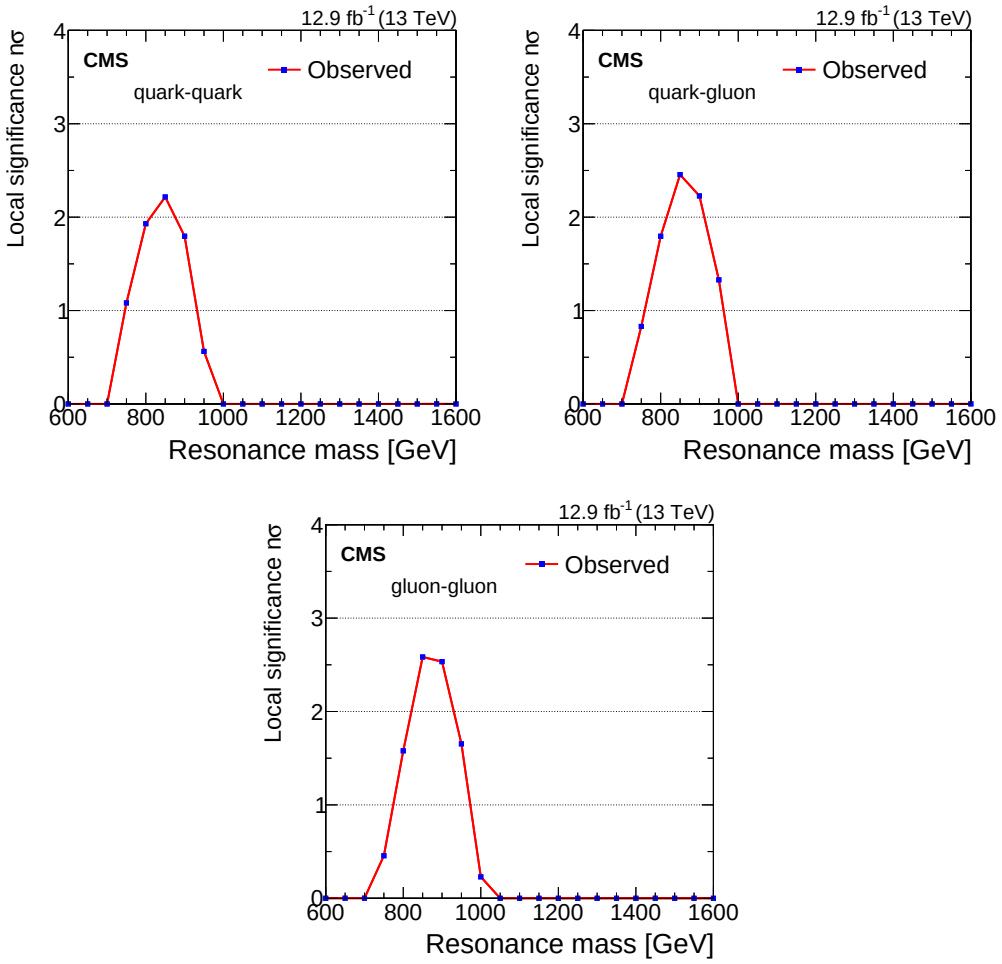

Figure B.8: Observed signal significance from the low-mass search for quark-quark (top left), quark-gluon (top right), and gluon-gluon (bottom) type dijet resonances [44].

B.4 Model-dependent interpretation

All upper limits presented can be compared to the parton-level predictions of $\sigma \times B \times A$, without detector simulation, to determine mass limits on new particles. The model predictions shown in Fig. B.5-B.7 are calculated in the narrow-width approximation [279] using the CTEQ6L1 [302] PDF at leading order, with a next-to-leading order correction factor included for the W′, Z′, and axigluon/coloron models [284]. The acceptance is evaluated at the parton level for the resonance decay to two partons. In the case of isotropic decays it is $A \approx 0.6$ independent of resonance mass. For a given model, new particles are excluded at 95% CL in mass regions where the theoretical prediction lies at or above the observed upper limit for the appropriate final

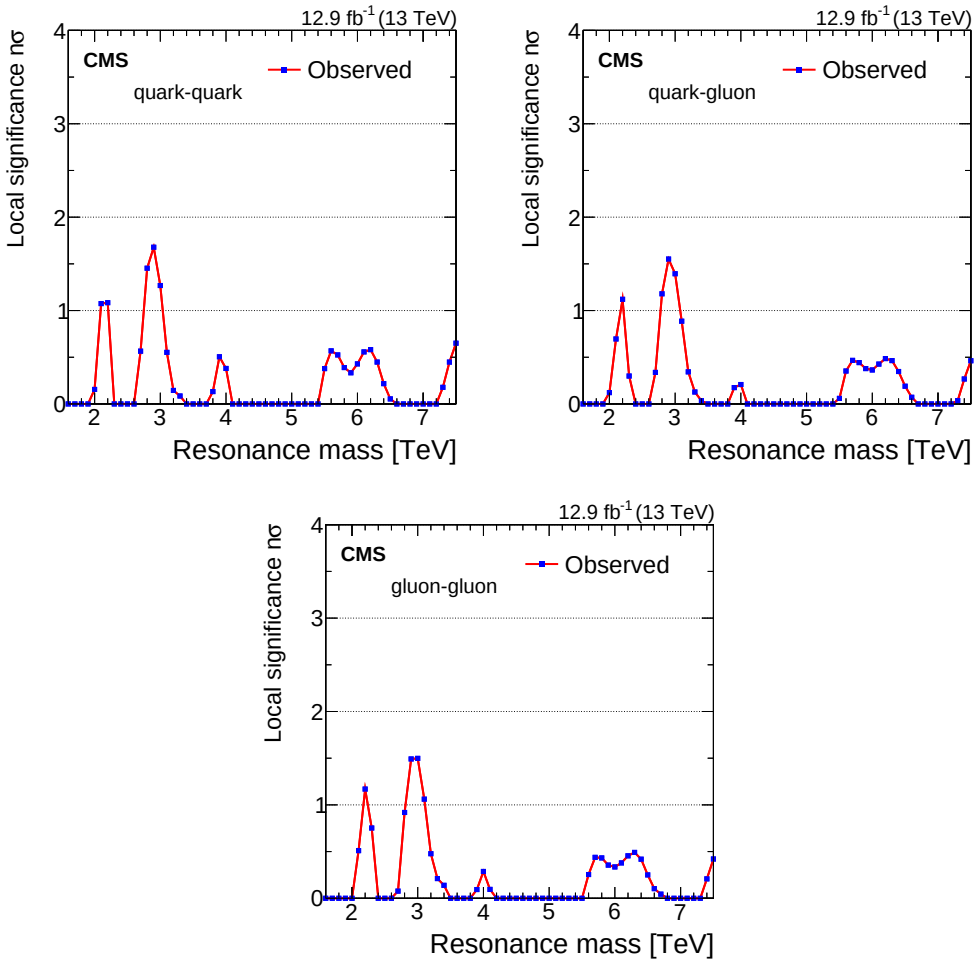

Figure B.9: Observed signal significance from the high-mass search for quark-quark (top left), quark-gluon (top right), and gluon-gluon (bottom) type dijet resonances [44].

state of Fig. B.5-B.7. For the RS graviton model, for which 60% (40%) of the cross section comes from sub-proceses with only quarks (gluons) in the final state, we obtain mass limits by comparing the RS graviton cross section curve to a weighted average of the limits in the quark-quark and gluon-gluon final states. Mass limits on all benchmark models are summarized in Table B.1 and are more stringent than the mass limits previously published by CMS [267] and ATLAS [268] in the dijet channel.

Following the theoretical framework of Ref. [293], the upper limits on the cross section of narrow qq resonances are translated into 95% CL upper limits on the coupling g_B of a hypothetical leptophobic resonance $Z'_B \to q\bar{q}$ as a function of its mass. The Z'_B production cross section scales with the square

Table B.1: Observed and expected mass limits at 95% CL from this analysis with 12.9 fb^{-1} at $\sqrt{s} = 13$ TeV compared to previously published limits on narrow resonances from CMS with 2.4 fb^{-1} at $\sqrt{s} = 13$ TeV [267] and with 20 fb^{-1} at $\sqrt{s} = 8$ TeV [269]. The listed models are excluded between 0.6 TeV and the indicated mass limit by this analysis. For the Z' model, in addition to the observed mass limit listed below, this analysis also excludes the mass interval between 2.3 and 2.6 TeV.

Model	Final State	Observed (expected) mass limit [TeV] 12.9 fb^{-1} 13 TeV	2.4 fb^{-1} 13 TeV	20 fb^{-1} 8 TeV
String	qg	7.4 (7.4)	7.0 (6.9)	5.0 (4.9)
Scalar diquark	qq	6.9 (6.8)	6.0 (6.1)	4.7 (4.4)
Axigluon/coloron	$q\bar{q}$	5.5 (5.6)	5.1 (5.1)	3.7 (3.9)
Excited quark	qg	5.4 (5.4)	5.0 (4.8)	3.5 (3.7)
Color-octet scalar ($k_s^2 = 1/2$)	gg	3.0 (3.3)	—	—
W'	$q\bar{q}$	2.7 (3.1)	2.6 (2.3)	2.2 (2.2)
Z'	$q\bar{q}$	2.1 (2.3)	—	1.7 (1.8)
DM mediator ($m_{DM} = 1$ GeV)	$q\bar{q}$	2.0 (2.0)	—	—
RS graviton	$q\bar{q}$, gg	1.9 (1.8)	—	1.6 (1.3)

of the coupling g_B. Fig. B.10 shows the upper limits obtained with the low-mass search in the mass region from 600 to 1600 GeV and with the high-mass search in the mass region from 1.6 TeV to 3.7 TeV. The limits are competitive with the coverage of previous CMS searches at $\sqrt{s} = 8$ TeV [157] in the low-mass range and improve upon previous limits in the high-mass range. Previous exclusions obtained with similar searches at various collider energies [157, 268, 293, 270] are also shown.

The results of the dijet search also have an impact on the allowed parameter space in models of dark matter (DM) production at the LHC if the mediator is also accessible. We may use a similar simplified model to quantify this impact, consisting of a leptophobic vector (V) or axial-vector (AV) mediator Z'_B with couplings to quarks and the DM particle χ [292, 293, 294]:

$$\mathcal{L}_V = -g_{DM} Z'_{B\mu} \bar{\chi} \gamma^\mu \chi - g'_q \sum_q Z'_{B\mu} \bar{q} \gamma^\mu q \,, \tag{B.3}$$

$$\mathcal{L}_{AV} = -g_{DM} Z'_{B\mu} \bar{\chi} \gamma^\mu \gamma_5 \chi - g'_q \sum_q Z'_{B\mu} \bar{q} \gamma^\mu \gamma_5 q \,, \tag{B.4}$$

where g_{DM} is the coupling of the mediator to the DM particles and $g'_q = g'_B/6$ is the universal coupling of all quark flavors to the mediator. Fig. B.11 shows the most important diagrams for monojet and dijet searches.

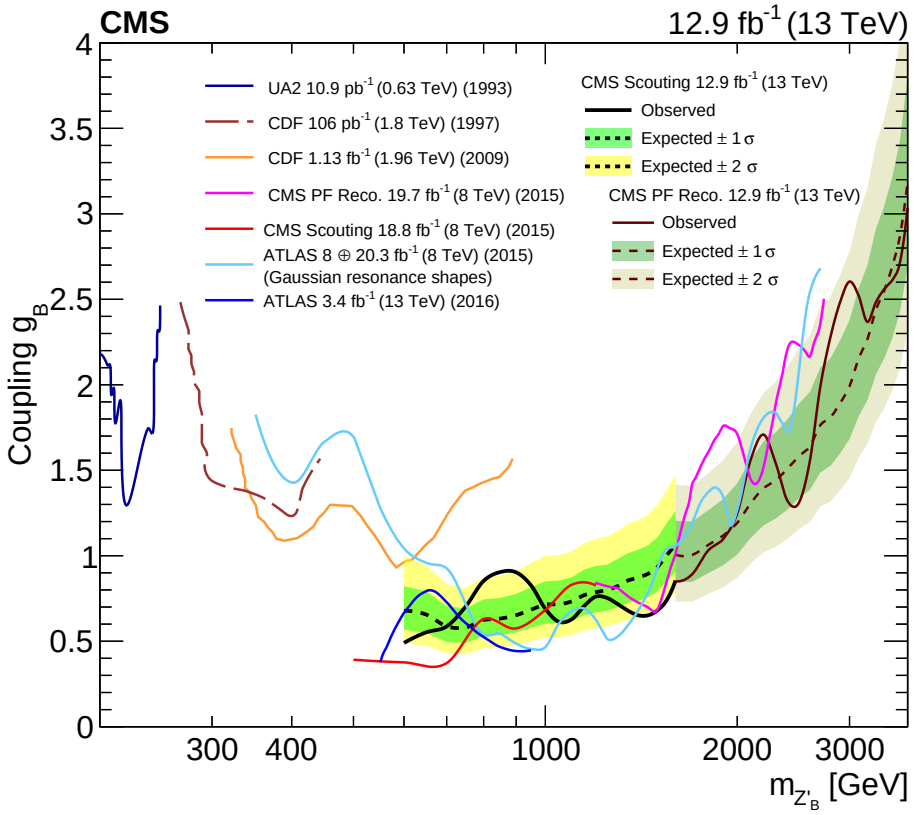

Figure B.10: Observed 95% CL upper limits on the coupling g_B of a hypothetical leptophobic resonance $Z'_B \to q\bar{q}$ [293] as a function of its mass [44]. The results from this study are compared to results obtained with similar searches at different collider energies [157, 268, 293, 270].

The results of the search for a narrow $q\bar{q}$ resonance may then be reinterpreted as a search for the mediator when it decays to quarks. In this model, the minimal decay width of the mediator is given by the sum of the partial widths for all decays into DM particles and quarks that are kinematically accessible, which we take to be $q = u, d, c, s, b$:

$$\Gamma^{tot} = \Gamma^{\chi\bar{\chi}} + 3\sum_{q}\Gamma^{q\bar{q}}\,. \tag{B.5}$$

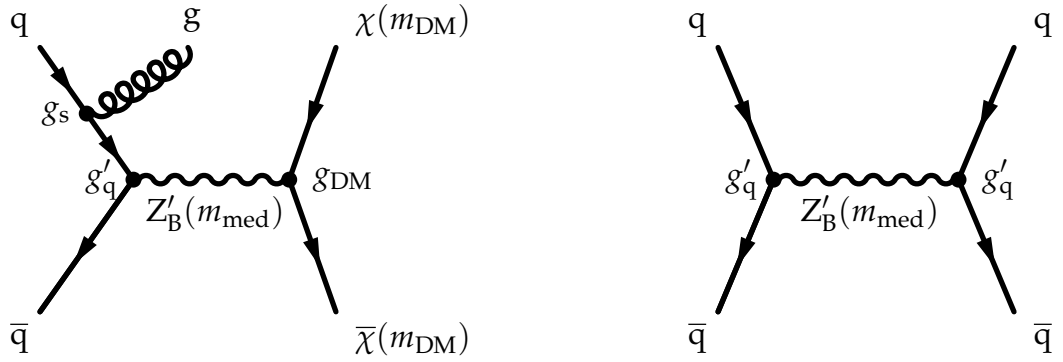

Figure B.11: Representative Feynman diagrams showing the pair production of dark matter particles in association with a radiated gluon from the initial state used in $E_T^{miss} + X$ (mono-X) searches (left) and the pair production of quarks used in dijet searches (right) via a vector or axial-vector Z'_B mediator [44]. The cross section and kinematics depend on the mediator and dark matter masses, and the mediator couplings to dark matter and quarks, respectively: (m_{med}, m_{DM}, g_{DM}, g'_q) [294].

The partial widths are given by:

$$\Gamma_V^{\chi\overline{\chi}} = \frac{g_{DM}^2 m_{med}}{12\pi}\left(1 - 4\frac{m_{DM}^2}{m_{med}^2}\right)^{1/2}\left(1 + 2\frac{m_{DM}^2}{m_{med}^2}\right), \tag{B.6}$$

$$\Gamma_{AV}^{\chi\overline{\chi}} = \frac{g_{DM}^2 m_{med}}{12\pi}\left(1 - 4\frac{m_{DM}^2}{m_{med}^2}\right)^{3/2}, \tag{B.7}$$

$$\Gamma_V^{q\overline{q}} = \frac{(g'_q)^2 m_{med}}{4\pi}\left(1 - 4\frac{m_q^2}{m_{med}^2}\right)^{1/2}\left(1 + 2\frac{m_q^2}{m_{med}^2}\right), \tag{B.8}$$

$$\Gamma_{AV}^{q\overline{q}} = \frac{(g'_q)^2 m_{med}}{4\pi}\left(1 - 4\frac{m_q^2}{m_{med}^2}\right)^{3/2}, \tag{B.9}$$

where m_{med} is the mediator mass, m_{DM} is the mass of the DM particle, which is assumed to be a Dirac fermion, and m_q is the quark mass. The two different types of contribution to the total width vanish for $m_{med} < 2m_{DM}$ and $m_{med} < 2m_q$, respectively.

To derive the limit on g'_B in this model in the case of a nonzero mediator decay width to DM particles $\Gamma^{\chi\overline{\chi}}$, it is simplest to begin with the limit on g_B in the case of zero decay width to DM particles (see Fig. B.10) and correct

for the DM width,

$$\sigma[Z'_B \to q\bar{q}|g'_B, g_{DM}] = \sigma(Z'_B \to q\bar{q}|g_B, g_{DM} = 0) \tag{B.10}$$

$$\Rightarrow \quad \frac{(g'_B)^4}{\Gamma^{q\bar{q}}(g'_B) + \Gamma^{\chi\bar{\chi}}} = \frac{g_B^4}{\Gamma^{q\bar{q}}(g_B)} \tag{B.11}$$

$$\Rightarrow \quad (g'_B)^2 = \frac{g_B^2}{2}\left(1 + \sqrt{1 + 4\frac{\Gamma^{\chi\bar{\chi}}}{\Gamma^{q\bar{q}}(g_B)}}\right) . \tag{B.12}$$

Fig. B.12 shows 95% CL exclusion regions in (m_{med},m_{DM}) plane for dijet searches [158, 157] and different E_T^{miss} based DM searches [303, 304, 305, 306] from CMS in the leptophobic vector and axial-vector models defined above. Following the recommendation of the LHC DM working group [292, 301, 294], the exclusions are computed for a universal quark coupling $g'_q = 0.25$ and for a DM coupling of $g_{DM} = 1.0$. The combination of the low- and high-mass searches as well as the search of Ref. [157] excludes all values of DM particle mass between 0.5 TeV and 2.0 TeV in mediator mass. The expected mediator mass exclusion limit increases with m_{DM} and goes as high as 2.7 TeV for heavy DM particles as the branching ratio to $q\bar{q}$ dominates. The exclusion limits are similar for the V and AV models, as expected. If $m_{DM} > m_{med}/2$, the mediator cannot decay to DM particles, and the dijet cross section from the mediator models becomes identical to that in the leptophobic Z′ model used in Fig. B.10 with a coupling $g'_q = g_q = 0.25$. Therefore for these values of m_{DM}, the limits on the mediator mass in Fig. B.12 are identical to the limits on the Z′ mass at $g'_q = 0.25$ in Fig. B.10. Similarly, if $m_{DM} = 0$, the limits on the mediator mass in Fig. B.12 are identical to the limits on the Z′ mass at $g'_q = g_q/\sqrt{1 + 16/(3N_f)} \approx 0.182$ in Fig. B.10, where N_f is the effective number of quark flavors contributing to the width of the resonance.

The search results presented in Fig. B.12 can also be compared with results from dark matter direct detection (DD) and indirect detection (ID) experiments [292]. As input for this comparison, we use the results for the (m_{med},m_{DM}) plane for fixed couplings g'_q and g_{DM}. To compare with DD and ID experiments, these limits are translated into the planes of DM mass versus the spin-independent (SI) or spin-dependent (SD) DM-nucleon cross section, $\sigma^{SI}_{DM\text{-}N}$ or $\sigma^{SD}_{DM\text{-}p}$, respectively. The SI DM-nucleon cross section takes

the form [292]:

$$\sigma^{\text{SI}}_{\text{DM-N}} = \frac{f^2(g'_{\text{q}}) g^2_{\text{DM}} \mu^2_{\text{N}\chi}}{\pi m^4_{\text{med}}} \tag{B.13}$$

$$\simeq 6.9 \times 10^{-41}\,\text{cm}^2 \cdot \left(\frac{g'_{\text{q}} g_{\text{DM}}}{0.25}\right)^2 \left(\frac{1\,\text{TeV}}{m_{\text{med}}}\right)^4 \left(\frac{\mu_{\text{N}\chi}}{1\,\text{GeV}}\right)^2 , \tag{B.14}$$

where $\mu_{\text{N}\chi} = m_{\text{N}} m_{\text{DM}}/(m_{\text{N}} + m_{\text{DM}})$ is the DM-nucleon reduced mass with $m_{\text{N}} \simeq 0.939\,\text{GeV}$, and for a vector mediator, $f(g'_{\text{q}}) = 3g'_{\text{q}}$. Similarly, the SD DM-nucleon cross section can be written as [292]:

$$\sigma^{\text{SD}}_{\text{DM-p}} = \frac{3 f^2(g'_{\text{q}}) g^2_{\text{DM}} \mu^2_{\text{N}\chi}}{\pi m^4_{\text{med}}} \tag{B.15}$$

$$\simeq 2.4 \times 10^{-42}\,\text{cm}^2 \cdot \left(\frac{g'_{\text{q}} g_{\text{DM}}}{0.25}\right)^2 \left(\frac{1\,\text{TeV}}{m_{\text{med}}}\right)^4 \left(\frac{\mu_{\text{N}\chi}}{1\,\text{GeV}}\right)^2 , \tag{B.16}$$

where, in general, the factor $f(g'_{\text{q}})$ could be different for protons and neutrons and depends separately on the individual quark-mediator couplings g'_{u}, g'_{d}, and g'_{s}:

$$f^{\text{p,n}}(g'_{\text{u}}, g'_{\text{d}}, g'_{\text{s}}) = \Delta^{(\text{p,n})}_{\text{u}} g'_{\text{u}} + \Delta^{(\text{p,n})}_{\text{d}} g'_{\text{d}} + \Delta^{(\text{p,n})}_{\text{s}} g'_{\text{s}} , \tag{B.17}$$

with $\Delta^{(\text{p})}_{\text{u}} = \Delta^{(\text{n})}_{\text{d}} = 0.84$, $\Delta^{(\text{p})}_{\text{d}} = \Delta^{(\text{n})}_{\text{u}} = -0.43$, and $\Delta^{(\text{p})}_{\text{s}} = \Delta^{(\text{n})}_{\text{s}} = -0.09$ [119]. Under the assumption that the coupling g'_{q} is universal, these factors are equal, $f^{\text{p}} = f^{\text{n}} = 0.32 g'_{\text{q}}$. As DD experiments quote 90% CL limits, the CMS limits are also recalculated to match this confidence level. Fig. B.13 shows the AV and V limits translated into the SD and SI planes, respectively, and compared to DD and ID experiments [307, 308, 309, 310, 311, 312, 313, 314].

B.5 Summary

This appendix presents two searches for narrow resonances decaying into a pair of jets, performed using proton-proton collisions at $\sqrt{s} = 13\,\text{TeV}$ corresponding to an integrated luminosity of $12.9\,\text{fb}^{-1}$. The first is a low-mass search based on calorimeter jets, reconstructed by the high level trigger and recorded in compact form (data scouting), and the second is a high-mass search based on particle-flow jets. The dijet mass spectra are observed to be smoothly falling distributions. In the analyzed data samples, there is no evidence for resonant particle production. Generic upper limits are

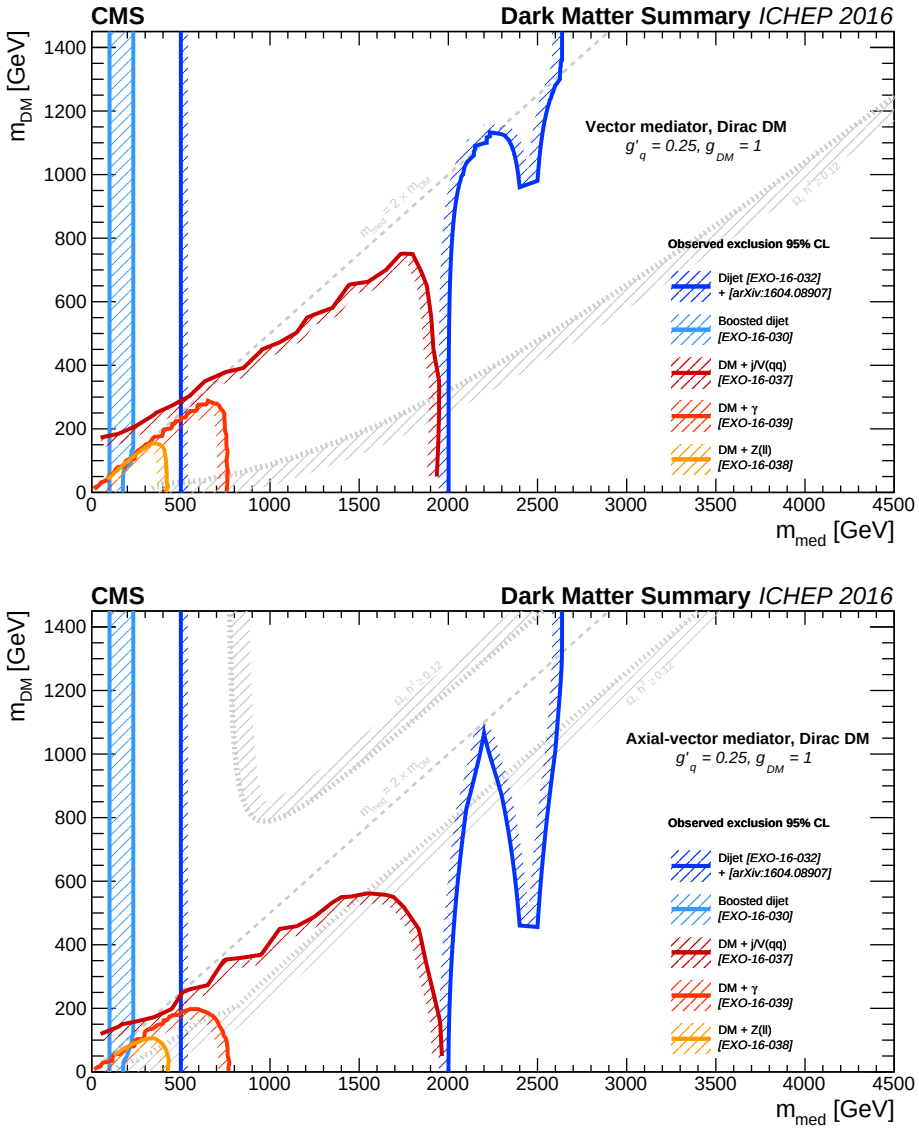

Figure B.12: 95% CL exclusion regions in (m_{med},m_{DM}) plane for dijet searches [158, 157] and different $E_{\text{T}}^{\text{miss}}$ based DM searches [303, 304, 305, 306] from CMS in the leptophobic vector (top) and axial-vector (bottom) models [315, 44]. Following the recommendation of the LHC DM working group [292, 301], the exclusions are computed for a universal quark coupling $g'_{\text{q}} = 0.25$ and for a DM coupling of $g_{\text{DM}} = 1.0$. It should be noted that the relic density contours, unitarity curves, and the exclusion regions of the different searches strongly depend on the chosen coupling and model scenario.

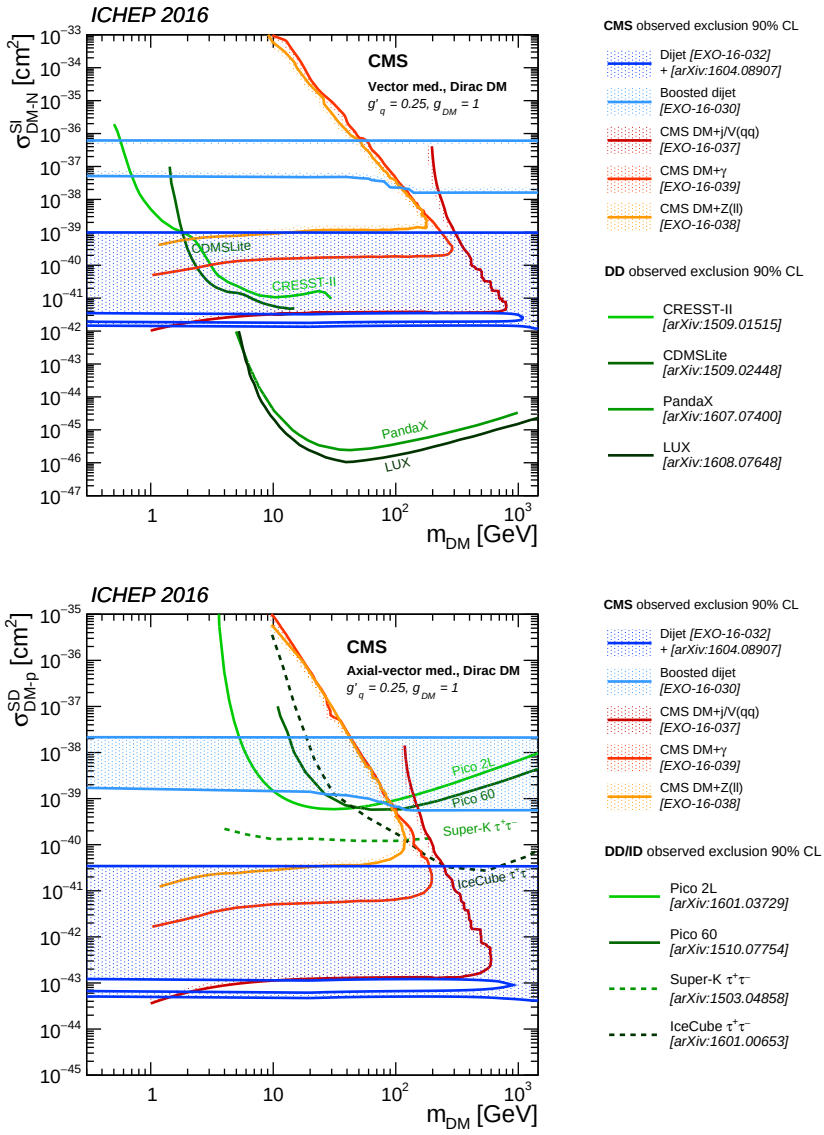

Figure B.13: A comparison of CMS results to direct and indirect dark matter detection results in the (m_{DM},$\sigma^{\mathrm{SI}}_{\mathrm{DM\text{-}N}}$) plane (top) and ($m_{\mathrm{DM}}$,$\sigma^{\mathrm{SD}}_{\mathrm{DM\text{-}p}}$) plane (bottom). Unlike in the (m_{med},m_{DM}) plane, the limits are shown at 90% CL [315, 44]. The CMS contour in the SI (SD) plane is for a vector (axial-vector) mediator, Dirac DM particle, and couplings $g'_{\mathrm{q}} = 0.25$ and $g_{\mathrm{DM}} = 1.0$. The CMS SI exclusion contour is compared with the LUX [307], PandaX-II [308], CDMSLite [309], and CRESST-II [310] limits, which have documented the most constraining results in the shown mass range. The SD exclusion contour is compared with limits from the PICO experiments [311, 312], the IceCube limit for the $\mathrm{t\bar{t}}$ annihilation channel [313] and the Super-Kamiokande limit for the $\mathrm{b\bar{b}}$ annihilation channel [314]. It should be noted that CMS exclusion regions of the different searches strongly depend on the chosen coupling and model scenario.

presented on the product of the cross section, the branching fraction, and the acceptance for narrow quark-quark, quark-gluon, and gluon-gluon resonances that are applicable to any model of narrow dijet resonance production. String resonances with masses below 7.4 TeV are excluded at 95% confidence level, as are scalar diquarks below 6.9 TeV, axigluons and colorons below 5.5 TeV, excited quarks below 5.4 TeV, color-octet scalars below 3.0 TeV, W′ bosons below 2.7 TeV, Z′ bosons with SM-like couplings below 2.1 TeV and between 2.3 and 2.6 TeV, and Randall–Sundrum gravitons below 1.9 TeV. This extends previously published limits in the dijet channel. Finally, the first CMS limits are set on a simplified model of dark matter mediators based on the dijet channel, excluding vector and axial-vector mediators below 2.0 TeV for a universal quark coupling $g_{\mathrm{q}} = 0.25$ and a dark matter coupling $g_{\mathrm{DM}} = 1.0$. Limits on the mass of a dark matter mediator are presented as a function of dark matter mass, and are translated into upper limits on the cross section for dark matter particles scattering on nucleons that are more sensitive than those of direct detection experiments for spin-dependent cross sections.

Table B.2: Limits from the low-mass search. Observed and expected upper limits at 95% CL on $\sigma \times B \times A$ for a gg resonance, a qg resonance, a qq resonance, and a 10% Gaussian lineshape as a function of the resonance mass.

Mass [GeV]	95% CL upper limit [pb]							
	gg		qg		qq		Gaussian, 10% width	
	Observed	Expected	Observed	Expected	Observed	Expected	Observed	Expected
600	2.14e+01	2.79e+01	9.89e+00	1.79e+01	4.57e+00	8.71e+00	2.47e+00	4.63e+00
650	1.75e+01	2.02e+01	8.20e+00	1.12e+01	3.97e+00	5.61e+00	2.35e+00	3.15e+00
700	1.07e+01	1.19e+01	6.34e+00	6.62e+00	3.63e+00	3.64e+00	2.70e+00	2.28e+00
750	9.54e+00	8.01e+00	6.26e+00	4.67e+00	4.00e+00	2.72e+00	3.10e+00	1.82e+00
800	1.08e+01	6.43e+00	6.69e+00	3.76e+00	4.19e+00	2.26e+00	3.09e+00	1.58e+00
850	1.20e+01	5.53e+00	6.85e+00	3.21e+00	4.02e+00	1.96e+00	2.76e+00	1.40e+00
900	1.08e+01	4.86e+00	5.99e+00	2.82e+00	3.30e+00	1.72e+00	2.10e+00	1.25e+00
950	7.96e+00	4.24e+00	4.21e+00	2.43e+00	2.18e+00	1.50e+00	1.27e+00	1.10e+00
1000	4.59e+00	3.58e+00	2.29e+00	2.04e+00	1.20e+00	1.28e+00	8.28e-01	9.52e-01
1050	2.36e+00	2.98e+00	1.32e+00	1.71e+00	8.01e-01	1.09e+00	6.61e-01	8.15e-01
1100	1.51e+00	2.45e+00	9.54e-01	1.43e+00	6.85e-01	9.33e-01	5.89e-01	6.98e-01
1150	1.31e+00	2.02e+00	8.57e-01	1.21e+00	6.69e-01	7.96e-01	5.21e-01	6.01e-01
1200	1.27e+00	1.70e+00	8.23e-01	1.02e+00	6.44e-01	6.88e-01	4.35e-01	5.32e-01
1250	1.22e+00	1.47e+00	7.46e-01	8.94e-01	5.41e-01	6.10e-01	3.41e-01	4.74e-01
1300	1.07e+00	1.30e+00	6.18e-01	7.96e-01	4.09e-01	5.42e-01	2.65e-01	4.25e-01
1350	8.50e-01	1.19e+00	4.78e-01	7.18e-01	3.08e-01	4.93e-01	2.13e-01	3.86e-01
1400	6.55e-01	1.07e+00	3.77e-01	6.59e-01	2.52e-01	4.54e-01	1.86e-01	3.66e-01
1450	5.35e-01	9.72e-01	3.22e-01	6.01e-01	2.20e-01	4.15e-01	1.74e-01	3.47e-01
1500	4.70e-01	8.94e-01	2.91e-01	5.62e-01	2.05e-01	3.86e-01	1.85e-01	3.37e-01
1550	4.31e-01	8.35e-01	2.77e-01	5.22e-01	1.99e-01	3.66e-01	2.24e-01	3.27e-01
1600	4.20e-01	7.86e-01	2.92e-01	4.93e-01	2.24e-01	3.47e-01	3.15e-01	3.27e-01

Table B.3: Limits from the high-mass search. Observed and expected upper limits at 95% CL on $\sigma \times B \times A$ for a gg resonance, a qg resonance, and a qq resonance as a function of the resonance mass.

Mass [TeV]	95% CL upper limit [pb]					
	gg		qg		qq	
	Observed	Expected	Observed	Expected	Observed	Expected
1.6	5.64e-01	8.22e-01	3.33e-01	4.86e-01	2.22e-01	3.10e-01
1.7	4.23e-01	6.11e-01	2.75e-01	3.70e-01	1.94e-01	2.46e-01
1.8	3.99e-01	4.86e-01	2.61e-01	3.02e-01	1.92e-01	2.04e-01
1.9	3.78e-01	4.05e-01	2.46e-01	2.54e-01	1.67e-01	1.73e-01
2.0	3.47e-01	3.45e-01	2.30e-01	2.18e-01	1.63e-01	1.49e-01
2.1	3.79e-01	2.98e-01	2.51e-01	1.88e-01	1.82e-01	1.28e-01
2.2	3.71e-01	2.55e-01	2.35e-01	1.62e-01	1.64e-01	1.10e-01
2.3	3.13e-01	2.16e-01	1.80e-01	1.37e-01	1.06e-01	9.34e-02
2.4	1.80e-01	1.84e-01	1.02e-01	1.17e-01	6.09e-02	8.01e-02
2.5	1.17e-01	1.56e-01	7.19e-02	9.88e-02	4.67e-02	6.82e-02
2.6	1.02e-01	1.32e-01	7.11e-02	8.48e-02	5.26e-02	5.84e-02
2.7	1.19e-01	1.12e-01	8.48e-02	7.29e-02	6.44e-02	5.06e-02
2.8	1.35e-01	9.65e-02	9.30e-02	6.27e-02	6.98e-02	4.39e-02
2.9	1.34e-01	8.32e-02	8.95e-02	5.49e-02	6.58e-02	3.82e-02
3.0	1.22e-01	7.29e-02	8.01e-02	4.82e-02	5.73e-02	3.35e-02
3.1	1.01e-01	6.43e-02	6.42e-02	4.28e-02	4.11e-02	3.00e-02
3.2	7.41e-02	5.72e-02	4.65e-02	3.82e-02	2.93e-02	2.69e-02
3.3	5.64e-02	5.10e-02	3.65e-02	3.43e-02	2.48e-02	2.39e-02
3.4	4.84e-02	4.55e-02	3.15e-02	3.08e-02	2.18e-02	2.16e-02
3.5	4.12e-02	4.12e-02	2.68e-02	2.78e-02	1.84e-02	1.95e-02
3.6	3.45e-02	3.70e-02	2.28e-02	2.53e-02	1.58e-02	1.76e-02
3.7	2.97e-02	3.35e-02	2.05e-02	2.28e-02	1.45e-02	1.60e-02
3.8	2.78e-02	3.02e-02	1.99e-02	2.08e-02	1.54e-02	1.45e-02
3.9	2.81e-02	2.74e-02	1.97e-02	1.88e-02	1.55e-02	1.31e-02
4.0	2.73e-02	2.47e-02	1.85e-02	1.70e-02	1.42e-02	1.19e-02
4.1	2.43e-02	2.26e-02	1.57e-02	1.55e-02	1.14e-02	1.08e-02
4.2	1.95e-02	2.04e-02	1.22e-02	1.41e-02	7.91e-03	9.81e-03
4.3	1.40e-02	1.85e-02	8.96e-03	1.28e-02	5.67e-03	8.84e-03
4.4	1.05e-02	1.67e-02	7.09e-03	1.17e-02	4.66e-03	8.06e-03
4.5	8.90e-03	1.52e-02	6.29e-03	1.06e-02	4.43e-03	7.28e-03
4.6	8.39e-03	1.37e-02	6.20e-03	9.62e-03	4.65e-03	6.59e-03
4.7	8.55e-03	1.25e-02	6.38e-03	8.74e-03	4.92e-03	6.01e-03
4.8	8.90e-03	1.12e-02	6.47e-03	7.96e-03	4.95e-03	5.42e-03
4.9	8.88e-03	1.01e-02	6.30e-03	7.18e-03	4.62e-03	4.93e-03
5.0	8.21e-03	9.16e-03	5.72e-03	6.53e-03	4.04e-03	4.45e-03
5.1	7.30e-03	8.41e-03	5.04e-03	5.97e-03	3.36e-03	4.03e-03
5.2	6.31e-03	7.72e-03	4.43e-03	5.47e-03	2.82e-03	3.66e-03
5.3	5.55e-03	7.09e-03	4.01e-03	4.97e-03	2.78e-03	3.34e-03
5.4	5.44e-03	6.53e-03	4.06e-03	4.59e-03	3.00e-03	3.03e-03
5.5	5.75e-03	6.03e-03	4.23e-03	4.16e-03	3.10e-03	2.78e-03
5.6	5.90e-03	5.53e-03	4.22e-03	3.84e-03	3.01e-03	2.53e-03
5.7	5.82e-03	5.09e-03	4.08e-03	3.53e-03	2.84e-03	2.34e-03
5.8	5.51e-03	4.72e-03	3.83e-03	3.22e-03	2.57e-03	2.09e-03
5.9	5.10e-03	4.34e-03	3.51e-03	2.97e-03	2.29e-03	1.97e-03
6.0	4.64e-03	4.05e-03	3.17e-03	2.72e-03	2.09e-03	1.78e-03
6.1	4.39e-03	3.85e-03	2.97e-03	2.55e-03	1.96e-03	1.65e-03
6.2	4.24e-03	3.65e-03	2.83e-03	2.38e-03	1.85e-03	1.53e-03
6.3	4.09e-03	3.45e-03	2.65e-03	2.25e-03	1.70e-03	1.35e-03
6.4	3.90e-03	3.25e-03	2.46e-03	2.13e-03	1.49e-03	1.25e-03
6.5	3.67e-03	3.16e-03	2.24e-03	1.98e-03	1.29e-03	1.18e-03
6.6	3.38e-03	3.05e-03	2.04e-03	1.85e-03	1.13e-03	1.08e-03
6.7	3.10e-03	2.95e-03	1.82e-03	1.76e-03	9.83e-04	1.03e-03
6.8	2.90e-03	2.85e-03	1.66e-03	1.65e-03	8.68e-04	9.25e-04
6.9	2.73e-03	2.75e-03	1.52e-03	1.58e-03	7.72e-04	8.62e-04
7.0	2.58e-03	2.72e-03	1.44e-03	1.53e-03	6.99e-04	8.25e-04
7.1	2.50e-03	2.72e-03	1.38e-03	1.46e-03	6.66e-04	7.25e-04
7.2	2.55e-03	2.72e-03	1.36e-03	1.43e-03	6.81e-04	7.25e-04
7.3	2.75e-03	2.76e-03	1.42e-03	1.43e-03	6.81e-04	6.62e-04
7.4	3.00e-03	2.85e-03	1.49e-03	1.35e-03	6.79e-04	6.25e-04
7.5	3.33e-03	2.95e-03	1.59e-03	1.45e-03	7.11e-04	5.91e-04

BIBLIOGRAPHY

[1] Serguei Chatrchyan et al. "Observation of a new boson at a mass of 125 GeV with the CMS experiment at the LHC". In: *Phys. Lett. B* 716 (2012), p. 30. DOI: 10.1016/j.physletb.2012.08.021. arXiv: 1207.7235 [hep-ex].

[2] Georges Aad et al. "Observation of a new particle in the search for the Standard Model Higgs boson with the ATLAS detector at the LHC". In: *Phys. Lett. B* 716 (2012), p. 1. DOI: 10.1016/j.physletb.2012.08.020. arXiv: 1207.7214 [hep-ex].

[3] V. C. Rubin, W. K. J. Ford, and N. . Thonnard. "Rotational properties of 21 SC galaxies with a large range of luminosities and radii, from NGC 4605 /R = 4kpc/ to UGC 2885 /R = 122 kpc/". In: *ApJ* 238 (June 1980), pp. 471–487. DOI: 10.1086/158003.

[4] K. G. Begeman. "H I rotation curves of spiral galaxies. I - NGC 3198". In: *A&A* 223 (Oct. 1989), pp. 47–60.

[5] Douglas Clowe et al. "A direct empirical proof of the existence of dark matter". In: *Astrophys. J.* 648 (2006), pp. L109–L113. DOI: 10.1086/508162. arXiv: astro-ph/0608407 [astro-ph].

[6] Pierre Ramond. "Dual theory for free fermions". In: *Phys. Rev. D* 3 (1971), p. 2415. DOI: 10.1103/PhysRevD.3.2415.

[7] Yu. A. Gol'fand and E. P. Likhtman. "Extension of the algebra of Poincare group generators and violation of P invariance". In: *JETP Lett.* 13 (1971), p. 323. URL: http://www.jetpletters.ac.ru/ps/1584/article_24309.pdf.

[8] D. V. Volkov and V. P. Akulov. "Possible universal neutrino interaction". In: *JETP Lett.* 16 (1972), p. 438. URL: http://www.jetpletters.ac.ru/ps/1766/article_26864.pdf.

[9] J. Wess and B. Zumino. "Supergauge transformations in four-dimensions". In: *Nucl. Phys. B* 70 (1974), p. 39. DOI: 10.1016/0550-3213(74)90355-1.

[10] Pierre Fayet. "Supergauge invariant extension of the Higgs mechanism and a model for the electron and its neutrino". In: *Nucl. Phys. B* 90 (1975), p. 104. DOI: 10.1016/0550-3213(75)90636-7.

[11] John R. Ellis et al. "Supersymmetric Relics from the Big Bang". In: *Nucl. Phys.* B238 (1984), pp. 453–476. DOI: 10.1016/0550-3213(84)90461-9.

[12] Gerard Jungman, Marc Kamionkowski, and Kim Griest. "Supersymmetric dark matter". In: *Phys. Rept.* 267 (1996), pp. 195–373. DOI: 10.1016/0370-1573(95)00058-5. arXiv: hep-ph/9506380 [hep-ph].

[13] S. Dimopoulos, S. Raby, and Frank Wilczek. "Supersymmetry and the Scale of Unification". In: *Phys. Rev.* D24 (1981), pp. 1681–1683. DOI: 10.1103/PhysRevD.24.1681.

[14] William J. Marciano and Goran Senjanovic. "Predictions of Supersymmetric Grand Unified Theories". In: *Phys. Rev.* D25 (1982), p. 3092. DOI: 10.1103/PhysRevD.25.3092.

[15] M. B. Einhorn and D. R. T. Jones. "The Weak Mixing Angle and Unification Mass in Supersymmetric SU(5)". In: *Nucl. Phys.* B196 (1982), p. 475. DOI: 10.1016/0550-3213(82)90502-8.

[16] Luis E. Ibanez and Graham G. Ross. "Low-Energy Predictions in Supersymmetric Grand Unified Theories". In: *Phys. Lett.* B105 (1981), p. 439. DOI: 10.1016/0370-2693(81)91200-4.

[17] Ugo Amaldi, Wim de Boer, and Hermann Furstenau. "Comparison of grand unified theories with electroweak and strong coupling constants measured at LEP". In: *Phys. Lett.* B260 (1991), pp. 447–455. DOI: 10.1016/0370-2693(91)91641-8.

[18] Paul Langacker and Nir Polonsky. "The Strong coupling, unification, and recent data". In: *Phys. Rev.* D52 (1995), pp. 3081–3086. DOI: 10.1103/PhysRevD.52.3081. arXiv: hep-ph/9503214 [hep-ph].

[19] Edward Witten. "Dynamical Breaking of Supersymmetry". In: *Nucl. Phys.* B188 (1981), p. 513. DOI: 10.1016/0550-3213(81)90006-7.

[20] Savas Dimopoulos and Howard Georgi. "Softly Broken Supersymmetry and SU(5)". In: *Nucl. Phys.* B193 (1981), p. 150. DOI: 10.1016/0550-3213(81)90522-8.

[21] Michael Dine, Willy Fischler, and Mark Srednicki. "Supersymmetric Technicolor". In: *Nucl. Phys.* B189 (1981), pp. 575–593. DOI: 10.1016/0550-3213(81)90582-4.

[22] Savas Dimopoulos and Stuart Raby. "Supercolor". In: *Nucl. Phys.* B192 (1981), p. 353. DOI: 10.1016/0550-3213(81)90430-2.

[23] N. Sakai. "Naturalness in Supersymmetric Guts". In: *Z. Phys.* C11 (1981), p. 153. DOI: 10.1007/BF01573998.

[24] Romesh K. Kaul and Parthasarathi Majumdar. "Cancellation of Quadratically Divergent Mass Corrections in Globally Supersymmetric Spontaneously Broken Gauge Theories". In: *Nucl. Phys.* B199 (1982), p. 36. DOI: 10.1016/0550-3213(82)90565-X.

[25] Vardan Khachatryan et al. "Search for resonant production of high-mass photon pairs in proton-proton collisions at sqrt(s) = 8 and 13 TeV". In: *Phys. Rev. Lett.* 117.5 (2016), p. 051802. DOI: 10.1103/PhysRevLett.117.051802. arXiv: 1606.04093 [hep-ex].

[26] Morad Aaboud et al. "Search for resonances in diphoton events at $\sqrt{s}$=13 TeV with the ATLAS detector". In: (2016). arXiv: 1606.03833 [hep-ex].

[27] *Search for resonant production of high mass photon pairs using* 12.9 fb^{-1} *of proton-proton collisions at* $\sqrt{s} = 13$ *TeV and combined interpretation of searches at 8 and 13 TeV*. Tech. rep. CMS-PAS-EXO-16-027. Geneva: CERN, 2016. URL: https://cds.cern.ch/record/2205245.

[28] ATLAS Collaboration. *Search for scalar diphoton resonances with 15.4* fb^1 *of data collected at* $\sqrt{s} = 13$ *TeV in 2015 and 2016 with the ATLAS detector*. ATLAS Conference Report ATLAS-CONF-2016-059. Aug. 2016. URL: https://atlas.web.cern.ch/Atlas/GROUPS/PHYSICS/CONFNOTES/ATLAS-CONF-2016-059.

[29] Steven Weinberg. "A Model of Leptons". In: *Phys. Rev. Lett.* 19 (21 Nov. 1967), pp. 1264–1266. DOI: 10.1103/PhysRevLett.19.1264. URL: http://link.aps.org/doi/10.1103/PhysRevLett.19.1264.

[30] 't Hooft, Gerardus. "Renormalizable Lagrangians for massive Yang-Mills fields". In: *Nucl. Phys. B* 35.1-3 (1971), pp. 167–188.

[31] W. Pauli. "The Connection Between Spin and Statistics". In: *Phys. Rev.* 58 (8 Oct. 1940), pp. 716–722. DOI: 10.1103/PhysRev.58.716. URL: http://link.aps.org/doi/10.1103/PhysRev.58.716.

[32] Chen-Ning Yang and Robert L. Mills. "Conservation of Isotopic Spin and Isotopic Gauge Invariance". In: *Phys. Rev.* 96 (1954), pp. 191–195. DOI: 10.1103/PhysRev.96.191.

[33] Yoichiro Nambu. "Quasiparticles and Gauge Invariance in the Theory of Superconductivity". In: *Phys. Rev.* 117 (1960), pp. 648–663. DOI: 10.1103/PhysRev.117.648.

[34] J. Goldstone. "Field Theories with Superconductor Solutions". In: *Nuovo Cim.* 19 (1961), pp. 154–164. DOI: 10.1007/BF02812722.

[35] Philip W. Anderson. "Plasmons, Gauge Invariance, and Mass". In: *Phys. Rev.* 130 (1963), pp. 439–442. DOI: 10.1103/PhysRev.130.439.

[36] F. Englert and R. Brout. "Broken Symmetry and the Mass of Gauge Vector Mesons". In: *Phys. Rev. Lett.* 13 (9 Aug. 1964), pp. 321–323. DOI: 10.1103/PhysRevLett.13.321. URL: http://link.aps.org/doi/10.1103/PhysRevLett.13.321.

[37] P.W. Higgs. "Broken symmetries, massless particles and gauge fields". In: *Physics Letters* 12.2 (1964), pp. 132–133. ISSN: 0031-9163. DOI: http://dx.doi.org/10.1016/0031-9163(64)91136-9. URL: http://www.sciencedirect.com/science/article/pii/0031916364911369.

[38] Peter W. Higgs. "Broken Symmetries and the Masses of Gauge Bosons". In: *Phys. Rev. Lett.* 13 (16 Oct. 1964), pp. 508–509. DOI: 10.1103/PhysRevLett.13.508. URL: http://link.aps.org/doi/10.1103/PhysRevLett.13.508.

[39] G. S. Guralnik, C. R. Hagen, and T. W. B. Kibble. "Global Conservation Laws and Massless Particles". In: *Phys. Rev. Lett.* 13 (20 Nov. 1964), pp. 585–587. DOI: 10.1103/PhysRevLett.13.585. URL: http://link.aps.org/doi/10.1103/PhysRevLett.13.585.

[40] Peter W. Higgs. "Spontaneous Symmetry Breakdown without Massless Bosons". In: *Phys. Rev.* 145 (4 May 1966), pp. 1156–1163. DOI: 10.1103/PhysRev.145.1156. URL: http://link.aps.org/doi/10.1103/PhysRev.145.1156.

[41] T. W. B. Kibble. "Symmetry Breaking in Non-Abelian Gauge Theories". In: *Phys. Rev.* 155 (5 Mar. 1967), pp. 1554–1561. DOI: 10.1103/PhysRev.155.1554. URL: http://link.aps.org/doi/10.1103/PhysRev.155.1554.

[42] Sheldon L. Glashow. "Partial-symmetries of weak interactions". In: *Nuclear Physics* 22.4 (1961), pp. 579–588. ISSN: 0029-5582. DOI: http://dx.doi.org/10.1016/0029-5582(61)90469-2. URL: http://www.sciencedirect.com/science/article/pii/0029558261904692.

[43] Abdus Salam. "Weak and Electromagnetic Interactions". In: *Conf. Proc.* C680519 (1968), pp. 367–377.

[44] Javier M. G. Duarte. *Figure created by Javier M. G. Duarte*. http://www.its.caltech.edu/~jduarte/. 2016.

[45] Stephen P. Martin. "A Supersymmetry primer". In: (1997). [Adv. Ser. Direct. High Energy Phys.18,1(1998)]. DOI: 10.1142/9789812839657_0001,10.1142/9789814307505_0001. arXiv: hep-ph/9709356 [hep-ph].

[46] Georges Aad et al. "Combined Measurement of the Higgs Boson Mass in pp Collisions at $\sqrt{s} = 7$ and 8 TeV with the ATLAS and CMS Experiments". In: *Phys. Rev. Lett.* 114 (2015), p. 191803. DOI: 10.1103/PhysRevLett.114.191803. arXiv: 1503.07589 [hep-ex].

[47] Dario Buttazzo et al. "Investigating the near-criticality of the Higgs boson". In: *JHEP* 12 (2013), p. 089. DOI: 10.1007/JHEP12(2013)089. arXiv: 1307.3536 [hep-ph].

[48] H. Georgi and S. L. Glashow. "Unity of All Elementary Particle Forces". In: *Phys. Rev. Lett.* 32 (1974), pp. 438–441. DOI: 10.1103/PhysRevLett.32.438.

[49] Sidney Coleman. "Fate of the false vacuum: Semiclassical theory". In: *Phys. Rev. D* 15 (10 May 1977), pp. 2929–2936. DOI: 10.1103/PhysRevD.15.2929. URL: http://link.aps.org/doi/10.1103/PhysRevD.15.2929.

[50] Curtis G. Callan and Sidney Coleman. "Fate of the false vacuum. II. First quantum corrections". In: *Phys. Rev. D* 16 (6 Sept. 1977), pp. 1762–1768. DOI: 10.1103/PhysRevD.16.1762. URL: http://link.aps.org/doi/10.1103/PhysRevD.16.1762.

[51] Ali H. Chamseddine, Richard L. Arnowitt, and Pran Nath. "Locally supersymmetric grand unification". In: *Phys. Rev. Lett.* 49 (1982), p. 970. DOI: 10.1103/PhysRevLett.49.970.

[52] Gordon L. Kane et al. "Study of constrained minimal supersymmetry". In: *Phys. Rev. D* 49 (1994), p. 6173. DOI: 10.1103/PhysRevD.49.6173. arXiv: hep-ph/9312272 [hep-ph].

[53] Riccardo Barbieri, S. Ferrara, and Carlos A. Savoy. "Gauge models with spontaneously broken local supersymmetry". In: *Phys. Lett. B* 119 (1982), p. 343. DOI: 10.1016/0370-2693(82)90685-2.

[54] Lawrence J. Hall, Joseph D. Lykken, and Steven Weinberg. "Supergravity as the messenger of supersymmetry breaking". In: *Phys. Rev. D* 27 (1983), p. 2359. DOI: 10.1103/PhysRevD.27.2359.

[55] Sidney Coleman and Jeffrey Mandula. "All Possible Symmetries of the S Matrix". In: *Phys. Rev.* 159 (5 July 1967), pp. 1251–1256. DOI: 10.1103/PhysRev.159.1251. URL: http://link.aps.org/doi/10.1103/PhysRev.159.1251.

[56] Glennys R. Farrar and Pierre Fayet. "Phenomenology of the Production, Decay, and Detection of New Hadronic States Associated with Supersymmetry". In: *Phys. Lett.* B76 (1978), pp. 575–579. DOI: 10.1016/0370-2693(78)90858-4.

[57] Nima Arkani-Hamed et al. "MARMOSET: The Path from LHC Data to the New Standard Model via On-Shell Effective Theories". 2007.

[58] Johan Alwall, Philip C. Schuster, and Natalia Toro. "Simplified models for a first characterization of new physics at the LHC". In: *Phys. Rev. D* 79 (2009), p. 075020. DOI: 10.1103/PhysRevD.79.075020. arXiv: 0810.3921 [hep-ph].

[59] Johan Alwall et al. "Model independent jets plus missing energy searches". In: *Phys. Rev. D* 79 (2009), p. 015005. DOI: 10.1103/PhysRevD.79.015005. arXiv: 0809.3264 [hep-ph].

[60] Daniele S. M. Alves, Eder Izaguirre, and Jay G. Wacker. "Where the sidewalk ends: jets and missing energy search strategies for the 7 TeV LHC". In: *JHEP* 10 (2011), p. 012. DOI: 10.1007/JHEP10(2011)012. arXiv: 1102.5338 [hep-ph].

[61] Daniele Alves et al. "Simplified models for LHC new physics searches". In: *J. Phys. G* 39 (2012), p. 105005. DOI: 10.1088/0954-3899/39/10/105005. arXiv: 1105.2838 [hep-ph].

[62] Michael L. Graesser and Jessie Shelton. "Hunting Mixed Top Squark Decays". In: *Phys. Rev. Lett.* 111 (2013), p. 121802. DOI: 10.1103/PhysRevLett.111.121802. arXiv: 1212.4495 [hep-ph].

[63] W. Beenakker et al. "Squark and gluino production at hadron colliders". In: *Nucl. Phys. B* 492 (1997), p. 51. DOI: 10.1016/S0550-3213(97)80027-2. arXiv: hep-ph/9610490 [hep-ph].

[64] A. Kulesza and L. Motyka. "Threshold Resummation for Squark-Antisquark and Gluino-Pair Production at the LHC". In: *Phys. Rev. Lett.* 102 (2009), p. 111802. DOI: 10.1103/PhysRevLett.102.111802. arXiv: 0807.2405 [hep-ph].

[65] A. Kulesza and L. Motyka. "Soft gluon resummation for the production of gluino-gluino and squark-antisquark pairs at the LHC". In: *Phys. Rev. D* 80 (2009), p. 095004. DOI: 10.1103/PhysRevD.80.095004. arXiv: 0905.4749 [hep-ph].

[66] W. Beenakker et al. "Soft-gluon resummation for squark and gluino hadroproduction". In: *JHEP* 12 (2009), p. 041. DOI: 10.1088/1126-6708/2009/12/041. arXiv: 0909.4418 [hep-ph].

[67] W. Beenakker et al. "Squark and gluino hadroproduction". In: *Int. J. Mod. Phys. A* 26 (2011), p. 2637. DOI: 10.1142/S0217751X11053560. arXiv: 1105.1110 [hep-ph].

[68] M. Krämer et al. "Supersymmetry production cross sections in pp collisions at $\sqrt{s} = 7$ TeV". 2012.

[69] Christoph Borschensky et al. "Squark and gluino production cross sections in pp collisions at $\sqrt{s}$ = 13, 14, 33 and 100 TeV". In: *Eur. Phys. J.* C74.12 (2014), p. 3174. DOI: 10.1140/epjc/s10052-014-3174-y. arXiv: 1407.5066 [hep-ph].

[70] Benjamin Fuks et al. "Gaugino production in proton-proton collisions at a center-of-mass energy of 8 TeV". In: *JHEP* 10 (2012), p. 081. DOI: 10.1007/JHEP10(2012)081. arXiv: 1207.2159 [hep-ph].

[71] Benjamin Fuks et al. "Precision predictions for electroweak superpartner production at hadron colliders with RESUMMINO". In: *Eur. Phys. J. C* 73 (2013), p. 2480. DOI: 10.1140/epjc/s10052-013-2480-0. arXiv: 1304.0790 [hep-ph].

[72] Benjamin Fuks et al. "Revisiting slepton pair production at the Large Hadron Collider". In: *JHEP* 01 (2014), p. 168. DOI: 10.1007/JHEP01(2014)168. arXiv: 1310.2621 [hep-ph].

[73] Christopher Brust et al. "SUSY, the Third Generation and the LHC". In: *JHEP* 03 (2012), p. 103. DOI: 10.1007/JHEP03(2012)103. arXiv: 1110.6670 [hep-ph].

[74] Michele Papucci, Joshua T. Ruderman, and Andreas Weiler. "Natural SUSY Endures". In: *JHEP* 09 (2012), p. 035. DOI: 10.1007/JHEP09(2012)035. arXiv: 1110.6926 [hep-ph].

[75] Riccardo Barbieri and G. F. Giudice. "Upper Bounds on Supersymmetric Particle Masses". In: *Nucl. Phys.* B306 (1988), pp. 63–76. DOI: 10.1016/0550-3213(88)90171-X.

[76] Andrey Katz, Matthew Reece, and Aqil Sajjad. "Naturalness, $b \to s\gamma$, and SUSY heavy Higgses". In: *JHEP* 10 (2014), p. 102. DOI: 10.1007/JHEP10(2014)102. arXiv: 1406.1172 [hep-ph].

[77] Howard Baer, Vernon Barger, and Dan Mickelson. "How conventional measures overestimate electroweak fine-tuning in supersymmetric theory". In: *Phys. Rev.* D88.9 (2013), p. 095013. DOI: 10.1103/PhysRevD.88.095013. arXiv: 1309.2984 [hep-ph].

[78] John F. Gunion and Howard E. Haber. "Two-body decays of neutralinos and charginos". In: *Phys. Rev. D* 37 (9 May 1988), pp. 2515–2532. DOI: 10.1103/PhysRevD.37.2515. URL: http://link.aps.org/doi/10.1103/PhysRevD.37.2515.

[79] Nathaniel Craig. "The State of Supersymmetry after Run I of the LHC". In: *Beyond the Standard Model after the first run of the LHC Arcetri, Florence, Italy, May 20-July 12, 2013*. 2013. arXiv: 1309.0528 [hep-ph]. URL: https://inspirehep.net/record/1252552/files/arXiv:1309.0528.pdf.

[80] Serguei Chatrchyan et al. "Search for electroweak production of charginos and neutralinos using leptonic final states in pp collisions at $\sqrt{s} = 7$ TeV". In: *JHEP* 11 (2012), p. 147. DOI: 10.1007/JHEP11(2012)147. arXiv: 1209.6620 [hep-ex].

[81] Serguei Chatrchyan et al. "Inclusive search for squarks and gluinos in pp collisions at $\sqrt{s} = 7$ TeV". In: *Phys. Rev. D* 85 (2012), p. 012004. DOI: 10.1103/PhysRevD.85.012004. arXiv: 1107.1279 [hep-ex].

[82] Serguei Chatrchyan et al. "Inclusive Search for Supersymmetry Using Razor Variables in pp Collisions at $\sqrt{s} = 7$ TeV". In: *Phys. Rev. Lett.* 111 (2013), p. 081802. DOI: 10.1103/PhysRevLett.111.081802. arXiv: 1212.6961 [hep-ex].

[83] Serguei Chatrchyan et al. "Search for supersymmetry in hadronic final states using MT2 in pp collisions at $\sqrt{s} = 7$ TeV". In: *JHEP* 10 (2012), p. 018. DOI: 10.1007/JHEP10(2012)018. arXiv: 1207.1798 [hep-ex].

[84] Serguei Chatrchyan et al. "Search for new physics in events with same-sign dileptons and b-tagged jets in pp collisions at $\sqrt{s} = 7$ TeV". In: *JHEP* 08 (2012), p. 110. DOI: 10.1007/JHEP08(2012)110. arXiv: 1205.3933 [hep-ex].

[85] Georges Aad et al. "Search for a supersymmetric partner to the top quark in final states with jets and missing transverse momentum at $\sqrt{s} = 7$ TeV with the ATLAS detector". In: *Phys. Rev. Lett.* 109 (2012), p. 211802. DOI: 10.1103/PhysRevLett.109.211802. arXiv: 1208.1447 [hep-ex].

[86] Georges Aad et al. "Search for direct top squark pair production in final states with one isolated lepton, jets, and missing transverse momentum in $\sqrt{s} = 7$ TeV pp collisions using 4.7 fb^{-1} of ATLAS data". In: *Phys. Rev. Lett.* 109 (2012), p. 211803. DOI: 10.1103/PhysRevLett.109.211803. arXiv: 1208.2590 [hep-ex].

[87] Georges Aad et al. "Search for light scalar top quark pair production in final states with two leptons with the ATLAS detector in $\sqrt{s} = 7$ TeV proton-proton collisions". In: *Eur. Phys. J. C* 72 (2012), p. 2237. DOI: 10.1140/epjc/s10052-012-2237-1. arXiv: 1208.4305 [hep-ex].

[88] Georges Aad et al. "Search for light top squark pair production in final states with leptons and b-jets with the ATLAS detector in $\sqrt{s} = 7$ TeV proton-proton collisions". In: *Phys. Lett. B* 720 (2013), p. 13. DOI: 10.1016/j.physletb.2013.01.049. arXiv: 1209.2102 [hep-ex].

[89] Georges Aad et al. "Multi-channel search for squarks and gluinos in $\sqrt{s} = 7$ TeV pp collisions with the ATLAS detector". In: *Eur. Phys. J. C* 73 (2013), p. 2362. DOI: 10.1140/epjc/s10052-013-2362-5. arXiv: 1212.6149 [hep-ex].

[90] Georges Aad et al. "Search for squarks and gluinos with the ATLAS detector in final states with jets and missing transverse momentum using 4.7 fb^{-1} of $\sqrt{s} = 7$ TeV proton-proton collision data". In: *Phys. Rev. D* 87 (2013), p. 012008. DOI: 10.1103/PhysRevD.87.012008. arXiv: 1208.0949 [hep-ex].

[91] Georges Aad et al. "Search for top and bottom squarks from gluino pair production in final states with missing transverse energy and at least three b-jets with the ATLAS detector". In: *Eur. Phys. J. C* 72 (2012), p. 2174. DOI: 10.1140/epjc/s10052-012-2174-z. arXiv: 1207.4686 [hep-ex].

[92] Georges Aad et al. "Search for direct slepton and gaugino production in final states with two leptons and missing transverse momentum with the ATLAS detector in pp collisions at $\sqrt{s} = 7$ TeV". In: *Phys. Lett.* B718 (2013), pp. 879–901. DOI: 10.1016/j.physletb.2012.11.058. arXiv: 1208.2884 [hep-ex].

[93] Georges Aad et al. "Search for direct production of charginos and neutralinos in events with three leptons and missing transverse momentum in $\sqrt{s} = 7$ TeV pp collisions with the ATLAS detector". In: *Phys. Lett.* B718 (2013), pp. 841–859. DOI: 10.1016/j.physletb.2012.11.039. arXiv: 1208.3144 [hep-ex].

[94] Vardan Khachatryan et al. "Search for Supersymmetry Using Razor Variables in Events with b-Tagged Jets in pp Collisions at $\sqrt{s} = 8$ TeV". In: *Phys. Rev.* D91 (2015), p. 052018. DOI: 10.1103/PhysRevD.91.052018. arXiv: 1502.00300 [hep-ex].

[95] Serguei Chatrchyan et al. "Interpretation of Searches for Supersymmetry with Simplified Models". In: *Phys. Rev. D* 88 (2013), p. 052017. DOI: 10.1103/PhysRevD.88.052017. arXiv: 1301.2175 [hep-ex].

[96] Vardan Khachatryan et al. "Search for supersymmetry in pp collisions at *sqrts* = 13 TeV in the single-lepton final state using the sum of masses of large-radius jets". In: (2016). arXiv: 1605.04608 [hep-ex].

[97] Georges Aad et al. "Search for new phenomena in final states with large jet multiplicities and missing transverse momentum at $\sqrt{s} =$ 8 TeV proton-proton collisions using the ATLAS experiment". In: *JHEP* 10 (2013), p. 130. DOI: 10.1007/JHEP10(2013)130. arXiv: 1308.1841 [hep-ex].

[98] Georges Aad et al. "Search for strong production of supersymmetric particles in final states with missing transverse momentum and at least three b-jets at $\sqrt{s} = 8$ TeV proton-proton collisions with the ATLAS detector". In: *JHEP* 10 (2014), p. 24. DOI: 10.1007/JHEP10(2014)024. arXiv: 1407.0600 [hep-ex].

[99] Georges Aad et al. "Search for supersymmetry at $\sqrt{s} = 8$ TeV in final states with jets and two same-sign leptons or three leptons with the ATLAS detector". In: *JHEP* 06 (2014), p. 035. DOI: 10.1007/JHEP06(2014)035. arXiv: 1404.2500 [hep-ex].

[100] Georges Aad et al. "Search for direct pair production of the top squark in all-hadronic final states in proton-proton collisions at $\sqrt{s} = 8$ TeV with the ATLAS detector". In: *JHEP* 09 (2014), p. 015. DOI: 10.1007/JHEP09(2014)015. arXiv: 1406.1122 [hep-ex].

[101] Georges Aad et al. "Search for direct top-squark pair production in final states with two leptons in pp collisions at $\sqrt{s} = 8$ TeV with the ATLAS detector". In: *JHEP* 06 (2014), p. 124. DOI: 10.1007/JHEP06(2014)124. arXiv: 1403.4853 [hep-ex].

[102] Serguei Chatrchyan et al. "Search for top-squark pair production in the single-lepton final state in pp collisions at $\sqrt{s} = 8$ TeV". In: *Eur. Phys. J. C* 73 (2013), p. 2677. DOI: 10.1140/epjc/s10052-013-2677-2. arXiv: 1308.1586 [hep-ex].

[103] Serguei Chatrchyan et al. "Search for gluino mediated bottom- and top-squark production in multijet final states in pp collisions at 8 TeV". In: *Phys. Lett. B* 725 (2013), p. 243. DOI: 10.1016/j.physletb.2013.06.058. arXiv: 1305.2390 [hep-ex].

[104] Serguei Chatrchyan et al. "Search for new physics in the multijet and missing transverse momentum final state in proton-proton collisions at $\sqrt{s} = 8$ TeV". In: *JHEP* 06 (2014), p. 055. DOI: 10.1007/JHEP06(2014)055. arXiv: 1402.4770 [hep-ex].

[105] Serguei Chatrchyan et al. "Search for supersymmetry in pp collisions at $\sqrt{s} = 8$ TeV in events with a single lepton, large jet multiplicity, and multiple b jets". In: *Phys. Lett. B* 733 (2014), p. 328. DOI: 10.1016/j.physletb.2014.04.023. arXiv: 1311.4937 [hep-ex].

[106] Serguei Chatrchyan et al. "Search for new physics in events with same-sign dileptons and jets in pp collisions at $\sqrt{s} = 8$ TeV". In: *JHEP* 01 (2014), p. 163. DOI: 10.1007/JHEP01(2014)163. arXiv: 1311.6736.

[107] Christopher Rogan. "Kinematical variables towards new dynamics at the LHC". 2010. URL: http://arxiv.org/abs/1006.2727.

[108] Serguei Chatrchyan et al. "Search for supersymmetry with razor variables in pp collisions at $\sqrt{s}$ = 7 TeV". In: *Phys. Rev. D* 90.11 (2014), p. 112001. DOI: 10.1103/PhysRevD.90.112001. arXiv: 1405.3961 [hep-ex].

[109] Christopher Sean Rogan. "Searches for new symmetries in pp collisions with the razor kinematic variables at $\sqrt{s} = 7$ TeV". PhD Thesis. 1200 E. California Blvd., Pasadena, CA 91125, USA: California Institute of Technology, 2013. URL: http://resolver.caltech.edu/CaltechTHESIS:05072013-174540453.

[110] Matthew R. Buckley et al. "Super-Razor and Searches for Sleptons and Charginos at the LHC". In: *Phys. Rev.* D89.5 (2014), p. 055020. DOI: 10.1103/PhysRevD.89.055020. arXiv: 1310.4827 [hep-ph].

[111] Lyndon Evans and Philip Bryant. "LHC Machine". In: *Journal of Instrumentation* 3.08 (2008), S08001. URL: http://stacks.iop.org/1748-0221/3/i=08/a=S08001.

[112] John Pauls Blewett. "200-GeV intersecting storage accelerators". In: *The 8th International Conference on High-Energy Accelerators*. 1971. URL: http://lss.fnal.gov/conf/C710920/p501.pdf.

[113] CMS Collaboration. *CMS Luminosity Based on Pixel Cluster Counting - Summer 2013 Update*. CMS Physics Analysis Summary CMS-PAS-LUM-13-001. (2013). URL: http://cdsweb.cern.ch/record/1598864.

[114] S. Chatrchyan et al. "The CMS experiment at the CERN LHC". In: *JINST* 3 (2008), S08004. DOI: 10.1088/1748-0221/3/08/S08004.

[115] Serguei Chatrchyan et al. "Description and performance of track and primary-vertex reconstruction with the CMS tracker". In: *JINST* 9.10 (2014), P10009. DOI: 10.1088/1748-0221/9/10/P10009. arXiv: 1405.6569 [physics.ins-det].

[116] Serguei Chatrchyan et al. "Energy Calibration and Resolution of the CMS Electromagnetic Calorimeter in pp Collisions at $\sqrt{s} = 7$ TeV". In: *JINST* 8 (2013). [JINST8,9009(2013)], P09009. DOI: 10.1088/1748-0221/8/09/P09009. arXiv: 1306.2016 [hep-ex].

[117] P. Adzic et al. "Energy resolution of the barrel of the CMS electromagnetic calorimeter". In: *JINST* 2 (2007), P04004. DOI: 10.1088/1748-0221/2/04/P04004.

[118] M. Oreglia. "A Study of the Reactions $\psi' \to \gamma\gamma\psi$". PhD thesis. SLAC, 1980. URL: http://www-public.slac.stanford.edu/sciDoc/docMeta.aspx?slacPubNumber=slac-r-236.

[119] K. A. Olive et al. "Review of Particle Physics". In: *Chin. Phys.* C38 (2014), p. 090001. DOI: 10.1088/1674-1137/38/9/090001.

[120] Vardan Khachatryan et al. "Performance of Photon Reconstruction and Identification with the CMS Detector in Proton-Proton Collisions at sqrt(s) = 8 TeV". In: *JINST* 10.08 (2015), P08010. DOI: 10.1088/1748-0221/10/08/P08010.

[121] Vardan Khachatryan et al. "Observation of the diphoton decay of the Higgs boson and measurement of its properties". In: *Eur. Phys. J.* C74.10 (2014), p. 3076. DOI: 10.1140/epjc/s10052-014-3076-z. arXiv: 1407.0558 [hep-ex].

[122] *CMS Physics: Technical Design Report Volume 1: Detector Performance and Software*. Technical Design Report CMS. There is an error on cover due to a technical problem for some items. Geneva: CERN, 2006. URL: http://cds.cern.ch/record/922757.

[123] S. Abdullin et al. "The CMS barrel calorimeter response to particle beams from 2-GeV/c to 350-GeV/c". In: *Eur. Phys. J.* C60 (2009). [Erratum: Eur. Phys. J.C61,353(2009)], pp. 359–373. DOI: 10.1140/epjc/s10052-009-0959-5, 10.1140/epjc/s10052-009-1024-0.

[124] Matteo Cacciari, Gavin P. Salam, and Gregory Soyez. "The catchment area of jets". In: *JHEP* 04 (2008), p. 005. DOI: 10.1088/1126-6708/2008/04/005. arXiv: 0802.1188 [hep-ph].

[125] Matteo Cacciari and Gavin P. Salam. "Pileup subtraction using jet areas". In: *Phys. Lett. B* 659 (2008), p. 119. DOI: 10.1016/j.physletb.2007.09.077. arXiv: 0707.1378 [hep-ph].

[126] Serguei Chatrchyan et al. "Determination of jet energy calibration and transverse momentum resolution in CMS". In: *JINST* 6 (2011), P11002. DOI: 10.1088/1748-0221/6/11/P11002.

[127] Vardan Khachatryan et al. "Jet energy scale and resolution in the CMS experiment in pp collisions at 8 TeV". In: *Submitted to: JINST* (2016). arXiv: 1607.03663 [hep-ex].

[128] S. Catani, B. Webber, and Yu. Dokshitzer. "The K(T) clustering algorithm for jets in deep inelastic scattering". In: *Nucl. Phys. Proc. Suppl.* 29A (1992). [,136(1992)], pp. 136–143. DOI: 10.1016/0920-5632(92)90435-U.

[129] S. Catani et al. "Longitudinally invariant K_t clustering algorithms for hadron hadron collisions". In: *Nucl. Phys.* B406 (1993), pp. 187–224. DOI: 10.1016/0550-3213(93)90166-M.

[130] Stephen D. Ellis and Davison E. Soper. "Successive combination jet algorithm for hadron collisions". In: *Phys. Rev.* D48 (1993), pp. 3160–3166. DOI: 10.1103/PhysRevD.48.3160. arXiv: hep-ph/9305266 [hep-ph].

[131] Matteo Cacciari, Gavin P. Salam, and Gregory Soyez. "The anti-k_T jet clustering algorithm". In: *JHEP* 04 (2008), p. 063. DOI: 10.1088/1126-6708/2008/04/063. arXiv: 0802.1189 [hep-ph].

[132] Matteo Cacciari, Gavin P. Salam, and Gregory Soyez. "FastJet user manual". In: *Eur. Phys. J. C* 72 (2012), p. 1896. DOI: 10.1140/epjc/s10052-012-1896-2. arXiv: 1111.6097 [hep-ph].

[133] Vardan Khachatryan et al. "Performance of the CMS missing transverse momentum reconstruction in pp data at $\sqrt{s} = 8$ TeV". In: *JINST* 10.02 (2015), P02006. DOI: 10.1088/1748-0221/10/02/P02006. arXiv: 1411.0511 [physics.ins-det].

[134] Serguei Chatrchyan et al. "Identification of b-quark jets with the CMS experiment". In: *JINST* 8 (2013), P04013. DOI: 10.1088/1748-0221/8/04/P04013. arXiv: 1211.4462 [hep-ex].

[135] *Performance of b tagging at sqrt(s)=8 TeV in multijet, ttbar and boosted topology events*. Tech. rep. CMS-PAS-BTV-13-001. Geneva: CERN, 2013. URL: https://cds.cern.ch/record/1581306.

[136] Mia Tosi. "Performance of Tracking, b-tagging and Jet/MET reconstruction at the CMS High Level Trigger". In: *J. Phys. Conf. Ser.* 664.8 (2015), p. 082055. DOI: 10.1088/1742-6596/664/8/082055.

[137] Andrea Bocci. "The Trigger of the CMS Experiment". In: *3rd Plenary KSETA Workshop, 22-24 Feb 2016, Durbach, Germany*. 2016. URL: https://twiki.cern.ch/twiki/pub/CMSPublic/TriggerStudiesTalks/CMS_trigger.pdf.

[138] Clint Richardson. "CMS High Level Trigger Timing Measurements". In: *J. Phys. Conf. Ser.* 664.8 (2015), p. 082045. DOI: 10.1088/1742-6596/664/8/082045.

[139] Gianluca Cerminara. *Alignment and Calibration of the CMS Detector*. Tech. rep. CMS-CR-2011-268. Geneva: CERN, Oct. 2011. URL: https://cds.cern.ch/record/1399496.

[140] M. Edelhoff and CMS Collaboration. "CMS alignment and calibration framework". In: *American Institute of Physics Conference Series*. Ed. by T. E. Simos and G. Maroulis. Vol. 1504. American Institute of Physics Conference Series. Dec. 2012, pp. 971–974. DOI: 10.1063/1.4771859.

[141] Federico De Guio. *CMS Alignement and Calibration workflows lesson learned and future plans*. Tech. rep. CMS-CR-2014-335. Geneva: CERN, Oct. 2014. URL: https://cds.cern.ch/record/2121268.

[142] M. Anfreville et al. "Laser monitoring system for the CMS lead tungstate crystal calorimeter". In: *Nucl. Instrum. Meth.* A594 (2008), pp. 292–320. DOI: 10.1016/j.nima.2008.01.104.

[143] Li-Yuan Zhang et al. "Performance of the monitoring light source for the CMS lead tungstate crystal calorimeter". In: *IEEE Trans. Nucl. Sci.* 52 (2005), pp. 1123–1130. DOI: 10.1109/TNS.2005.852661.

[144] Federico De Guio. "The CMS data quality monitoring software: experience and future prospects". In: *J. Phys. Conf. Ser.* 513 (2014), p. 032024. DOI: 10.1088/1742-6596/513/3/032024.

[145] *The CMS electromagnetic calorimeter project: Technical Design Report*. Technical Design Report CMS. Geneva: CERN, 1997. URL: http://cds.cern.ch/record/349375.

[146] P. Adzic et al. "Radiation hardness qualification of PbWO(4) scintillation crystals for the CMS Electromagnetic Calorimeter". In: *JINST* 5 (2010), P03010. DOI: 10.1088/1748-0221/5/03/P03010. arXiv: 0912.4300 [physics.ins-det].

[147] "CMS ECAL first results with 2016 data". In: (June 2016). URL: https://cds.cern.ch/record/2194169.

[148] A Van Lysebetten and P Verrecchia. *Performance and Measurements of the Light Monitoring System for CMS-ECAL from 2002 Test Beam Data*. Tech. rep. CMS-RN-2004-001. Geneva: CERN, Feb. 2004. URL: http://cds.cern.ch/record/787485.

[149] P. Adzic et al. "Results of the first performance tests of the CMS electromagnetic calorimeter". In: *Eur. Phys. J.* C44S1 (2006), pp. 1–10. DOI: 10.1140/epjcd/s2005-02-011-3.

[150] Alessio Ghezzi et al. *Analysis of the response evolution of the CMS electromegnetic calorimeter under electron and pion irradiation*. Tech. rep. CMS-NOTE-2006-038. Geneva: CERN, Feb. 2006. URL: http://cds.cern.ch/record/934066.

[151] *EGamma HLT 2015 Laser correction validation week to week reports*. Accessed: 2016-08-15. URL: https://twiki.cern.ch/twiki/bin/viewauth/CMS/EGammaHLT2015LaserCorrValWeeklyReport.

[152] *Electron reconstruction and identification at sqrt(s) = 7 TeV*. Tech. rep. CMS-PAS-EGM-10-004. Geneva: CERN, 2010. URL: https://cds.cern.ch/record/1299116.

[153] Vardan Khachatryan et al. "Measurements of Inclusive W and Z Cross Sections in pp Collisions at sqrt(s)=7 TeV". In: *JHEP* 01 (2011), p. 080. arXiv: 1012.2466 [hep-ex].

[154] "Validation of 2015 laser corrections with electrons". In: (Dec. 2015). URL: https://cds.cern.ch/record/2116255.

[155] Dustin Anderson. "Data Scouting in CMS". In: *38th International Conference on High Energy Physics, 3-10 August 2016, Chicago, IL, USA*. 2016. URL: https://indico.cern.ch/event/432527/contributions/1071749/attachments/1321125/1981229/08062016scoutingichep.pdf.

[156] "Data Parking and Data Scouting
at the CMS Experiment". In: (Sept. 2012). URL: https://cds.cern.ch/record/1480607.

[157] Vardan Khachatryan et al. "Search for narrow resonances in dijet final states at $\sqrt{(s)} = 8$ TeV with the novel CMS technique of data scouting". In: *Phys. Rev. Lett.* 117.3 (2016), p. 031802. DOI: 10.1103/PhysRevLett.117.031802. arXiv: 1604.08907 [hep-ex].

[158] *Searches for narrow resonances decaying to dijets in proton-proton collisions at 13 TeV using 12.9 inverse femtobarns.* Tech. rep. CMS-PAS-EXO-16-032. Geneva: CERN, 2016. URL: http://cds.cern.ch/record/2205150.

[159] Vardan Khachatryan et al. "Search for dark matter particles in proton-proton collisions at $\sqrt{s} = 8$ TeV using the razor variables". In: *JHEP* 12 (2016), p. 088. DOI: 10.1007/JHEP12(2016)088. arXiv: 1603.08914 [hep-ex].

[160] Georges Aad et al. "Search for new phenomena with the monojet and missing transverse momentum signature using the ATLAS detector in $\sqrt{s} = 7$ TeV proton-proton collisions". In: *Phys. Lett.* B705 (2011), pp. 294–312. DOI: 10.1016/j.physletb.2011.10.006. arXiv: 1106.5327 [hep-ex].

[161] Serguei Chatrchyan et al. "Search for dark matter and large extra dimensions in monojet events in pp collisions at $\sqrt{s} = 7$ TeV". In: *JHEP* 09 (2012), p. 094. DOI: 10.1007/JHEP09(2012)094. arXiv: 1206.5663 [hep-ex].

[162] Patrick J. Fox et al. "Taking a Razor to Dark Matter Parameter Space at the LHC". In: *Phys. Rev.* D86 (2012), p. 015010. DOI: 10.1103/PhysRevD.86.015010. arXiv: 1203.1662 [hep-ph].

[163] Michele Papucci, Alessandro Vichi, and Kathryn M. Zurek. "Monojet versus the rest of the world I: t-channel models". In: *JHEP* 11 (2014), p. 024. DOI: 10.1007/JHEP11(2014)024. arXiv: 1402.2285 [hep-ph].

[164] *Search for SUSY with Higgs in the diphoton final state using the razor variables*. Tech. rep. CMS-PAS-SUS-14-017. Geneva: CERN, 2015. URL: https://cds.cern.ch/record/2047472.

[165] Andrea Bocci. "The Trigger of the CMS Experiment". In: *3rd KSETA Plenary Workshop*. 2016. URL: https://indico.scc.kit.edu/indico/event/187/contribution/2/material/slides/0.pdf.

[166] Serguei Chatrchyan et al. "Missing transverse energy performance of the CMS detector". In: *JINST* 6 (2011), P09001. DOI: 10.1088/1748-0221/6/09/P09001. arXiv: 1106.5048 [physics.ins-det].

[167] Serguei Chatrchyan et al. "Search for New Physics in the Multijet and Missing Transverse Momentum Final State in Proton-Proton Collisions at $\sqrt{s} = 7$ TeV". In: *Phys. Rev. Lett.* 109 (2012), p. 171803. DOI: 10.1103/PhysRevLett.109.171803. arXiv: 1207.1898 [hep-ex].

[168] CMS Collaboration. *Particle–flow event reconstruction in CMS and performance for jets, taus, and E_T^{miss}*. CMS Physics Analysis Summary CMS-PAS-PFT-09-001. 2009. URL: http://cdsweb.cern.ch/record/1194487.

[169] CMS Collaboration. *Commissioning of the particle-flow event reconstruction with the first LHC collisions recorded in the CMS detector*. CMS Physics Analysis Summary CMS-PAS-PFT-10-011. 2010. URL: http://cdsweb.cern.ch/record/1247373.

[170] Serguei Chatrchyan et al. "Measurement of Higgs boson production and properties in the WW decay channel with leptonic final states". In: *JHEP* 01 (2014), p. 096. DOI: 10.1007/JHEP01(2014)096. arXiv: 1312.1129 [hep-ex].

[171] Serguei Chatrchyan et al. "Measurement of the properties of a Higgs boson in the four-lepton final state". In: *Phys. Rev. D* 89 (2014), p. 092007. DOI: 10.1103/PhysRevD.89.092007. arXiv: 1312.5353 [hep-ex].

[172] Johan Alwall et al. "MadGraph5: going beyond". In: *JHEP* 06 (2011), p. 128. DOI: 10.1007/JHEP06(2011)128. arXiv: 1106.0522 [hep-ph].

[173] J. Alwall et al. "The automated computation of tree-level and next-to-leading order differential cross sections, and their matching to parton shower simulations". In: *JHEP* 07 (2014), p. 079. DOI: 10.1007/JHEP07(2014)079. arXiv: 1405.0301 [hep-ph].

[174] Torbjörn Sjöstrand, Stephen Mrenna, and Peters Skands. "PYTHIA 6.4 physics and manual". In: *JHEP* 05 (2006), p. 026. DOI: 10.1088/1126-6708/2006/05/026. arXiv: hep-ph/0603175 [hep-ph].

[175] Stefan Höche et al. "Matching parton showers and matrix elements". 2006.

[176] S. Agostinelli et al. "GEANT4—a simulation toolkit". In: *Nucl. Instrum. Meth. A* 506 (2003), p. 250. DOI: 10.1016/S0168-9002(03)01368-8.

[177] Jake Anderson. "Integration and Convolution". In: *2007 BaBar RooFit Workshop*. 2007. URL: https://www.slac.stanford.edu/BFROOT/www/doc/Workshops/2007/BaBar_RooFit/talks/jake.pdf.

[178] William H. Press et al. *Numerical Recipes in C (2Nd Ed.): The Art of Scientific Computing*. New York, NY, USA: Cambridge University Press, 1992. ISBN: 0-521-43108-5.

[179] Wouter Verkerke and David P. Kirkby. "The RooFit toolkit for data modeling". In: *2003 Computing in High Energy and Nuclear Physics (CHEP03)*. eConf C0303241 (2003) MOLT007. 2003, p. 186. arXiv: physics/0306116 [physics].

[180] R. A. Fisher. "On the Mathematical Foundations of Theoretical Statistics". In: *Philosophical Transactions of the Royal Society of London A: Mathematical, Physical and Engineering Sciences* 222.594-604 (1922), pp. 309–368. ISSN: 0264-3952. DOI: 10.1098/rsta.1922.0009. URL: http://rsta.royalsocietypublishing.org/content/222/594-604/309.

[181] T. Junk. "Confidence level computation for combining searches with small statistics". In: *Nucl. Instr. and Meth. A* 434 (1999), p. 435. DOI: 10.1016/S0168-9002(99)00498-2. arXiv: hep-ex/9902006 [hep-ex].

[182] Alexander L. Read. "Modified frequentist analysis of search results (The CL_s method)". In: *Workshop on confidence limits, CERN, Geneva, Switzerland, 17-18 Jan 2000: Proceedings*. 2000. URL: http://weblib.cern.ch/abstract?CERN-OPEN-2000-205.

[183] Glen Cowan et al. "Asymptotic formulae for likelihood-based tests of new physics". In: *Eur. Phys. J.* C71 (2011). [Erratum: Eur. Phys. J.C73,2501(2013)], p. 1554. DOI: 10.1140/epjc/s10052-011-1554-0, 10.1140/epjc/s10052-013-2501-z. arXiv: 1007.1727 [physics.data-an].

[184] ATLAS and CMS Collaborations. *Procedure for the LHC Higgs boson search combination in Summer 2011*. CMS Note/ATLAS Pub CMS-NOTE-2011-005, ATL-PHYS-PUB-2011-11. 2011. URL: http://cdsweb.cern.ch/record/1379837.

[185] Mike Williams. "How good are your fits? Unbinned multivariate goodness-of-fit tests in high energy physics". In: *JINST* 5 (2010), P09004. DOI: 10.1088/1748-0221/5/09/P09004. arXiv: 1006.3019 [hep-ex].

[186] Mark F. Schilling. "Multivariate Two-Sample Tests Based on Nearest Neighbors". In: *Journal of the American Statistical Association* 81.395

(1986), pp. 799–806. ISSN: 01621459. URL: http://www.jstor.org/stable/2289012.

[187] Abraham Wald. "Tests of Statistical Hypotheses Concerning Several Parameters When the Number of Observations is Large". In: *Transactions of the American Mathematical Society* 54.3 (1943), pp. 426–482. ISSN: 00029947. URL: http://www.jstor.org/stable/1990256.

[188] S. S. Wilks. "The Large-Sample Distribution of the Likelihood Ratio for Testing Composite Hypotheses". In: *Annals Math. Statist.* 9.1 (1938), pp. 60–62. DOI: 10.1214/aoms/1177732360.

[189] Isaac Asimov. *Isaac Asimov: The Complete Stories, Vol. 1*. New York City, USA: Broadway Books, 1990.

[190] Louis Lyons. "Discovering the Significance of 5 sigma". In: (2013). arXiv: 1310.1284 [physics.data-an].

[191] Robert D. Cousins. "The JeffreysLindley paradox and discovery criteria in high energy physics". In: *Synthese* (2014). DOI: 10.1007/s11229-014-0525-z,10.1007/s11229-015-0687-3. arXiv: 1310.3791 [physics.data-an].

[192] Eilam Gross and Ofer Vitells. "Trial factors or the look elsewhere effect in high energy physics". In: *Eur. Phys. J.* C70 (2010), pp. 525–530. DOI: 10.1140/epjc/s10052-010-1470-8. arXiv: 1005.1891 [physics.data-an].

[193] CMS Collaboration. *CMS Luminosity Based on Pixel Cluster Counting - Summer 2013 Update*. CMS Physics Analysis Summary CMS-PAS-LUM-13-001. 2013. URL: https://cds.cern.ch/record/1598864.

[194] D Bourilkov, R C Group, and M R Whalley. "LHAPDF: PDF use from the Tevatron to the LHC". 2006.

[195] Sergey Alekhin et al. "The PDF4LHC Working Group Interim Report". 2011.

[196] Michiel Botje et al. "The PDF4LHC Working Group Interim Recommendations". 2011.

[197] Pavel M. Nadolsky et al. "Implications of CTEQ global analysis for collider observables". In: *Phys. Rev. D* 78 (2008), p. 013004. DOI: 10.1103/PhysRevD.78.013004. arXiv: 0802.0007 [hep-ph].

[198] A. D. Martin et al. "Update of parton distributions at NNLO". In: *Phys. Lett. B* 652 (2007), p. 292. DOI: 10.1016/j.physletb.2007.07.040. arXiv: 0706.0459 [hep-ph].

[199] Georges Aad et al. "ATLAS Run 1 searches for direct pair production of third-generation squarks at the Large Hadron Collider". In: *Eur. Phys. J. C* 75 (2015), p. 510. DOI: 10.1140/epjc/s10052-015-3726-9. arXiv: 1506.08616 [hep-ex].

[200] Georges Aad et al. "Summary of the searches for squarks and gluinos using $\sqrt{s} = 8$ TeV pp collisions with the ATLAS experiment at the LHC". In: *JHEP* 10 (2015), p. 054. DOI: 10.1007/JHEP10(2015)054. arXiv: 1507.05525 [hep-ex].

[201] Georges Aad et al. "Search for squarks and gluinos in events with isolated leptons, jets and missing transverse momentum at $\sqrt{s} = 8$ TeV with the ATLAS detector". In: *JHEP* 04 (2015), p. 116. DOI: 10.1007/JHEP04(2015)116. arXiv: 1501.03555 [hep-ex].

[202] Serguei Chatrchyan et al. "Search for supersymmetry in hadronic final states with missing transverse energy using the variables AlphaT and b-quark multiplicity in pp collisions at 8 TeV". In: *Eur. Phys. J. C* 73 (2013), p. 2568. DOI: 10.1140/epjc/s10052-013-2568-6. arXiv: 1303.2985 [hep-ex].

[203] Vardan Khachatryan et al. "Searches for supersymmetry using the M_{T2} variable in hadronic events produced in pp collisions at 8 TeV". In: *JHEP* 05 (2015), p. 078. DOI: 10.1007/JHEP05(2015)078. arXiv: 1502.04358 [hep-ex].

[204] Vardan Khachatryan et al. "Search for supersymmetry in the multijet and missing transverse momentum final state in pp collisions at 13 TeV". In: *Phys. Lett.* B758 (2016), p. 152. DOI: 10.1016/j.physletb.2016.05.002. arXiv: 1602.06581 [hep-ex].

[205] Vardan Khachatryan et al. "Search for new physics with the MT2 variable in all-jets final states produced in pp collisions at $\sqrt{s} = 13$ TeV". In: (2016). arXiv: 1603.04053 [hep-ex].

[206] Vardan Khachatryan et al. "Search for new physics in same-sign dilepton events in proton-proton collisions at $\sqrt{s} = 13$ TeV". In: (2016). arXiv: 1605.03171 [hep-ex].

[207] Vardan Khachatryan et al. "Search for new physics in final states with two opposite-sign, same-flavor leptons, jets, and missing transverse momentum in pp collisions at $\sqrt{s} = 13$ TeV". In: (2016). arXiv: 1607.00915 [hep-ex].

[208] Georges Aad et al. "Search for new phenomena in final states with large jet multiplicities and missing transverse momentum with ATLAS using $\sqrt{s} = 13$ TeV proton-proton collisions". In: *Phys. Lett. B* 757 (2016), p. 334. DOI: 10.1016/j.physletb.2016.04.005. arXiv: 1602.06194 [hep-ex].

[209] Georges Aad et al. "Search for supersymmetry at $\sqrt{s} = 13$ TeV in final states with jets and two same-sign leptons or three leptons with the ATLAS detector". In: *Eur. Phys. J. C* 76 (2016), p. 259. DOI: 10.1140/epjc/s10052-016-4095-8. arXiv: 1602.09058 [hep-ex].

[210] Morad Aaboud et al. "Search for new phenomena in final states with an energetic jet and large missing transverse momentum in pp collisions at $\sqrt{s} = 13$ TeV using the ATLAS detector". In: (2016). arXiv: 1604.07773 [hep-ex].

[211] Morad Aaboud et al. "Search for squarks and gluinos in final states with jets and missing transverse momentum at $\sqrt{s} = 13$ TeV with the ATLAS detector". In: (2016). arXiv: 1605.03814 [hep-ex].

[212] Georges Aad et al. "Search for gluinos in events with an isolated lepton, jets and missing transverse momentum at $\sqrt{s}$ = 13 TeV with the ATLAS detector". In: (2016). arXiv: 1605.04285 [hep-ex].

[213] Georges Aad et al. "Search for pair production of gluinos decaying via stop and sbottom in events with b-jets and large missing transverse momentum in pp collisions at $\sqrt{s} = 13$ TeV with the ATLAS detector". In: (2016). arXiv: 1605.09318 [hep-ex].

[214] Morad Aaboud et al. "Search for top squarks in final states with one isolated lepton, jets, and missing transverse momentum in $\sqrt{s} = 13$ TeV pp collisions with the ATLAS detector". In: (2016). arXiv: 1606.03903 [hep-ex].

[215] Morad Aaboud et al. "Search for bottom squark pair production in proton–proton collisions at $\sqrt{s}$ =13 TeV with the ATLAS detector". In: (2016). arXiv: 1606.08772 [hep-ex].

[216] Morad Aaboud et al. "Search for supersymmetry in a final state containing two photons and missing transverse momentum in $\sqrt{s}$ = 13 TeV pp collisions at the LHC using the ATLAS detector". In: (2016). arXiv: 1606.09150 [hep-ex].

[217] Simone Alioli et al. "NLO single-top production matched with shower in POWHEG: s- and t-channel contributions". In: *JHEP* 09 (2009). [Erratum: JHEP02,011(2010)], p. 111. DOI: 10.1007/JHEP02(2010)011, 10.1088/1126-6708/2009/09/111. arXiv: 0907.4076 [hep-ph].

[218] Emanuele Re. "Single-top Wt-channel production matched with parton showers using the POWHEG method". In: *Eur. Phys. J.* C71 (2011), p. 1547. DOI: 10.1140/epjc/s10052-011-1547-z. arXiv: 1009.2450 [hep-ph].

[219] Torbjörn Sjöstrand, Stephen Mrenna, and Peter Skands. "A brief introduction to PYTHIA 8.1". In: *Computer Physics Communications* 178.11 (2008), pp. 852–867. ISSN: 0010-4655. DOI: http://dx.doi.org/10.1016/j.cpc.2008.01.036. URL: http://www.sciencedirect.com/science/article/pii/S0010465508000441.

[220] Richard D. Ball et al. "Parton distributions for the LHC Run II". In: *JHEP* 04 (2015), p. 040. DOI: 10.1007/JHEP04(2015)040. arXiv: 1410.8849 [hep-ph].

[221] Salavat Abdullin et al. "The fast simulation of the CMS detector at LHC". In: *J. Phys.: Conf. Ser.* 331 (2011), p. 032049. DOI: 10.1088/1742-6596/331/3/032049.

[222] Vardan Khachatryan et al. "Performance of Electron Reconstruction and Selection with the CMS Detector in Proton-Proton Collisions at $\sqrt{s}$ = 8 TeV". In: *JINST* 10.06 (2015), P06005. DOI: 10.1088/1748-0221/10/06/P06005. arXiv: 1502.02701 [physics.ins-det].

[223] CMS Collaboration. *Study of pileup removal algorithms for jets*. CMS Physics Analysis Summary CMS-PAS-JME-14-001. 2014. URL: http://cds.cern.ch/record/1751454.

[224] Serguei Chatrchyan et al. "Performance of CMS muon reconstruction in pp collision events at $\sqrt{s} = 7$ TeV". In: *JINST* 7 (2012), P10002. DOI: 10.1088/1748-0221/7/10/P10002. arXiv: 1206.4071 [physics.ins-det].

[225] Vardan Khachatryan et al. "Reconstruction and identification of τ lepton decays to hadrons and ν_τ at CMS". In: *JINST* 11.01 (2016), P01019. DOI: 10.1088/1748-0221/11/01/P01019. arXiv: 1510.07488 [physics.ins-det].

[226] *Identification of b quark jets at the CMS Experiment in the LHC Run 2*. Tech. rep. CMS-PAS-BTV-15-001. Geneva: CERN, 2016. URL: https://cds.cern.ch/record/2138504.

[227] Vardan Khachatryan et al. "Inclusive search for supersymmetry using razor variables in pp collisions at $\sqrt{s} = 13$ TeV". In: *Phys. Rev. D* (2016). [Phys. Rev.D95,012003(2017)]. DOI: 10.1103/PhysRevD.95.012003. arXiv: 1609.07658 [hep-ex].

[228] *CMS Luminosity Measurement for the 2015 Data Taking Period*. Tech. rep. CMS-PAS-LUM-15-001. 2016. URL: https://cds.cern.ch/record/2138682.

[229] Michael Dine, Alex Kagan, and Stuart Samuel. "Naturalness in supersymmetry, or raising the supersymmetry breaking scale". In: *Physics Letters B* 243.3 (1990), pp. 250–256. ISSN: 0370-2693. DOI: http://dx.doi.org/10.1016/0370-2693(90)90847-Y. URL: ht

tp://www.sciencedirect.com/science/article/pii/037026939090847Y.

[230] Andrew G. Cohen, D. B. Kaplan, and A. E. Nelson. "The More minimal supersymmetric standard model". In: *Phys. Lett.* B388 (1996), pp. 588–598. DOI: 10.1016/S0370-2693(96)01183-5. arXiv: hep-ph/9607394 [hep-ph].

[231] "Projected Performance of an Upgraded CMS Detector at the LHC and HL-LHC: Contribution to the Snowmass Process". In: *Community Summer Study 2013: Snowmass on the Mississippi (CSS2013) Minneapolis, MN, USA, July 29-August 6, 2013*. 2013. arXiv: 1307.7135. URL: https://inspirehep.net/record/1244669/files/arXiv:1307.7135.pdf.

[232] *Study of the Discovery Reach in Searches for Supersymmetry at CMS with 3000/fb*. Tech. rep. CMS-PAS-FTR-13-014. Geneva: CERN, 2013. URL: http://cds.cern.ch/record/1607141.

[233] L. Rossi, and O. Brüning. *High Luminosity Large Hadron Collider A description for the European Strategy Preparatory Group*. Tech. rep. CERN-ATS-2012-236. Geneva: CERN, Aug. 2012.

[234] L. Zhang, R. Mao, F. Yang, and R. Zhu. "LSO/LYSO Crystals for Calorimeters in Future HEP Experiments". In: *IEEE Transactions on Nuclear Science* 61.1 (Feb. 2014), pp. 483–488. ISSN: 0018-9499.

[235] R. Mao, L. Zhang, and R. Zhu. "Gamma ray induced radiation damage in PWO and LSO/LYSO crystals". In: *Nuclear Science Symposium Conference Record (NSS/MIC), 2009 IEEE*. Oct. 2009, pp. 2045–2049. DOI: 10.1109/NSSMIC.2009.5402126.

[236] J. Chen, R. Mao, L. Zhang, and R. Zhu. "Gamma-Ray Induced Radiation Damage in Large Size LSO and LYSO Crystal Samples". In: *IEEE Transactions on Nuclear Science* 54.4 (Aug. 2007), pp. 1319–1326. ISSN: 0018-9499. DOI: 10.1109/TNS.2007.902370.

[237] L. Zhang, R. Mao, and R. Zhu. "Effects of neutron irradiations in various crystal samples of large size for future crystal calorimeter". In: *Nuclear Science Symposium Conference Record (NSS/MIC), 2009 IEEE*. Oct. 2009, pp. 2041–2044. DOI: 10.1109/NSSMIC.2009.5402125.

[238] G. Dissertori, D. Luckey, Nessi-Tedaldi, et al. "Results on damage induced by high-energy protons in LYSO calorimeter crystals". In: *NIM A 745 (2014) 1-6* (). DOI: 10.1016/j.nima.2014.02.003. arXiv: 1309.3872 [physics.ins-det].

[239] D Contardo and J Spalding. *CMS Phase 2 Upgrade: Preliminary Plan and Cost Estimate*. Tech. rep. CERN-RRB-2013-124. Geneva: CERN, Oct. 2013.

[240] W. W. Moses and S. E. Derenzo. "Prospects for Time-of-Flight PET using LSO Scintillator". In: *IEEE Transactions on Nuclear Science* 46.3 (June 1999), pp. 474–478. ISSN: 0018-9499. DOI: 10.1109/TNS.2007.902370.

[241] D. Anderson et al. "On timing properties of LYSO-based calorimeters". In: *Nuclear Instruments and Methods in Physics Research Section A: Accelerators, Spectrometers, Detectors and Associated Equipment* 794 (2015), pp. 7–14. ISSN: 0168-9002. DOI: http://dx.doi.org/10.1016/j.nima.2015.04.013. URL: http://www.sciencedirect.com/science/article/pii/S0168900215004829.

[242] A. Ronzhin, S. Los, E. Ramberg, et al. "Development of a new fast shower maximum detector based on microchannel plates photomultipliers (MCP-PMT) as an active element". In: *NIM A 759 (2014) 65-73* (). ISSN: 0168-9002. DOI: http://dx.doi.org/10.1016/j.nima.2014.05.039. URL: http://www.sciencedirect.com/science/article/pii/S016890021400566X.

[243] http://www.hamamatsu.com/resources/pdf/etd/R3809U-50_TPMH1067E.pdf.

[244] http://www.photek.com/pdf/datasheets/detectors/DS006_Photomultipliers.pdf.

[245] S. Ritt, R. Dinapoli, and U. Hartmann. "Application of the DRS chip for fast waveform digitizing". In: *NIM A 623 (2010) 486-488* ().

[246] http://www.ellsworth.com/dow-corning-q2-3067-optical-couplant-453g-bottle.

[247] M. Albrecht, K. Andert, P. Anselmino, et al. "Scintillators and Wavelength Shifters for the Detection of Ionizing Radiation". In: *Proceedings of the 8th Conference on astroparticle, particle and space physics, detectors and medical physics applications* (2003), pp. 502–511. DOI: 10.1142/9789812702708_0074.

[248] *Search for physics beyond the standard model in events with two opposite-sign same-flavor leptons, jets, and missing transverse energy in pp collisions at sqrt[s] = 8 TeV*. Tech. rep. CMS-PAS-SUS-12-019. Geneva: CERN, 2014. URL: http://cds.cern.ch/record/1751493.

[249] Georges Aad et al. "Search for supersymmetry in events containing a same-flavour opposite-sign dilepton pair, jets, and large missing transverse momentum in $\sqrt{s} = 8$ TeV pp collisions with the ATLAS detector". In: *Eur. Phys. J.* C75.7 (2015). [Erratum: Eur. Phys. J.C75,no.10,463(2015)], p. 318. DOI: 10.1140/epjc/s10052-015-3661-9,10.1140/epjc/s10052-015-3518-2. arXiv: 1503.03290 [hep-ex].

[250] Peisi Huang and Carlos E. M. Wagner. "CMS kinematic edge from sbottoms". In: *Phys. Rev.* D91.1 (2015), p. 015014. DOI: 10.1103/PhysRevD.91.015014. arXiv: 1410.4998 [hep-ph].

[251] Ben Allanach, Are R. Raklev, and Anders Kvellestad. "Interpreting a CMS excess in $lljj + missing$-transverse-momentum with the golden cascade of the minimal supersymmetric standard model". In: *Phys. Rev.* D91.11 (2015), p. 115022. DOI: 10.1103/PhysRevD.91.115022. arXiv: 1409.3532 [hep-ph].

[252] Ben Allanach, Are Raklev, and Anders Kvellestad. "Consistency of the recent ATLAS $Z + E_T^{miss}$ excess in a simplified GGM model". In: *Phys. Rev.* D91 (2015), p. 095016. DOI: 10.1103/PhysRevD.91.095016. arXiv: 1504.02752 [hep-ph].

[253] Junjie Cao et al. "Explanation of the ATLAS Z-Peaked Excess in the NMSSM". In: *JHEP* 06 (2015), p. 152. DOI: 10.1007/JHEP06(2015)152. arXiv: 1504.07869 [hep-ph].

[254] Ulrich Ellwanger. "Possible explanation of excess events in the search for jets, missing transverse momentum and a Z boson in pp collisions". In: *Eur. Phys. J.* C75.8 (2015), p. 367. DOI: 10.1140/epjc/s10052-015-3591-6. arXiv: 1504.02244 [hep-ph].

[255] Archil Kobakhidze et al. "ATLAS Z-peaked excess in the MSSM with a light sbottom or stop". In: *Phys. Rev.* D92.7 (2015), p. 075008. DOI: 10.1103/PhysRevD.92.075008. arXiv: 1504.04390 [hep-ph].

[256] *Search for SUSY in Events with a Higgs Decaying to Two Photons Using the Razor Variables*. Tech. rep. CMS-PAS-SUS-16-012. Geneva: CERN, 2016. URL: https://cds.cern.ch/record/2205153.

[257] Ann Miao Wang. "New Physics Models in the Diphoton Final State at CMS". Senior Thesis (Major). 1200 E. California Blvd., Pasadena, CA 91125, USA: California Institute of Technology, 2015. DOI: 10.7907/Z9CC0XMN. URL: http://resolver.caltech.edu/CaltechTHESIS:01152016-102117113.

[258] Torbjörn Sjöstrand, Stephen Mrenna, and Peter Z. Skands. "PYTHIA 6.4 Physics and Manual". In: *JHEP* 05 (2006), p. 026. DOI: 10.1088/1126-6708/2006/05/026. arXiv: hep-ph/0603175 [hep-ph].

[259] Torbjörn Sjöstrand et al. "An Introduction to PYTHIA 8.2". In: *Comput. Phys. Commun.* 191 (2015), pp. 159–177. DOI: 10.1016/j.cpc.2015.01.024. arXiv: 1410.3012 [hep-ph].

[260] Richard D. Ball et al. "Parton distributions with QED corrections". In: *Nucl. Phys.* B877 (2013), pp. 290–320. DOI: 10.1016/j.nuclphysb.2013.10.010. arXiv: 1308.0598 [hep-ph].

[261] Stefano Carrazza. "Towards the determination of the photon parton distribution function constrained by LHC data". In: *PoS* DIS2013 (2013), p. 279. arXiv: 1307.1131 [hep-ph].

[262] Stefano Carrazza. "Towards an unbiased determination of parton distributions with QED corrections". In: *Proceedings, 48th Rencontres de Moriond on QCD and High Energy Interactions*. 2013, pp. 357–360. arXiv: 1305.4179 [hep-ph]. URL: http://inspirehep.net/record/1234242/files/arXiv:1305.4179.pdf.

[263] J. de Favereau et al. "DELPHES 3, A modular framework for fast simulation of a generic collider experiment". In: *JHEP* 02 (2014), p. 057. DOI: 10.1007/JHEP02(2014)057. arXiv: 1307.6346 [hep-ex].

[264] *Phenomenological MSSM interpretation of CMS results at* $\sqrt{s} = 7$ *and 8 TeV*. Tech. rep. CMS-PAS-SUS-15-010. Geneva: CERN, 2015. URL: http://cds.cern.ch/record/2063744.

[265] Mikael Chala et al. "Constraining Dark Sectors with Monojets and Dijets". In: *JHEP* 07 (2015), p. 089. DOI: 10.1007/JHEP07(2015)089. arXiv: 1503.05916 [hep-ph].

[266] ATLAS Collaboration. *Search for light dijet resonances with the ATLAS detector using a Trigger-Level Analysis in LHC pp collisions at* $\sqrt{s} = 13$ *TeV*. ATLAS Conference Report ATLAS-CONF-2016-030. June 2016. URL: http://cds.cern.ch/record/2161135.

[267] Vardan Khachatryan et al. "Search for narrow resonances decaying to dijets in proton-proton collisions at $\sqrt{s} = 13$ TeV". In: *Phys. Rev. Lett.* 116 (2016), p. 071801. DOI: 10.1103/PhysRevLett.116.071801. arXiv: 1512.01224 [hep-ex].

[268] Georges Aad et al. "Search for new phenomena in dijet mass and angular distributions from pp collisions at $\sqrt{s} = 13$ TeV with the ATLAS detector". In: *Phys. Lett.* B754 (2016), pp. 302–322. DOI: 10.1016/j.physletb.2016.01.032. arXiv: 1512.01530 [hep-ex].

[269] V. Khachatryan et al. "Search for resonances and quantum black holes using dijet mass spectra in proton-proton collisions at $\sqrt{s} = 8$ TeV". In: *Phys. Rev. D* 91 (2015), p. 052009. DOI: 10.1103/PhysRevD.91.052009. arXiv: 1501.04198 [hep-ex].

[270] G. Aad et al. "Search for new phenomena in the dijet mass distribution using pp collision data at $\sqrt{s} = 8$ TeV with the ATLAS detector". In: *Phys. Rev. D* 91 (2015), p. 052007. DOI: 10.1103/PhysRevD.91.052007. arXiv: 1407.1376 [hep-ex].

[271] Serguei Chatrchyan et al. "Search for narrow resonances using the dijet mass spectrum in pp collisions at $\sqrt{s} = 8$ TeV". In: *Phys. Rev. D* 87 (2013), p. 114015. DOI: 10.1103/PhysRevD.87.114015. arXiv: 1302.4794 [hep-ex].

[272] Serguei Chatrchyan et al. "Search for narrow resonances and quantum black holes in inclusive and b-tagged dijet mass spectra from pp collisions at $\sqrt{s} = 7$ TeV". In: *JHEP* 01 (2013), p. 013. DOI: 10.1007/JHEP01(2013)013. arXiv: 1210.2387 [hep-ex].

[273] Georges Aad et al. "Search for new physics in the dijet mass distribution using 1 fb^{-1} of pp collision data at $\sqrt{s} = 7$ TeV collected by the ATLAS detector". In: *Phys. Lett. B* 708 (2012), p. 37. DOI: 10.1016/j.physletb.2012.01.035. arXiv: 1108.6311 [hep-ex].

[274] Georges Aad et al. "ATLAS search for new phenomena in dijet mass and angular distributions using pp collisions at $\sqrt{s} = 7$ TeV". In: *JHEP* 01 (2013), p. 029. DOI: 10.1007/JHEP01(2013)029. arXiv: 1210.1718 [hep-ex].

[275] Serguei Chatrchyan et al. "Search for resonances in the dijet mass spectrum from 7 TeV pp collisions at CMS". In: *Phys. Lett. B* 704 (2011), p. 123. DOI: 10.1016/j.physletb.2011.09.015. arXiv: 1107.4771 [hep-ex].

[276] Georges Aad et al. "Search for new physics in dijet mass and angular distributions in pp collisions at $\sqrt{s} = 7$ TeV measured with the ATLAS detector". In: *New J. Phys.* 13 (2011), p. 053044. DOI: 10.1088/1367-2630/13/5/053044. arXiv: 1103.3864 [hep-ex].

[277] Vardan Khachatryan et al. "Search for Dijet Resonances in 7 TeV pp Collisions at CMS". In: *Phys. Rev. Lett.* 105 (2010), p. 211801. DOI: 10.1103/PhysRevLett.105.211801. arXiv: 1010.0203 [hep-ex].

[278] G. Aad et al. "Search for New Particles in Two-Jet Final States in 7 TeV Proton-Proton Collisions with the ATLAS Detector at the LHC". In: *Phys. Rev. Lett.* 105 (2010), p. 161801. DOI: 10.1103/PhysRevLett.105.161801. arXiv: 1008.2461 [hep-ex].

[279] Robert M. Harris and Konstantinos Kousouris. "Searches for dijet resonances at hadron colliders". In: *Int. J. Mod. Phys. A* 26 (2011), p. 5005. DOI: 10.1142/S0217751X11054905. arXiv: 1110.5302 [hep-ex].

[280] Luis A. Anchordoqui et al. "Dijet Signals for Low Mass Strings at the LHC". In: *Phys. Rev. Lett.* 101 (2008), p. 241803. DOI: 10.1103/PhysRevLett.101.241803. arXiv: 0808.0497 [hep-ph].

[281] Schuyler Cullen, Maxim Perelstein, and Michael E. Peskin. "TeV strings and collider probes of large extra dimensions". In: *Phys. Rev. D* 62 (2000), p. 055012. DOI: 10.1103/PhysRevD.62.055012. arXiv: hep-ph/0001166 [hep-ph].

[282] JoAnne L. Hewett and Thomas G. Rizzo. "Low-energy phenomenology of superstring-inspired E(6) models". In: *Phys. Rept.* 183 (1989), p. 193. DOI: 10.1016/0370-1573(89)90071-9.

[283] Paul H. Frampton and Sheldon L. Glashow. "Chiral Color: An Alternative to the Standard Model". In: *Phys. Lett. B* 190 (1987), p. 157. DOI: 10.1016/0370-2693(87)90859-8.

[284] R. Sekhar Chivukula et al. "Hadron collider production of massive color-octet vector bosons at next-to-leading order". In: *Phys. Rev. D* 87 (2013), p. 094011. DOI: 10.1103/PhysRevD.87.094011. arXiv: 1303.1120 [hep-ph].

[285] Elizabeth H. Simmons. "Coloron phenomenology". In: *Phys. Rev. D* 55 (1997), p. 1678. DOI: 10.1103/PhysRevD.55.1678. arXiv: hep-ph/9608269 [hep-ph].

[286] U. Baur, I. Hinchliffe, and D. Zeppenfeld. "Excited Quark Production at Hadron Colliders". In: *Int. J. Mod. Phys. A* 02 (1987), p. 1285. DOI: 10.1142/S0217751X87000661.

[287] U. Baur, M. Spira, and P. M. Zerwas. "Excited quark and lepton production at hadron colliders". In: *Phys. Rev. D* 42 (1990), p. 815. DOI: 10.1103/PhysRevD.42.815.

[288] Tao Han, Ian Lewis, and Zhen Liu. "Colored resonant signals at the LHC: largest rate and simplest topology". In: *JHEP* 12 (2010), p. 085. DOI: 10.1007/JHEP12(2010)085. arXiv: 1010.4309 [hep-ph].

[289] E. Eichten et al. "Supercollider physics". In: *Rev. Mod. Phys.* 56 (1984), p. 579. DOI: 10.1103/RevModPhys.56.579.

[290] Lisa Randall and Raman Sundrum. "An Alternative to compactification". In: *Phys. Rev. Lett.* 83 (1999), p. 4690. DOI: 10.1103/PhysRevLett.83.4690. arXiv: hep-th/9906064 [hep-th].

[291] R. Sekhar Chivukula, Elizabeth H. Simmons, and Natascia Vignaroli. "Distinguishing dijet resonances at the LHC". In: *Phys. Rev.* D91.5 (2015), p. 055019. DOI: 10.1103/PhysRevD.91.055019. arXiv: 1412.3094 [hep-ph].

[292] Giorgio Busoni et al. "Recommendations on presenting LHC searches for missing transverse energy signals using simplified *s*-channel models of dark matter". In: (2016). Ed. by Antonio Boveia et al. arXiv: 1603.04156 [hep-ex].

[293] Bogdan A. Dobrescu and Felix Yu. "Coupling-mass mapping of dijet peak searches". In: *Phys. Rev.* D88.3 (2013), p. 035021. DOI: 10.1103/PhysRevD.88.035021, 10.1103/PhysRevD.90.079901. arXiv: 1306.2629 [hep-ph].

[294] Daniel Abercrombie et al. "Dark Matter Benchmark Models for Early LHC Run-2 Searches: Report of the ATLAS/CMS Dark Matter Forum". In: (2015). Ed. by Antonio Boveia et al. arXiv: 1507.00966 [hep-ex].

[295] Matteo Cacciari and Gavin P. Salam. "Dispelling the N^3 myth for the k_t jet-finder". In: *Phys. Lett. B* 641 (2006), p. 57. DOI: 10.1016/j.physletb.2006.08.037. arXiv: hep-ph/0512210 [hep-ph].

[296] Serguei Chatrchyan et al. "Determination of jet energy calibration and transverse momentum resolution in CMS". In: *JINST* 6 (2011), P11002. DOI: 10.1088/1748-0221/6/11/P11002. arXiv: 1107.4277 [physics.ins-det].

[297] CMS Collaboration. *Jet Performance in pp Collisions at* $\sqrt{s} = 7$ *TeV*. CMS Physics Analysis Summary CMS-PAS-JME-10-003. 2010. URL: http://cdsweb.cern.ch/record/1279362.

[298] T. Aaltonen et al. "Search for new particles decaying into dijets in proton-antiproton collisions at $\sqrt{s} = 1.96$ TeV". In: *Phys. Rev. D* 79 (2009), p. 112002. DOI: 10.1103/PhysRevD.79.112002. arXiv: 0812.4036 [hep-ex].

[299] Torbjörn Sjöstrand, Stephen Mrenna, and Peter Skands. "A brief introduction to PYTHIA 8.1". In: *Comp. Phys. Comm.* 178 (2008), p. 852. DOI: 10.1016/j.cpc.2008.01.036. arXiv: 0710.3820 [hep-ph].

[300] A. L. Read. "Presentation of search results: the CL_s technique". In: *J. Phys. G* 28 (2002), p. 2693. DOI: 10.1088/0954-3899/28/10/313.

[301] Jalal Abdallah et al. "Simplified Models for Dark Matter Searches at the LHC". In: *Phys. Dark Univ.* 9-10 (2015), pp. 8–23. DOI: 10.1016/j.dark.2015.08.001. arXiv: 1506.03116 [hep-ph].

[302] Jonathan Pumplin et al. "New generation of parton distributions with uncertainties from global QCD analysis". In: *JHEP* 07 (2002), p. 012. DOI: 10.1088/1126-6708/2002/07/012. arXiv: hep-ph/0201195 [hep-ph].

[303] *Search for light vector resonances decaying to quarks at 13 TeV*. Tech. rep. CMS-PAS-EXO-16-030. Geneva: CERN, 2016. URL: https://cds.cern.ch/record/2202715.

[304] *Search for dark matter in final states with an energetic jet, or a hadronically decaying W or Z boson using* 12.9 fb^{-1} *of data at* $\sqrt{s} = 13$ TeV. Tech. rep. CMS-PAS-EXO-16-037. Geneva: CERN, 2016. URL: https://cds.cern.ch/record/2205746.

[305] *Search for dark matter and graviton produced in association with a photon in pp collisions at sqrts = 13 TeV*. Tech. rep. CMS-PAS-EXO-16-039. Geneva: CERN, 2016. URL: https://cds.cern.ch/record/2205148.

[306] *Search for dark matter and unparticles in events with a Z boson and missing transverse momentum in proton-proton collisions at sqrt(s) = 13 TeV*. Tech. rep. CMS-PAS-EXO-16-010. Geneva: CERN, 2016. URL: https://cds.cern.ch/record/2204920.

[307] D. S. Akerib et al. "Results from a search for dark matter in LUX with 332 live days of exposure". In: (2016). arXiv: 1608.07648 [astro-ph.CO].

[308] Andi Tan et al. "Dark Matter Results from First 98.7-day Data of PandaX-II Experiment". In: (2016). arXiv: 1607.07400 [hep-ex].

[309] R. Agnese et al. "New Results from the Search for Low-Mass Weakly Interacting Massive Particles with the CDMS Low Ionization Threshold Experiment". In: *Phys. Rev. Lett.* 116.7 (2016), p. 071301. DOI: 10.1103/PhysRevLett.116.071301. arXiv: 1509.02448 [astro-ph.CO].

[310] G. Angloher et al. "Results on light dark matter particles with a low-threshold CRESST-II detector". In: *Eur. Phys. J.* C76.1 (2016), p. 25. DOI: 10.1140/epjc/s10052-016-3877-3. arXiv: 1509.01515 [astro-ph.CO].

[311] C. Amole et al. "Improved dark matter search results from PICO-2L Run 2". In: *Phys. Rev.* D93.6 (2016), p. 061101. DOI: 10.1103/PhysRevD.93.061101. arXiv: 1601.03729 [astro-ph.CO].

[312] C. Amole et al. "Dark matter search results from the PICO-60 CF_3I bubble chamber". In: *Phys. Rev.* D93.5 (2016), p. 052014. DOI: 10.1103/PhysRevD.93.052014. arXiv: 1510.07754 [hep-ex].

[313] M. G. Aartsen et al. "Improved limits on dark matter annihilation in the Sun with the 79-string IceCube detector and implications for supersymmetry". In: *JCAP* 1604.04 (2016), p. 022. DOI: 10.1088/1475-7516/2016/04/022. arXiv: 1601.00653 [hep-ph].

[314] K. Choi et al. "Search for neutrinos from annihilation of captured low-mass dark matter particles in the Sun by Super-Kamiokande". In: *Phys. Rev. Lett.* 114.14 (2015), p. 141301. DOI: 10.1103/PhysRevLett.114.141301. arXiv: 1503.04858 [hep-ex].

[315] CMS collaboration. "Dark Matter Summary Plots from CMS for ICHEP 2016". Aug. 2016. URL: https://cds.cern.ch/record/2208044.